



**THE ADSORPTION AND REACTION  
OF KETONES ON THE SURFACE OF  
GROUP 10 METAL CATALYSTS,  
A DENSITY FUNCTIONAL THEORY  
STUDY**

Rajinder K. Mann

Submitted in fulfilment of the requirements for the  
degree of Ph. D.

Cardiff University

September 2004

UMI Number: U583974

All rights reserved

INFORMATION TO ALL USERS

The quality of this reproduction is dependent upon the quality of the copy submitted.

In the unlikely event that the author did not send a complete manuscript and there are missing pages, these will be noted. Also, if material had to be removed, a note will indicate the deletion.



UMI U583974

Published by ProQuest LLC 2013. Copyright in the Dissertation held by the Author.  
Microform Edition © ProQuest LLC.

All rights reserved. This work is protected against  
unauthorized copying under Title 17, United States Code.



ProQuest LLC  
789 East Eisenhower Parkway  
P.O. Box 1346  
Ann Arbor, MI 48106-1346



## *Acknowledgements*

The easy bit!!!...Who to acknowledge? Well I guess over the years so many people have cared, encouraged and supported me emotionally and financially that it only seems right to express my sincerest gratitude towards them.

Firstly, many thanks to my supervisor Dr. David Willock without his continual guidance, support and enthusiasm I sure as hell wouldn't have got as far as writing this!

Secondly, a big massive "Cheers!!!" for showing me the "ropes" go to Drs. Robert Hayes, Anthony Dickinson, Mark Norton, Karen Avery, Christopher Cooper and Natasha Galea. I am also grateful to everybody in the computer lab for their help and friendship: Jon, Farah, Bob, Olivier, Rudy, Arturo and Gareth. To my housemates: Susan Hammond and Ruth Osiname - we eventually come to a halt. Big respect for Carl Snellgrove, the most reliable locksmith I know! To the gang: Marie, Hayley, George, Beanie, Aaron (just in case you check!), German Karin, Meinir and the rest of my friends - time to get drunk!

To my parents: Mum, Harbhajan Kaur, and Dad, Avtar Singh, thank you for understanding the need for me to learn and grow into the person I am today. If I knew how to write these words in Punjabi then I would! To my elder sisters Harps and Satwinder, thanks for spoiling me rotten over the years, which are now well and truly over thanks to the birth of gorgeous baby Amar! I'll make up for missing your 1<sup>st</sup> Birthday. To my brother, Narinder - cheers for making me so broke!!! To my very dysfunctional family - thanks for everything!

Finally, I must acknowledge EPSRC and the PI-IMI consortium for their financial funding and contribution of technical expertise throughout the course of this research. Many thanks to the industrialists and academics involved in this project from the chemical engineering and catalysis divisions of Johnson Matthey, BP-Amoco, Robinson Brothers, Grace Davidson and the universities of Glasgow, Cambridge and Birmingham. We are grateful for the use of software provided by Accelrys and their cooperation *via* Dr. Xenophon Krokidis and Dr. Victor Milman. Special thanks go to Prof. Graham Hutchings and Dr. Stuart Taylor from Cardiff University for advice and expertise on catalysis and co-worker Nick Dummer.

"Cheers, Ed for running the elastic bands - sorry it was all last minute!"

# *Abstract*

Cardiff University

## THE ADSORPTION AND REACTION OF KETONES ON THE SURFACE OF GROUP 10 METAL CATALYSTS, A DENSITY FUNCTIONAL THEORY STUDY

by Rajinder K. Mann

The hydrogenation of ketones over cinchona modified transition metal surfaces is an important step in many applications in heterogeneous catalysis, such as the production of unsaturated alcohols from  $\alpha$ - $\beta$  unsaturated ketones. In the gas-phase simple ketones, such as acetone, do not have a significant population of the *enol* isomer. Even so deuterium exchange studies clearly point to the involvement of the *enol* form in hydrogenation catalysis over some group 10 metals.

Two different aspects of the nature of the intermediates involved in the model enantioselective hydrogenation reaction are investigated in this work. In Chapter 5, a combined semi-empirical and *ab initio* conformational analysis of cinchonidine reveals four stable structures of the alkaloid, two Open and two Closed forms. The reaction energies for the formation of the diastereomeric complex between protonated cinchonidine conformers and the *s-cis* and *s-trans* isomers of ethyl pyruvate and butane-2,3-dione are used to predict the relative concentrations of these intermediates. For both reactants, the complex involving the Open(3)H<sup>+</sup> structure with the *s-cis* conformation of the reactant, favouring the pro (*R*) lactate and hydroxybutanone are optimised to be the dominant intermediates formed in the hydrogenation reaction, providing theoretical enantiomeric excesses of 33% and 98%, respectively.

In Chapters 6 and 7, periodic density functional theory calculations are used to examine the chemisorption of formaldehyde and acetone as model *keto* groups for the pyruvate on (111) surfaces of Pd and Pt. To test computational methods the adsorption of ethene on Pt(111) is investigated. The CASTEP program is found to overbind the ethene molecule to the surface. The corresponding adsorption energies are overestimated by between 10 and 20% when compared to analogous data generated with the VASP code. The overestimation is caused by the use of ultrasoft pseudopotentials generated at the local density approximation level. Reliable adsorption data for the chemisorption of formaldehyde and acetone is obtained with the VASP program, which uses pseudopotentials based on the projector augmented-wave model. The relative energies suggest that the Pt surface is more reactive than the Pd, and that the adsorption of the *enol* isomer of acetone is thermodynamically stable compared to the *keto* form. Small activation barriers for the favourable modes of chemisorption are calculated.

## ***Publications***

- [1] K. A. Avery, R. K. Mann, M. Norton and D. J. Willock, in “*Computer Simulation of Structural Aspects of Enantioselective Heterogeneous Catalysis and the Prospects for Direct Calculation of Selectivity*”, *Topics. Catal.*, **25**, 89, (2003).
- [2] *Forthcoming*, E. L. Jeffrey, R. K. Mann, G. J. Hutchings, S. H. Taylor and D. J. Willock, in “*A Density Functional Theory Study of the Adsorption of Acetone to the (111) Surface of Pt: Implications for Hydrogenation Catalysis*”, *Catal. Today*, (2005).

# Contents

	<i>Page</i>
<i>Declaration and Statements</i> .....	ii
<i>Acknowledgements</i> .....	iii
<i>Abstract</i> .....	iv
<i>Publications</i> .....	v
<i>Contents</i> .....	vi
<i>List of Figures</i> .....	xii
<i>List of Tables</i> .....	xvi
<i>Glossary of Terms and Abbreviations</i> .....	xviii
<b>1    <i>An Introduction to Catalysis and the Design of New Catalytic Systems</i> ...</b>	<b>1</b>
1.0 <i>Introduction</i> .....	3
1.1 <i>Research Aims</i> .....	7
1.2 <i>References</i> .....	9
<b>2    <i>A Review of the Enantioselective Hydrogenation of Pyruvates and Butane-2,3-dione Using Cinchona Modified Group 10 Catalysts and Related Systems</i> .....</b>	<b>11</b>
2.0 <i>Introduction</i> .....	12
2.1 <i>A Brief History into Enantioselective Catalysis</i> .....	12
2.2 <i>The Hydrogenation of <math>\alpha</math>-Ketoesters over Alkaloid Modified Pt Catalysts</i> .....	13
2.2.1 <i>The “Orito” Reaction</i> .....	13
2.2.2 <i>Renewed Interests in the “Orito” Reaction</i> .....	15
2.2.3 <i>Cinchona Modifiers</i> .....	15
2.2.4 <i>Modifier:Catalyst Ratios</i> .....	17
2.2.5 <i>Catalyst Morphology and Supports</i> .....	17
2.2.6 <i>Solvents</i> .....	18
2.2.7 <i>The Mechanistic Debate for <math>\alpha</math>-Ketoester Hydrogenation</i> ..	18
2.2.8 <i>The Template Model</i> .....	19

2.2.9	<i>Augustine's Model</i>	20
2.2.10	<i>The Shielding Model</i>	21
2.2.11	<i>Baiker's Model</i>	23
2.2.12	<i>Conformational Behaviour of Cinchonidine</i>	26
2.2.13	<i>Adsorption Mode of Cinchonidine</i>	31
2.2.14	<i>Conformational Behaviour of <math>\alpha</math>-Ketoester</i>	32
2.2.15	<i>Adsorption Mode of <math>\alpha</math>-Ketoester</i>	33
2.3	<i>The Hydrogenation of Butane-2,3-dione over Cinchona Modified Pt Catalysts</i>	35
2.4	<i>The Adsorption of Hydrogen on Pd and Pt Surfaces</i>	38
2.5	<i>The Adsorption of Ethene on Pt Surfaces</i>	40
2.6	<i>The Adsorption of Aldehydes and Ketones on Pd, Pt and Related Surfaces</i>	41
2.6.1	<i>The Adsorption of Formaldehyde</i>	42
2.6.2	<i>The Adsorption of Acetone</i>	46
2.6.3	<i>The Keto-Enol Tautomerism of Acetone and the Adsorption of the Enolate</i>	50
2.7	<i>Conclusions</i>	52
2.8	<i>References</i>	56
<b>3</b>	<b><i>Theoretical Background</i></b>	<b>65</b>
3.0	<i>Introduction</i>	66
3.1	<i>Quantum Mechanics</i>	67
3.1.1	<i>Ab Initio Methods</i>	68
3.1.2	<i>Semi-Empirical Methods</i>	68
3.1.3	<i>Density Functional Methods</i>	69
3.1.4	<i>Pseudopotential Theory and Supercell Approximation</i>	69
3.2	<i>Computational Quantum Mechanics</i>	70
3.2.1	<i>The Schrödinger Equation</i>	70
3.2.2	<i>The Born-Oppenheimer Approximation</i>	72
3.2.3	<i>The Molecular Hamiltonian</i>	73
3.2.4	<i>Restrictions on the Wavefunction</i>	74
3.2.5	<i>Hartree-Fock Theory</i>	74

3.2.6	<i>Molecular Orbitals</i>	75
3.2.7	<i>Electron Spin</i>	75
3.2.8	<i>Basis Sets</i>	76
3.2.9	<i>The Variational Principle</i>	76
3.2.10	<i>The Roothaan-Hall Equations</i>	77
3.2.11	<i>The Hartree-Fock Self Consistent Field Method</i>	78
3.2.12	<i>Open-Shell Methods</i>	79
3.2.13	<i>Limitations to Hartree-Fock Theory</i>	79
3.2.14	<i>Density Functional Theory</i>	80
3.2.15	<i>The Kohn-Sham Energy Functional</i>	81
3.2.16	<i>Kohn-Sham Equations</i>	82
3.2.17	<i>Local Density Approximation</i>	83
3.2.18	<i>Limitations to Local Density Approximation</i>	84
3.2.19	<i>Generalised Gradient Approximation</i>	84
3.2.20	<i>Hybrid Functionals</i>	85
3.3	<i>Methods for Studying the Solid State</i>	85
3.3.1	<i>Surfaces</i>	86
3.3.2	<i>Miller Indices</i>	86
3.3.3	<i>Periodic Supercells</i>	87
3.3.4	<i>Limitations to Periodic Boundary Conditions</i>	88
3.3.5	<i>Bloch's Theorem</i>	89
3.3.6	<i>Brillouin Zone and K-Point Sampling</i>	89
3.3.7	<i>Mönkhorst-Pack Special Points</i>	90
3.3.8	<i>Plane-Wave Basis Sets</i>	91
3.3.9	<i>Plane-Wave Representation of Kohn-Sham Equations</i>	93
3.3.10	<i>Non-Periodic Systems</i>	93
3.3.11	<i>Pseudopotential Approximation</i>	94
3.3.12	<i>Limitations to Pseudopotential Approximation</i>	96
3.4	<i>Geometry Optimisation</i>	97
3.4.1	<i>Optimisation Techniques</i>	98
3.4.2	<i>Gradient and Hessian</i>	99
3.4.3	<i>Steepest Descent Approach</i>	100
3.4.4	<i>Conjugate Gradient Method</i>	100

3.4.5	<i>Quasi-Newton Methods</i>	101
3.4.6	<i>Eigenvector Following Routine</i>	102
3.5	<i>Transition State Searches</i>	103
3.5.1	<i>Plain Elastic Band Method</i>	104
3.5.2	<i>Nudged Elastic Band Method</i>	105
3.6	<i>References</i>	106
<b>4</b>	<b><i>Computational Methods and Parameters</i></b>	<b>110</b>
4.0	<i>Introduction</i>	111
4.1	<i>Semi-Empirical Optimisations</i>	111
4.1.1	<i>Method and Parameters Used in Cinchonidine Calculations</i>	111
4.2	<i>Ab Initio Optimisations</i>	113
4.2.1	<i>Method and Parameters Used in Cinchonidine and Cinchonidine-Reactant Complex Calculations</i>	113
4.3	<i>Periodic Optimisations</i>	114
4.3.1	<i>Method and Parameters Used in Comparative Study of Ethene Adsorption on Pt(111)</i>	115
4.3.2	<i>Method and Parameters Used in Formaldehyde and Acetone Adsorption on Pd and Pt(111)</i>	117
4.3.3	<i>Justification and Convergence Tests of Parameters Used in Periodic Optimisations</i>	117
4.3.4	<i>Method and Parameters Used in Transition State Searches for the Adsorption Modes of Formaldehyde and Acetone on Pd and Pt(111)</i>	124
4.4	<i>References</i>	125
<b>5</b>	<b><i>A Semi-Empirical and Ab Initio Study of the Conformational Behaviour of Cinchonidine and its Interaction with Ethyl Pyruvate and Butane-2,3-dione</i></b>	<b>128</b>
5.0	<i>Introduction</i>	129
5.1	<i>Theoretical Calculations</i>	132
5.2	<i>Results</i>	135

5.2.1	<i>Conformational Analysis of Cinchonidine</i>	135
5.2.2	<i>Interaction Between Cinchonidine and Ethyl Pyruvate</i>	141
5.2.3	<i>Analysis of Diastereomeric Complexes of Protonated Cinchonidine and Ethyl Pyruvate</i>	142
5.2.4	<i>Interaction Between Cinchonidine and Butane-2,3-dione</i>	148
5.2.5	<i>Analysis of Diastereomeric Complexes of Protonated Cinchonidine and Butane-2,3-dione</i>	148
5.3	<i>Discussion</i>	152
5.3.1	<i>The Conformation of Cinchonidine</i>	152
5.3.2	<i>The Approximate Intermediate Complexes of Cinchonidine-Ethyl Pyruvate and Cinchonidine-Butane-2,3-dione</i>	154
5.4	<i>Conclusions</i>	159
5.5	<i>Future Work</i>	161
5.6	<i>References</i>	165
<b>6</b>	<b><i>A Comparative Density Functional Theory Study of the Adsorption of Ethene and Simple Ketones over Group 10 Metal Surfaces, Using Two Alternative Plane-Wave Codes</i></b>	<b>168</b>
6.0	<i>Introduction</i>	169
6.1	<i>The Adsorption of Ethene on Pt(111)</i>	170
6.2	<i>The Adsorption of Formaldehyde on Pd and Pt(111)</i>	178
6.3	<i>The Adsorption of Acetone on Pd and Pt(111)</i>	181
6.4	<i>Discussion</i>	186
6.4.1	<i>The Adsorption of Ethene on Pt(111)</i>	186
6.4.2	<i>The Adsorption of Formaldehyde on Pd and Pt(111)</i>	193
6.4.3	<i>The Adsorption of Acetone on Pd and Pt(111)</i>	196
6.5	<i>Conclusions</i>	198
6.6	<i>References</i>	203
<b>7</b>	<b><i>A Repeat of the Density Functional Theory Study of the Adsorption of Ethene and Simple Ketones over Group 10 Metal Surfaces, Using the VASP Code</i></b>	<b>206</b>



7.0	<i>Introduction</i>	207
7.1	<i>The Adsorption of Ethene on Pt(111)</i>	208
7.2	<i>The Adsorption of Formaldehyde on Pd and Pt(111)</i>	210
7.3	<i>The Adsorption of Acetone on Pd and Pt(111)</i>	214
7.4	<i>Discussion</i>	224
7.4.1	<i>The Adsorption of Ethene on Pt(111)</i>	224
7.4.2	<i>The Adsorption of Formaldehyde on Pd and Pt(111)</i>	226
7.4.3	<i>The Adsorption of Acetone on Pd and Pt(111)</i>	228
7.5	<i>Conclusions</i>	231
7.6	<i>Future Work</i>	236
7.7	<i>References</i>	239
<b>8</b>	<b><i>Conclusions</i></b>	<b>241</b>
8.0	<i>Conclusions</i>	242
8.1	<i>References</i>	250
 <b>Appendix A <i>Derivation of Relative Concentrations of Cinchonidine and Cinchonidine-Reactant Complexes</i></b>		
A.1	<i>Kinetic Model</i>	253
 <b>Appendix B <i>Vanderbilt Ultrasoft-Pseudopotentials Employed in CASTEP Calculations</i></b>		
B.1	<i>Pt US-PP</i>	257
B.2	<i>C US-PP</i>	258
B.3	<i>H US-PP</i>	259
 <b>Appendix C <i>Projector Augmented-Wave Pseudopotentials Employed in VASP Calculations</i></b>		
C.1	<i>Pt PAW-PP</i>	263
C.2	<i>C PAW-PP</i>	263
C.3	<i>H PAW-PP</i>	264

# **List of Figures**

(In Numerical Order)

<i>Number</i>		<i>Page</i>
1.1	<i>The effect of catalysis for an exothermic reaction .....</i>	3
1.2	<i>Flow chart for the steps involved in a reaction catalysed by a heterogeneous catalyst .....</i>	7
1.3	<i>Keto-enol tautomerism for acetone .....</i>	8
2.1	<i>Summary of the “Orito” reaction .....</i>	14
2.2	<i>Structures of cinchona modifiers, (1a) and (b): CD and QN, (2a) and (b): CN and QD, (3a), (b) and (c): HCD, methoxy and desoxy alkaloid .....</i>	16
2.3	<i>Reaction intermediate proposed by Well for the heterogeneous enantioselective hydrogenation of EtPy over CD modified Pt .....</i>	20
2.4	<i>Reaction intermediate proposed by Augustine for the heterogeneous enantioselective hydrogenation of EtPy over CD modified Pt .....</i>	21
2.5	<i>Reaction intermediate proposed by Margitfalvi for the heterogeneous enantioselective hydrogenation of EtPy over CD modified Pt .....</i>	22
2.6	<i>Reaction intermediates proposed by Baiker for the heterogeneous enantioselective hydrogenation of EtPy over CD modified Pt .....</i>	24
2.7	<i>Two-step, two-cycle mechanism suggested for the enantioselective hydrogenation of EtPy over CD modified Pt .....</i>	25
2.8	<i>Energy minimised CD conformers .....</i>	27
2.9	<i>Graphs representing pathways of interconversion of CD conformers</i>	28
2.10	<i>Geometric isomers of EtPy: (a) s-trans and (b) s-cis .....</i>	32
2.11	<i>The hydrogenation of butane-2,3-dione, illustrating the calculated rate constants predicted by Studer et al. ....</i>	35
2.12	<i>Surface bonding configurations of ethene: (a) <math>\pi</math>-bonding and (b) di-<math>\sigma</math> bonding .....</i>	40
2.13	<i>Destructive adsorption of primary alcohols and EtPy on Pt .....</i>	41
2.14	<i>Surface bonding configurations of keto groups: (a) <math>\eta^1(O)</math> (endon) and (b) <math>\eta^2(C,O)</math> (di-<math>\sigma</math>) .....</i>	42

2.15	<i>The modelled adsorption geometries of formaldehyde on a Pt(111) surface as investigated by Delbecq et al.</i>	44
2.16	<i>Keto-enol tautomerism for acetone</i>	50
2.17	<i>RAIR spectra of Ni(111) and Ni(111)/O</i>	51
3.1	<i>The (111) Miller index plane of a fcc lattice</i>	86
3.2	<i>Plan views of the most common faces studied in surface science</i>	87
3.3	<i>Periodic boundary conditions in two-dimensions</i>	88
3.4	<i>Schematic representation of the cutoff energy concept</i>	92
3.5	<i>Schematic illustration of a supercell geometry for a surface of a bulk solid</i>	94
3.6	<i>Schematic illustration of a supercell geometry for a molecule</i>	94
3.7	<i>An illustration of the full all-electron wavefunction and electronic potential plotted against distance, <math>r</math>, from the atomic nucleus</i>	95
3.8	<i>Schematic illustration of the features of a PES</i>	98
3.9	<i>Schematic illustration of convergence to the centre of an anisotropic harmonic potential using the steepest descent method</i>	100
3.10	<i>Schematic illustration of convergence to the centre of an anisotropic harmonic potential using the conjugate gradient method</i>	101
3.11	<i>Flow diagram illustrating the steps involved during an optimisation procedure</i>	103
3.12	<i>Schematic illustration of equidistant images separated by a spring constant in a PEB calculation</i>	104
4.1	<i>The effect of <math>k</math>-points and cutoff energies on the convergence of the bulk Pt energy</i>	118
4.2	<i>The effect of cutoff energies on the convergence of the bulk Pt energy and lattice constant</i>	119
5.1	<i>Geometric isomers of EtPy: (a) <i>s</i>-cis and (b) <i>s</i>-trans</i>	130
5.2	<i>Space filling models for the proposed diastereomeric complexes between Open(3)<math>H^+</math>-EtPy leading to (a) <i>R</i>- and (b) <i>S</i>-lactate on hydrogenation</i>	134
5.3	<i>(a) Atom labelling of CD and definition of <math>\tau_1</math>, <math>\tau_2</math> and <math>\tau_3</math> dihedral angles</i>	136
5.4	<i>Space filling, minimum-energy structures of <math>CDH^+</math>-EtPy complexes</i>	147

5.5	<i>Space filling, minimum-energy structures of <math>CDH^+</math>-diketone complexes</i>	151
5.6	<i>Space filling, minimum-energy structures of <math>Open(3)H^+</math>-s-trans EtPy complexes</i>	156
5.7	<i>Enol tautomers of EtPy derived from (a) s-cis and (b) s-trans EtPy</i>	162
5.8	<i>Formula models for the proposed (a) CD-s-trans enol-EtPy and (b) CD-s-trans enol-butane-2,3-dione complexes</i>	164
6.1	<i>The CASTEP <math>p(2 \times 2)</math> Pt(111) surface used in the ethene adsorption studies</i>	172
6.2	<i>The effects of surface relaxation on atomic layers</i>	172
6.3	<i>Schematic illustration of the four adsorption modes of ethene investigated: (a) cross bridge, (b) atop-bridge, (c) bridge and (d) atop-hollow</i>	174
6.4	<i>Schematic representation of the geometric parameters used to measure the extent of molecular distortion of a Pt adsorbed ethene molecule</i>	175
6.5	<i>Surface bonding configurations of keto groups: (a) <math>\eta^1(O)</math> (endon) and (b) <math>\eta^2(C,O)</math> (di-<math>\sigma</math>)</i>	178
6.6	<i>CASTEP adsorption geometries of formaldehyde: (a) <math>\eta^1(O)</math> and (b) <math>\eta^2(C,O)</math> on Pd(111)</i>	179
6.7	<i>Keto-enol tautomerism for acetone</i>	181
6.8	<i>Possible scenarios for the adsorption of the keto-enol energetics of acetone: (a) keto isomer and (b) enol isomer preferred adsorbed states</i>	182
6.9	<i>CASTEP adsorption geometries of the most stable <math>\eta^1(O)</math> keto isomer of acetone on: (a) Pd and (b) Pt(111)</i>	183
6.10	<i>CASTEP adsorption geometries of the enol isomer of acetone on: (a) Pd and (b) Pt(111)</i>	185
6.11	<i>Energy profiles summarising the CASTEP data for the surface adsorbed acetone intermediates on: (a) Pd and (b) Pt(111)</i>	202
7.1	<i>VASP adsorption geometries of formaldehyde: (a) <math>\eta^1(O)</math> and (b) <math>\eta^2(C,O)</math> on Pt(111)</i>	211
7.2	<i>VASP energy as a function of reaction coordinate for the</i>	213

	<i>transformation of endon, <math>\eta^1(O)</math> to di-<math>\sigma</math>, <math>\eta^2(C,O)</math> formaldehyde on the (111) surface of: (a) Pd and (b) Pt, obtained from elastic band calculations .....</i>	
7.3	<i>VASP energy as a function of height of the di-<math>\sigma</math>, <math>\eta^2(C,O)</math> formaldehyde on the (111) surface of: (a) Pd and (b) Pt, obtained from elastic band calculations .....</i>	214
7.4	<i>VASP adsorption geometries of the keto isomer of acetone: (a) <math>\eta^1(O)</math> and (b) <math>\eta^2(C,O)</math> on Pt(111) .....</i>	215
7.5	<i>VASP energy as a function of reaction coordinate for the transformation of the endon, <math>\eta^1(O)</math> keto isomer of acetone to di-<math>\sigma</math>, <math>\eta^2(C,O)</math> adsorption mode on the (111) surface of: (a) Pd and (b) Pt, obtained from elastic band calculations .....</i>	218
7.6	<i>VASP energy as a function of height of the di-<math>\sigma</math>, <math>\eta^2(C,O)</math> keto isomer of acetone on the (111) surface of: (a) Pd and (b) Pt, obtained from elastic band calculations .....</i>	219
7.7	<i>VASP adsorption geometry of the enol isomer of acetone on Pt(111) .....</i>	220
7.8	<i>VASP adsorption geometry of the most stable enolate ion of acetone on Pt(111) .....</i>	222
7.9	<i>VASP energy as a function of reaction coordinate for the transformation of acetone enolate .....</i>	223
7.10	<i>VASP energy as a function of abstracted H atom of the <math>\eta^1(C)</math> enolate to the formation of di-<math>\sigma</math> acetone on Pt(111) .....</i>	224
7.11	<i>Energy profiles summarising the VASP data for the surface adsorbed acetone intermediates on (a) Pd and (b) Pt(111) .....</i>	235
7.12	<i>Keto-enol tautomerism for the geometric isomers of butane-2,3-dione (diketone): (a) s-cis and (b) s-trans .....</i>	236
7.13	<i>VASP adsorption geometry of the s-cis isomer of butane-2,3-dione on Pt(111): (a) <math>\eta^2(O,O)</math> and (b) <math>\mu_3(C,O,O)</math> coordinations .....</i>	237

# *List of Tables*

(In Numerical Order)

<i>Number</i>		<i>Page</i>
2.1	<i>Vicinal <math>^3J_{H8H9}</math> coupling constants for CD and derived population of conformer Open(3) in different solvents .....</i>	30
2.2	<i>The dependence of the relative abundance of the s-trans EtPy on solvent polarity .....</i>	32
4.1	<i>VASP calculations to test the width and level of electron smearing with and without the Vosko Wilk and Nusair interpolation formula for the PW91 functional required for adequate bulk relaxation of Pt .....</i>	122
4.2	<i>VASP calculations to test the same electron smearing parameters as defined in table 4.1 .....</i>	122
5.1	<i>Semi-empirical and ab initio dihedral angles and electronic energies relative to the lowest energy conformer .....</i>	137
5.2	<i>Literature electronic energies and dihedral angles of CD conformers</i>	138
5.3	<i>Relative energies of CD, CDH<sup>+</sup> conformers, EtPy isomers and resultant diastereomeric complexes upon reaction of these reactants</i>	144
5.4	<i>Energies of diketone isomers and resultant CDH<sup>+</sup>-diketone diastereomeric complexes relative to the minimum-energy structures</i>	149
5.5	<i>Energies for the s-cis and s-trans keto and enol gas-phase structures for EtPy and butane-2,3-dione .....</i>	162
6.1	<i>Relaxed lattice constants and interlayer surface atom spacing of bulk Pt .....</i>	171
6.2	<i>Theoretical adsorption energies of ethene on Pt(111) .....</i>	174
6.3	<i>Theoretical geometries of adsorbed ethene on Pt(111) as modelled by CASTEP and VASP .....</i>	176
6.4	<i>CASTEP adsorption energies and geometries of adsorbed formaldehyde on Pd and Pt(111) .....</i>	180
6.5	<i>CASTEP adsorption energies and geometries of adsorbed keto isomer of acetone on Pd and Pt(111) .....</i>	184
6.6	<i>CASTEP adsorption energies and geometries of adsorbed enol isomer of acetone on Pd and Pt(111) .....</i>	186

7.1	<i>Relaxed lattice constants and interlayer surface atom spacing of bulk Pt</i> .....	208
7.2	<i>Theoretical adsorption energies of ethene on Pt(111)</i> .....	209
7.3	<i>VASP adsorption energies and geometries of adsorbed formaldehyde on Pd and Pt(111)</i> .....	211
7.4	<i>VASP adsorption energies and geometries of adsorbed keto isomer of acetone on Pd and Pt(111)</i> .....	216
7.5	<i>VASP adsorption energies and geometries of adsorbed enol isomer of acetone on Pd and Pt(111)</i> .....	220
7.6	<i>VASP adsorption energies of adsorbed acetone enolate species on Pd and Pt(111)</i> .....	222
7.7	<i>VASP adsorption energies for the interaction of s-cis butane-2,3-dione on Pd and Pt(111)</i> .....	238

# ***Glossary of Terms and Abbreviations***

(In Numerical, Alphabetical and Case Order)

<b>3-21G</b>	Split Valence Basis Set – core orbitals described by a set of 3 contracted GTO, valence orbitals described by a set of 2 contracted GTO and one, more diffuse GTO.
<b>6-31G(d)</b>	Split Valence Basis Set – core orbitals described by a set of 6 contracted GTO, valence orbitals described by 3 contracted GTO and one, more diffuse GTO. A single <i>d</i> -type polarisation function is applied to heavy atoms.
<b>6-31G**</b>	Split Valence Basis Set – as in the case for 6-31G(d) with polarisation <i>i.e.</i> <i>p</i> functions on hydrogen and helium.
<b>6-31+G*</b>	Split Valence Basis Set – as in the case for 6-31G(d) but with the + notation denoting that one set of diffuse <i>sp</i> -type functions are present on heavy atoms only.
<b>6-31++G(d,p)</b>	Split Valence Basis Set – as in the case for 6-31G(d), ++ notation denotes diffuse functions included for hydrogen as well as for heavy atoms, <i>i.e.</i> one set of <i>d</i> functions for first-row atoms and one set of <i>p</i> functions for hydrogen.
<b>Å</b>	Angstrom – Bond length Unit (1 Å = 1.89 Bohrs)
<b>AcOH</b>	Acetic Acid
<b>AE</b>	All-Electron
<b>AM1</b>	Austin Model 1
<b>ATR</b>	Attenuated Total Reflection
<b><i>bcc</i></b>	Body-Centred Cubic
<b>B3</b>	Becke-3 Gradient-Corrected Hybrid Exchange Functional
<b>BFGS</b>	Broyden-Fletcher-Goldfarb-Shannon
<b>BSSE</b>	Basis Set Superposition Error
<b>CASTEP</b>	Cambridge Sequential Total Energy Package
<b>CC</b>	Coupled-Cluster Theory
<b>CD</b>	Cinchonidine
<b>CDH<sup>+</sup></b>	Protonated Cinchonidine
<b>CETEP</b>	Cambridge Edinburgh Total Energy Package



<b>CG</b>	Conjugate Gradient
<b>CI</b>	Configuration Interaction
<b>CN</b>	Cinchonine
<b>CPU</b>	Central Processing Unit
<b>COSMO</b>	Conductor-like Screening Model
<b>diketone</b>	Butane-2,3-dione
<b>deoxyCD</b>	Deoxycinchonidine
<b>D</b>	Debye – Dipole Moment Unit (1 D = $3.338 \times 10^{-30}$ Coulomb Per Meters)
<b>DELHOF</b>	Herbert's Test Satisfied
<b>DFT</b>	Density Functional Theory
<b>DHCD</b>	9-deoxy-10,11-dihydrocinchonidine
$\epsilon_r$	Dielectric Constant
<b><i>ed</i></b>	Enantiodifferentiation
<b><i>ee(s)</i></b>	Enantiomeric Excess(es)
<b>expt</b>	Experimental
<b>eV</b>	Electron Volt – Energy Unit (1 eV = 96.49 kJ mol <sup>-1</sup> )
<b>E<sub>a</sub></b>	Activation Energy
<b>E<sub>F</sub></b>	Fermi Level
<b>EtLt</b>	Ethyl Lactate
<b>EtPy</b>	Ethyl Pyruvate
<b>EDIFF</b>	Energy Difference
<b>EELS</b>	Electron Energy Loss Spectroscopy
<b>EF</b>	Eigenvector Following
<b>ETOT_TOL</b>	Tolerance for Total Energy
<b><i>fcc</i></b>	Face-Centred Cubic
<b>FFT</b>	Fast Fourier Transform
<b>FTIR</b>	Fourier Transform Infra Red
<b>GAMES</b>	General Atomic and Molecular Electronic Structure System
<b>GGA</b>	Generalised Gradient Approximation
<b>GGA-PP(s)</b>	Gradient Corrected Pseudopotential(s)
<b>GGS</b>	Generalised Gradient Spin
<b>GTO</b>	Gaussian Type Orbital
<b><i>hcp</i></b>	Hexagonal Close-Packed

<b>HCD</b>	10,11-dihydrocinchonidine
<b>H/D</b>	Hydrogen-Deuterium Exchange
<b>HF</b>	Hartree-Fock
<b>HOMO</b>	Highest Occupied Molecular Orbital
<b>HREELS</b>	High-Resolution Electron Energy Loss Spectroscopy
<b>IR</b>	Infrared Spectroscopy
<b>J m<sup>-2</sup></b>	Joules Per Meter Squared – Energy Unit
<b>JCM</b>	Johnston Matthey Catalyst
<b>kcal mol<sup>-1</sup></b>	Kilo Calories Per Mole – Energy Unit (23.06 kcal mol <sup>-1</sup> = 1 eV)
<b>kJ mol<sup>-1</sup></b>	Kilo Joules Per Mole – Energy Unit (96.49 kJ mol <sup>-1</sup> = 1 eV)
<b>K</b>	Kelvin – Temperature Unit (0° Celsius = 273 K)
<b>KE</b>	Kinetic Energy
<b>KS</b>	Kohn-Sham
<b>LAPW</b>	Linear Augmented-Plane-Wave
<b>LDA</b>	Local Density Approximation
<b>LDA-PP(s)</b>	Local Density Approximation Pseudopotential(s)
<b>LEED</b>	Low-Energy Electron Diffraction
<b>LSDA</b>	Local Spin-Density Approximation
<b>LYP</b>	Lee, Yang and Parr's Gradient-Corrected Correlation Energy Functional
<b>MeOCD</b>	O-Methyl-Cinchonidine
<b>MeOHCD</b>	O-Methyl-10,11-dihydrocinchonidine
<b>MtPy</b>	Methyl Pyruvate
<b>MBPT</b>	Many-Body Perturbation Theory
<b>MD</b>	Molecular Dynamics
<b>MEP(s)</b>	Minimum-Energy Path(s)
<b>MINDO/3</b>	Third Generation Modified Intermediate Neglect of Differential Overlap
<b>MM2</b>	Molecular Mechanics Force Field of Allinger and Co-workers
<b>MM+</b>	Extended Molecular Mechanics
<b>MNDO</b>	Modified Neglect of Diatomic Overlap
<b>MO(s)</b>	Molecular Orbital(s)
<b>MOPAC</b>	Molecular Orbital Package
<b>NC-PP(s)</b>	Norm-Conserving Pseudopotential(s)
<b>NDDO</b>	Neglect of Differential Diatomic Overlap

<b>NEB</b>	Nudged Elastic Band
<b>NEXAFS</b>	Near-Edge X-ray Absorption Fine Structure
<b>NMR</b>	Nuclear Magnetic Resonance
<b>NOESY</b>	Nuclear Overhauser Enhancement Spectroscopy
<b>pK<sub>a</sub></b>	Acid Dissociation Constant
<b>pK<sub>E</sub></b>	Equilibrium Constant for Enolisation
<b>PM3</b>	Parameterised Model 3
<b>PS</b>	Soft Pseudo
<b>PW91</b>	Perdew and Wang's Gradient-Corrected Correlation Energy Functional
<b>PAW</b>	Projector Augmented-Wave
<b>PAW-PP(s)</b>	Projector Augmented-Wave Pseudopotential(s)
<b>PBC</b>	Periodic Boundary Conditions
<b>PDHCD</b>	2-phenyl-9-deoxy-10,11-dihydrocinchonidine
<b>PEB</b>	Plain Elastic Band
<b>PES</b>	Potential Energy Surface
<b>PI-IMI</b>	Process Industries Innovative Manufacturing Initiative
<b>PP(s)</b>	Pseudopotential(s)
<b>P-RFO</b>	Partitioned Rational Function Optimisation
<b>QA</b>	Quadratic Approximation
<b>QD</b>	Quindine
<b>QN</b>	Quinine
<b><i>ra</i></b>	Rate Acceleration
<b>RAIRS</b>	Reflection Absorption Infra Red Spectroscopy
<b>RMS</b>	Root Mean Square
<b><i>sc</i></b>	Simple Cubic
<b>SCF</b>	Self-Consistent Field
<b>SCFCRT</b>	Self-Consistent Field Criteria
<b>STM</b>	Scanning Tunnelling Microscopy
<b>TDS</b>	Thermal Desorption Spectroscopy
<b>TMA</b>	Trimethyl Ammonium
<b>TOLERF</b>	Heat of Formation Test Satisfied
<b>TOLERG</b>	Test on Gradient Satisfied
<b>TOLERX</b>	Test on X Satisfied

<b>TPD</b>	Temperature Programmed Desorption
<b>UHV</b>	Ultrahigh Vacuum
<b>UPS</b>	Ultraviolet Photoemission Spectroscopy
<b>US</b>	Ultrasoft
<b>US-PP(s)</b>	Ultrasoft Pseudopotential(s)
<b>VAMP</b>	Vienna <i>Ab Initio</i> Molecular Dynamics Package
<b>VASP</b>	Vienna <i>Ab Initio</i> Simulation Package
<b>VOSKOWN</b>	Vosko, Wilk and Nusair
<b>XANES</b>	X-ray Absorption Near-Edge Structure
<b>XPS</b>	X-ray Photoemission Spectroscopy
<b>XRD</b>	X-ray Diffraction
<b>ZINDO</b>	Zerner's Intermediate Neglect of Differential Overlap

# ***Chapter 1***

## ***An Introduction to Catalysis and the Design of New Catalytic Systems***

*“Many bodies...have the property of exerting on other bodies an action which is very different from chemical affinity. By means of this action they produce decomposition in bodies, and form new compounds into the composition of which they do not enter. This new power, hitherto unknown, is common both in organic and inorganic nature...I shall call it catalytic power. I shall also call catalysis the decomposition of bodies by this force”.*

*J. J. Berzelius, Edinburgh New Philosophical Journal, XXI, 223, (1836).*

## 1.0. Introduction

Modern day catalysis is based on Berzelius's famous quotation of the nineteenth century, which marked the origin of the term catalysis in a scientific context. Originally postulated to describe a number of experimental observations such as the discovery of ammonia decomposition by metals (Thenard, 1813) and the rate of decomposition of potassium chlorate by manganese dioxide (Dobereiner, 1825), it argued the case for reactions to proceed *via* the surface of solids that possessed some form of "catalytic force". In so, creating a whole new branch of chemistry and philosophy.

A multitude of studies have been conducted since the postulate in an attempt to try and understand catalytic phenomenon *i.e.* materials which accelerate chemical reactions by reducing the activation energy,  $E_a$ , (figure 1.1), with the most influential work achieved in the early to mid twentieth century.

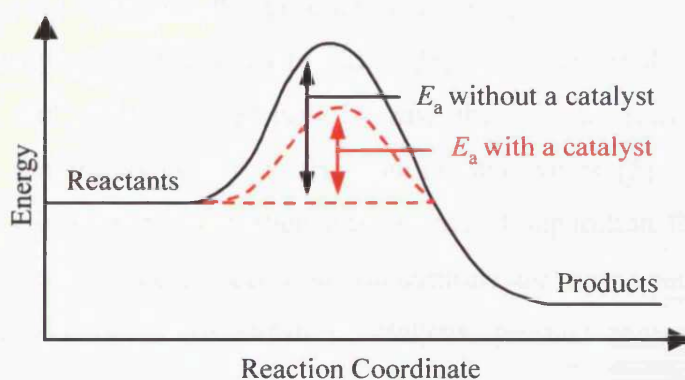


**Figure 1.1:** The effect of catalysis for an exothermic reaction.

Catalytic systems can be split into two broad categories (1) homogeneous; where all the reacting partners are present in one phase, usually the liquid phase. A diverse range of dissolved homogeneous catalysts are known for example, Brønsted and Lewis acids and bases, metal complexes and ions, organometallic complexes, organic molecules and natural and artificial enzymes. Nowadays, the terminology "homogeneous catalysis" often refers to catalysis with organometallic and coordination complexes. Over the past four decades this has led to a large number of industrial applications such as the processes of oxidation of ethene to ethanal, ester condensation to polyesters, and the hydrosilylation of alkenes *etc.* (details of which can be found in other works on this topic [1]). (2) Heterogeneous catalysis; where the catalyst and reactant are in different

phases. Since the beginning of the twentieth century this form of catalysis has been the mainstay of bulk chemical manufacture and processing [2].

A third branch of biological (enzymic and living cell) catalysis exists where enzymes aid biological reactions by providing sites in which a reaction between two biological molecules can easily occur. As the process is very much sensitive to the shape of the enzyme and how accessible the active site is to the reactant species *etc*, reaction temperature plays a governing role. Unlike traditional industrial catalysts, enzymic activity reaches a maximum at a given temperature (typically close to the temperature of the organism that is using the enzyme) with selective action greater than solid surfaces. Much of today's biological catalysts are considered to be analogous to heterogeneous systems.

All three types of catalysis are evident in modern day industrial applications *e.g.* the most recognisable heterogeneous catalytic process of the hydrogenation of vegetable oils using Ni supported silica for the production of margarine [3], the homogeneous process of hydroformylation of alkenes to aldehydes essential for the manufacture of solvents, detergent and plasticiser alcohols [4] and the enzyme usage of malic acid dehydrogenase for the improvement of fruit juices and wines [5]. It appears that heterogeneous catalytic systems with their advantages of separation from the product over homogeneous (despite its enhanced reaction control) are more economically viable for large-scale industrial use. For enzymic catalysis, product separation occurs *via* specific biochemical pathways.

Industrially, the most important aspect of catalysis is the ability of the catalyst to provide the required products with high selectivity and with the minimisation of the production of wasteful, unwanted side products. In particular, chiral products should ideally be produced with high enantioselectivities. A particularly challenging aspect of selectivity is the need to produce chirally selective catalyst systems that will allow the production of a single enantiomer of a desired product. As a result, bench-level catalyst performance has been researched for several decades with efforts directed towards improving the activity and lifetime of the catalyst through the gradual refinement of catalyst formation and reaction conditions.

In recent times the pressure to adopt cleaner technologies has increased the urgency for the chemicals industry to revise their synthetic routes so as to achieve optically pure products *via* atom-efficient and green methods. Of course, all three branches of traditional catalysis are affected by such demands, however, heterogeneous catalysis



poses difficulties in the sense that few reactions are known which provide high optical yields, let alone are the principles that govern enantioselectivity at the solid surface completely understood.

Heterogeneous catalysis mainly used for the production of fine chemicals is the prime concern of this thesis. At present, new heterogeneous systems are being based on homogeneous, transition metal catalytic complexes with tailored ligands as they have shown exceptional powers of selectivity.

Experimentally, enantiomeric excess (*ee*) is used to gauge the utility of a catalyst in terms of the amount of the preferred chiral product produced compared to that of the opposite enantiomer. The *ee* of a reaction is defined by the equation:

$$ee = \frac{[P_R] - [P_S]}{[P_R] + [P_S]} \times 100 \quad (\text{Equation 1.1})$$

where  $[P_{RS}]$  stands for the concentration of the product in its *R* or *S* enantiomer. Enantiomeric excess is always quoted as a positive percentage, and so this equation is appropriate for the case when the *R* enantiomer is favoured.

Although very cheap acids and bases are fit to catalyse the majority of modern synthesis reactions, more demanding catalysts based on metals and oxides of various kinds are required for complex products. Such materials possess very high surface energies that are therefore very active towards many catalytic reactions. For the synthesis of fine chemicals, precious metal catalysts are used and often drastic measures have to be taken to amend the limited reactivity of the elementary metals [2]. The active sites of most heterogeneous catalysts involve the mounting of the pure metal onto a suitable support such as alumina or silica oxides as this helps to reduce the rate of sintering of metal particles [2]. With metal surfaces prepared in this way it is extremely difficult to achieve chiral selectivity in heterogeneous catalysis, as they possess no inherent chiral qualities [6]. In principle, chirality can be induced by adsorbing a chiral substance known as a modifier onto the active phase of a conventional supported metal catalyst [6].

Nowadays, catalyst modification is a strategy that is applied widely in heterogeneous catalytic hydrogenation. The addition of organic modifiers to either the catalysts or to the reaction mixture is known to enhance the selectivity and activity of the system [7].

However, in reality modification has only been successful for a limited number of reactions because of the high substrate specificity of certain catalysts *i.e.* a particular combination of a metal and a modifier is enantioselective only for a rather narrow class of starting materials [7].

Historically, over half a century ago Lipkin and Stewart were the first to report the effects of modification by treating Ni catalyst with glucose and Pt catalysts with cinchonine (CN) [8]. Since then a number of modified metal catalysts have been examined for a variety of reactions [2] and among those the first to be catalysed by a heterogeneous chiral catalyst with high and reproducible optical yields was the hydrogenation of  $\beta$ -ketoesters. The best system of this type and certainly the most reviewed is the modification of Ni with tartaric acid [9]. The second most popular reaction with great industrial relevance is the enantioselective hydrogenation of  $\alpha$ -ketoesters using Pt catalysts modified with cinchona alkaloids [10-13].

Due to the major advances in several fields essential for catalysis such as surface analytical instrumentation, surface science, organometallic chemistry, theoretical techniques, solid-state chemistry, material science and reaction engineering detailed mechanistic studies of these systems have emerged [14-16].

With a change in attitude towards the design of solid catalysts from the purely traditional empirical routes towards rational methods, a clear understanding of the above systems on both the macro and microscopic levels is essential to guide the rational design of future enantioselective heterogeneous hydrogenation catalysts open to a variety of starting reagents. At present, the well established hydrogenations of  $\beta$ - and  $\alpha$ -ketoesters over modified group 10 metals stand as good starting points and model systems for similar research ventures within the catalysis community.

Unlike empirical methods, rational design of a catalyst not only requires the knowledge of the reaction mechanism but also an understanding of the control of the crucial structural and chemical properties of the solid catalyst under reaction conditions. To help facilitate this new concept of design, analytical techniques have developed to characterise catalyst surfaces under reaction or near reaction conditions to reveal the nature of adsorbed surface species and their concentrations, whereas, isotope tracers and dynamic techniques can distinguish between catalytically important and spectator species. Surface science techniques based on particle scattering, spectroscopy and diffraction can essentially provide data to help gain insight into the molecular-level

understanding of the elementary processes on which catalytic reactions are based. Whereas, recent advancements in molecular modelling, particularly quantum chemical techniques at the *ab initio* and semi-empirical levels have broaden the scope of systems to be investigated and is now used as a valuable tool in aiding the understanding of molecular interactions relevant to catalytic processes and catalyst design.

The general consensus for the reaction mechanism of a heterogeneous catalysis can be summarised in a few simple steps, as illustrated below (figure 1.2).

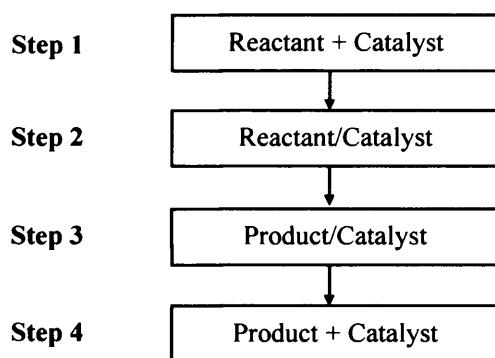


**Figure 1.2:** Flow chart for the steps involved in a reaction catalysed by a heterogeneous catalyst. Figure obtained from reference 17.

It is commonly assumed that the reactant molecules absorb at active sites onto the surface of the catalyst. This adsorption is accompanied with the formation of weak bonds between the reactant molecules and the catalyst, which ultimately causes the other bonds in the reactant molecule to be stretched and weakened. The weakened structure is then converted to another complex, which in essence is the product attached to the catalyst. Eventually, the complex breaks down to release the product molecule leaving the catalyst surface free to interact with another reactant molecule.

For enantioselective heterogeneous catalysis the problem in the mechanism lies in the origin of selectivity, at present, as discussed in Chapter 2, section 2.2.11 it is debatable as to whether the preferential favouring of one chiral diastereoisomer complex over the alternatives is thermodynamically or kinetically controlled.

### 1.1. Research Aims

This research project was part of a large collaborative effort involving a team of industrialists and academic co-workers under the PI-IMI (Process Industries, Innovative

Manufacturing Initiative) programme [18] to develop and enhance existing trickle bed technology for heterogeneous catalysis using silica supported Pt for hydrogenation reactions, with the aim of scaling up from the bench to the industrial level. Although, the experimental side of the project is tackled in parallel to this work at Cardiff [19], the specific role of this computational study is to expand the current scope of knowledge concerning hydrogenation reactions with a view to understanding enantioselectivity, in particular focussing on the nature of chemisorbed intermediates on transition metal catalysts.

With reference to the model hydrogenation reaction of  $\alpha$ -ketoesters into product (*R*)- and (*S*)-lactates over cinchona modified Pd and Pt catalysts, mechanistic models have identified the importance of the *keto* group to interact with the modifier to promote selectivity and induce a rate enhancement [15,16]. However, these models neglect the concept of the hydrogenation of the pyruvate to be activated *via* an adsorbed *enol* species, despite them being characterised and confirmed on the catalyst surface [20-22].

The simplest tautomerism to be modelled is the *keto-enol* equilibrium of acetone (figure 1.3), and the energetics of this system will help confirm whether or not this is a viable route for the hydrogenation of  $\alpha$ -ketoesters. The information gained will hopefully prompt further investigation into the role of the *enol* and enolate species as possible transition state intermediates in hydrogenation reactions and thus refine existing mechanistic models, for which new modifiers and heterogeneous hydrogenation catalysis are modelled upon.

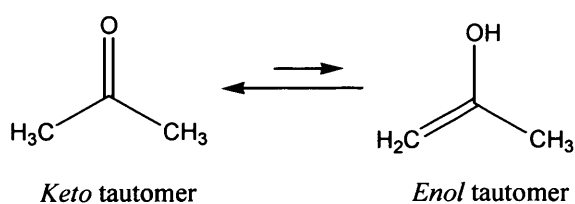


**Figure 1.3:** *Keto-enol tautomerism for acetone.*

## 1.2. References

- [1] G. W. Parshall and S. D. Ittel, in "*Homogeneous Catalysis. The Applications and Chemistry of Catalysis by Soluble Transition Metal Complexes*", Wiley, New York, 2<sup>nd</sup> Ed., (1992). C. Masters, in "*Homogeneous Transition-Metal Catalysis*", Chapman and Hall, London, (1981). F. G. A. Stone (Editor.), in "*Advances in Organometallic Chemistry*", 17, Wiley, New York, (1979). R. Ugo (Editor), in "*Aspects of Homogeneous Catalysis*", 1-7, Kluwer Academic Publishers, Dordrecht, (1990).
- [2] H. -U. Blaser and M. Müller, in "*Heterogeneous Catalysis and Fine Chemicals II*", M. Guisnet *et al.*, (Editors), Elsevier, Amsterdam, 73, (1977).
- [3] G. C. Bond, in "*Heterogeneous Catalysis: Principles and Applications*", Oxford University Press, 2<sup>nd</sup> Ed., 146, (1987).
- [4] M. V. Twigg, in "*Catalyst Handbook*", Manson Publishing, 2<sup>nd</sup> Ed., 259, (1996).
- [5] P. Rotheim, in "*C-147 NA, Enzymes for Industrial Applications: Products, Technologies and Economic Values*", (1998).
- [6] K. E. Simons, P. A. Meheux, S. P. Griffiths, I. M. Sutherland, P. Johnston, P. B. Wells, A. F. Carley, M. K. Rajumon, M. W. Roberts and A. Ibbotson, *Rec. Trav. Chim. Pays-Bas.*, **113**, 465, (1994).
- [7] H. -U. Blaser, H. -P. Jalett, M. Müller and M. Studer, *Catal. Today*, **37**, 441, (1997).
- [8] D. Lipkin and T. D. Stewart, *J. Am. Chem. Soc.*, **61**, 3295, (1939).
- [9] Y. Izumi, *Adv. Cat.*, **32**, 2151, (1983). A. Tai and T. Harada, in "*Tailored Metal Catalysts*", Y. Iwasawa (Editor), D. Reidel, Dordrecht, 265, (1986). A. Tai, *Shokubai*, **37**, 522, (1995).
- [10] Y. Orito, S. Imai, S. Niwa and N. G. Hung, *J. Synth. Org. Chem.*, **37**, 173, (1979).
- [11] Y. Orito, S. Imai and S. Niwa, *J. Chem. Soc. Jpn.*, 1118, (1979).
- [12] Y. Orito, S. Imai and S. Niwa, *J. Chem. Soc. Jpn.*, 670, (1980).
- [13] Y. Orito, S. Imai and S. Niwa, *J. Chem. Soc. Jpn.*, 137, (1982).
- [14] G. V. Smith and F. Notheisz, in "*Heterogeneous Catalysis in Organic Chemistry*", Academic Press, San Diego, (1999).

- [15] P. B. Wells, K. E. Simons, J. A. Slipszenko, S. P. Griffiths and D. F. Ewing, *J. Mol. Catal. A*, **146**, 159, (1999).
- [16] A. Baiker, *J. Mol. Catal. A*, **163**, 205, (2000).
- [17] <http://www.schoolscience.co.uk/content/5/chemistry/catalysis/>
- [18] <http://www.epsrc.ac.uk>, search site for the latest on innovative manufacturing.
- [19] N. Dummer, Ph. D. Thesis, Cardiff University, Park Place, Cardiff, S. Wales, (2005).
- [20] T. J. Hall, P. Johnston, W. A. H. Vermeer, S. R. Watson and P. B. Wells, *Stud. Surf. Sci. Catal.*, **101**, 221, (1996).
- [21] A. Solladié-Cavallo, C. Marsol, F. Hoernel and F. Garin, *Tetrahedron Lett.*, **42**, 4741, (2001).
- [22] W. -S. Sim, T. -C. Li, P. -X. Yang and B. -S. Yeo, *J. Am. Chem. Soc.*, **124**, 4970, (2002).

## ***Chapter 2***

*A Review of the Enantioselective  
Hydrogenation of Pyruvates and Butane-  
2,3-dione Using Cinchona Modified Group  
10 Catalysts and Related Systems*

## 2.0. Introduction

As highlighted in the previous Chapter, the explicit nature of enantioselective hydrogenation reactions is of interest to this research to improve existing industrial methods. In this section, a general review of the experimental observations as well as a discussion regarding the origin of enantioselectivity in terms of a valid mechanistic model for the hydrogenation reactions of  $\alpha$ -ketoesters over cinchona modified Pt and Pd surfaces will be addressed.

Computationally, it is expensive to simulate the catalytic adsorption of these large molecular systems and so this research focuses on the chemisorption of smaller component systems of the pyruvate reaction. Since experimental evidence suggests that the *keto* group is hydrogenated in the  $\alpha$ -ketoesters, the systems of interest include formaldehyde and acetone intermediates. For the latter species, it is well known that a *keto-enol* equilibrium exists, and so the literature is assessed to clarify the behaviour and adsorption mode in both *keto* and *enol* form on the low index surfaces.

Although, steady progress is being made to expand the scope of the cinchona modified Pt catalysts [1-3], at present one of the new systems showing promising *ees* is the butane-2,3-dione [4]. Since a theoretical approach is considered in this work, details of the experimental results for the reaction are considered here.

Finally, to identify an appropriate computational method to investigate the effect of chemisorption of the adsorbates mentioned above, we will consider the interaction of ethene with the (111) surface of Pt in future chapters, since literature reference calculations are available for comparison [5]. As this study plays a significant role in this research, with the results validated against the available thermodynamic data, it seems appropriate to briefly discuss the general literature concerning this system.

### 2.1. A Brief History into Enantioselective Catalysis

For enantioselectivity to be achieved under metal-catalysed conditions, it is essential that the reactions take place in a chiral environment. During hydrogenation, conventional metal catalysts lacking chiral environments will yield enantiomers in racemic mixtures only, thus to induce enantioselectivity a chiral environment maybe achieved by one of two methods. The first of which, involves supporting a metal



complex active phase on a chiral support with the second, involving the adsorption of a chiral modifier onto the active phase of the metallic catalyst.

In the early 1930s, Schwab pioneered the first approach by examining the optical yields from metals supported on cleaved quartz surfaces; unfortunately these enantiomeric yields were very poor [6,7]. Seven years later, Lipkin and Stewart introduced the reactions of Raney Ni modified by glucose and of Pt modified by the alkaloid CN [8]. Reasonable optical yields were achieved and so Lipkin and Stewart were successful in demonstrating the potential for catalysis modification for enantioselective reactions. In 1956, with the use of Schwab's technique, a group of Japanese chemists working on Pd/silk catalysts were able to sustain relatively high enantioselectivities (*ees* 66%) for the hydrogenation of carbon-nitrogen and carbon-carbon double bonds in a number of complex molecules [6-11].

However, more recently the second method of catalysis modification has come into the foreground. For example, extensive studies by Blaser and Müller [9] in which fifty or so enantioselective catalyst reaction combinations were screened, forty of them resulted in higher *ees* for hydrogenation reactions with the use of modified heterogeneous catalysts rather than the conventionally metal supported systems.

At present, three main groups of chiral modifiers or auxiliaries: alkaloids,  $\alpha$ -hydroxy acids and  $\alpha$ -amino acids dominate the known heterogeneous catalytic enantioselective hydrogenation chemistry. Despite the vast range of chiral compounds, only a few of them are effective in heterogeneous catalytic systems. The most well known examples include the asymmetric hydrogenations of  $\beta$ -ketoesters by Ni catalysts modified by optically active acids such as tartaric acid and amino acids [12-18] and  $\alpha$ -ketoesters hydrogenated over cinchona modified Pt and Pd catalysts as well as Pd-vinca alkaloid systems [19-22]. The work of this thesis is generally focussed around the possible adsorbed intermediates involved in the latter reaction.

## 2.2. The Hydrogenation of $\alpha$ -Ketoesters over Alkaloid Modified Pt Catalysts

### 2.2.1. The "Orito" Reaction

In 1978, Orito, Imai and Niwa investigated the enantioselective hydrogenation of methyl pyruvate (MtPy) using a Pt/C catalysis modified by the adsorption of the

alkaloid cinchonidine (CD). Under conditions of 70 bar pressure and room temperature with ethanol as solvent [23] *R*-(+)-methyl lactate was achieved in excess only when CD or quinine (QN) was used as the modifier. When switching to the alternatives CN or quindine (QD) [24] the *S*-(-)-lactate was preferentially produced. The reaction scheme below (figure 2.1) illustrates the hydrogenation of MtPy catalysed by cinchona modified Pt catalysts as observed by Orito *et al.* [23,24].

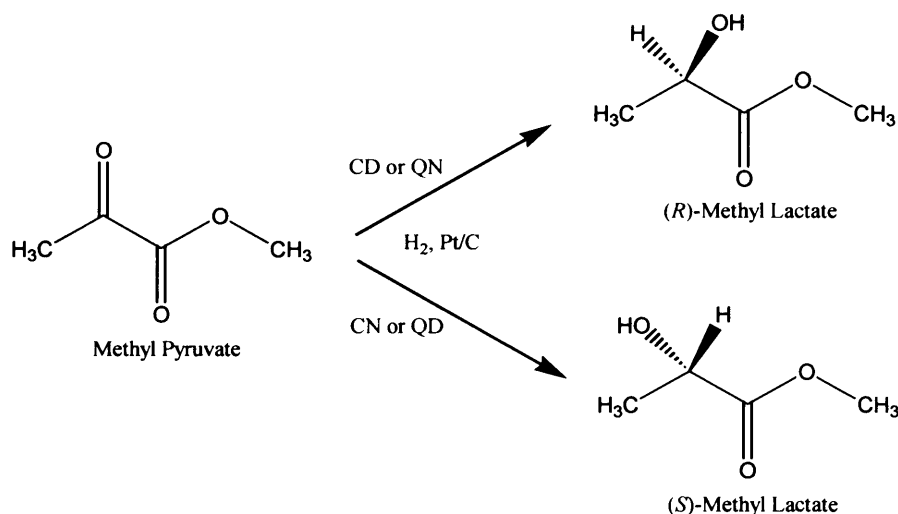


**Figure 2.1:** Summary of the “Orito” reaction. Refer to figure 2.2(1-2), for structures of the modifiers and related alkaloids.

Elaborating on their initial findings and extending their range of enantioselective hydrogenation reactions, the group was further able to demonstrate that under a variety of polar and non-polar solvents the related ester ethylbenzoylformate readily converted to *R*-ethylmandelate with the Pt/CD system [25,26]. Work continued on this reaction until 1982 [24-26] with their published papers focussing on various aspects of the reaction, some of which are highlighted here.

The exact experimental procedure used by Orito *et al.* [23,24] involved a number of steps starting with (i) the reduction of the Pt/C catalyst, followed by (ii) the modification of the catalyst by immersion in a 1% solution of the alkaloid modifier, (iii) washing and finally (iv) the transfer of the modified catalyst to the high pressure reactor. The sensitivity of the optical yields obtained (defined as % *R* and % *S* and vice versa depending on the choice of modifier) were found to depend on experimental variables such as the origin of the catalyst support, the reductant used to activate the catalyst, the temperature of catalyst activation, the solvent and, of course, the exact nature of the alkaloid used in the reaction mixture.

### 2.2.2. Renewed Interests in the “Orito” Reaction

A sudden surge of interest in the “Orito” reaction, with respect to optimising the yields and understanding the origins of selectivity came about in the 1990s, with continued efforts still reported today. At present, there are clearly three leading catalysis groups working on the system: the British group directed by Hutchings [27] in collaboration with Wells [28] and co-workers (original work conducted in Hull, England with recent contributions from Cardiff, Wales) and the collaborative effort between the Swiss colleagues Blaser [29] and Baiker [30] and their co-workers based in Basle and Zurich, Switzerland. Each of these groups have studied the effects of the enantioselective hydrogenation of  $\alpha$ -ketoesters over a range of reaction variables under experimental conditions similar to those reported by Orito *et al.* [23-26].

In an attempt to understand the reaction mechanism so that the concepts developed could be extrapolated to other enantioselective reactions their efforts are based on studying the reaction rates and product *ees*. To accomplish this, the latest studies incorporate catalytic amounts of supported Pt on silica ( $\text{SiO}_2$ ) [31-36] or alumina ( $\text{Al}_2\text{O}_3$ ) [37-41] in the presence of catalytic amounts of cinchona alkaloids under a range of experimental conditions *e.g.* substrate concentrations, temperature,  $\text{H}_2$  pressures (ranging from 10-100 bar) and solvents (of different polarities). The effects of these reaction variables on the hydrogenation reaction are discussed below.

### 2.2.3. Cinchona Modifiers

To date all of the major cinchona alkaloids have been used as modifiers. Common to these structures (figure 2.2, alkaloids (1-3)) are the two heterocycles, the quinuclidine and the quinoline ring. The QN (figure 2.2(1b)) and QD (figure 2.2(2b)) structures differ from CN (figure 2.2(2a)) and CD (figure 2.2(1a)) through the methoxy group on the quinoline ring. The major alkaloids are differentiated by their configuration at  $\text{C}_8$  and  $\text{C}_9$ . Each alkaloid possesses four chiral centres with those at  $\text{C}_3$  and  $\text{C}_4$  being common to all of the cinchona alkaloids [42-44].

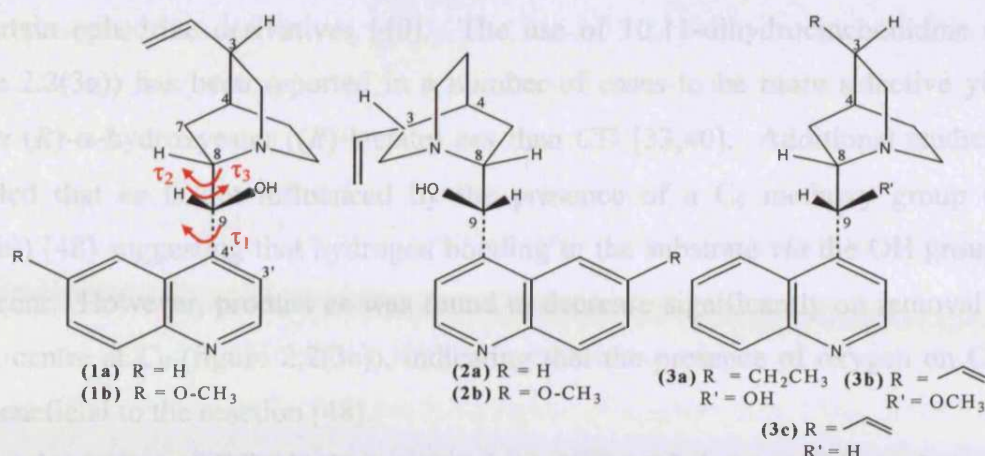


**Figure 2.2:** Structures of cinchona modifiers, (1a) and (b): CD and QN, (2a) and (b): CN and QD, (3a), (b) and (c): HCD, methoxy and desoxy alkaloid. For CD, torsional angles labelled  $\tau_1$  ( $C_3-C_4-C_9-C_8$ ),  $\tau_2$  ( $C_4-C_9-C_8-N$ ) and  $\tau_3$  ( $C_4-C_9-C_8-C_7$ ) govern the conformation of the alkaloid. Figure obtained from reference 45.

A definite relationship exists between the alkaloid used to modify the Pt catalysts and the product enantiomer formed, generally both CD and QN give rise to the (*R*)- $\alpha$ -hydroxyester in excess whereas CN and QD favour the alternative (*S*) enantiomer [24] (refer to figure 2.1). However, when MtPy is hydrogenated over modified Pd (4% Pd on Fe<sub>2</sub>O<sub>3</sub>) at 293K and 10 bar pressure, the *ees* observed are smaller and in the opposite sense to the corresponding reactions over Pt [41]. On Pd metal CN gives rise to the *R*-product in excess while CD gives the *S*-product [41]. For the Pd/alumina system modified with simple derivatives of CD the same results are observed *i.e.* lower *ees* with the (*S*)-product favoured [46,47].

Only two of the chiral centres, those determined at C<sub>8</sub> and C<sub>9</sub> are thought to be involved in the enantioselection process whereas that at C<sub>3</sub> is most definitely not. If this site is ignored, then structures 1 and 2 (figure 2.2) *i.e.* CD and CN are mirror images. The actual configurations of the “active” chiral sites C<sub>8</sub> and C<sub>9</sub> are the same in QN and CD (8(*S*)-9(*R*)) but reversed for QD and CN (8(*R*)-9(*S*)) [44].

Not only does the modifier provide the chiral environment for the catalyst to encourage reaction enantioselectivity but also its presence, compared to unmodified Pt reactions is found to increase the rate of hydrogenation [32,40].

For the hydrogenation reactions of  $\alpha$ -ketoesters it appears that cinchona alkaloids are the only suitable modifiers to provide the appropriate chiral environment on the Pt and Pd catalyst, although their simple derivatives have been reported to yield small *ees* such

as certain ephedrine derivatives [40]. The use of 10,11-dihydrocinchonidine (HCD, figure 2.2(3a)) has been reported in a number of cases to be more selective yielding higher (*R*)- $\alpha$ -hydroxyester ((*R*)-lactate) *ees* than CD [33,40]. Additional studies have revealed that *ee* is not influenced by the presence of a C<sub>9</sub> methoxy group (figure 2.2(3b)) [48] suggesting that hydrogen bonding to the substrate *via* the OH group does not occur. However, product *ee* was found to decrease significantly on removal of the chiral centre at C<sub>9</sub> (figure 2.2(3c)), indicating that the presence of oxygen on C<sub>9</sub> is in fact beneficial to the reaction [48].

Kinetic studies of EtPy hydrogenation have indicated that not only is the enantio-differentiation, *ed* (the process of obtaining product enantiomers) induced but also the rate acceleration, *ra*, which is defined in this case as the acceleration in reaction rate of the hydrogenation process. For the pyruvates the *ra* is found to alter from a factor of 10-100 under the presence of a cinchona modifier compared to an unmodified reaction [32,40].

#### 2.2.4. Modifier:Catalyst Ratios

Generally, for experiments in which the modifier:catalyst ratio has been varied a maximum *ee* and reaction rate is observed when a given amount of catalyst is modified by small amounts of alkaloid. The addition of further amounts of modifier was found to have very little or no effect on the rate or the enantioselectivities [35,40]. Under the conditions of these studies the modifier adsorption was discovered to be reversible. When CN is added to a CD/Pt catalyst the yield of the (*S*)-lactate is found to increase as the reaction proceeds [49].

#### 2.2.5. Catalyst Morphology and Supports

When considering the properties of the supported Pt catalyst, proper Pt dispersion [38], support material [40,50] and pore size distribution [51] are important. A number of different supports have been reported to be effective for the enantioselective hydrogenation, the majority of work conducted by Wells *et al.* have been with the well characterised EUROPt-1 (6.3% Pt/SiO<sub>2</sub>) [36] system whereas Baiker and Blaser opt for

the original Pt/C and Pt/Al<sub>2</sub>O<sub>3</sub> catalysts [37,40,52]. Other successful approaches include the use of zeolites [50] and polymer-stabilised colloidal Pt [53,54].

To investigate the performance of catalyst specification on pyruvate hydrogenation Blaser and co-workers prepared a variety of Pt/Al<sub>2</sub>O<sub>3</sub> catalysts using different Pt and alumina sources under a range of impregnation methods and reduction procedures. Under their experimental conditions they concluded that there is no direct correlation between the metal surface area of the catalyst and the overall performance in hydrogenation [37-39,40,52], although catalysts with either low dispersions or large metal particles were found to provide the highest *ees* [39]. This dispersion versus *ee* relationship is the basis of the template mechanism (to be discussed later) proposed by Wells *et al.* [55].

#### 2.2.6. Solvents

Solvents are important because they can influence the catalytic behaviour by affecting the solubility of reactants ( $\alpha$ -ketoester and hydrogen), as well as their interaction with the modifier,  $\alpha$ -ketoester and Pt surface. Solvents with a dielectric constant ( $\epsilon_r$ ) in the range of 2-10 are found to be most applicable to the reaction [37]. Acetic acid ( $\epsilon_r = 6.2$ ) and toluene ( $\epsilon_r = 2.3$ ) are the most suitable solvents, as the former affords an *ee* reaching over 95% under optimised conditions [56,57]. Under acetic acid conditions the quinuclidine N-atom of the CD is found to be protonated [58]. Although the use of alcohols, such as ethanol and propanol ( $\epsilon_r \approx 30$ ) can afford reasonably high *ee*, they tend to be avoided because under the presence of basic modifier the solvents undergo side reactions leading to the formation of an undesired hemiketal [59].

#### 2.2.7. The Mechanistic Debate for $\alpha$ -Ketoester Hydrogenation

Despite the great wealth of data accumulated over the years the exact mechanism for the reaction is still unclear especially the nature of the interactions responsible for the observed *ra* and *ed* steps [32,33,45,55,60-65]. However, it is generally thought that the reaction of the adsorbed species at the catalysed Pt cinchona modified surface governs the inducement of these effects. A number of models to help predict a plausible mechanism for the reaction have been proposed, and these are based on two different

proposals for the interactions responsible for the *ra* and *ed* steps. The first involves the modifier-active phase (Pt) interaction and the second envisages modifier-substrate interactions taking place in the liquid phase.

Earlier concepts namely the template [32,33] and the ligand acceleration models [60,61] favoured the modifier-metal interaction but failed to discuss the exact chemical nature of the interactions. Advancing on these theories and accounting for the shortfalls of the existing models Augustine *et al.* proposed another model, which again was based on the Pt-modifier interaction [55]. However, with the aid of computer modelling Margitfalvi *et al.* over the last ten years or so have been able to perform molecular mechanics calculations to reinforce their contrasting opinion as to the nature of interactions controlling the *ra* and *ed* steps. Based on experimental evidence obtained in earlier studies [49,64-67] they suggest that the *ed* step occurs *via* the formation of a weak substrate-modifier complex in the liquid phase.

Generally, the mechanistic models have been tested by the systematic variation of the reactant and modifier structure and more recently by theoretical calculations as there is a lack of *in situ* spectroscopic data. The models tend to focus on the aspects of chiral induction and tend to neglect the occurrence of hindering side reactions, which are well documented [68]. The proposed mechanistic models for enantioselectivity are briefly discussed below.

#### 2.2.8. The Template Model

In 1990, Wells and co-workers proposed that the enantioselectivity observed in the hydrogenation reaction over cinchona modified Pt was due to the formation of an ordered array of CD molecules on the Pt surface, producing an array of chiral template sites for adsorption of the reactant [32]. However, adsorption studies on single crystal Pt surfaces later revealed that it was impossible to accommodate the assumed ordered array [55]. Although, recently scanning tunnelling microscopy (STM) studies by Ravel *et al.* have illustrated the adsorption of ordered structures of chiral hydroxy and amino acids on Cu [69].

As more and more experimental data became available, the original template model was continuously refined, in the last version (1994) the authors discarded the importance of the ordered array and proposed the formation of a 1:1 complex in which the reactant interacts with the modifier [55], (the basis of all other models). In this

approach they assumed an N-H-O type H-bond interaction between CD in its most stable Open(3) conformation and the *s-trans* pyruvate ester, as illustrated in figure 2.3. The half-hydrogenated state under solvents such as toluene can also be sufficiently stabilised by the chiral base [70] and bond polarisation due to the H-bond may explain the *ra*.

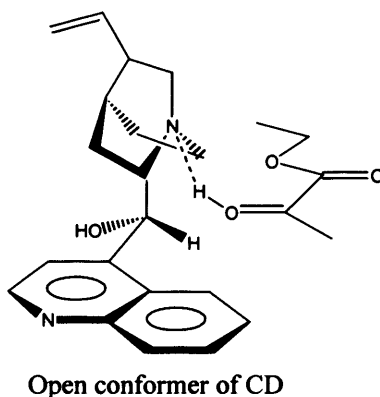
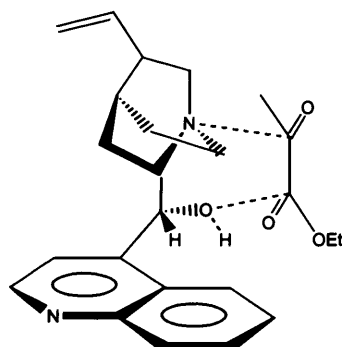


**Figure 2.3:** Reaction intermediate proposed by Wells for the heterogeneous enantioselective hydrogenation of EtPy over CD modified Pt. Note that the Pt surface (not drawn) lies below the complex. Figure obtained from reference 68.

#### 2.2.9. Augustine's Model

A completely different approach involving the edge-on adsorption of CD *via* the quinoline N atom was proposed by Augustine in 1993 [45]. This was later changed to a parallel adsorption mode with respect to the Pt surface. The active site for the hydrogenation reaction was assumed to be a coordinatively unsaturated metal adatom [71]. In both the earlier and latter model a “bidentate” complex was proposed in which the CD and the  $\alpha$ -ketoester stabilise *via* the formation of a six-membered ring, (figure 2.4).





Open conformer of CD

**Figure 2.4:** Reaction intermediate proposed by Augustine for the heterogeneous enantioselective hydrogenation of EtPy over CD modified Pt. Note that the Pt surface (not drawn) lies below the complex. Figure obtained from reference 68.

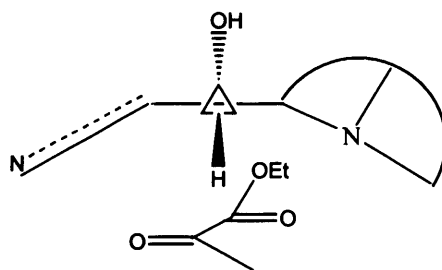
In this arrangement, the lone pairs of the quinuclidine N and O atom of CD interact with the C atoms of the *keto* and ester carbonyl groups of the pyruvate ester, respectively. Feasibility for this complex was argued in terms of the ability of alcohols and amines to react with activated ketones *via* nucleophilic attack at the carbonyl group.

However, one of the major limitations of the model is that it cannot interpret the enantioselectivity observed when the chiral N-base modifier is protonated, *i.e.* the good *ee* achieved when for example, CD is replaced by CD·HCl [72], or the result of an even higher *ee* on methylation of the C<sub>9</sub>-OH group of CD (as in the case of O-methyl-CD (MeOCD) or O-methyl-HCD (MeOHCD) [68,73]). This is because interaction between the “bidentate” complex and either of these modifiers would be sterically hindered.

The importance of the proposed active sites for hydrogenation *i.e.* unsaturated corner atoms and adatoms are also questionable when considering the yields achieved with colloidal Pt (consisting of small particles) [54,74,75] or with the extended flat surfaces of heat treated Pt/alumina [76,77].

#### 2.2.10. The Shielding Model

In this model the 1:1 complex between the  $\alpha$ -ketoester and the modifier is envisaged to occur in solution *via* an electronic interaction involving the aromatic ring of the CD with the  $\pi$ -orbitals of the reactant [78,79]. The complex adsorbs on the Pt surface *via* the unshielded side of the reactant (figure 2.5) resulting in the preferential formation of one predominant enantiomer, and is thus termed the “shielding” model.



Closed conformer of CD

**Figure 2.5:** Reaction intermediate proposed by Margitfalvi for the heterogeneous enantioselective hydrogenation of EtPy over CD modified Pt. Note that the Pt surface (not drawn) lies below the complex. Figure obtained from reference 68.

The desired geometry of the complex, one in which a simultaneous activating interaction occurs between the quinuclidine N of the modifier with the carbonyl C atom of the pyruvate ester, can only be achieved with the CD existing in its closed conformations. The activated complex is thought to be hydrogenated either *via* an Eley-Rideal [65] or Langmuir-Hinshelwood type mechanism [80].

Although it is highly feasible for the reactant and the modifier to interact in solution, the complex cannot control or direct the enantioselection on the Pt surface. Unfortunately, this model contradicts a number of experimental observations such as: (i) it cannot interpret the high *ee* observed once the quinuclidine N atom of CD is protonated. (ii) Account for the observation made by Bartok and co-workers [81,82] in which no *ee* was lost for the EtPy hydrogenation when the modifier was fixed in an open conformation, or explain the 76% *ee* afforded by the  $\alpha$ -isocinchonine, which primarily exists in an “anti-open” conformation [83]. The shielding model states that only the closed conformations of the cinchona alkaloids can provide the *ed*, whilst the open forms give rise to the racemic product mixtures. (iii) On a kinetic basis the model is invalid as cited by two independent studies [84,85]. (iv) The model also fails to adequately interpret the *ra* observed in the presence of trace amounts of chiral modifier [86]. For example, Margitfalvi *et al.* achieved 56% *ee* to (*R*)-lactate with a pyruvate/CD molar ratio of  $1.5 \times 10^5$ , and a *ra* of 5.5 compared to the unmodified reaction [87]. The low modifier concentration ( $6.8 \times 10^{-6}$  M) limits the concentration of the proposed CD-pyruvate complex in solution. The adsorption rate of the reactant-modifier complex is expected to be very low. This is thought to limit the overall hydrogenation rate assuming a Langmuir-Hinshelwood mechanism [80]. To obtain the observed 5.5 fold

*ra*, the intrinsic reaction rate should be higher by a factor of  $8 \times 10^5$  compared to the unmodified reaction, an unrealistic scenario.

### 2.2.11. Baiker's Model

The two-step, two-cycle mechanism of Baiker *et al.* is at present the most widely accepted approach [86]. Originally, the group's efforts were carried out in parallel with Wells' work and during the period of 1993-1994 a model for the enantioselection in acetic acid (AcOH), the best solvent for  $\alpha$ -ketoester hydrogenation was devised. Under this solvent the quinuclidine N of the CD is found to be protonated, reinforced by theoretical calculations [59]. A complex involving the protonated quinuclidine N of the CD interacting with the *keto*-carbonyl O atom of the pyruvate ester was proposed [62,88]. The diastereomeric transition states in AcOH [89] were later shown to be similar to those predicted by Wells *et al.* for aprotic solvents [55] (figure 2.3). In these complexes the attractive interaction between the reactant and the modifier arises from the N-H-O H-bond. In AcOH a direct interaction between the protonated CD and the reactant can occur whereas under ethanol and toluene a half-hydrogenated state of the pyruvate ester is formed first before the modifier interacts [86,90].

Molecular modelling calculations performed in 2000 showed how both MtPy and EtPy could interact with the quinuclidine N of CD in either its *s-cis* or *s-trans* conformations *via* a bifurcated H-bond [91,92] (figure 2.6). The latter complex (figure 2.6(a)) thought to yield the (*R*)-methyl lactate upon hydrogenation was found to be energetically less stable but more reactive than the former complex (figure 2.6(c)). The 92% *ee* was accounted for by the calculated energy difference of  $7.5 \text{ kJ mol}^{-1}$  between the two complexes. This was found to be in good agreement with experiment. Analogous to this, the  $0.8 \text{ kJ mol}^{-1}$  energy difference between the *s-cis* complexes (figure 2.6(b) and (c)) in favour of the pro (*R*) structure was thought to correspond to an *ee* of 17%, in contrast to experiment. For MtPy, the hydrogen-bonded complexes involving the *s-cis* conformer were predicted to be more stable than the corresponding *s-trans* complexes.

The effect of solvent by applying a reaction field method, was found to reduced the energy differences between the various complexes. At this stage the *s-cis* MtPy was found to complex with the protonated CD with the reactant forming a bifurcated

hydrogen bond to the quinuclidine H involving the oxygen atoms of both carbonyl groups. For the pro (*R*) complex the average hydrogen bond distances to the *keto* groups were found to be shorter and hence more likely to be hydrogenated than the pro (*S*) complexes and the alternative *s-trans* MtPy. Further calculations highlighted the fact that the complexes are relatively flexible with the effects of repulsion between the MtPy and the “anchoring” quinoline ring of CD influencing *ed*.

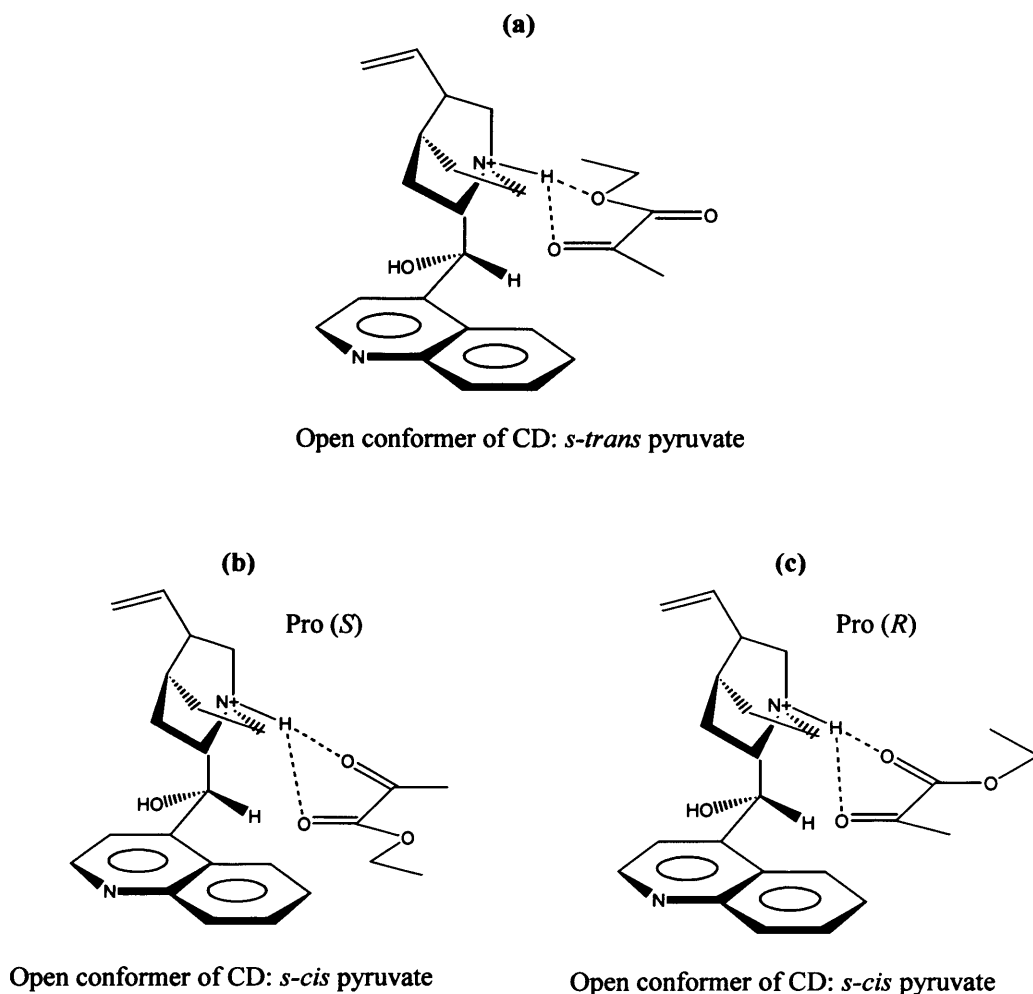


**Figure 2.6:** Reaction intermediates proposed by Baiker for the heterogeneous enantioselective hydrogenation of EtPy over CD modified Pt. (a) Most reactive diastereomeric complex, (b) least reactive and least stable complex and (c) most stable complex, as modelled in reference 91 and 92. Note that the Pt surface (not drawn) lies below the complexes. Figure obtained from reference 68.

The general mechanism (figure 2.7) incorporating the model assumes that the active chiral sites associated with the adsorbed CD ( $[CD]_{ad}$ ) are formed by adsorption of the cinchona modifier on the Pt surface. EtPy from the fluid phase adsorbs reversibly on these sites in its two enantiofacial configurations forming the diastereomeric

intermediate complexes  $[EtPy-CD]_{ad}^R$  and  $[EtPy-CD]_{ad}^S$  (of type figure 2.6), which upon hydrogenation afford the (*R*)- and (*S*)-ethyl lactate (EtLt), respectively. The question as to whether the enantioselectivity is thermodynamically (stability of  $[EtPy-CD]_{ad}^R$  versus  $[EtPy-CD]_{ad}^S$ ) or kinetically controlled (different activation energies of hydrogenation of intermediate complexes) has not been definitively answered yet.

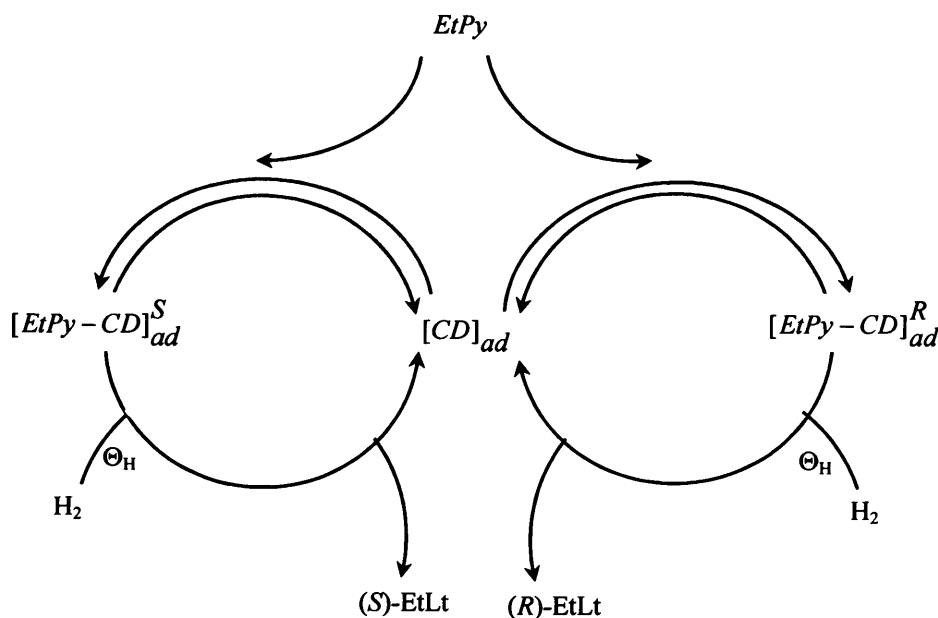


**Figure 2.7:** Two-step, two-cycle mechanism suggested for the enantioselective hydrogenation of EtPy over CD modified by Pt. The  $[CD]_{ad}$  represents an active chiral site on the Pt surface formed by adsorbed CD, and  $[EtPy-CD]_{ad}^R$  and  $[EtPy-CD]_{ad}^S$  represent diastereomeric intermediate complexes formed by interaction of chiral sites with EtPy, affording (*R*)- and (*S*)-ethyl lactate (EtLt), respectively, upon hydrogen addition. Figure obtained from reference 86.

Blaser *et al.* [84] suggested that for the hydrogenation on the unmodified catalyst, leading to racemic product mixtures, addition of the first hydrogenation is rate determining whereas for the hydrogenation to the major enantiomer occurring on modified chiral sites, the rate-determining step is the addition of the second hydrogen. Albeit this scenario may be feasible, its experimental verification is still lacking. A major constraint of the kinetic studies available is that they do not allow any conclusions concerning the structures of the intermediate complexes  $[EtPy-CD]_{ad}^R$  and

$[EtPy-CD]_{ad}^S$ , which may be assumed to resemble the structure of the corresponding transition states leading to (*R*)- and (*S*)-products, respectively.

However, theoretical studies have shown the mechanistic model to be successful in predicting experimental *ees* for EtPy hydrogenation using chiral modifiers other than the cinchona alkaloids [86]. At present, the model is being used as a tool for searching new modifiers and reactants and is gaining credibility within the catalysis community.

In summary, the latest models proposed by Wells and Baiker agree that the enantioselective step depends on a surface 1:1 complex formed between the modifier and the reactant. These diastereomeric complexes will clearly be affected by the dominant conformations of the modifier and reactant present under reaction conditions. In the following sections we examine results, both experimental and theoretical, from work addressing these aspects.

#### 2.2.12. Conformational Behaviour of Cinchonidine

As illustrated in figure 2.2(1a), three functional parts of CD can be distinguished, (i) the quinoline conjugated ring, (ii) the asymmetric region embracing C<sub>9</sub> and C<sub>8</sub>, and (iii) the bicyclic substituted quinuclidine part joined by a single sp<sup>3</sup> carbon atom to the rest of the molecule. The most important degrees of freedom are the two torsional angles,  $\tau_1$ : C<sub>3</sub>'-C<sub>4</sub>'-C<sub>9</sub>-C<sub>8</sub> and  $\tau_2$ : C<sub>4</sub>'-C<sub>9</sub>-C<sub>8</sub>-N, as these determine the relative orientation of the quinoline and quinuclidine moieties. The flexibility of the bridging bond between atoms C<sub>9</sub> and C<sub>8</sub> allows the molecule to take up two types of conformation: the closed and the open form. The terms “Open” or “Closed” are used to indicate whether the quinuclidine N points away or towards the heteroaromatic moiety.

A number of computational studies using a whole range of methods varying from empirical potentials to *ab initio* calculations have investigated the conformational behaviour of cinchona alkaloids. In particular, the detailed analysis in the two-dimensional conformational subspace,  $\tau_1$  and  $\tau_3$  (C<sub>4</sub>'-C<sub>9</sub>-C<sub>8</sub>-C<sub>7</sub>) (refer to figure 2.2(1a)) of the potential energy surface (PES) of the CD molecule at the semi-empirical Austin model 1 (AM1) [93] and parameterised model 3 (PM3) levels [94] of Aranda *et al.* [95], located nine different minima corresponding to nine conformers of CD, as shown in figure 2.8. The different forms were distinguished by the direction of the lone pair orbital of the quinuclidine nitrogen. Of these conformers, three were assigned as the

Closed forms (prefixed C) whilst the others were distinguished as the Open structures (prefixed A and B).

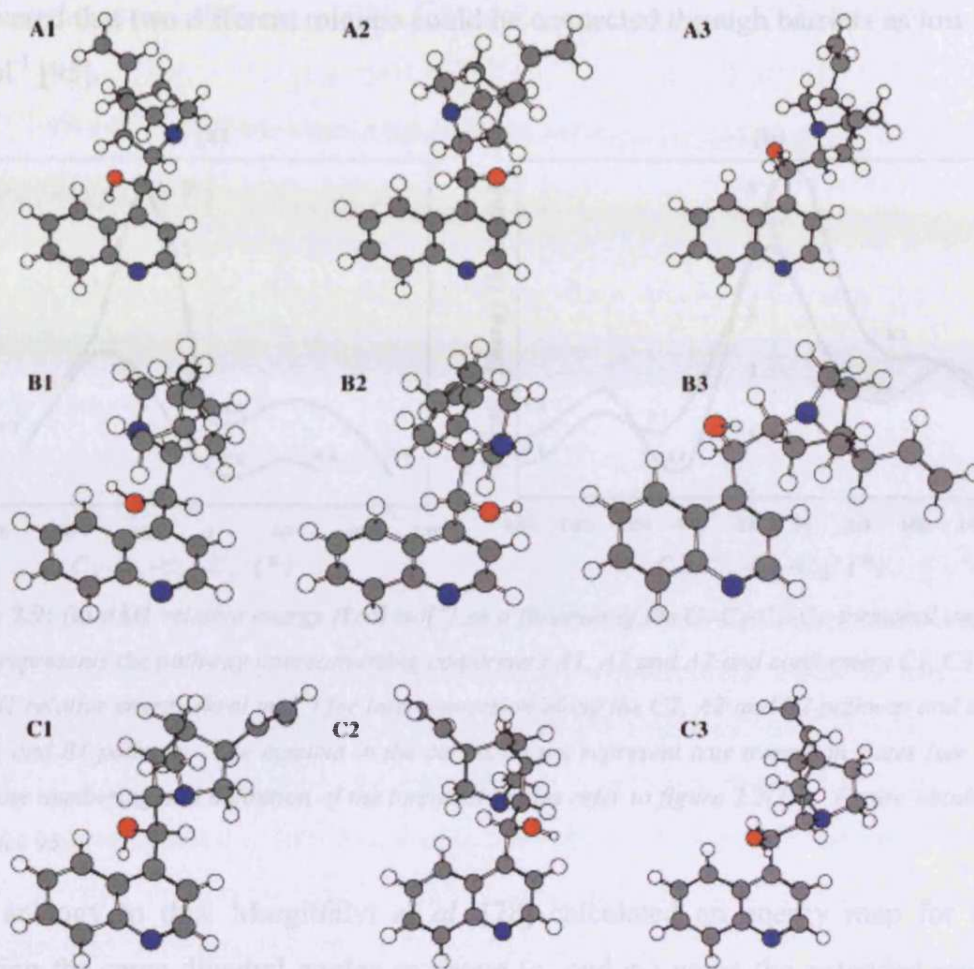


**Figure 2.8:** Energy minimised CD conformers. Molecular atoms are colour coded: H white, C grey, O red and N blue. Figure obtained from reference 95.

The most stable conformer in the AM1 method was the Open A2 structure found to correspond to the conformation found in the crystallographic experiment of Margitfalvi and Tfirst [78]. This structure assigned to the Open(3) conformation was more stable than the closed conformers C3 and C2 which in turn were more stable than the Open(4) conformer A3. The energy values for these four conformers were calculated to be within an  $8.4 \text{ kJ mol}^{-1}$  range.

In contrast to this, the PM3 method accompanied with small differences in the calculated energies gave a different order of stability compared to the AM1 method as the closed conformer C2 was found to be the most stable. As with the AM1 values, the PM3 calculated C3, A2 and C1 conformers were found to be of the same order of stability as C2 with relative energies of less than  $8.4 \text{ kJ mol}^{-1}$ . Figure 2.9 illustrates the

calculated PES for interconversion between the nine minima with the AM1 method. Although some barriers between them were found to be relatively high, it was discovered that two different minima could be connected through barriers as low as 12.5 kJ mol<sup>-1</sup> [95].

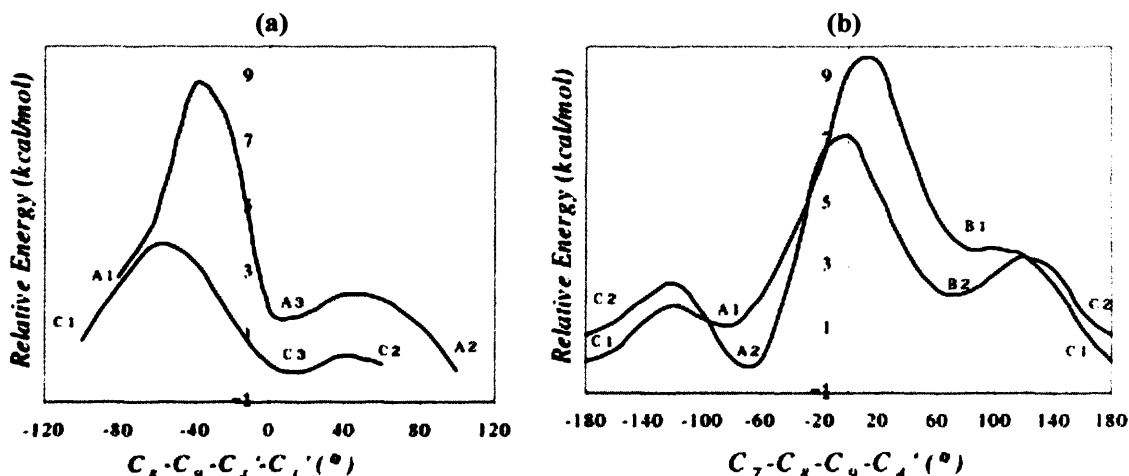


**Figure 2.9:** (a) AM1 relative energy (kcal mol<sup>-1</sup>) as a function of the C<sub>8</sub>-C<sub>9</sub>-C<sub>4</sub>-C<sub>3</sub> torsional angle. The graph represents the pathway interconverting conformers A1, A3 and A2 and conformers C1, C3 and C2. (b) AM1 relative energy (kcal mol<sup>-1</sup>) for interconversion along the C2, A2 and B2 pathway and along the C1, A1 and B1 pathway. The maxima in the curves do not represent true transition states (see text 95). For atom numbering and definition of the torsional angles refer to figure 2.2(1a). Figure obtained from reference 95.

In analogy to this, Margitfalvi *et al.* [78] calculated an energy map for CD by changing the same dihedral angles as above ( $\tau_1$  and  $\tau_3$ ) using the extended molecular mechanics (MM+) forcefield to reveal the same nine conformers. Of these only three stable conformers were found to exist the two closed and one open. The other conformers were unstable and an energy barrier of roughly 4 kJ mol<sup>-1</sup> was calculated to convert them into other more stable conformers.

These predicted interconversion barrier values of 12.5 and 4.0 kJ mol<sup>-1</sup> coincide well with the range quoted in reference 49 for the four stable conformations Closed(1) (figure 2.8, C1), Closed(2) (figure 2.8, C2), Open(3) and Open(4) (figure 2.8, A3), which were found to possess similar internal energies with the transformation barriers of between 2-14 kJ mol<sup>-1</sup> [49]. The conformers in this study were modelled using the alternative approach whereby rigid quinoline and quinuclidine parts were geometry optimised in the forms believed to represent the lowest conformations of CD. Computationally, all four conformers of CD are expected to be present under experimental conditions.



As with the gas-phase modelling of CD, theoretical methods have been applied to investigate the effect of solvent on the stability of the conformations in solution. Bürgi and Baiker [96] employed a continuum self-consistent reaction field solvent model (related to the Onsager reaction field model [97]). Under HF 6-31G\*\* theory, it was found that the Closed conformers in particular, were preferentially stabilised relative to the Open(3) conformer when going from the gas-phase to polar solvents, whereas the Open(4) was hardly stabilised at all. The inclusion of diffuse basis functions had no prominent effect on the stabilisation, however when density functional theory (DFT) was employed the same stabilisation trend from gas-phase to polar solvents was discovered to be slightly less prominent, amounting to about  $2.9 \text{ kJ mol}^{-1}$ . In reference to this work, the same conclusions were drawn from the lower level, semi-empirical study of Aranda *et al.* [95], which used the conductor-like screening model (COSMO) as specified in the work of Stewart *et al.* [98]. With both the AM1 and PM3 method the influence of water (polar solvent) was found to stabilise the Closed conformers within an  $8.4 \text{ kJ mol}^{-1}$  relative energy range compared to the more stable Open conformers.

To further extend the analysis of CD conformers under solvents, it is possible, by calculating the change in Gibbs free energy ( $\Delta G$ ), to estimate the relative populations of each at room temperature. In reference 96, the authors illustrated how nuclear magnetic resonance (NMR) techniques can be used to gain quantitative values for the populations of the different conformers of the CD by measuring the  $^3J_{\text{H8H9}}$  coupling constant. At room temperature the measured coupling constant  $^3J_{\text{H8H9}(\text{exp})}$  is averaged over the populations  $P_{(i)}$  of the different conformers in solution  $^3J_{\text{H8H9}(\text{exp})} = \sum P_{(i)} ^3J_{\text{H8H9}(i)}$ . The coupling constant ( $^3J_{\text{H8H9}(i)}$ ) for the different conformers is then obtained by using the calculated  $\tau_3$  dihedral angles from DFT or HF calculated geometries and substituting them into the Karplus equation, which is modified for substituent effects [99]. This method suggests that only two conformers dominate the solution phase in contrast to nuclear Overhauser enhancement spectroscopy (NOESY) experiments showing three conformers to be present at room temperature. With the relevant dihedral angles calculated at theory level HF 6-31G\*\*, the authors were able to determine the population of conformer Open(3) and sum the populations of the Closed conformers in different solvents, as illustrated in table 2.1.

Solvent	$\epsilon_r$	$^3J_{H8H9}$	$P_{Open(3)}$	$P_{Closed}$
Benzene	2.28	5.0	0.58	0.42
Toluene	2.34	4.1	0.70	0.30
Ethyl Ether	4.30	4.0	0.71	0.29
Tetrahydrofurane	7.60	4.7	0.62	0.38
Acetone	20.7	6.4	0.40	0.60
Ethanol	24.3	3.5	0.77	0.23
Dimethylformamide	36.7	7.0	0.33	0.67
Dimethyl Sulfoxide	40.0	7.5	0.27	0.73
Water	78.5	7.2	0.30	0.70

**Table 2.1:** Vicinal  $^3J_{H8H9}$  coupling constants for CD and derived population of conformer Open(3) in different solvents. For Open(3)  $^3J_{H8H9}$  is calculated as 1.7 Hz and for Closed(1) and (2), respectively,  $^3J_{H8H9}$  is calculated as 9.6 and 9.4 Hz. In the determination of  $P_{closed}$  a value of 9.6 Hz was used. The accuracy of the measured coupling constants is about 0.1 Hz, except for the measurement in water where the uncertainty is a little higher because of poor solubility of CD. Data obtained from reference 96.

Comparison of this data with the enantioselectivity in the hydrogenation of ketopantolacetone over CD modified Pt showed a correlation of the concentration of the Open(3) conformer with the observed *ee* data. This helped to explain the striking dependence of *ee* on the solvent used in the reaction which is found to be near 80% in low dielectric constant solvents, such as toluene, and falls to practically zero in more polar solvents such as formamide. In this way, the calculations clearly identified the Open(3) conformer of CD as an important factor in obtaining high enantioselectivities in these reactions. Note that similar behaviour is observed in the case of EtPy hydrogenation over CD modified Pt in an earlier study dating back to 1994 [59].

Other factors, apart from solvent effects are also known to influence *ee* and the fraction of Open(3) CD in solution. It has been reported that the addition of small amounts of water to apolar solvents such as toluene generally act to decrease the *ee* and the concentration of Open(3) by about 10% [100]. Generally, lower reaction temperatures yield higher *ees* and in turn are found to favour the Open(3) form over the others [33,40,89,101]. When CD is protonated at the quinuclidine N the *ee* increases and this appears to be due to the conformation of the CD, *i.e.* the stabilisation of the Open(3). This is indicated by the decrease in the  $^3J_{H8H9}$  coupling constant and loss of the cross peak between the  $H_1$  and  $H_8$  in the NOESY spectra [56,100]. The changes in the spectra are thought to occur from the initial structural change of the conformers on protonation. This is reinforced by *ab initio* methods, which illustrate the stabilisation of the Open(3) upon protonation [102]. For the enantioselective hydrogenation of EtPy in

which the CD was substituted by deoxyCD, both theoretical calculations and the NMR spectra illustrated the destabilisation of the Open(3) with respect to the Closed(1), which resulted in a loss of *ee* from 79% to 44% [103].

To further support the role of the Open(3) conformation of CD, Bartok *et al.* [81] have recently demonstrated that high *ees* can be achieved by using rigid (C<sub>8</sub>-C<sub>9</sub> rotations prohibited) open conformations of cinchona alkaloids,  $\alpha$ -isocinchonine and  $\alpha$ -isoquinidine.

### 2.2.13. Adsorption Mode of Cinchonidine

As emphasised in the proposed mechanistic models (section 2.2.7), the two most feasible adsorption modes of CD are (i) *via* the aromatic  $\pi$ -bonding system of the quinoline ring, resulting in a flat adsorption parallel to the Pt surface and (ii) *via* the quinoline N lone pair, causing the quinoline ring to be tilted or even perpendicular to the surface.

Based on the considerable evidence available *i.e.* near-edge X-ray absorption fine structure (NEXAFS) studies [104], hydrogen-deuterium exchange experiments (H/D) [31] and comparative catalytic behaviour studies of 2-phenyl-9-deoxy-10,11-dihydroCD (PDHCD), a CD derivative arylated in 2-position at the quinoline ring, and 9-deoxy-10,11-dihydroCD (DHCD) [105], it appears that the most likely adsorption mode of CD, especially at low coverages is the planar adsorption.

Regarding the latter study, it was found that PDHCD could not adsorb onto the surface through the quinoline N atom because the bulky phenyl group at C<sub>2</sub> afforded steric hindrance. However, it was possible for the modifier to adsorb *via* the  $\pi$ -bonding system of the quinoline ring. Since the same *ed* effects were observed for both modifiers as in the case of CD and CN, the study supports the argument that parallel adsorption of the quinoline ring to the Pt surface is favourable under reactions conditions. However, it should be noted that at present there is a lack of direct data concerning the adsorption modes of CD under reaction conditions.

### 2.2.14. Conformational Behaviour of $\alpha$ -Ketoester

By altering the dihedral angle  $\text{O}=\text{C}-\text{C}=\text{O}$ , Mt- and EtPys as with all  $\alpha$ -ketoesters can adopt either the *s-cis* or *s-trans* conformations. A combined infrared spectroscopy (IR) and *ab initio* study by Ferri and co-workers [92] investigated the conformational behaviour of a number of  $\alpha$ -ketoesters under different solvents. Their results indicated that the *s-cis/s-trans* energy difference for EtPy is small and that the torsional angle around  $\text{O}=\text{C}-\text{C}=\text{O}$  is extremely flexible. At room temperature it was found that both geometric isomers coexist with the *s-trans* conformer predominate under apolar solvent conditions. In polar solvents, the fraction of *s-cis* EtPy becomes comparable to that of *s-trans* EtPy. Experimentally, it was found that as solvent polarity increases so does the stability of the *s-cis* EtPy as it has a larger dipole moment than the corresponding *s-trans* EtPy. The relative abundances of the *s-trans* EtPy in solvents of different polarity as taken from reference 86 are presented in table 2.2.

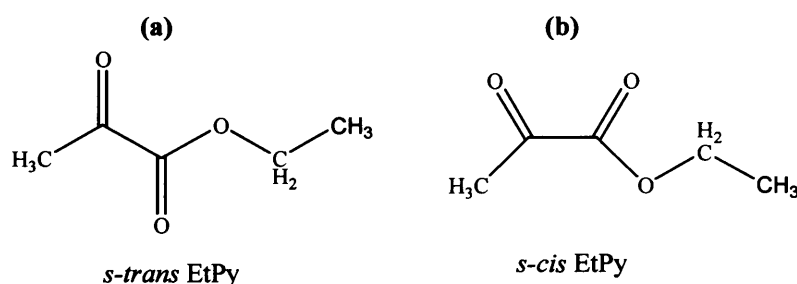


**Figure 2.10:** Geometric isomers of EtPy: (a) *s-trans* and (b) *s-cis*.

Dielectric Constant ( $\epsilon_r$ )	$\Delta E$ ( $\text{kJ mol}^{-1}$ )	% <i>s-trans</i>
1.0 (vacuum)	1.62	93.9
2.2 (carbon tetrachloride)	1.03	85.0
8.9 (dichloromethane)	0.42	66.9
37.5 (acetonitrile)	0.22	59.0

**Table 2.2:** The dependence of the relative abundance of the *s-trans* EtPy on solvent polarity. Relative energies calculated from  $\Delta E = E_{(s-cis)} - E_{(s-trans)}$ . DFT calculations were performed at the theory level B3PW91 with a 6-31++G(d,p) basis set. Data obtained from reference 86.

The fraction of *s-cis* EtPy observed was found to increase as the dielectric constant increased, this is because higher dipole moment conformers are stabilised by solvent as predicted by the Onsager model of solvation [97]. The Onsager model is a

computational method, which allows systems to be studied in solution. The solvent is modelled as a continuum of dielectric constant and the solute is placed in a cavity within the solvent. The Onsager model is a dipole-induced dipole model. Stabilisation of the *s-cis* EtPy is also achieved with alcoholic solvents where hydrogen bonding prevails. With regards to this it was found that the *s-cis* conformations with larger dipole moments than the *s-trans* EtPy, favour in terms of energetics the intermolecular interactions with charged species such as  $R_3N^+-H$ .

Even though *s-trans* EtPy has been found to be the most stable isomer under the preferred solvents used in enantioselective hydrogenation *i.e.* acetic acid and toluene, the stability of the *s-cis* EtPy in the diastereomeric complexes has not been excluded. The relative stability of the *s-cis* and *s-trans* conformers could also be affected by the presence of the Pt surface upon adsorption as interaction of the molecule's dipole moment with its image charge could play a prominent role. This dipole induced dipole interaction is expected to be much stronger for *s-cis* EtPy than *s-trans* EtPy as it possesses a larger dipole moment.

#### 2.2.15. Adsorption Mode of $\alpha$ -Ketoester

The essential functionality for bonding of the Mt- and EtPy is the presence of the two carbonyls groups. Bonding can thus arise from either donating the O atom lone pair or *via* the  $\pi$ -electron density from the conjugated double bond of the C=O groups. Binding in the former mode usually occurs with the C=O group orientated in an upright position with the C=O group tilted with respect to the surface. Whereas with the  $\pi$ -bonding mode, the C=O groups have a tendency to lie parallel to the Pt surface.

Over the last few years a number of spectroscopic and surface science techniques have been applied to investigate the adsorption of the model Mt- and EtPy reactants on low index surfaces. Recently, an IR study revealed a *s-cis*-bidentate species orientated perpendicular to a Ni(111) surface to be most stable, with the adsorption stabilised through O lone pairs of the MtPy [106].

A combined X-ray and ultraviolet photoemission spectroscopy (XPS and UPS) study focussed on the binding of EtPy on a Pt(111) surface [107]. The results highlighted the fact that EtPy is predominantly bonded to the Pt surface through its lone pair upon chemisorption at low temperatures, as the highest occupied molecular orbital (HOMO)

lone pair orbital was stabilised by roughly 0.7 eV with respect to the other orbitals. This lone pair bonding was observed not only in the fully saturated chemisorption layer but also far below the saturation. As a result the lone pair adsorption of EtPy was found predominantly in its tilted mode.

To gain direct information concerning the orientation of adsorbed EtPy in the presence and absence of hydrogen, an *in situ* X-ray absorption near-edge structure (XANES) study was applied [108]. From the resonances of the angular dependent shift of  $\pi^*$  and  $\sigma^*$ , the coexistence of differently adsorbed EtPy was deduced. It was found that depending on the hydrogen and EtPy pressure, different angular dependencies were observed on the C and O K-edge spectra. When hydrogen was excluded from the system the mean tilt angle of the molecular plane of chemisorbed EtPy with respect to the surface was determined as  $72^\circ$ , verifying the O lone pair bonding mode in either a perpendicular or tilted orientation as deduced from the XPS and UPS studies [107]. However, under an atmosphere of hydrogen, the mean tilt angle was measured at the reduced value of  $58^\circ$ , significantly demonstrating the tendency of EtPy to move toward a parallel adsorption mode under these conditions. Two explanations are feasible to account for these changes in the adsorption geometries of EtPy, firstly, the change from lone pair bonded to  $\pi$ -bonded EtPy maybe directly influenced by coadsorbed hydrogen or there is simply a change in the relative abundance of the two EtPy species, both of which are always present.

As emphasised earlier, EtPy can easily adsorb as its *s-cis* and *s-trans* conformers. Of the two, it seems as though the *s-cis* conformer would most likely be favoured to bond *via* the lone pair model, as the bidentate species in which both carbonyls interact with the metal surface would be stabilised. Currently, insight into the adsorption behaviour of EtPy suggests a tilted adsorption mode and as a consequence it is difficult to assess the structure of the CD-EtPy diastereomeric complex.

In summary, the experimental results have clearly indicated two different adsorption modes of EtPy, *i.e.* the lone pair and  $\pi$ -bonded states to be present at low temperatures. The population density of these adsorbed species as well as the conformation of the EtPy are expected to depend on various factors such as surface coverage, temperature, and the presence of coadsorbed species. This implies the likelihood of several structurally and energetically different adsorbed complexes to exist.

The general conclusions drawn from these experiments point towards a rather complicated adsorption mode for either Mt- or EtPy. In particular the presence of hydrogen affects the preferred adsorption mode and it can be expected that solvent and CD will also have an influence. As a result further *in situ* information is required. Despite this, in order for catalytic hydrogenation of the  $\alpha$ -ketoesters to occur, the C=O group must have access to the activated hydrogen on the metal surface and for this to be feasible the ideal geometry of the substrate needs to be as flat as possible as emphasised by the models proposed by Wells and Baiker (sections 2.2.8 and 2.2.11).

### 2.3. The Hydrogenation of Butane-2,3-dione over Cinchona Modified Pt Catalysts

Parallel to the efforts of investigating the hydrogenation of  $\alpha$ -ketoesters over cinchona modified surfaces, Vermeer *et al.* [1] in 1993 investigated the enantioselective hydrogenation of butane-2,3-dione (figure 2.11, structure 1) to (*R*)- and (*S*)-3-hydroxybutan-2-one (figure 2.11, structures 2). The reaction was found to occur in dichloromethane, toluene, acetone, and ethanol as solvent. An *ee* of 38% was achieved when using a 6.3% Pt/silica catalyst modified with CD in CH<sub>2</sub>Cl<sub>2</sub> at 273 K and 10 bar pressure, which dropped to 8% in ethanol [1].

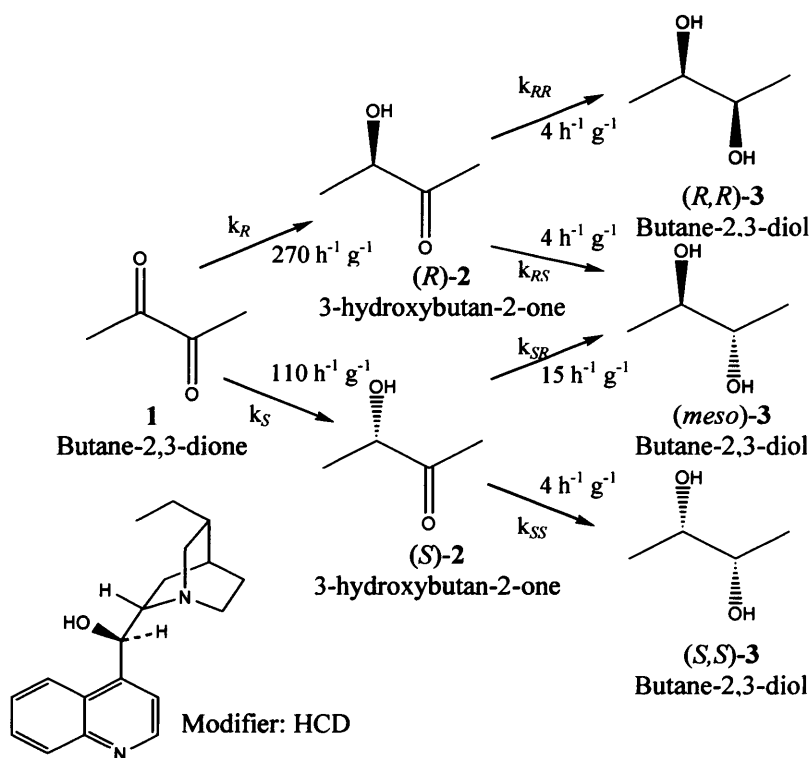


**Figure 2.11:** The hydrogenation of butane-2,3-dione, illustrating the calculated rate constants predicted by Studer *et al.* Reaction scheme obtained from reference 4.

The possibility that the *ees* could be optimised by varying the reaction conditions as with the  $\alpha$ -ketoester system, lead to an renewed interest in the system in the late 1990s. Studer *et al.* [4] were one of the first groups to work on the substrate, and draw comparisons against the  $\alpha$ -ketoester system. Using a catalyst, which afforded high enantioselectivities for pyruvate esters (*i.e.* 5% Pt/Al<sub>2</sub>O<sub>3</sub>, JMC type 94 (Johnson Matthey Catalyst [109]), pretreated for 2 h at 673 K with H<sub>2</sub>) [56] the effect of several reaction parameters was investigated and reported [110]. As with  $\alpha$ -ketoesters, the enantioselectivity was strongly affected by the choice and concentration of modifier type, as well as the solvent, whilst the effects of H<sub>2</sub> pressure (25-135 bar) and temperature (273-298 K) were negligible. The highest *ees* obtained in this study (*ee*  $\approx$  50%) were with the HCD in toluene solution, however, most importantly as conversions reached > 80% the *ee* continued to rise with the reaction progressing to give the corresponding diols (figure 2.11, structures 3), something which Vermeer *et al.* failed to notice [1] for toluene but cited for dichloromethane [111]. Thus, it was concluded that the butane-2,3-dione hydrogenates in a two step process first to 3-hydroxybutan-2-one and then to butane-2,3-diol.

With the use of a kinetic model (for details refer to original publication [4]) that assumed the reactions of 1 or 2 to be first order in the substrate and in the catalyst at constant pressure, the rate constants for the individual steps in the reaction scheme, illustrated in figure 2.11, were predicted. The model devised not only adequately described the measured data but confirmed Vermeer *et al.*'s view that the hydrogenation of butane-2,3-dione is a ligand accelerated reaction as observed for several  $\alpha$ -keto acid derivatives [73].

The hydrogenation can be summarised as follows: (i) the first stage of the reaction shows a modest enantioselectivity (50% *ee*) and (ii) kinetic resolution is responsible for the increase in *ee* (up by 35-40%) of the hydroxybutan-2-one during the second step of the reaction, as  $k_{RS}$  is significantly larger for the modified than for unmodified catalysts, while  $k_{RS}$ ,  $k_{RR}$  and  $k_{SS}$  remain virtually unchanged. This results in the (*S*)-3-hydroxybutan-2-one disappearing quickly whilst the meso-butane-2,3-diol begins to dominate, as well as gradually increasing the *ee* of the two chiral diol molecules in favour of the (*R,R*)-butane-2,3-diol.

Shortly after this publication, Slipszenko *et al.* [112] published a similar study in which the reaction in dichloromethane at 268-298 K and 10 bar pressure over Pt/silica



modified by CD and CN was investigated. In contrast to Studer's work [4] they found the reaction to proceed in three stages rather than two. About 85% of the butane-2,3-dione was converted to 3-hydroxybutan-2-one in the first step, with 15% forming three higher molecular weight products by hydrodimerisation. The overall *ees* recorded were similar to the previous communications [1,4,111], however with CN, the initial *ee* in the hydroxybutanone was 10% in favour of the (*S*) form. The second stage is analogous to that quoted by Studer *et al.* [4] with the same kinetic effects giving rise to the *ees* in the remaining hydroxybutanones (in the range of 62 to 89% for (*R*) and 30% (*S*)) whilst the minority enantiomer converts preferentially into the corresponding diol. However, the additional third stage sees the three dimers slowly converting by hydrogenation, dissociation, followed by a further hydrogenation into the butane-2,3-diol. Dimer formation was found to occur only in a modified dichloromethane system. As with the hydrogenation of  $\alpha$ -ketoesters, the butane-2,3-dione reaction proceeds to a racemic mixture in the absence of a cinchona modifier.

Generally, the behaviour of butane-2,3-dione hydrogenation is in many cases similar to the reaction of pyruvates over cinchona modified surfaces. Each reaction step is zero order in diketone and first order in hydrogen, implying that the former is strongly and the latter weakly adsorbed. The calculated activation energy for the butane-2,3-dione is comparable at 30 kJ mol<sup>-1</sup> to that for the pyruvate hydrogenation (38 kJ mol<sup>-1</sup>) [33]. In both reactions, CD favours the (*R*)-product whilst CN induces enantioselectivities in preference of the (*S*)-product, however, increasing the temperature above 300 K can result in the loss of activity and enantioselectivity. Unlike the pyruvate reaction, for which the single stage hydrogenation is normally rate-enhanced over modified catalysts, the diketone hydrogenation is not. In addition, the *ee* for the diketone hydrogenation is not conversion dependent over the first 20% or so of reaction as found for the case of the pyruvate reaction [32,37,113,114]. However, the *ee* in the diketone reaction is dependent on the amount of alkaloid used in the modification step [112] whereas in the pyruvate reaction maximum *ee* is achieved with low concentrations of the modifier [35]. These differences imply that the diketone is more strongly adsorbed on the Pt surface than the pyruvate and could easily displace the alkaloid, as investigated by Slipszenko *et al.* [112].

So far mechanistic work is limited and at present the observed enantioselectivity in the conversion of butane-2,3-dione to 3-hydroxybutan-2-one in the first stage of the

reaction is thought to follow the same model proposed for the pyruvate model [55]. As an analogous modelling study for the 1:1 interaction of the diketone with CD and CN in their appropriate lowest energy states illustrates from the calculated interaction energies that the selective enantioface adsorption of the reactant occurs within the vicinity of the adsorbed CD and CN [115].

#### 2.4. The Adsorption of Hydrogen on Pd and Pt Surfaces

Hydrogen is a chemically reactive gas, which adsorbs dissociatively onto most transition metals with heats of chemisorption between 30 and 60 kJ mol<sup>-1</sup> (per atom). Due to its small size hydrogen is capable of adsorbing not only onto the surface but also by penetrating deep into the metal causing a strong perturbation of its electronic structure. For most metals such as Ni and Pt this perturbation results in a relaxation of the surface lattice only but for others such as Pd the hydrogen can adsorb into the bulk structure forming PdH *via* the process of surface reconstruction. A combination of temperature programmed desorption (TPD) methods [116] and H/D exchange reactions [117] have illustrated the presence of sub-surface H in Pd.

The adsorption energy at the low coverage limit of hydrogen on Pt powders has been measured by microcalorimetry to be 45 kJ mol<sup>-1</sup> [118]. Thermal desorption spectroscopy (TDS) studies show that the heat of dissociative adsorption of H<sub>2</sub> over Pt(111) is about 83 kJ mol<sup>-1</sup> [119-121]. Low-energy electron diffraction (LEED) experiments show the formation of an ordered  $p(1 \times 1)$  hydrogen layer on Pt(111) and at low H coverages an adsorption of 38.6 kJ mol<sup>-1</sup> is measured with TPD [116,122,123]. The observation of a relatively low electron energy loss spectroscopy (EELS) frequency for H on Pt(111) has been interpreted as implying a central position for absorption (atop) [116,122,123]. The electronic structure of H adsorption on Pt(111) has been studied by UPS, an adsorbate-induced peak at 7.3 eV (prior to background noise subtraction) below the fermi level ( $E_F$ ) represents the H chemisorption, implying a significant redistribution in the *d*-band region [124,125].

Results of low energy recoil scattering experiments [126] point towards the stable adsorption of hydrogen in the face-centred cubic (*fcc*) hollow site on Pt with a bond length of  $1.78 \pm 0.08$  Å. This is found to agree well with the later study of Lui *et al.* [127] whose quantitative analysis of the Pt(111)-(1 × 1)-H surface with low energy ion

channelling using 5 keV  $\text{Ne}^+$  ions as a probe (sensitive to low coverages of adsorbed hydrogen) showed the same preferential population of the *fcc* sites with a height of  $0.9 \pm 0.1$  Å above the first-layer Pt atoms and a corresponding Pt-H bond length of  $1.9 \pm 0.1$  Å. These values are in excellent agreement with measurements of Umezawa *et al.* [126,128,129].

The result of the occupation of the *fcc* hollow site on Pt surfaces is also consistent with theoretical calculations of Feibelman and Hamman [130] which predict the energy of the *fcc* site to be  $19.3 \text{ kJ mol}^{-1}$  lower than that of the hexagonal close-packed (*hcp*) site. With the use of periodic DFT calculations ( $p(2 \times 2)$  unit cell, 3-layer slab, 330 eV cutoff,  $5 \times 5 \times 1$  *k*-point grid) Desai *et al.* [131] reported an adsorption energy of  $86 \text{ kJ mol}^{-1}$  for hydrogen adsorbed in a *fcc* hollow site on Pt(111), found to be in good agreement with the value of  $83 \text{ kJ mol}^{-1}$  over a quarter-monolayer surface coverage reported by Hoffmann *et al.* [132] as well as the TDS data referenced above. An analogous study by Watson *et al.* [133], ( $p(2 \times 2)$  unit cell, 5-layer slab, 300 eV cutoff,  $5 \times 5 \times 1$  *k*-point grid) calculated the H-*fcc* hollow site adsorption ( $46.0 \text{ kJ mol}^{-1}$ ) to be more stable than the corresponding *hcp* site ( $43.4 \text{ kJ mol}^{-1}$ ) which in turn was similar to both the atop and bridge adsorptions.

For Pd(111), LEED detected the formation of a  $p(1 \times 1)$  layer of adsorbed H on the surface with heats of adsorption measured at  $86.8 \text{ kJ mol}^{-1}$  [116,122,123]. Further diffraction data from Felter *et al.* [134] suggested that hydrogen is stabilised by the *fcc* hollow site with a Pd-H distance of 1.78-1.80 Å. An adsorption energy of  $43.4 \text{ kJ mol}^{-1}$  has also been measured on the surface with hydrogen coverage at  $\theta = 0.3$  by TDS [116]. UPS studies of H on Pd(111) [124,125] show an adsorbate-induced peak roughly 6.5 eV below  $E_F$ , implying a smaller redistribution in the *d*-band region compared to the analogous case above for Pt(111).

As with Pt(111) the stability of the adsorption sites for the preference of the *fcc* over the *hcp* hollow site was predicted by the DFT simulations of Paul and Sautet [135] and Løvvik and Olsen [136] who used Slater orbitals and a plane-wave pseudopotential method respectively. The same trend was also observed in the periodic simulations of Watson *et al.* [133] over 3- and 5-layer relaxed Pd(111) surfaces. In each case a difference of 3.1 and  $4.6 \text{ kJ mol}^{-1}$  in adsorption energy was calculated between the two H adsorbed sites, the actual adsorption energies for the *fcc* hollow sites are 47.9 and  $50.1 \text{ kJ mol}^{-1}$  respectively.

### 2.5. The Adsorption of Ethene on Pt Surfaces

Experimentally, *i.e.* a combination of vibrational spectroscopy methods has found ethene to adsorb molecularly in a non-dissociative manner onto metal surfaces in two very different and stable modes at different temperatures. The first being a  $\pi$ -bonded species coupled to a single metal site (figure 2.12(a)) and the second, a di- $\sigma$  bonding bridged between two surface atoms (figure 2.12(b)). When the temperature is above 240 K the di- $\sigma$  ethene molecules are found to fragment and decompose into ethylidyne ( $\text{CCH}_3$ ) intermediates which, unlike the  $\pi$  and di- $\sigma$  modes, interact *via* a geometry where the C-C bond is perpendicular to the surface.

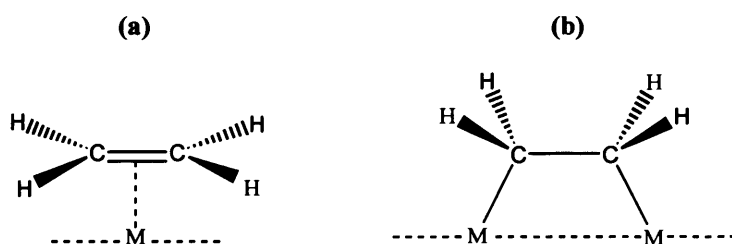


**Figure 2.12:** Surface bonding configurations of ethene: (a)  $\pi$ -bonding and (b) di- $\sigma$  bonding.  $M$  = surface metal atom.

A range of TPD estimates of the activation energy for the desorption of ethene have been reported from as low as 37.6 and 71.4  $\text{kJ mol}^{-1}$  [137] to as high as 202.6  $\text{kJ mol}^{-1}$  measured by collision-induced desorption by Szulczewski and Lewis [138]. The general reactivity of ethene on the Pt(111) surface was assumed to be responsible for the degree of variation of the desorption values as not all of the experiments are measuring the desorption of the same surface species. However, such studies have implied that the thermally induced desorption involves a number of steps principally where the breaking of Pt-C bonds occur to leave a  $\pi$  bonded species which then later desorbs.

Microcalorimetry has also been used to determine the heats of adsorption for ethene on various Pt metal surfaces, such as the (111) [139] and the (110) [140] as well as Pt powders [118,141]. For the (111) plane, at a temperature of 300 K, only the adsorption of ethylidyne was resolved at 174  $\text{kJ mol}^{-1}$ , whereas on the (110) surface both the  $\pi$  and di- $\sigma$  adsorptions were identified with respective adsorption energies of 120 and 136  $\text{kJ mol}^{-1}$ . With regard to the Pt powders the adsorbed ethylidyne species was once again

observed at 300 K and with a drop in temperature to about 173 K a mixture of both di- $\sigma$  and  $\pi$  adsorbed ethene followed with an adsorption measuring 120 kJ mol<sup>-1</sup>.

Theoretical cluster calculations using the extended Hückel theory [142,143] and atom superposition and electron delocalisation molecular orbital methods [144] have shown that the di- $\sigma$  adsorption mode is favoured over the  $\pi$  configuration. Although the adsorption values of 56 ( $\pi$  mode) and 197 kJ mol<sup>-1</sup> (di- $\sigma$  mode) do not correlate with the experimental energies, the trend observed is consistent.

## 2.6. The Adsorption of Aldehydes and Ketones on Pd, Pt and Related Surfaces

Adsorbed aldehydes or ketones are key intermediates for the general metal-catalysed synthesis reactions of oxygenate products from CO and H<sub>2</sub> as well as the reverse of this, the decomposition of alcohols on a metal surface. The destructive adsorption of alcohols and ketones on Pt metals in aqueous acidic mediums for the oxidation of alcohols is well documented [145,146]. For  $\alpha$ -ketoesters and small chain primary alcohols on Pt/Al<sub>2</sub>O<sub>3</sub> this can also occur in the absence of acid.

In the context of the  $\alpha$ -ketoester hydrogenation, the first step of this side reaction, involves both the (*R*)- and (*S*)-product lactates being dehydrogenated to the corresponding aldehyde, which then proceeds to decarbonylate to the appropriate structures (figure 2.13(a)). This is also common for the  $\alpha$ -ketoester degradation, which results in strongly adsorbed C<sub>x</sub>H<sub>y</sub>O<sub>z</sub> fragments (figure 2.13(b)). The high CO coverage of Pt/Al<sub>2</sub>O<sub>3</sub> detected by Fourier transform IR (FTIR) when the catalyst is flushed with Ar saturated with ethanol or EtPy supports the series of reactions in figure 2.13 [147].

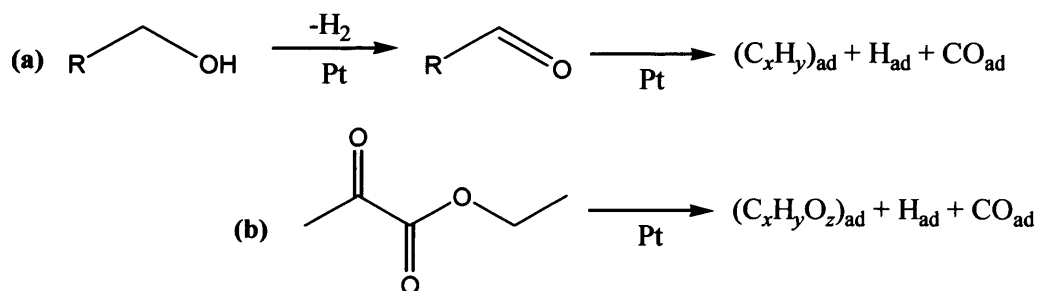


**Figure 2.13:** Destructive adsorption of primary alcohols and EtPy on Pt. *x*, *y* and *z* indicate that the composition of the adsorbed hydrocarbon fragments is unknown. Reaction scheme obtained from reference 68.

Generally, especially under low temperature conditions, aldehydes and ketones are found to chemisorb non-dissociatively to metal surfaces in two distinct adsorption geometries as illustrated in figure 2.14. The first, termed either  $\eta^1$  or endon, involves the molecule standing up with the C=O bond making a large angle to the surface plane and binding to the surface *via* the oxygen lone pair (figure 2.14(a)) whilst the second  $\eta^2$  (di- $\sigma$ ) adsorption mode has the molecule lying flat, with both the carbon and oxygen binding to Pt atoms (figure 2.14(b)). A number of different experimental characterisation techniques have reported these two adsorption modes [148-151].

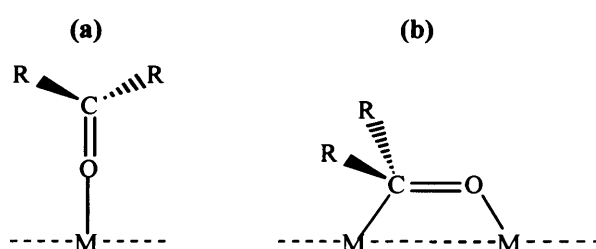


**Figure 2.14:** Surface bonding configurations of keto groups: (a)  $\eta^1(O)$  (endon) and (b)  $\eta^2(C,O)$  (di- $\sigma$ ).  $R = H$  or  $CH_3$  to give formaldehyde and acetone, respectively.  $M$  = surface metal atom.

For adsorbed acetone or hexafluoroacetone the  $\eta^1$  geometry has been identified on Pt(111) [152-154] whereas both species, although with a large preference for the  $\eta^2$ , are present on Pd(111) [149] (to be discussed in detail later), Ru(001) [152] and Rh(111) [155]. At low temperature this coexistence of the  $\eta^1$  and  $\eta^2$  adsorption is also preferred for aldehydes such as acetaldehyde or propanal on Pd(111) [148,150], Rh(111) [156,157], Ru(001) [158], Ni(100) [159] and Pt(S)[6(111)×(100)] [160].

### 2.6.1. The Adsorption of Formaldehyde

Experimentally, it is very difficult to characterise the adsorbed species of formaldehyde on transition metal surfaces such as Pt(111) [161,162], Pt(110) [163], Pd(111) [148], Rh(111) [151] and Ni(110) [164] because the molecule decomposes or polymerises quickly. However, the  $\eta^2$  coordination of formaldehyde has been identified on the Ru(001) surface [165,166]. Although, modification of the above surfaces with an oxygen adatom overlayer saw the preferential adsorption of the  $\eta^1$  mode.

With the use of TPD experiments, Abbas *et al.* [161] have estimated the adsorption energy of formaldehyde on Pt(111) to be about 52 kJ mol<sup>-1</sup>, this is in excellent

agreement with the analogous adsorption found on the Pd(111) surface (51 kJ mol<sup>-1</sup>) by Davis and Barteau [148].

Often in the literature, analysis of formaldehyde adsorption is referenced in terms of intermediate species in the decomposition process of methanol, which is known to adsorb at low temperatures on Pd and Pt(111) [150,167]. Note that the desorption/decomposition of methanol follows the steps highlighted in figure 2.13. High-resolution electron energy loss spectroscopy (HREELS) experiments conducted by Davis and Barteau [150] provided evidence for the adsorption of formaldehyde in the  $\eta^2$  configuration. TPD experiments have shown that desorption of molecular methanol occurs at 200 K, suggesting that molecular species are present following adsorption at 170 K. At 170 K, the HREEL spectrum indicates the presence of the  $\eta^2$  species. The vibrations of the  $\eta^2$  formaldehyde are clearly recognisable after the surface is annealed to 240 K, the characteristic CO stretch is observed at 1420 cm<sup>-1</sup>. An analogous vibration was observed at 1435 cm<sup>-1</sup> following CD<sub>3</sub>OD adsorption and annealing the adlayer to 260 K. The dehydrogenation of  $\eta^2$  formaldehyde to CO<sub>(ad)</sub> is completed at temperatures above 300 K and the assignment of this  $\nu(\text{CO})$  vibration to the  $\eta^2$  formaldehyde agrees with the assignments for other  $\eta^2$  adsorbed carbonyl compounds on Pd(111) [148,149]. The presence of the  $\eta^2$  formaldehyde is further verified by the replacement of the 705 cm<sup>-1</sup> peak for the CH<sub>3</sub>OH derived adlayer with the 710 cm<sup>-1</sup> peak following the adsorption of CD<sub>3</sub>OD. With reference to spectra for acetone [149] and aldehydes [148] adsorbed on Pd(111), this loss was assigned to the  $\pi(\text{CO})$  vibration of the carbonyl group of  $\eta^2$  formaldehyde.

A theoretical approach to examine the interaction of formaldehyde on a flat and stepped (111) surface of Pd and Pt has been reported by Delbecq *et al.* [168,169]. For the flat surface, adsorption geometries of several different modes as illustrated in figure 2.15 were investigated. To represent the (111) extended surface planes, semi-spheric-like clusters *i.e.* Pd<sub>49</sub> and Pt<sub>49</sub> were used. Extended Hückel calculations incorporating a correction procedure for the edge effects were employed to obtain the energetics of adsorption.

For Pt, both the  $\eta^1$  and  $\eta^2$  geometries were found to be plausible on the surface, with the latter more strongly adsorbed (46.0 vs. 95.8 kJ mol<sup>-1</sup>). In addition to these geometries a third species termed  $\eta^1\mu^2$  (bridge (figure 2.15(b))) was found to be stabilised on the Pd surface more so than the  $\eta^1$  endon mode (47.3 vs. 43.1 kJ mol<sup>-1</sup>),

however, as with Pt the  $\eta^2$  was found to be predominant at 133.1 kJ mol<sup>-1</sup> (refer to figure 2.15(e) for analogous Pt geometry).

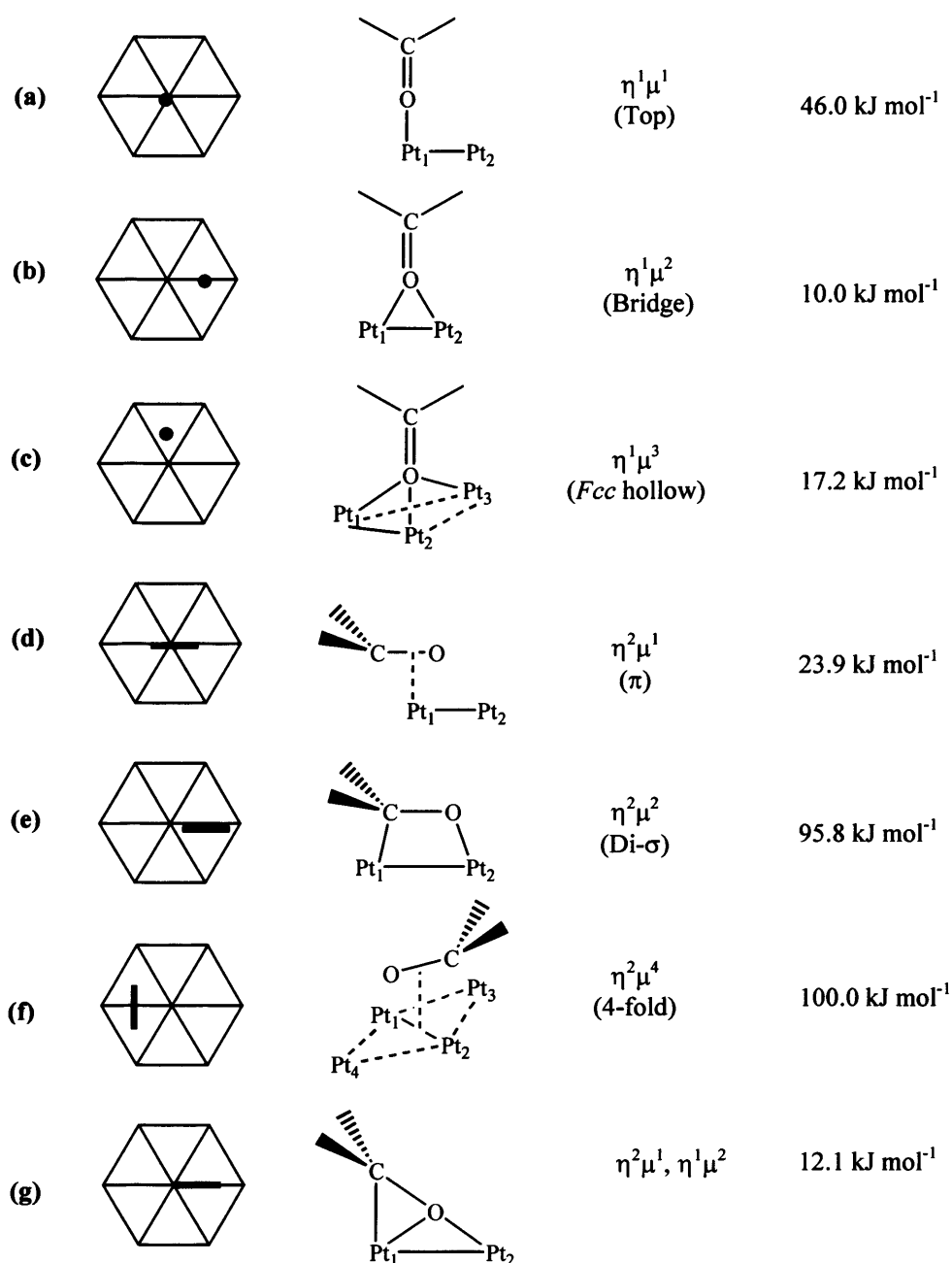


**Figure 2.15:** The modelled adsorption geometries of formaldehyde on a Pt(111) surface as investigated by Delbecq et al. The final column gives the corresponding adsorption energies, calculated from  $-(E(\text{cluster} + \text{adsorbed H}_2\text{CO}) - E(\text{cluster}) - E(\text{free H}_2\text{CO}))$ . (c) and (f) are endothermic energies representing unstable adsorptions. Note that chemisorption must be exothermic since a spontaneous process requires a negative change in Gibbs free energy ( $\Delta G$ ). As the translational freedom of the adsorbate is reduced when it is adsorbed, the change in entropy ( $\Delta S$ ) is negative. Therefore, in order for  $\Delta G = \Delta H - T \Delta S$  to be negative,  $\Delta H$ , the change in enthalpy must be negative and the process exothermic.  $T$  represents temperature measured in K. Figure obtained and adapted from reference 168.



For the stepped surface only Pt was investigated by Delbecq *et al.* [169]. To generate terraces, half of the first layer of a 114 atom cluster ( $\text{Pt}_{114}$ ) with a core of 49 atoms was removed to construct a  $[n(111) \times (100)]$  step. A stepped  $\text{Pt}_{96}(111)$  cluster was obtained by this operation and three different adsorption sites for the  $\eta^1$  and  $\eta^2$  formaldehyde were considered on this cluster, (1) the  $\text{Pt}_{114}(111)$  surface which is restored on moving away from the step edge and (2) and (3) the angle of adsorption of the molecule on the step, at  $0^\circ$  and  $20^\circ$ .

As with the  $\text{Pt}_{49}$  calculations, the di- $\sigma$   $\eta^2$  adsorptions had lower energy than the endon  $\eta^1$  modes, the corresponding adsorption energies for the stepped Pt surface were measured as follows: (i) on  $\text{Pt}_{114}$ , 38.9 vs. 95.8  $\text{kJ mol}^{-1}$ , (ii) on  $\text{Pt}_{96}$  with  $0^\circ$  tilt, 45.6 vs. 106.7  $\text{kJ mol}^{-1}$ , (ii) on  $\text{Pt}_{96}$  with  $20^\circ$  tilt, 48.1 vs. 114.2  $\text{kJ mol}^{-1}$ . The adsorption energy is calculated to be larger on the step site than it is on the (111) terrace. Generally, since catalytic surfaces are very rarely flat, a number of studies have reported stronger adsorptions for aldehydes and ketones on a step than on a flat surface [169].

The results correlated well against experimental data. TPD identified the intermediate of the decomposition of formaldehyde on  $\text{Pt}(111)$  into CO and  $\text{H}_2$  lying parallel to the surface, thus, implying that the first adsorption mode is the  $\eta^2$  species [161]. This adsorbed geometry is generally perceived as the precursor to dissociation of aldehydes or ketones on a surface [148-153,155-157,170].

At higher surface coverage, there are a low number of sites available for dissociation and so formaldehyde adsorbs in the  $\eta^1$  top geometry (figure 2.15(a)), because only a small number of metallic atoms are required and so accommodates dense packing. The adsorbed  $\eta^1$  then initiates polymerisation and decomposition, forming products such as  $\text{CH}_4$ ,  $\text{CH}_3\text{-OH}$ , or methyl formate, which are different from those of the low-coverage reaction [162]. Moreover, in the study of methanol decomposition on  $\text{Pd}(111)$ , a  $\eta^2$  form of adsorbed formaldehyde has been spectroscopically observed [150].

Common to each study above is the marked effect surface adsorption has on the geometry of the formaldehyde. The previous work of Delbecq *et al.* [168] paid great attention to the analysis of orbital interactions involved in the adsorption geometries in figure 2.15 on the Pt surface. Hybridisation of the atom sites from  $\text{sp}^2$  to  $\text{sp}^3$  was found to be optimum for the  $\pi$  (figure 2.15(d)) and di- $\sigma$  (figure 2.15(e)) formaldehyde coordinations. For the  $\eta^2\mu^1, \eta^1\mu^2$  mode (figure 2.15(g)) only partial hybridisation of the carbon atom was observed as this is a hybrid involving both the  $\eta^2$  and  $\eta^1$  geometries.

Aldehydes on Pd(111) have also been reported to display this high distortion in the molecular adsorption geometries on coordination with the surface [148,151]. Compared to the gas-phase formaldehyde structure the C=O bond (1.21 Å) is lengthened to 1.35 Å (Chapter 6, section 6.2, table 6.4) and typical of those found in organometallic complexes (C=O bond length 1.40-1.41 Å) such as  $\text{Pt}_2(1,5\text{-C}_8\text{H}_{12})_2\eta_2(\text{CF}_3)_2\text{CO}$  [171] and in  $(\text{Cp}_2\text{ZrX})_2(\text{HRCO})$  or  $(\text{Cp}_2\text{-Zr}(\eta_2\text{CH}_2\text{O}))_3$  [172]. In the former, the hybridisation of  $(\text{CF}_3)_2\text{CO}$  is total to  $\text{sp}^3$ .

The stabilisation of formaldehyde on a metallic cluster is reported to be achieved by a significant contribution of back-donation of electron density from the metal surface into  $\pi^*$  CO orbitals of the adsorbate [168], in a fashion analogous to that of organometallic complexes [173]. The resulting  $\text{sp}^3$  hybridisation lowers the  $\pi^*$  CO orbital energy and in turn increases the two-electron interaction, which ultimately drives towards a strong distortion in which the geometry is fully hybridised.

A periodic approach to modelling the  $\eta^2$  formaldehyde species in context of the intermediate formed from dehydrogenation of methanol over Pt(111) is presented by Desai *et al.* [131]. Gradient corrected, periodic DFT calculations ( $p(2 \times 2)$  unit cell, 3-layer slab, 330 eV cutoff,  $5 \times 5 \times 1$   $k$ -point grid) illustrated the preferential binding of formaldehyde in the di- $\sigma$  mode on the Pt(111) surface, as suggested by Delbecq and Sautet [168]. In the optimised structure, the C=O bond is orientated parallel to the metal surface with the Pt-C and Pt-O bonds nearly the same length (2.12 and 2.06 Å, respectively), while the hydrogen atoms are directed away from the surface. The adsorption energy for the  $\eta^2$  formaldehyde is calculated at 49 kJ mol<sup>-1</sup>, in good agreement with the TPD estimates [161]. As a comparison the same calculations were performed over the Pd(111) surface, the di- $\sigma$  adsorption energy was calculated at 54 kJ mol<sup>-1</sup> closely resembling the Pt value. Once again the calculated adsorption energy is in excellent agreement with the experimental TPD values. For formaldehyde, it appears that in the gas-phase it is a closed shell, stable species that interacts weakly both with Pd and Pt.

### 2.6.2. The Adsorption of Acetone

Although, the catalytic hydrogenation of acetone over metals has been studied extensively [174] the interaction of the substrate, particularly with the clean surfaces has

received much less attention. In an early UPS study by Lüth *et al.* [175] the interaction of acetone with polycrystalline Pd films was found to lead to decomposition to adsorbed CO at 300 K. At lower temperature (120 K) decomposition was inhibited and an intermediate surface-bound molecular specie was detected, with coordination to the surface *via* the oxygen lone pair electron orbital (figure 2.14(a)). At the time, IR studies of acetone adsorption on dispersed metals such as Co and Ni [176,177] were found to be contradictory.

To date, ultrahigh vacuum (UHV) surface science studies [149,153,155,178] of acetone adsorption on metal single-crystal surfaces (exception of Ag, to be discussed later) point towards two dominant adsorption states, the  $\eta^1$  and  $\eta^2$  geometries (as discussed above, figure 2.14), similar to those found for the adsorption of formaldehyde.

Much of the principle work regarding the adsorbed species from acetone adsorption on Pt(111) surfaces has been conducted by Avery and co-workers [152,154,179]. Initially, HREELS and TDS was used to probe the clean Pt surface for adsorbed acetone species at 120 K. The two structures, the  $\eta^1$  and  $\eta^2$  were characterised and determined.

TDS illustrated the presence of the more weakly bound,  $\eta^1(\text{O})$  acetone at 185 K and at high coverage which corresponds to an adsorption energy of  $48.5 \text{ kJ mol}^{-1}$ . At low coverage the desorption of a second minority species ( $\eta^2(\text{C,O})$  acetone) in conjunction with some decomposition to  $\text{CO}_a$ ,  $\text{H}_a$  and an adsorbed hydrocarbon,  $[\text{C}_2\text{H}_x]_a$  (fragments  $a$  and  $x$  indicate that the composition is unknown) occurred in the region of 220-240 K. A small amount of second layer acetone adsorption was observed as implied by the tail on the multilayer acetone spectrum, and this was detected to desorb at  $35.6 \text{ kJ mol}^{-1}$ , found to be comparable to the latent heat of vaporisation of acetone from the liquid state ( $32.0 \text{ kJ mol}^{-1}$  [180]).

EELS was used to determine the bonding configuration of acetone in the two monolayer states. The more strongly bound minority form of acetone (determined by TDS) showed no EELS bands due to skeletal modes, although methyl stretching, deformation and rocking modes associated to side-on bonding (*i.e.*  $\eta^2(\text{C,O})$ ) were observed. However, at 160 K the acetone multilayer (for which a weak, EELS  $\pi(\text{CO})$  mode was seen) desorbed to reveal the EELS bands of the monolayer state. The EELS spectrum for the weakly bound species displayed a characteristic carbonyl stretching band ( $\text{A}_1$  symmetry) red-shifted by  $80 \text{ cm}^{-1}$ , together with two  $\text{B}_1$  skeletal modes *viz.*

$\nu_{as}(CC)$  and  $\delta(CO)$ . The spectrum indicated weakening of the C=O bond as a result of bonding through the O atom, implying an end-on adsorbed geometry ( $\eta^1(O)$  configuration), with the Pt-O-C bent most probably in the molecular plane. Similar band assignments for this form of adsorbed acetone are observed in a range of inorganic acetone complexes of the type  $[((CH_3)_2CO)_6M]^{2+}$  [181].

The  $\eta^1$  form is most associated with the well defined close packed regions of the flat (ideal) Pt(111) surface whereas the  $\eta^2$  species have been proposed to adsorb on low-coordination step sites, as a result of the accidental probing of the EELS beam [179]. Similar species have been proposed to exist on the Ru(001) and Pd(111) surfaces [149,152,182].

For the hydrogenation of acetone over Pt, the importance of the different reactivities of the above species has been discussed by Sen and Vannice, in which the observed 400-fold enhancements in turnover frequency with certain supports is thought to be attributed to the presence of sites favouring an  $\eta^2$  configuration [183].

To explore the  $\eta^2$  mode identified by Avery [179], reflection absorption infrared spectroscopy (RAIRS), HREELS and TDS was employed by Vannice *et al.* to further characterise adsorbed acetone on a clean Pt(111) surface as well as acetone coadsorbed with hydrogen on this surface [178]. All of the RAIR spectra peaks were resolved as expected from liquid-phase IR spectra and gave very similar peak positions for all the multilayer acetone bands as assigned by Avery [179]. The characteristic C=O stretch frequency for the  $\eta^1$  monolayer state was red-shifted to  $1638\text{ cm}^{-1}$ . The  $\eta^2$  species with its C=O bond parallel to the surface as reported for Pt(111) [179], Ru(001) [149,152] and Pd(111) [182] was not so clearly defined on the defect-free Pt(111) surface.

Desorption energies close to those predicted by Avery [179] were calculated at 52.3, 48.1 and  $33.5\text{ kJ mol}^{-1}$  for the  $\eta^2$ ,  $\eta^1$  and multilayer acetone species, respectively. However, a second desorption peak at 199 K was resolved from the  $\eta^1$  peak at 184 K and was associated as with Avery's work [179] with the more strongly bound  $\eta^2$  adsorbed state of acetone. For this surface, decomposition of acetone did not occur during the desorption process.

Both the RAIRS and HREELS spectra also indicated the presence of the  $\eta^2$  in addition to the  $\eta^1$  phase on the monolayer, unlike Avery's EELS spectra [179]. It was found that as the multilayer phase develops the initial  $\eta^1$  species gradually disappear, with the associated  $1638\text{ cm}^{-1}$  peak removed at temperatures below 200 K. At this stage

the methyl peaks (1086, 1360, and 1428  $\text{cm}^{-1}$ ) were found to strengthen in intensity whilst new weak bands thought to represent  $\eta^2$  species in different configurations [149,152,179] appeared between 1500 and 1610  $\text{cm}^{-1}$ . These latter bands have also been reported for the dissociative adsorption of isopropyl alcohol to give adsorbed hydrogen and acetone [184].

In which case, TPD experiments demonstrated that 2-propanol undergoes selective dehydrogenation on a clean Pd(111) surface to produce acetone, which further desorbs or decomposes (as with the methanol case) to the decarbonylate products as in figure 2.13 [185]. HREEL spectra were able to confirm the presence of both molecular 2-propanol and stable isopropoxide intermediates. Although the exact presence of the  $\eta^2$  acetone on the surface between 200 and 230 K could not be confirmed directly from the vibrational data (normal modes being obscured by the isopropoxides), annealing the surface to 240 K (decomposition of isopropoxides) resulted in a loss appearing at 1450  $\text{cm}^{-1}$  (similar to Vannice *et al.*'s [178] peak) and was assigned to the  $\nu(\text{CO})$  mode of  $\eta^2$  acetone. The frequency of this vibration is also in agreement with that of  $\eta^2$  acetone species produced by acetone adsorption on Pd(111) [149]. Further annealing of the surface to 300 K resulted in the disappearance of the vibrations of  $\eta^2$  acetone, consistent with TPD experiments that showed acetone desorption at this temperature [185].

Both HREELS and TPD have identified the adsorption of acetone on Pd(111) in two forms [149]. The first mode corresponds to an adsorption energy of 69.0  $\text{kJ mol}^{-1}$  and is associated to a  $\eta^2$  geometry, whilst the second is assumed to be the  $\eta^1$  mode with an adsorption energy of 48.1  $\text{kJ mol}^{-1}$ . Conversion of  $\eta^1$  to the  $\eta^2$  state has been shown to occur rapidly on Pd(111) above 200 K [149].

Theoretically, in parallel to the adsorption of formaldehyde Delbecq *et al.* [169] also investigated the energetics of acetone on the corresponding Pt and Pd(111) surface clusters. On the flat  $\text{Pt}_{49}$  surface both the  $\eta^1$  and  $\eta^2$  species were possible with adsorption energies measured at 46.0 and 25.5  $\text{kJ mol}^{-1}$ . However, on Pd an additional third mode,  $\eta^1\mu^2$  (analogous formaldehyde structure, figure 2.15(b)) in which the O atom of the acetone bridges with two different surface atoms was found to be preferred over the endon  $\eta^1$  geometry (47.3 vs. 43.1  $\text{kJ mol}^{-1}$ ). The di- $\sigma$  was stabilised with an adsorption energy of 79.9  $\text{kJ mol}^{-1}$ .

For the stepped Pt surface, binding of acetone to the step site was found to be larger than on the (111) terrace, following the same trend as displayed with formaldehyde

[169]. The binding energy of  $\eta^1$  acetone on the Pt<sub>114</sub> terrace was measured at 38.5 kJ mol<sup>-1</sup> with the corresponding  $\eta^2$  less strongly adsorbed (20.9 kJ mol<sup>-1</sup>). In this approach, the preferred adsorption mode for acetone is the endon  $\eta^1$  geometry, in contrast with formaldehyde and in agreement with the experimental data [152,179].

### 2.6.3. The Keto-Enol Tautomerism of Acetone and the Adsorption of the Enolate

Acetone is known to undergo *keto-enol* tautomerism, a rearrangement of a proton, which results in another isomeric structure termed the *enol* to form. The *enol* is an unsaturated alcohol (figure 2.16). The isomers are rapidly interconverted and the equilibrium between them under normal conditions strongly favours the *keto* isomer (99.999%). Even in such one-sided equilibria, evidence for the presence of the minor *enol* comes from the chemical behaviour of the compound. The tautomeric equilibria can be catalysed by either acids or bases and so in principle could be evident in the  $\alpha$ -ketoester hydrogenation, depending on the solvent used. However, reaction of the enolate ion with an electrophile is known to remove it from the equilibrium, *i.e.* shifting the *keto-enol* equilibrium towards the formation of more *enol*, and so could clearly, as proposed by Wells *et al.* [41], and Solladié-Cavallo [186] be an intermediate in hydrogenation reactions.

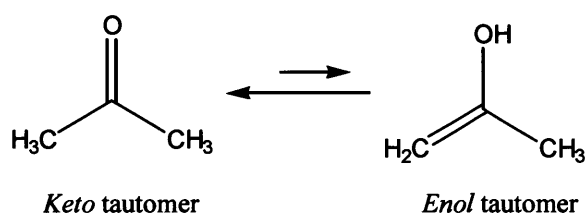


**Figure 2.16:** Keto-enol tautomerism for acetone.

The importance of metal enolate species have been identified as key intermediates in both organometallic chemistry and heterogeneous catalysis. Surface enolate intermediates have been recognised as part of the industrial process of acetone condensation over transition metal oxide catalysts, in particular, when powered samples of ill-defined surface structure and composition are involved [187]. An enolate species has been postulated for the case of preoxidised Ag [188,189] and recently, been isolated on both the clean and preoxidised Ni(111) surface by Sim *et al.* [187]. These authors use RAIRS, isotopic substitution studies and DFT calculations to fingerprint the surface

species present. Under a variety of temperatures a set of distinct absorption bands are detected for acetone on the Ni surfaces by the RAIRS, and these are illustrated in figure 2.17.

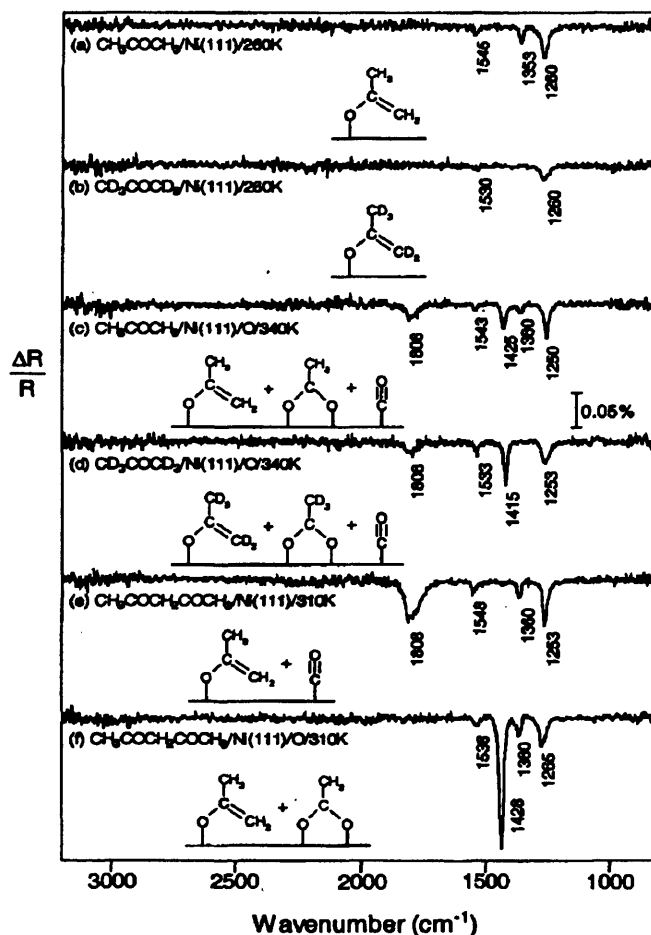


**Figure 2.17:** RAIR spectra of Ni(111) and Ni(111)/O exposed to  $>0.2$  L of acetone or acetylacetone at the temperatures indicated. Figure obtained from reference 187.

The characteristic bands for the main surface-bound acetone enolate species as reinforced by H/D exchange studies on both the clean and preoxidised (0.1 monolayer of O prior to the dosing of acetone isotopomers at 340 K) surfaces are 1260, 1353 and 1545  $\text{cm}^{-1}$ , and assigned to the mixed vibrational modes involving the CC stretch  $\nu(\text{CC})$ ,  $\text{CH}_3$  symmetric deformation  $\delta_s(\text{CH}_3)$ , and CO stretch  $\nu(\text{CO})$ , (refer to figure 2.17, spectra (a)-(d)). Using acetylacetone as a precursor molecule, the acetone enolate is also found to occur on the Ni(111) at 310 K. The same trio of absorption bands at 1253, 1360 and 1548  $\text{cm}^{-1}$  were obtained as illustrated in figure 2.17, spectra (e) and (f). A number of byproducts for the surface reactions were also characterised and these are highlighted in figure 2.17. Several different adsorption species, *i.e.*  $\eta^1(\text{C})$  acetyl,  $\eta^1(\text{C})$

acetonyl,  $\eta^1(\text{O})$  acetone enolate and bridging  $\mu(\text{C},\text{O})$  acetone enolate including the well characterised  $\eta^1(\text{O})$  acetone and  $\eta^2(\text{C},\text{O})$  acetone are thought to be the most probable interactions between acetone and a transition metal (figure 2.17).

To distinguish between these species Sim *et al.* [187] used a perturbative Becke-Perdew DFT method [190] to predict the vibrational spectra of the minimum-energy structures of a series of model Ni complexes containing the above ligands. Only the computations for  $\eta^1(\text{O})$  and  $\mu(\text{C},\text{O})$  acetone enolate complexes, even on deuteration, gave rise to adsorption bands that were in full agreement with the observed RAIR data [191]. Sim *et al.* [187] rule out the possibility of the other species on the basis of their DFT calculations and vibrational spectra of them on surfaces and in organometallic compounds. For example, the  $\eta^1(\text{O})$  acetone is predicted to have a  $\nu(\text{CO})$  frequency of  $1647\text{ cm}^{-1}$ , which for clean and preoxidised Ni(111) is observed at  $1655$  and  $1682\text{ cm}^{-1}$ , respectively. Higher frequencies for the vibrational mode is also detected on the Pt(111) [178], Pd(111) [149], Rh(111) [155] and Ru(001) [153] surfaces at  $1638$ ,  $1670$ ,  $1665$  and  $1690\text{ cm}^{-1}$ . For metal complexes of the type  $[\text{M}((\text{bz})_2\text{SO})_4(\eta^1(\text{O})\text{-acetone})_2]^{2+}$  where  $\text{M} = \text{Mn}, \text{Fe}, \text{Co}, \text{Ni}, \text{Zn}$  or  $\text{Cu}$ , the  $\nu(\text{CO})$  frequency varies between  $1680\text{-}1694\text{ cm}^{-1}$  [192].

In addition to the work of Sim *et al.* [187], independent IR spectroscopic studies of the adsorption of acetone on various metal oxide catalysts such as, NiO [193],  $\text{Fe}_2\text{O}_3$  [194] and  $\text{Al}_2\text{O}_3$  [195,196] have reported the presence of surface-bound acetone enolate. Organometallic complexes comprising of the  $\eta^1(\text{O})$ - and  $\mu(\text{C},\text{O})$ -acetone enolate ligands are also known to display the characteristic  $\nu(\text{CO})$  frequencies, in particular  $\text{Ru}(\text{PMe}_3)_4(\text{H})(\eta^1(\text{O})\text{-acetone enolate})$  [197],  $[\text{Pd}(\mu(\text{C},\text{O})\text{-acetone enolate})\text{X}]_n$  ( $\text{X} = \text{Cl}$  or  $\text{I}$ ) [198] and  $(\text{PdX})_2(\mu(\text{C},\text{O})\text{-acetone enolate})_2$  ( $\text{X} = o\text{-C}_6\text{H}_4\text{CH}_2\text{NMe}_2$  or  $(\text{AsPh}_3)(\text{C}_6\text{F}_5)$ ) [199]. Although, not stated the reported  $\nu(\text{CO})$  frequencies for the above catalysts and metallic complexes are found corroborate well against the predicted values of Sim *et al.* [187] ( $1511\text{-}1574\text{ cm}^{-1}$ ) and the RAIR spectra acquired for the species on the Ni(111) surface ( $1545\text{ cm}^{-1}$ ).

## 2.7. Conclusions

With over a decade's worth of research on the heterogeneous enantioselective hydrogenation of  $\alpha$ -ketoesters over chirally modified Pt, significant progress has been



achieved in understanding the origin of the *ra* and mechanism of *ed* and broadening the scope of the reaction to other activated ketones, such as butane-2,3-dione [1,4] and ketopantolactone [2,101]. By trying to unravel the interactions occurring between the reactants, solvent, product, cinchona modifier and the Pt catalyst, various models to account for the experimental behaviour have been proposed. The available mechanistic models are limited to the chiral induction step in the hydrogenation of the  $\alpha$ -ketoester and are concerned mainly with the formation of a reaction intermediate in which a surface dimer between the  $\alpha$ -ketoester and the cinchona modifier is created. These models are mainly based on the systematic variation of the reactant and the modifier structure and with the aid of theoretical calculations, the structures and stabilities of the various reactant-modifier complexes have been rationalised and refined over the past years.

The most widely accepted model is the two-step, two-cycle mechanism proposed by Baiker *et al.* [86]. In this mechanism, it is assumed that the active chiral sites are associated with the adsorption of CD on the Pt surface. The  $\alpha$ -ketoester from the fluid phase then adsorbs reversibly on these sites in its two enantiofacial configurations to form the diastereomeric intermediate complexes  $[\text{pyruvate} - \text{CD}]_{ad}^R$  and  $[\text{pyruvate} - \text{CD}]_{ad}^S$  which upon hydrogenation give the (*R*)- and (*S*)-lactate products, respectively. Limitations to this approach is the assumption that *ed* can be traced to different stability of the adsorbed diastereomeric reactant-modifier complexes (thermodynamic control) and so it will fail if the kinetics of hydrogen addition are different for the complexes affording the (*R*)- and (*S*)-products.

Due to a lack of *in situ* techniques in the fluid phase it is clear that little is known about the adsorptive interactions occurring on the Pt catalyst and as a result the role of the surface in the enantio-differentiating step is poorly understood. To make progress it is obvious that the effect of surface adsorption must be understood and surface science experiments on the adsorption of ketone molecules to metal surfaces are clearly in the right direction [148-151].

Although, a parallel adsorption of the pyruvates to the Pt surface is envisaged in the mechanistic model, the interaction of formaldehyde and acetone to the (111) surface of single-crystals is stabilised in two geometries: the endon,  $\eta^1(\text{O})$  and the di- $\sigma$ ,  $\eta^2(\text{C}, \text{O})$  mode [148,149,153,155,161,178]. For the chemisorption of acetone the former is the dominant species [179] whereas for formaldehyde the latter mode is observed

[161,162]. The structure and stability of these adsorption geometries have been rationalised by a range of theoretical models [131,168,169]. The steric clash between the methyl groups of the acetone and the surface destabilise the  $\eta^2(\text{C},\text{O})$  mode driving the adsorption into the  $\eta^1(\text{O})$  geometry. It is assumed that such an effect will be common to any larger ketone-containing molecule such as the pyruvates and so immediately the adsorption geometry of the reactant in the mechanistic model is questioned.

However, since acetone can undergo *keto-enol* tautomerism it is possible that either of the isomers can be present on the metal surface as intermediates as surface RAIRS on Ni(111) illustrates the stabilisation of the surface enolate at low temperature [187]. Thus, it is reasonable to assume that the pyruvates can interconvert into such isomers. Although at present the *keto* isomer is assumed to be the important reactant form in the pyruvate hydrogenation, observations by Wells *et al.* suggest otherwise [41]. D-tracer experiments imply that the hydrogenation of the pyruvate takes place *via* the *enol* isomer of the reactant on the Pd surface [41]. So far little is known about the role of the *enol* in the mechanism and work in this direction is badly needed.

To date most of the theoretical work is limited to the modelling of the reactant-modifier complexes. The surface interactions have either been ignored completely or included only as a geometric constraint. It is clear that modelling work should be aimed towards investigating the adsorptive interactions occurring on the catalyst. However, modelling of the complete system has still not been successfully attempted because the binding energies and structures of large complexes adsorbed on metal surfaces are still out of reach for accurate quantum chemical calculations. Nevertheless, before model predictions for complex systems can be achieved boundary conditions such as adsorption modes, conformations, interactions *etc.* have to be verified experimentally.

It emerges from the catalytic data, that, for the hydrogenation of  $\alpha$ -ketoesters, acetic acid is the most favourable solvent and that alcohol solvents lead to unfavourable side reactions such as the formation of a hemiketal, and so should be avoided. Although such side products do not take part in the enantio-differentiating step it is assumed that they affect the stereochemical outcome of the target reaction as they act to poison the active sites on the catalyst [68]. The enantioselectivity observed in the conversion of butan-2,3-dione to hydroxybutanone during the first stage of the reaction is thought to follow that for hydrogenation of  $\alpha$ -ketoester to lactate [55]. Theoretical calculations

illustrate that the conformation of the chiral modifier is particularly important due to its low concentration in the reaction mixture and that the reactant is conformation specific to maximise the interaction between itself and the modifier so to stabilise the diastereomeric complex [91]. Care should be taken in molecular models to ensure that the reactant, modifier, hydrogen and catalyst are contracted in the right manner so as to mimic experimental conditions.

## 2.8. References

- [1] W. A. H. Vermeer, A. Fulford, P. Johnston and P. B. Wells, *J. Chem. Soc., Chem. Commun.*, 1053, (1993).
- [2] T. Mallat, M. Bodmer and A. Baiker, *Catal. Lett.*, **44**, 95, (1997).
- [3] G. Z. Wang, T. Mallat and A. Baiker, *Tetrahedron: Asymmetry*, **8**, 2133, (1997).
- [4] M. Studer, V. Okafor and H. -U. Blaser, *Chem. Commun.*, 1053, (1998).
- [5] G. W. Watson, R. P. K. Wells, D. J. Willock and G. J. Hutchings, *J. Phys. Chem. B*, **104**, 6439, (2000).
- [6] G. -M. Schwab and L. Rudolph, *Naturwiss*, **20**, 362, (1932).
- [7] G. -M. Schwab, F. Rost and L. Rudolph, *Kolloid-Zeitschrift*, **68**, 157, (1934).
- [8] D. Lipkin and T. D. Stewart, *J. Am. Chem. Soc.*, **61**, 3295, (1939).
- [9] H. -U. Blaser and M. Müller, in “*Heterogeneous Catalysis and Fine Chemicals II*”, M. Guisnet *et al.*, (Editors), Elsevier, Amsterdam, 73, (1991).
- [10] H. -U. Blaser, *Tetrahedron: Asymmetry*, **2**, 843, (1991).
- [11] S. Akabori, Y. Izumi, Y. Fuji and S. Sukurai, *Nature*, **178**, 323, (1956).
- [12] Y. Izumi, *Advan. Catal.*, **32**, 215, (1983).
- [13] G. Webb and P. B. Wells, *Catal. Today*, **12**, 319, (1992).
- [14] T. Osawa, Y. Hayashi, A. Ozawa, T. Harada and O. Takayasu, *J. Mol. Catal. A*, **169**, 289, (2001).
- [15] T. Sugimura, *Catal. Surv. Jpn.*, **3**, 37, (1999).
- [16] T. Osawa, T. Harada and O. Takayasu, *Topics Catal.*, **13**, 155, (2000).
- [17] T. Osawa, T. Harada and A. Tai, *Catal. Today*, **37**, 465, (1997).
- [18] S. Nakagawa, T. Sugimura and A. Tai, *Chem. Lett.*, 859, (1997).
- [19] Y. Nitta, *Topics Catal.*, **13**, 179, (2000).
- [20] W. -R. Huck, T. Mallat and A. Baiker, *J. Catal.*, **1**, 193, (2000).
- [21] K. Borszeky, T. Bürgi, Z. Zhaohui, T. Mallat and A. Baiker, *J. Catal.*, **187**, 160, (1999).
- [22] A. Tungler, T. Tarnai, L. Hegedüs, K. Fodor and T. Mátthé, *Plat. Met. Rev.*, **42**, 108, (1998).
- [23] Y. Orito, S. Imai and S. Niwa, *Collected Papers of the 43<sup>rd</sup> Catalyst Forum, Jpn.*, **30**, (1978).
- [24] Y. Orito, S. Imai and S. Niwa, *Nippon Kagaku Kaishi*, 1118, (1979); *idem ibid*, 670, (1980).

- [25] Y. Orito, S. Imai, S. Niwa and G. N. Hung, *Yuki Gosei Kagaku Kyokaishi*, **37**, 173, (1979).
- [26] S. Niwa, S. Imai and Y. Orito, *Nippon Kagaku Kaishi*, 137, (1982).
- [27] <http://www.cf.ac.uk/chemy/staff/hutch.html>
- [28] <http://www.cf.ac.uk/chemy/staff/wells.html>
- [29] H. -U. Blaser, Solvias AG, R 1055.6, P. O. Box 4002, Basel, Switzerland.
- [30] <http://baiker.ethz.ch/people/Head/Baiker/>
- [31] G. Bond and P. B. Wells, *J. Catal.*, **150**, 329, (1994).
- [32] I. M. Sutherland, A. Ibbotson, R. B. Moyes and P. B. Wells, *J. Catal.*, **125**, 77, (1990).
- [33] P. A. Meheux, A. Ibbotson and P. B. Wells, *J. Catal.*, **128**, 387, (1991).
- [34] G. Bond, P. A. Meheux, A. Ibbotson and P. B. Wells, *Catal. Today*, **10**, 371, (1991).
- [35] G. Bond, K. E. Simons, A. Ibbotson, P. B. Wells and D. A. Whan, *Catal. Today*, **12**, 421, (1992).
- [36] G. Bond and P. B. Wells, *Appl. Catal.*, **18**, 221, (1985).
- [37] J. T. Wehrli, A. Baiker, D. M. Monti, H. -U. Blaser and H. -P. Jalett, *J. Mol. Catal.*, **57**, 245, (1989).
- [38] J. T. Wehrli, A. Baiker, D. M. Monti and H. -U. Blaser, *J. Mol. Catal.*, **49**, 195, (1989).
- [39] J. T. Wehrli, A. Baiker, D. M. Monti and H. -U. Blaser, *J. Mol. Catal.*, **61**, 207, (1990).
- [40] H. -U. Blaser, H. -P. Jalett, D. M. Monti, J. F. Reber and J. T. Wehrli, *Stud. Surf. Sci. Catal.*, **41**, 153, (1988).
- [41] T. J. Hall, P. Johnston, W. A. H. Vermeer, S. R. Watson and P. B. Wells, *Stud. Surf. Sci. Catal.*, **101**, 221, (1996).
- [42] R. B. Turner and R. B. Woodward, in "*The Alkaloids, Vol. III*", R. H. F. Manske, H. L. Holmes (Editors), Academic Press, New York, 1, (1953).
- [43] M. R. Uskokovic and G. Grethe, in "*The Alkaloids, Vol. XIV*", R. H. F. Manske (Editor), Academic Press, New York, 181, (1973).
- [44] R. Verpoorte, J. Schripsema and T. van der Leer, in "*The Alkaloids, Vol. 34*", A. Brossi (Editor), Academic Press, New York, 331, (1998).
- [45] R. L. Augustine, S. K. Tanielyan and L. K. Doyle, *Tetrahedron: Asymmetry*, **8**, 1803, (1993).

- [46] K. Borszeky, T. Mallat and A. Baiker, *Catal. Lett.*, **59**, 95, (1999).
- [47] T. Mallat, S. Szabo, M. Schürz, U. W. Göbel and A. Baiker, *Catal. Lett.*, **47**, 221, (1997).
- [48] H. -U. Blaser and M. Müller, *Stud. Surf. Sci. Catal.*, **59**, 73, (1991).
- [49] J. L. Margitfalvi, P. Marti, A. Baiker, L. Bötzt and O. Sticher, *Catal. Lett.*, **6**, 281, (1990).
- [50] W. Reschetilowski, U. Bohmer and J. Wiehl., *Stud. Surf. Sci. Catal.*, **84**, 2021, (1994).
- [51] H. -U. Blaser, H. -P. Jalett, D. M. Monti, A. Baiker and J. T. Wehrli, *Stud. Surf. Sci. Catal.*, **67**, 147, (1991).
- [52] H. -U. Blaser, H. -P. Jalett and D. M. Monti, *Appl. Catal.*, **52**, 19, (1989).
- [53] H. Bönemann and G. A. Braun, *Angew. Chem. Int. Ed. Eng.*, **35**, 1992, (1996).
- [54] X. Zuo, H. Liu and M. Liu, *Tetrahedron Lett.*, **39**, 1941, (1998).
- [55] K. E. Simons, P. A. Meheux, S. P. Griffiths, I. M. Sutherland, P. Johnston, P. B. Wells, A. F. Carley, M. K. Rajumon, M. W. Roberts and A. Ibbotson, *Rec. Trav. Chim. Pays-Bas.*, **113**, 465, (1994).
- [56] H. -U. Blaser, H. -P. Jalett and J. Wiehl, *J. Mol. Catal.*, **68**, 215, (1991).
- [57] B. Török, K. Felföldi, G. Szakonyi, K. Balazsik and M. Bartok, *Catal. Lett.*, **52**, 81, (1998).
- [58] D. Ferri, T. Bürgi and A. Baiker, *J. Chem. Soc., Perkin Trans.*, **7**, 1305, (1999).
- [59] B. Minder, T. Mallat, P. Skrabal and A. Baiker, *Catal. Lett.*, **29**, 115, (1994).
- [60] M. Garland and H. -U. Blaser, *J. Am. Chem. Soc.*, **112**, 7048, (1990).
- [61] H. -U. Blaser, M. Garland and H. -P. Jalett, *J. Catal.*, **144**, 569, (1993).
- [62] O. Schwalm, J. Weber, J. Margitfalvi and A. Baiker, *J. Mol. Struct.*, **297**, 285, (1993).
- [63] K. E. Simons, G. Wang, T. Heinz, T. Giger, T. Mallat, A. Pfaltz and A. Baiker, *Tetrahedron: Asymmetry*, **6**, 505, (1995).
- [64] J. L. Margitfalvi, *Chem. Ind. (Dekker)*, *Catal. Org. React.*, M. G. Scaros and M. L. Prunier (Editors), **62**, 189, (1995).
- [65] J. L. Margitfalvi and M. Hegedüs, *J. Catal.*, **156**, 175, (1995).
- [66] J. L. Margitfalvi, B. Minder, E. Tálas, L. Botz and A. Baiker, in "New Frontiers in Catalysis", *Proc, 10<sup>th</sup> Int. Cong. Catal.*, Budapest, 1992, L. Gucci et al. (Editors), Elsevier, **24**, 71, (1993).

- [67] E. Tálas, L. Botz, J. L. Margitfalvi, O. Sticher and A. Baiker, *J. Planar. Chrom.*, **5**, 28, (1992).
- [68] M. von Arx, T. Mallat and A. Baiker, *Topics Catal.*, **19**, 1, (2002).
- [69] R. Ravel, *Cattech.*, **5**, 12, (2001).
- [70] C. Bond, P. A. Meheux, A. Ibbotson and P. B. Wells, *Catal. Today*, **10**, 371, (1991).
- [71] R. L. Augustine and S. K. Tanielyan, *J. Mol. Catal. A.*, **112**, 93, (1996).
- [72] A. Saus, K. Zimmermann and O. Gürtler, *Chem. Ztg.*, **115**, 252, (1991).
- [73] H. -U. Blaser, H. -P. Jalett, M. Müller and M. Studer, *Catal. Today*, **37**, 441, (1997).
- [74] X. Zuo, H. Liu, C. Guo and X. Yang, *Tetrahedron*, **55**, 7787, (1999).
- [75] H. Bönemann and G. A. Braun, *Chem. Eur. J.*, **3**, 1200, (1997).
- [76] T. Mallat, S. Frauchiger, P. J. Kooyman, M. Schürch and A. Baiker, *Catal. Lett.*, **63**, 121, (1999).
- [77] B. Török, K. Bonazsik, G. Szöllösi, K. Felföldi and M. Bartok, *Chirality*, **11**, 470, (1999).
- [78] J. L. Margitfalvi and E. Tfirst, *J. Mol. Catal. A.*, **139**, 81, (1999).
- [79] J. L. Margitfalvi, M. Hegedüs and E. Tfirst, *Stud. Surf. Sci. Catal.*, **101A**, 241, (1996).
- [80] J. L. Margitfalvi, M. Hegedüs and E. Tfirst, *Tetrahedron: Asymmetry*, **7**, 571, (1996).
- [81] M. Bartok, K. Felföldi, G. Szöllösi and T. Bartok, *Catal. Lett.*, **61**, 1, (1999).
- [82] M. Bartok, K. Felföldi, B. Török and T. Bartok, *Chem. Commun.*, 2605, (1998).
- [83] M. Bartok, B. Török, K. Balazsik and T. Bartok, *Catal. Lett.*, **73**, 127, (2001).
- [84] H. -U. Blaser, H. -P. Jalett, M. Garland, M. Studer, H. Thies and A. Wirth-Tijani, *J. Catal.*, **173**, 282, (1998).
- [85] D. Y. Murzin, *Ind. Eng. Chem. Res.*, **36**, 4784, (1997).
- [86] A. Baiker, *J. Mol. Catal. A*, **163**, 205, (2000).
- [87] J. L. Margitfalvi, E. Talas and M. Hegedus, *Chem. Commun.*, 645, (1999).
- [88] O. Schwalm, B. Minder, J. Weber and A. Baiker, *Catal. Lett.*, **23**, 271, (1994).
- [89] M. Schürch, O. Schwalm, T. Mallat, J. Weber and A. Baiker, *J. Catal.*, **169**, 275, (1997).
- [90] A. Baiker, *J. Mol. Catal. A*, **115**, 473, (1997).
- [91] T. Bürgi and A. Baiker, *J. Catal.*, **194**, 445, (2000).

- [92] D. Ferri, T. Bürgi and A. Baiker, *J. Chem. Soc., Perkin Trans.*, **2**, 221, (2000).
- [93] M. J. S. Dewar, E. G. Zoebisch, E. F. Healy and J. J. P. Stewart, *J. Am. Chem. Soc.*, **107**, 3902, (1985).
- [94] J. J. P. Stewart, *J. Comp. Chem.*, **10**, 209, (1989).
- [95] D. A. G. Aranda, J. W. M. Carneiro, C. S. B. Oliveira, F. B. Passos, P. R. N. Souza and O. A. C. Antunes, *Braz. J. Chem. Eng.*, **18**, 3, (2001).
- [96] T. Bürgi and A. Baiker, *J. Am. Chem. Soc.*, **120**, 12920, (1998).
- [97] L. Onsager, *J. Am. Chem. Soc.*, **58**, 1486, (1936).
- [98] J. J. P. Stewart, *MOPAC93 Manual Ver. Number 2*, Fujitsu Ltd., (1994).
- [99] M. J. Karplus, *J. Chem. Phys.*, **30**, 11, (1959).
- [100] N. Künzle, T. Mallat, T. Bürgi and A. Baiker, unpublished results.
- [101] M. Schürch, N. Künzle, T. Mallat, J. Weber and A. Baiker, *J. Catal.*, **176**, 569, (1998).
- [102] T. Bürgi and A. Baiker, unpublished results.
- [103] G. D. H. Dijkstra, R. M. Kellogg and H. Wynberg, *J. Org. Chem.*, **55**, 6121, (1990).
- [104] T. Evans, A. P. Woodhead, A. Gutierrez. Sosa, G. Thornton, T. J. Hall, A. A. Davis, N. A. Young, P. B. Wells, R. J. Oldman, O. Plashkevych, O. Vahtras, H. Agren and V. Carravetta, *Surf. Sci.*, **436**, L69, (1999).
- [105] T. Bürgi, Z. Zhou, N. Künzle, T. Mallat and A. Baiker, *J. Catal.*, **183**, 405, (1999).
- [106] M. Castonguay, J. -R. Roy, A. Rochefort and P. H. McBreen, *J. Am. Chem. Soc.*, **122**, 518, (2000).
- [107] T. Bürgi, F. Atamny, R. Schlögl, A. Baiker, *J. Phys. Chem. B*, **104**, 5953, (2000).
- [108] T. Bürgi, F. Atamny, A. Knop-Gericke, M. Hävecker, T. Schedel-Niedrig, R. Schlögl and A. Baiker, *Catal. Lett.*, **66**, 109, (2000).
- [109] <http://www.jmcatalysts.com>
- [110] V. Okafor, H. -U. Blaser and M. Studer, unpublished results.
- [111] W. A. H. Vermeer, A. Fulford, P. Johnston, P. B. Wells and A. M. de Wit, poster presentation in "Koninklijke Nederlandse Chemische Vereniging Zomer Congres.", Amsterdam, (1993).
- [112] J. A. Slipszenko, S. P. Griffiths, P. Johnston, K. E. Simms, W. A. H. Vermeer and P. B. Wells, *J. Catal.*, **179**, 267, (1998).



- [113] U. K. Singh, R. N. Landau, Y. Sun, C. LeBlond, D. G. Blackmond, S. K. Tanielyan and R. L. Augustine, *J. Catal.*, **154**, 91, (1995).
- [114] J. Wang, Y. Sun, C. LeBlond, R. N. Landau and D. G. Blackmond, *J. Catal.*, **161**, 752, (1996).
- [115] W. A. H. Vermeer, Ph. D. Thesis, University of Hull, (1995).
- [116] H. Conrad, G. Ertl and E. E. Latta, *Surf. Sci.*, **41**, 435, (1974).
- [117] T. Engel and H. Kuipers, *Surf. Sci.*, **90**, 162, (1979).
- [118] B. E. Spiewak, R. D. Cortright and J. A. Dumesic, *J. Catal.*, **176**, 405, (1998).
- [119] B. E. Nieuwenhuys, *Surf. Sci.*, **59**, 439, (1976).
- [120] K. Christmann, *Surf. Sci. Rep.*, **9**, 1, (1988).
- [121] D. J. Godbey and G. A. Somorjai, *Surf. Sci.*, **204**, 301, (1988).
- [122] K. Christmann, G. Ertl and T. Pignet, *Surf. Sci.*, **54**, 365, (1976).
- [123] H. Ibach, private communication (1978).
- [124] H. Conrad, G. Ertl and E. E. Latta, *Surf. Sci.*, **58**, 578, (1976).
- [125] J. E. Demuth, *Surf. Sci.*, **65**, 369, (1977).
- [126] B. J. J. Koeleman, S. T. de Zwart, A. L. Boers, B. Poelsema and L. K. Verheij, *Phys. Rev. B.*, **56**, 1152, (1986).
- [127] K. M. Lui, Y. Kim, W. M. Lau and J. W. Rabalais, *App. Phys. Lett.*, **75**, 587, (1997).
- [128] K. Umezawa, T. Ito, M. Asada, S. Nakanishi, P. Ding, W. A. Lanford and B. Hjorvarsson, *Surf. Sci.*, **387**, 320, (1997).
- [129] B. J. J. Koeleman, S. T. de Zwart, A. L. Boers, B. Poelsema and L. K. Verheij, *Nucl. Instrum. Methods Phys. Res.*, **218**, 225, (1993).
- [130] P. J. Feibelman and D. R. Hamman, *Surf. Sci.*, **182**, 411, (1987).
- [131] S. K. Desai, M. Neurock and K. Kourtakis, *J. Phys. Chem. B*, **106**, 2559, (2002).
- [132] G. Papoian, J. Norskov and R. Hoffman, *J. Am. Chem. Soc.*, **122**, 4129, (2000).
- [133] G. W. Watson, R. P. K. Wells, D. J. Willock and G. J. Hutchings, *J. Phys. Chem. B.*, **105**, 4889, (2001).
- [134] T. E. Felter, E. C. Sowa and M. A. van Hove, *Phys. Rev. B*, **40**, 891, (1989).
- [135] J. F. Paul and P. Sautet, *Surf. Sci.*, **356**, L403, (1996).
- [136] O. M. Løvvik and R. A. Olsen, *Phys. Rev. B*, **58**, 10890, (1998).
- [137] R. G. Windham, M. E. Bartman and B. E. Koel, *J. Phys. Chem.*, **92**, 2862, (1988).
- [138] G. Szulczewski and R. J. Levis, *J. Am. Chem. Soc.*, **118**, 3521, (1996).

- [139] Y. Y. Yeo, A. Stuck, C. E. Wartnaby and D. A. King, *Chem. Phys. Lett.*, **259**, 28, (1996).
- [140] A. Stuck, C. E. Wartnaby, Y. Y. Yeo and D. A. King, *Phys. Rev. Lett.*, **74**, 578, (1995).
- [141] J. Shen, J. M. Hill, M. Watwe, B. E. Spiewak and J. A. Dumesic, *J. Phys. Chem. B*, **103**, 3923, (1999).
- [142] P. Sautet and J. F. Paul, *Catal. Lett.*, **9**, 245, (1991).
- [143] Y. T. Wong and R. Hoffman, *J. Chem. Soc., Faraday Trans.*, **86**, 4083, (1990).
- [144] D. B. Kang and A. B. Anderson, *Surf. Sci.*, **155**, 639, (1985).
- [145] A. P. Markusse, B. F. M. Kuster and J. C. Schouten, *J. Mol. Catal. A*, **158**, 215, (2000).
- [146] B. Beden, J. M. Léger and L. C., in “*Modern Aspects of Electrochemistry*”, O. M. Bockris, B. E. Conway and R. E. White (Editors), Plenum, New York, **22**, (1992).
- [147] T. Mallat, Z. Bodnar, B. Minder, K. Borszeky and A. Baiker, *J. Catal.*, **168**, 183, (1997).
- [148] J. L. Davis and M. A. Barteau, *J. Am. Chem. Soc.*, **111**, 1782, (1989).
- [149] J. L. Davis and M. A. Barteau, *Surf. Sci.*, **208**, 383, (1989).
- [150] J. L. Davis and M. A. Barteau, *Surf. Sci.*, **235**, 235, (1990).
- [151] M. A. Barteau, *Catal. Lett.*, **8**, 175, (1991).
- [152] N. R. Avery, W. H. Weinberg, A. B. Anton and B. H. Toby, *Phys. Rev. Lett.*, **51**, 682, (1983).
- [153] A. B. Anton, N. R. Avery, B. H. Toby and W. H. Weinberg, *J. Am. Chem. Soc.*, **108**, 684, (1986).
- [154] N. R. Avery, *Langmuir*, **1**, 162, (1985).
- [155] C. J. Houtman and M. A. Barteau, *J. Phys. Chem.*, **95**, 3755, (1991).
- [156] C. J. Houtman and M. A. Barteau, *J. Catal.*, **130**, 528, (1991).
- [157] N. F. Brown and M. A. Barteau, *Langmuir*, **8**, 862, (1992).
- [158] M. A. Henderson, Y. Zhou and J. M. White, *J. Am. Chem. Soc.*, **111**, 1185, (1989).
- [159] R. J. Madix, T. Yamada and S. W. Johnston, *Appl. Surf. Sci.*, **19**, 43, (1984).
- [160] R. W. McCabe, C. L. DiMaggio and R. J. Madix, *J. Phys. Chem.*, **89**, 854, (1985).
- [161] N. M. Abbas and R. J. Madix, *J. Appl. Surf. Sci.*, **7**, 241, (1981).

- [162] M. A. Henderson, G. E. Mitchell and J. M. White, *Surf. Sci.*, **188**, 206, (1987).
- [163] G. A. Attard, H. D. Ebert and R. Parsons, *Surf. Sci.*, **240**, 125, (1990).
- [164] L. J. Richter and W. Ho, *J. Chem. Phys.*, **83**, 2165, (1985).
- [165] A. B. Anton, J. E. Parmeter and W. H. Weinberg, *J. Am. Chem. Soc.*, **107**, 5558, (1985).
- [166] A. B. Anton, J. E. Parmeter and W. H. Weinberg, *J. Am. Chem. Soc.*, **108**, 1823, (1986).
- [167] I. Villegas, M. J. Weaver, *J. Chem. Phys.*, **103**, 2295, (1995).
- [168] F. Delbecq and P. Sautet, *Langmuir*, **9**, 197, (1993).
- [169] F. Delbecq and P. Sautet, *Surf. Sci.*, **295**, 353, (1993).
- [170] C. J. Houtman and M. A. Barteau, *Surf. Sci.*, **248**, 57, (1991).
- [171] M. Green, J. A. K. Howard, A. Laguna, L. E. Smart, J. L. Spencer and F. G. A. Stone, *J. Chem. Soc., Dalton Trans.*, **278**, (1977).
- [172] G. Erker, *Acc. Chem. Res.*, **17**, 103, (1984).
- [173] F. Delbecq and P. Sautet, *J. Am. Chem. Soc.*, **114**, 2446, (1992).
- [174] G. C. Bond, in “*Catalysis by Metals*”, Academic Press, (1962).
- [175] H. Lüth, G. W. Rubloff and W. D. Grobman, *Surf. Sci.*, **63**, 325, (1977).
- [176] R. P. Young and N. Sheppard, *J. Catal.*, **7**, 223, (1967).
- [177] G. Blyholder and D. Shihabi, *J. Catal.*, **46**, 91, (1977).
- [178] M. A. Vannice, W. Erley and H. Ibach, *Surf. Sci.*, **254**, 1, (1991).
- [179] N. R. Avery, *Surf. Sci.*, **125**, 771, (1983).
- [180] R. C. Weast, Ed., in “*CRC Handbook of Chemistry and Physics*”, 59<sup>th</sup> Edition, CRC Press, Boca Raton, (1978).
- [181] W. L. Driessen and W. L. Groeneveld, *Rev. Trav. Chim.*, **88**, 977, (1969).
- [182] N. R. Avery, A. B. Anton, B. H. Toby and W. H. Weinberg, *J. Electron Spectrosc. Relat. Phenom.*, **29**, 233, (1983).
- [183] B. Sen and M. A. Vannice, *J. Catal.*, **52**, 113, (1988).
- [184] M. A. Vannice, W. Erley and H. Ibach, *Surf. Sci.*, **254**, 12, (1991).
- [185] J. L. Davis and M. A. Barteau, *Surf. Sci.*, **187**, 387, (1987).
- [186] A. Solladié-Cavallo, C. Marsol, F. Hoernel and F. Garin, *Tetrahedron Lett.*, **42**, 4741, (2001).
- [187] W. -S. Sim, T. -C. Li, P. -X. Yang and B. -S. Yeo, *J. Am. Chem. Soc.*, **124**, 4970, (2002).
- [188] C. R. Ayre and R. J. Madix, *J. Am. Chem. Soc.*, **117**, 230L, (1995).

- [189] W. -S. Sim and D. A. King, *J. Phys. Chem.*, **100**, 14794, (1996).
- [190] Spartan, version 5.1, Wavefunction Inc., Irvine, California, (1998).
- [191] The assignment of the  $1353\text{ cm}^{-1}$  band to  $\delta_s(\text{CH}_3)$  is preferred over  $\delta(\text{CH}_2)$  as it has a larger perpendicular surface dynamic dipole moment and would thus possess a stronger IR adsorption cross-section, according to the metal-surface selection rule, and be the more likely mode to be detected. The  $\delta_s(\text{CD}_3)$  band is not observed as it lies below the spectral noise level given the weakness of all the absorption bands.
- [192] J. H. Weber, *Inorg. Chem.*, **8**, 2813, (1969).
- [193] H. Miyata, Y. Toba and Y. Kubokawa, *J. Catal.*, **32**, 155, (1974).
- [194] G. Busca and V. Lorenzelli, *J. Chem. Soc., Faraday Trans.*, **78**, 2911, (1982).
- [195] B. E. Hanson, L. F. Wieserman, W. G. Wagner, R. A. Kaufman, *Langmuir*, **3**, 549, (1987).
- [196] M. I. Zaki, M. A. Hasan, F. A. Al-Sagheer and L. Pasupulety, *Langmuir*, **16**, 430, (2000).
- [197] J. F. Hartwig, R. G. Bergmann and R. A. Anderson, *Organometallics*, **10**, 3326, (1991).
- [198] J. Vicente, J. A. Abad, M. T. Chicote, M. D. Abrisqueta, J. A. Lorca and M. C. R. de Arellano, *Organometallics*, **17**, 1564, (1998).
- [199] J. Ruiz, V. Rodriguez, N. Cutillas, M. Pardo, J. Perez, G. Lopez, P. Chaloner and P. B. Hitchcock, *Organometallics*, **20**, 1973, (2001).

## ***Chapter 3***

### ***Theoretical Background***

### *3.0. Introduction*

Over the years all physical sciences have undergone major development and improvement of fundamental theories, and seen an increase in their applications over short spaces of time. In the case of computational chemistry this has been aided by advances and availability of computing technology. Numerous chemical drawing programs now exist which help to visualise and understand the structures of molecules as well as a range of sophisticated computer software allowing the simulation of these structures and molecular reactions, based on the fundamental laws of physics. As highlighted in Chapter 2, most chemical properties ranging from any physical observable to thermodynamics and the relative kinetics of a system can be predicted by running calculations either in the gas-phase or in solution, and in their ground state or in an excited state on a computer. Information concerning the nature of short-lived and unstable intermediates such as transition states cannot be obtained through experimental observation and as a result theoretical prediction of chemical properties are a valuable aid to experimental measurements.

With regards to the nature of this research, the underlying theory of the computer codes: MOPAC [1], GAUSSIAN [2], CASTEP [3] and VASP [4] used to generate molecular and periodic models will be discussed in this Chapter. To get to grips with the theory the latter part of this work will focus on its application, although, the exact computational methodology used in our calculations will be specified in Chapter 4, a brief description of the parameters and their overall significance will be provided here.

Another important issue to address is the fact that the computational methods used throughout this thesis are purely based on quantum mechanics rather than the alternative molecular mechanic approach. Although, each method performs the same basic types of calculations to determine the structure and reactivity of molecules, such as computing energy and properties of a particular molecular structure, molecular mechanics techniques are parameterised against experimental data to provide reliable structures of covalently bonded molecules. However, in this work we wish to study the adsorption of molecules to metal surfaces for which no good force fields exist. This is largely due to the complexity of the interaction between the extended electronic states of the metal and the molecular orbitals of the adsorbate. Sufficient accuracy can only be obtained from electronic structure methods and we have chosen to work almost exclusively with DFT [5,6].

To fully appreciate the range of quantum and molecular mechanic approaches to modelling the following textbooks are recommended as additional reading Leach [7], Cramer [8] and Hinchliffe [9].

### 3.1. Quantum Mechanics

Quantum theory was developed in the first half of the 20<sup>th</sup> century and revolutionised the understanding of atomic level phenomena, which could not be described by classical physics. The new approach with surprising accuracy and predictive power was found to explain the properties of matter and radiation, and thus initiated the field of quantum chemistry. To model real processes and real materials, at the level of electronic structure the relevant quantum theory equations must be solved. The most fundamental equation of quantum mechanics for stationary states is the Schrödinger equation, which in its barest form is:

$$H\Psi = E\Psi \quad (\text{Equation 3.1})$$

In this treatment the electrons are considered as wave-like particles represented by a set of wavefunctions,  $\Psi$ .  $H$ , represents the shorthand notation for the Hamiltonian operator, which operates on  $\Psi$  to give the system energy  $E$ . Quantum mechanics postulates that the wavefunction within the Schrödinger equation contains all information that is known or can be known about a molecule, therefore finding solutions to the equation, *i.e.* determining the wavefunction, is imperative. Such an entity can help to resolve the heats of formation, conformational stability, chemical reactivity, spectral properties *etc* of molecules and solids.

Computationally, exact solutions to the Schrödinger equation are only practical for describing the smallest of systems such as atomic hydrogen, which is one of the best-known examples [10]. Therefore, when considering molecular systems the equation can only be solved approximately: two different types of approximation methods exist and these are categorised as either *ab initio* or semi-empirical.

### 3.1.1. *Ab Initio* Methods

*Ab initio*, means “from the beginning” and implies an approach which contains no empirical parameters, *i.e.* all the terms in the Schrödinger equation are derived exclusively from the first principles of quantum mechanics and on the physical constants of the speed of light,  $c$ , the masses and charges of electrons and nuclei as well as Planck’s constant,  $h$ . The purpose of *ab initio* methods is to compute solutions to the Schrödinger equation *via* a series of mathematical approximations. For molecules these methods are implemented within computer programs such as GAMESS [11] and GAUSSIAN [2] and include Hartree-Fock (HF) as well as “post HF” methods such as configuration interaction (CI) [12], many-body perturbation theory (MBPT) [13] and coupled-cluster (CC) theory [14] *etc.* These later developed methods include correlation effects neglected by the initial HF approach.

Relevant to this thesis is the Hartree-Fock theory (example of application provided in the next section), and the background to this will be discussed in more detail later on.

### 3.1.2. *Semi-Empirical* Methods

To try and simplify the computations for molecular systems and to be able to solve an approximate form of the Schrödinger equation, some of the time consuming mathematical terms in the equation, which are neglected by the semi-empirical methods are compensated by the use of parameters derived from experimental data. A number of different methods have been formulated and each one is characterised by its unique parameter set. The methods are usually referred to through acronyms, initially these encoded the underlying theoretical assumptions but for some of the more modern parameter sets the acronym is simply the location of the authors or methodology used.

The most frequently used methods include MNDO, AM1 and PM3 and are all based on the Neglect of Differential Diatomic Overlap (NDDO) integral approximation [15]. Although all or some of the derived semi-empirical methods are implemented within programs such as AMPAC [16], HyperChem [17] and ZINDO [18], it is the PM3 method coupled with HF theory and executed within the MOPAC7 software, which is of importance to this thesis as it has been used to simulate and analyse the conformational behaviour of CD (Chapter 5, section 5.2.1).



### 3.1.3. Density Functional Methods

A third class of electronic structure methods, known as density functional approaches have come into wide use for molecular systems. These DFT [5,6] methods are quantum mechanical approaches which are hard to categorise as either *ab initio* or *semi-empirical*. Some DFT methods are free from empirical parameters, while others rely heavily on calibration with experiment. The present trend in DFT research is to employ increasing numbers of empirical factors, making recent DFT techniques semi-empirical. Currently, DFT calculations require about the same amount of computational resources as HF theory, the least expensive of the *ab initio* methods.

DFT methods are attractive because they include the effects of electron correlation *i.e.* the fact that electrons in a molecular system react to one another's motion. HF calculations consider this effect only in an average sense *i.e.* each electron sees and reacts to an averaged electron density, whereas DFT methods account for the instantaneous interactions of pairs of electrons. This approximation causes HF results to be less accurate than some more expensive *ab initio* methods. DFT includes correlation at essentially the cost of a HF calculation. DFT within the GAUSSIAN, CASTEP and VASP codes has been widely implemented within our geometry optimisation calculations of this thesis, and examples can be found in the corresponding results Chapters 5-7.

### 3.1.4. Pseudopotential Theory and Supercell Approximation

Pseudopotential approaches [19] are an extension of quantum mechanic *ab initio* methods. Chemical reactivity of an element is governed by its valence electrons, with the core electrons being chemically inert. Based on this, pseudopotential theory replaces the inert core electrons with an effective potential, by doing so it significantly reduces the number of electrons to be solved in the Schrödinger equation. However, even more importantly, the use of pseudopotentials results in much smoother wavefunctions for the remaining valence electrons, making the problem much easier to solve numerically.

The supercell approximation is a method used for the study of solid-state systems with periodic boundary conditions (PBC) [20]. In this approach a large unit cell containing the atomic structure in question is constructed and then repeated periodically

throughout space. The periodicity is imposed on the simulation cell to better model the continuum properties of the system. Bloch's theorem [21] may then be applied to the wavefunctions so as to improve efficiency in solving the many-body electron Hamiltonian.

Both approximations are essential for modelling surface adsorption calculations, in particular those involving transition metals, and hence have been used coupled with DFT *via* the codes CASTEP and VASP for the treatment of our non-supported catalytic surfaces, refer to results Chapters 6 and 7.

### 3.2. Computational Quantum Mechanics

Practical implementation of the aforementioned quantum mechanics methods is based on the following principles: (i) nuclei and electrons are differentiated from each other, (ii) the electron-electron (typically averaged) and electron-nuclear interactions are explicit, (iii) the interactions are governed by nuclear and electronic potential energy and electron motions and (iv) the interactions themselves determine the spatial distribution of the nuclei and the electrons and the corresponding energy. The mathematical foundations for these quantum chemical concepts are considered in the following sections. In this work they are mainly applied to the study of isolated gas-phase molecules and intermolecular complexes in which the computations are conducted at different levels of theory depending on the accuracy required, refer to Chapter 4.

#### 3.2.1. The Schrödinger Equation

The quantum mechanical equation corresponding to Newton's second law of motion of classical mechanics for a particle of mass  $m$  moving in a three-dimensional system is the time-dependent Schrödinger equation, which essentially describes the wavefunction of a particle:

$$\left\{ \frac{-\hbar^2}{8\pi^2 m} \nabla^2 + V \right\} \Psi(\vec{r}, t) = \frac{i\hbar}{2\pi} \frac{\partial \Psi(\vec{r}, t)}{\partial t} \quad (\text{Equation 3.2})$$

Here,  $\Psi$  is the wavefunction and describes the displacement of the particle at any point along the wave and  $V$  is the potential field in which the particle is moving,  $\nabla^2$  (“del squared”) is the Laplacian operator and is defined below:

$$\nabla^2 = \frac{\partial^2}{\partial x^2} + \frac{\partial^2}{\partial y^2} + \frac{\partial^2}{\partial z^2} \quad (\text{Equation 3.3})$$

Usually it is assumed that  $|\Psi|^2$  (which is the product of  $\Psi$  with its complex conjugate ( $\Psi^*\Psi$ )) represents the probability density for the particle(s) it describes. The equation is easily adapted to represent a molecule *i.e.* a collection of particles by simply using the  $\Psi$  to incorporate the coordinates of all the particles in the system as well as  $t$  (time).

By solving the Schrödinger equation *i.e.* finding the correct  $\Psi$  subject to appropriate boundary conditions the energy and any other property of a particle can be obtained. Note that there are many different solutions *i.e.* different wavefunctions to the equation and each corresponds to a different state of the system. The equation can be simplified by using a separation of variables. If  $V$  is not a function of time the wavefunction can be expressed as the product of a spatial function and a time function:

$$\Psi(\vec{r}, t) = \Psi(\vec{r})\tau(t) \quad (\text{Equation 3.4})$$

If this is then substituted into equation 3.2, two equations are obtained, one for the dependence of the position of the particle independent of time and the other is a function of time alone. This separation is crucial for the modelling encountered in this thesis, all the wavefunctions produced are stationary states with no time dependence, and so we concentrate on the time-independent expression:

$$H\psi(\vec{r}) = E\psi(\vec{r}) \quad (\text{Equation 3.5})$$

where  $E$  represents the energy of the system, and  $H$  is the Hamiltonian operator equivalent to:

$$H = \frac{-\hbar^2}{8\pi^2 m} \nabla^2 + V \quad (\text{Equation 3.6})$$

Each solution of the time-independent form equation 3.5 has various solutions, each one, relating to the different stationary states of the particle (molecule). The one with the lowest energy is called the ground state. However, one of the limitations of equation 3.5 is that it cannot give an accurate description of the core electrons in large nuclei, since it is not valid when the particle velocities approach the speed of light as it is non-relativistic. Note that equation 3.5 is in the form of an eigenvalue equation, the function  $\Psi$  is described as an eigenfunction and is different for each eigenvalue, *i.e.* the energy of the system,  $E$ .

In the Schrödinger equation representing a molecular system, the  $\Psi$  is a function of the positions of the electrons and the nuclei within the molecule, and these are symbolised by  $\vec{r}$  and  $\vec{R}$  respectively. In the following text the subscripted versions will represent the vector corresponding to a particular electron or nucleus *e.g.*  $\vec{r}_i$  and  $\vec{R}_j$ .

### 3.2.2. The Born-Oppenheimer Approximation

One of the first approximations to simplify the solution of the Schrödinger equation is the Born-Oppenheimer approximation, in which the nuclear system is treated using a classical Newtonian approach. Essentially it simplifies the general molecular problem by separating nuclear and electronic motions. Since there is a large difference between the mass of a nucleus and an electron (typically thousands of times greater), the nuclei move very slowly with respect to the electrons. Accordingly, the electrons respond instantaneously to the motion of the nuclei and so, the electronic distribution within a molecular system depends on the positions of the nuclei, and not on their velocities. Consequently the nuclei are treated adiabatically, and to the electrons they appear to be fixed. In turn this leads to the separation of the electronic and nuclear coordinates in the many-body wavefunction. For the molecular system the full Hamiltonian can be expressed as:

$$H = T^{electrons}(\vec{r}) + T^{nuclei}(\vec{R}) + V^{nuclei-electrons}(\vec{R}, \vec{r}) + V^{electrons}(\vec{r}) + V^{nuclei}(\vec{R}) \quad (\text{Equation 3.7})$$

where  $T$  represents the kinetic and  $V$  the potential energies. The approximation is practical since it allows both the nuclear and electronic parts of the problem to be solved independently. By neglecting the kinetic energy term for the nuclei it is possible to construct the following electronic Hamiltonian:

$$H^{electrons} = -\frac{1}{2} \sum_i^{electrons} \left( \frac{\partial^2}{\partial x_i^2} + \frac{\partial^2}{\partial y_i^2} + \frac{\partial^2}{\partial z_i^2} \right) - \sum_i^{electrons} \sum_l^{nuclei} \left( \frac{Z_l}{|\bar{R}_l - \bar{r}_i|} \right) + \sum_i^{electrons} \sum_{j < i} \left( \frac{1}{|\bar{r}_i - \bar{r}_j|} \right) \quad (\text{Equation 3.8})$$

Note that the above Hamiltonian has been written in atomic units ( $e = m_e = \hbar = 4\pi\epsilon_0 = 1$ ) since they eliminate fundamental constants and thus simplify the equations of quantum mechanics. Future equations will be based on these units.

### 3.2.3. The Molecular Hamiltonian

In the molecular system the Hamiltonian consists of a kinetic and a potential energy term:

$$H = T + V \quad (\text{Equation 3.9})$$

Here, the kinetic energy is the summation of  $\nabla^2$  over all the particles:

$$T = -\frac{\hbar^2}{8\pi^2} \sum_k \frac{1}{m_k} \left( \frac{\partial^2}{\partial x_k^2} + \frac{\partial^2}{\partial y_k^2} + \frac{\partial^2}{\partial z_k^2} \right) \quad (\text{Equation 3.10})$$

The potential energy represents the Coulomb repulsion between each of the charged species *i.e.* electron-electron or nucleus-electron (the atomic nucleus is treated as a single charged mass):

$$V = \frac{1}{4\pi\epsilon_0} \sum_j \sum_{k < j} \frac{q_j q_k}{\Delta r_{jk}} \quad (\text{Equation 3.11})$$

where  $\Delta r_{jk}$  represents the distance between the two particles, and  $q_j$  and  $q_k$  are the charges on particles  $j$  and  $k$ . The charge on the electron is designated  $e$ , whereas  $Ze$  corresponds to the charge on the nucleus, with  $Z$  giving the atomic number for the particular atom. Equation 3.11 can thus be expanded to:

$$V = \frac{1}{4\pi\epsilon_0} \left( - \sum_i^{electrons} \sum_l^{nuclei} \left( \frac{Z_l e^2}{\Delta r_{il}} \right) + \sum_i^{electrons} \sum_{j < i} \left( \frac{e^2}{\Delta r_{ij}} \right) \right) \quad (\text{Equation 3.12})$$

In this expression the first term relates to the electron-nuclear attraction and the second to the electron-electron repulsion.

### 3.2.4. Restrictions on the Wavefunction

To satisfy the Pauli principle [22], the electronic wavefunction must be antisymmetric *i.e.* it must change sign when two identical particles are interchanged, since electrons are identical fermion particles. To obtain a valid wavefunction the following conditions must be satisfied:

$$\Psi(\bar{r}_1, \dots, \bar{r}_i, \dots, \bar{r}_j, \dots, \bar{r}_n) = -\Psi(\bar{r}_1, \dots, \bar{r}_j, \dots, \bar{r}_i, \dots, \bar{r}_n) \quad (\text{Equation 3.13})$$

The wavefunction must also be normalised, *i.e.* to ensure  $\Psi^2$  integrated over all space represents the actual number of particles. Normalisation is a mathematical feature of the solutions to the Schrödinger equation which implies that if  $\Psi$  is a solution, then so is  $c\Psi$ , where  $c$  is any constant. By being able to vary the wavefunction by a constant factor a normalisation constant can be found, which allows the proportionality of the Born interpretation to become an equality. The normalisation constant is found by ensuring that, for a normalised wavefunction  $c\Psi$ , the probability that a particle is in the region  $dx$  is equal to  $(c\Psi^*)(c\Psi)dx$  and that the probability of the particle being anywhere in the system is equal to 1. The expression below illustrates how the integration is multiplied by the normalisation constant,  $c$ :

$$\int_{-\infty}^{\infty} [c\Psi]^2 dx = n_{\text{particles}} \quad (\text{Equation 3.14})$$

### 3.2.5. Hartree-Fock Theory

Earlier, it was stated that exact solutions to the Schrödinger equation only arise for some of the most trivial molecular systems, however, an approximate solution for a larger range of molecules can be obtained by using a number of simplifying assumptions and procedures. One of the simplest approximate theories for solving the many-body Hamiltonian is HF theory used in parts of Chapter 5.

### 3.2.6. Molecular Orbitals

The basic principle behind HF theory is that the electrons in a system can be described by molecular orbital(s) (MO(s)). HF theory decomposes the  $\Psi$  into a combination of one electron MO(s) *e.g.*  $\phi_1, \phi_2, \dots$  etc, the most appropriate are those which are normalised and orthogonal:

$$\begin{aligned}\iiint \phi_i^* \phi_i dx dy dz &= 1 \\ \iiint \phi_i^* \phi_j dx dy dz &= 0; \quad i \neq j\end{aligned}\quad (\text{Equation 3.15})$$

The easiest way of making  $\Psi$  as a combination of these MO(s) is by forming their Hartree product:

$$\Psi(\vec{r}) = \phi_1(\vec{r}_1) \phi_2(\vec{r}_2) \dots \phi_n(\vec{r}_n) \quad (\text{Equation 3.16})$$

However, this is an inadequate wavefunction because it is not antisymmetric, as swapping over the orbitals of two electrons does not result in a sign change. This is most commonly achieved by representing  $\Psi$  as a determinant of one electron wavefunctions, known as the Slater determinant.

### 3.2.7. Electron Spin

To obtain an antisymmetric function which is a combination of MO(s) a determinant must be formed, however, the fact that electrons can exist in either spin up (+1/2) or spin down (-1/2) must also be taken into account. The previous equation (equation 3.16) only accounts for one electron in each MO, although most calculations are of the closed-shell form in which the orbitals are doubly occupied holding two electrons of opposite spin. The electron spins are usually classified as spin  $\alpha$  and spin  $\beta$ :

$$\begin{aligned}\text{spin up } \alpha(\uparrow) &= 1 & \alpha(\downarrow) &= 0 \\ \beta(\uparrow) &= 0 & \beta(\downarrow) &= 1 \text{ spin down}\end{aligned}\quad (\text{Equation 3.17})$$

In forming the determinant, the following notations are used  $\alpha(i)$  and  $\beta(i)$  for electron  $i$ , so that  $\alpha(1)$  is the value of  $\alpha$  for electron 1 *etc.* Electron spins are incorporated into the overall electronic wavefunction by multiplying the MO functions by  $\alpha$  and  $\beta$  to give

spin-orbitals. These orbitals are a function of both the electron's location and spin. With electron spin accounted for, a closed-shell wavefunction can be built, which is antisymmetric in nature.

### 3.2.8. Basis Sets

Once the MO(s) are incorporated into the electronic wavefunction, they need to be expressed as a linear combination of simpler standard functions, which are pre-defined and termed as basis functions. In this approximation the basis functions are based on the atomic nuclei and so to a certain extent can be said to resemble atomic orbitals. However, the actual mathematical treatment is more general than this, and any set of appropriately defined functions maybe used, for example, plane-waves in periodic systems. The general expression used to define an individual MO is:

$$\phi_i = \sum_{\mu=1}^N c_{\mu i} \chi_{\mu} \quad (\text{Equation 3.18})$$

Here, the molecular orbital expansion coefficients are denoted by the term  $c_{\mu i}$  and the basis functions by  $\chi_1 \dots \chi_N$ .

In GAUSSIAN and similar programs the basis functions are based on gaussian-type atomic functions and the general form of these follow:

$$g(\alpha, \vec{r}) = cx^n y^m z^l e^{-\alpha r^2} \quad (\text{Equation 3.19})$$

where  $\vec{r}$  signifies the position vector with components  $x$ ,  $y$ , and  $z$  and the constant  $\alpha$  determines the size *i.e.* the radial extent of the function.

### 3.2.9. The Variational Principle

Now that the molecular orbitals are expanded in a basis set the next step involves finding a set of coefficients that will minimise the energy of the resultant  $\Psi$ . To do this HF theory takes advantage of the variational principle, which states that the expected energy value corresponding to the ground state electronic coordinates of any



antisymmetric normalised function ( $\Xi$ ) will always be greater than the energy for the exact  $\Psi$ :

$$E(\Xi) > E(\Psi); \quad \Xi \neq \Psi \quad (\text{Equation 3.20})$$

This implies that the energy of the exact wavefunction acts as a lower bound to the corresponding values calculated by any other normalised antisymmetric function, and so these energy values need to be minimised and the best way to achieve this is by using the equations of Roothaan-Hall.

### 3.2.10. The Roothaan-Hall Equations

In 1954, Roothaan and Hall described matrix algebraic equations that permitted HF calculations to be carried out using a basis set representation for the MO(s).

For a closed-shell system, the Fock operator is defined for each electron  $i$  as:

$$f_i = H^{core} + \sum_{j=1}^N \{2J_j - K_j\} \quad (\text{Equation 3.21})$$

where  $J_j$  is the Coulomb and  $K_j$  is the exchange operator. Essentially, the Fock operator is an effective one-electron Hamiltonian for the electron in the poly-electronic system. The expansion of the MO(s) can be described by coefficients,  $c_{vi}$ :

$$\sum_{\nu=1}^N (F_{\mu\nu} - \varepsilon_i S_{\mu\nu}) c_{\nu i} = 0 \quad \mu = 1, 2, \dots, N \quad (\text{Equation 3.22})$$

where  $F_{\mu\nu}$  are the Fock matrix elements for basis functions  $\mu$  and  $\nu$  and  $S_{\mu\nu}$  is the corresponding element of the overlap matrix. The above expression is usually expressed in the matrix form:

$$FC = SC\varepsilon \quad (\text{Equation 3.23})$$

Here,  $F$ ,  $C$  and  $S$  are matrices and  $\varepsilon$  represents a diagonal matrix of orbital energies where each of its elements for example,  $\varepsilon_i$  is the one-electron orbital energy of molecular orbital  $\chi_i$ . The overlap matrix,  $S$ , ensures sufficient overlap between the orbitals.

The *Fock matrix*,  $F$ , corresponds to the average effects of the field of all the electrons on each orbital, for a closed-shell system, the elements would be:

$$F_{\mu\nu} = H_{\mu\nu}^{core} + \sum_{\lambda=1}^N \sum_{\sigma=1}^N P_{\lambda\sigma} \left[ (\mu\nu|\lambda\sigma) - \frac{1}{2}(\mu\lambda|\nu\sigma) \right] \quad (\text{Equation 3.24})$$

Here,  $H_{\mu\nu}^{core}$  is another matrix, which represents the energy of a single electron in the field of the bare nuclei, and  $P$  is the density matrix, which can be defined as:

$$P_{\lambda\sigma} = 2 \sum_{i=1}^{occupied} c_{\lambda i}^* c_{\sigma i} \quad (\text{Equation 3.25})$$

In this expression the coefficients are summed over the occupied orbitals only, in which each holds two electrons, hence the factor of two implied in the equation. Referring back to equation 3.24 the term  $(\mu\nu|\lambda\sigma)$  represents the two-electron repulsion integrals.

Since the Fock matrix (*via* the density matrix) depends on the MO expansion coefficients, equation 3.23 must be solved iteratively, by using the Self-Consistent Field (SCF) method. In this procedure the energy is at a minimum at convergence with the orbitals generating a field, which produces the same orbitals, thus accounting for the method's name. The solution to the eigenvalue problem then produces a set of occupied and virtual (unoccupied) orbitals. The number of basis functions used are then equal to the total number of these orbitals.

The actual SCF process is conducted *via* a number of explicit steps, and these can be summarised as follows: (i) the integrals of the Fock matrix are first evaluated which are used to (ii) estimate the molecular orbital coefficients used to construct a density matrix, leading to the formation of (iii) the Fock matrix. Next, (iv) the density matrix is solved and finally (v) the energy is tested for convergence, if it has not reached a minimum value then the process is repeated to begin the next iteration. If convergence has been reached then the calculation continues to obtain other properties specified by the user. The exact mathematical premise for this method is outlined in the next section.

### 3.2.11. The Hartree-Fock Self-Consistent Field Method

The Hartree SCF method is a variational approach for computing the Fock product, which aims to solve the one-electron Schrödinger equation, but more accurately takes

into account the antisymmetric nature of the wavefunction. In doing so, the trial wavefunctions are then expressed as Slater determinants of variational spin-orbitals, such as:

$$\phi = \frac{1}{\sqrt{n!}} \begin{vmatrix} 1S(1)\alpha(1) & 1S(1)\beta(1) & \dots \\ \dots & \dots & \dots \\ 1S(n)\alpha(n) & 1S(n)\beta(n) & \dots \end{vmatrix} \quad (\text{Equation 3.26})$$

in which the basis functions for the spatial orbitals  $1S, 2S, \dots$ , *etc*, are typically linear combinations of Gaussians, or Slater type orbitals.

### 3.2.12. Open-Shell Methods

Until now only the restricted HF method has been considered. For open-shell systems *i.e.* those that possess unequal numbers of spin up and spin down electrons such as certain ions and excited states *etc*, an unrestricted method is required. Since the  $\alpha$  and  $\beta$  electrons in these systems use separate spatial orbitals the resulting two sets of MO expansion coefficients are:

$$\begin{aligned} \phi_i^\alpha &= \sum_{\mu} c_{\mu}^{\alpha} \chi_{\mu} \\ \phi_i^{\beta} &= \sum_{\mu} c_{\mu}^{\beta} \chi_{\mu} \end{aligned} \quad (\text{Equation 3.27})$$

From these two coefficients then, two sets of Fock matrices and hence their associated density matrices can be obtained, which in turn will give two sets of orbitals. These separate orbitals will then possess all the characteristic features required for open-shell systems such as obtain the correct delocalisation for resonant systems.

### 3.2.13. Limitations to Hartree-Fock Theory

In the HF approach each electron feels only the average Coulomb repulsion of all the other electrons, and so generates wavefunctions that are antisymmetric with respect to the exchange of two electron positions and includes exchange between like-spin electrons. Under this treatment, there is no instantaneous electron-electron interaction included. By doing so, the approximation makes HF theory much simpler than the real

problem, which is an  $N$ -body problem. The cost of a HF calculation usually depends on the number of basis functions and normally scales as the cube of it, however, depending on the implementation the scaling can be between linear and quartic with system size.

One of the downfalls of the theorem is that it cannot accurately make quantitative predictions for the properties of many compounds, for example, interaction energies are calculated poorly because the effects of electron correlation are ignored. However, since the HF wavefunction is a well-controlled approximation to the many-body wavefunction, the approach is widely used due to its good qualitative nature as indicated by our calculations (Chapter 5, section 5.2.1) and is good for determining information such as trends in a structural parameter with system size. Although the HF approximation can give poor answers in many cases, it can be corrected by explicitly accounting for electron correlation by methods such as CI [12], MBPT [13] and by other means. DFT has the advantage of speed over post-HF methods and so the large systems required in this work can be tackled.

#### 3.2.14. Density Functional Theory

Density functional theory-based methods developed by Hohenberg and Kohn [5] and Kohn and Sham [6] ultimately derive from quantum mechanics research of the Thomas-Fermi-Dirac model from the 1920s, and from Slater's fundamental work in the 1950s. It is a powerful approach in the sense that it is a formally exact theory and is distinct from quantum chemical methods in that it does not yield a correlated  $N$ -body wavefunction. Essentially, the DFT approaches describe the effects of exchange and correlation in an electron gas with the modelling based upon general functionals of the electron density. A functional is referred to as a function whose argument is itself a function *i.e.* a function of a function.

The Hohenberg-Kohn theorem proved that for an electron gas the total-energy (inclusive of exchange and correlation) is a unique functional of the electron density. It was found that the minimum value of the unique total-energy functional corresponded to the ground state energy of the system, whilst the density generating this value was the exact single-particle ground state density. However, unfortunately, the theorem did not provide the form of this functional and it was not until 1965 that Kohn and Sham showed that the many-electron problem could be replaced by an exactly equivalent set of self-consistent one-electron equations. Exchange and correlation were included by

adding energy functions of the electron density to replace the electron-electron interactions. As a consequence, the resulting Kohn-Sham DFT theory shares many similarities with HF.

DFT has come into prominence over the last decade as a method potentially capable of predicting very accurate results at a low cost. In practice, approximations are required to implement the theory, the accuracy of results are then dependent on the approximations made. Calibration studies are therefore required to establish the likely accuracy in a given class of systems. For further details about DFT refer to von Barth [23], Dreizler and da Providencia [24], Jones and Gunnarson [25], and Kryachko and Ludena [26].

### 3.2.15. The Kohn-Sham Energy Functional

The most common expression for the total-energy functional derived by Kohn and Sham for a system of electrons with an external field,  $V_{ext}(x)$  is:

$$E[\rho(r)] = T[\rho(r)] + E_{es}[\rho(r)] + E_{xc}[\rho(r)] + E_{ext}[\rho(r)] \quad (\text{Equation 3.28})$$

where the terms,  $T[\rho(r)]$  represent the kinetic energy functional of the non-interacting electrons of density  $\rho(r)$ ,  $E_{es}[\rho(r)]$  is the electrostatic energy,  $E_{xc}[\rho(r)]$  is the exchange-correlation energy and  $E_{ext}[\rho(r)]$  is the potential energy of the non-interacting electrons in the external field  $V_{ext}(x)$ , which can include atomic nuclei of molecules. The electron density for the doubly occupied set of electronic states  $\Psi_i$  is calculated from:

$$\rho(r) = 2 \sum_i |\Psi_i(r)|^2 \quad (\text{Equation 3.29})$$

Only the minimum value of the Kohn-Sham energy functional is significant and that is because it represents the ground-state energy of the electrons.

### 3.2.16. Kohn-Sham Equations

In order to minimise the Kohn-Sham energy functional a set of wavefunctions  $\Psi_i$  are required and these are provided by the self-consistent solutions to the Kohn-Sham equations:

$$\left[ \frac{-\hbar^2}{2m} \nabla^2 + V_{ion}(r) + V_H(r) + V_{xc}(r) \right] \Psi_i(r) = \varepsilon_i \Psi_i(r) \quad (\text{Equation 3.30})$$

Here,  $\Psi_i$  denotes the wavefunction of the electronic state  $i$ ,  $\varepsilon_i$  is equal to the Kohn-Sham eigenvalue and  $V_H$  is calculated to be the Hartree potential of the electrons from the expression:

$$V_H(r) = e^2 \int \frac{\rho(r')}{|r - r'|} dr'^3 \quad (\text{Equation 3.31})$$

Note that the integration over the element  $dr'^3$  means over all space accessible to the particle. Finally  $V_{xc}$ , the exchange-correlation potential is derived from the functional derivative:

$$V_{xc}(r) = \frac{\delta E_{xc}[\rho(r)]}{\delta \rho(r)} \quad (\text{Equation 3.32})$$

The Kohn-Sham equations represent a mapping of the interacting many-electron system onto a system of non-interacting electrons moving in an effective potential due to all the other electrons. Sadly, since the exchange-correlation energy functional is not known exactly it is impossible to derive a potential for which the exchange and correlation effects are represented correctly. As with the HF Roothaan-Hall equations (section 3.2.10), the Kohn-Sham equations are solved self-consistently, in order for the occupied electronic states to create a charge density which produces an electronic potential, used in the construction of the original equations.

In the Kohn-Sham eigenvalues the effects of electron-electron interaction in the Hartree energy and in the exchange-correlation energy are overestimated, and so the sum of the eigenvalues would not represent the total electronic energy. To be exact the eigenvalues are not the energies of the single-particle electron states but instead

correspond to the derivatives of the total-energy with respect to the occupation numbers of these states [27]. Bearing this in mind, then, the highest occupied eigenvalue in a molecular calculation would then represent an approximate value for the unrelaxed ionisation energy for that system [28].

To summarise, the Kohn-Sham equations are a set of eigen equations, and it is the problem of finding a solution to the eigenvalue once an approximate expression for the exchange-correlation energy is specified which constitutes the bulk of the work in a total-energy calculation.

### 3.2.17. Local Density Approximation

The Hohenberg-Kohn theorem illustrates the need for approximate methods to describe the exchange and correlation energy as a function of electron density. In 1965, Kohn and Sham developed one of the simplest approaches in describing the exchange-correlation energy of an electronic system, the local density approximation (LDA). For the construction of the exchange and correlation energy LDA assumes that the density locally can be treated as a uniform electron gas, with the density being a slowly varying function. In other words it considers that the exchange-correlation energy per electron at a point  $r$  in the electron density, denoted as  $\varepsilon_{xc}(r)$ , is equal to the exchange-correlation energy per electron in a homogeneous electron gas which has the same density as the molecular electron density at point  $r$ , hence:

$$E_{xc}[\rho(r)] = \int \varepsilon_{xc}(r) \rho(r) dr^3 \quad (\text{Equation 3.33})$$

and

$$\frac{\delta E_{xc}[\rho(r)]}{\delta \rho(r)} = \frac{\partial [\rho(r) \varepsilon_{xc}(r)]}{\partial \rho(r)} \quad (\text{Equation 3.34})$$

with

$$\varepsilon_{xc}(r) = \varepsilon_{xc}^{\text{hom}}[\rho(r)] \quad (\text{Equation 3.35})$$

As the local density approximation is frequently used in total-energy pseudopotential calculations, it was found that the inclusion of any of the several parameterisations for

the exchange-correlation energy of the homogeneous electron gas [6,29-32] all simulated very similar total-energy results. The basis of the parameterisation methods lie in the use of interpolation formulae to link the results of exchange-correlation energies calculated at various electron gas densities (high to low).

### 3.2.18. Limitations to Local Density Approximation

Despite the known accuracy in calculating the total-energy, one of the downfalls of LDA is the fact that it ignores non-local exchange-correlation effects. The most important corrections to the exchange-correlation energy at a point  $r$  will be caused by the nearby inhomogeneities in the electron density. Therefore, it is surprising that the calculations including the LDA approximation work so well.

### 3.2.19. Generalised Gradient Approximation

A method commonly used to improve the LDA is the generalised gradient approximation (GGA), which involves applying gradient expansions (corrections) to make the  $E_{XC}$  a functional of the density and its gradient:

$$E_{XC}^{GGA}[\rho(r)] = \int \varepsilon_{XC}(\rho(r))\rho(r)dr + \int F_{XC}[\rho(r), |\nabla\rho(r)|]dr \quad (\text{Equation 3.36})$$

$F_{XC}$  is a correction chosen to satisfy one or several known limits for  $E_{XC}$ . There is no clear method by which it should be developed but parameters based on experimental observations over a test suite of molecules are often substituted in.

One of the most popular GGA exchange and correlation functionals to date and that applied in our DFT calculations (Chapters 6 and 7) is one developed by Perdew and Wang, abbreviated PW91. The PW91 functional uses a different expression than the earlier derived local functionals of Vosko, Wilk and Nusair [31] for the LDA correlation energy density and contains no empirical parameters. The derivation of the functional is long and can be found in reference 33.



### 3.2.20. Hybrid Functionals

Hybrid functionals are a further development of the above exchange-correlation functionals. One of the most well known is the Becke-3- (B3) GGA hybrid exchange functional [34] combined with the GGA correlation functional of Lee-Yang-Parr (LYP) [35], which is applied in this work for isolated molecular systems. The hybrid notation of B3LYP [36] arises as HF exchange is mixed with the DFT definitions in defining the exchange-correlation term:

$$E_{XC} = a_0 E_X^{HF} + (1 - a_0) E_X^{LDA} + a_x \Delta E_X^B + (1 - a_c) E_C^{VWN} + a_c \Delta E_C^{LYP} \quad (\text{Equation 3.37})$$

The 3 parameters for the exchange-correlation term  $a_0$ ,  $a_x$  and  $a_c$  were optimised to 0.20, 0.72 and 0.81 respectively. These values are derived from thermodynamic and spectroscopic properties of various systems.

### 3.3. Methods for Studying the Solid State

The quantum mechanical methods used to study solid-phase systems such as surface applications are different to those discussed above, *i.e.* those employed to study individual molecules or isolated intermolecular complexes. To best simulate solid surfaces a method in which a supercell is constructed and repeated periodically in space is used. Although DFT theory is specified in these calculations, the electronic states for solids are best expanded *via* a plane-wave basis set rather than the conventional Gaussian orbitals. This is due to a number of reasons, firstly, the plane-wave basis set sits naturally with a periodic simulation since the fourier transform into reciprocal space is easier than for localised basis sets. Secondly, it is much easier to check convergence with plane-waves in contrast to atom-centred basis sets because it depends only on the parameter  $E_{cut}$ , (further discussed in section 3.3.8). Thirdly, the calculation of the forces on the nuclei is very easy with plane-waves and finally, the use of atom-centred basis sets can lead to spurious effects because of the superposition of basis functions centred on different atoms. When plane-waves are used a pseudopotential is required, which means that for heavy elements and transition metals the core state functions are replaced with a simple potential that mimics the interaction of the core and valence states. The pseudopotential therefore sacrifices an explicit treatment of the core states to reduce the

computational burden. The mathematical foundations for these concepts and those specific to our calculations are presented in the following sections.

### 3.3.1. Surfaces

The latter part of this thesis is concerned with the effect of chemisorption of simple adsorbates on Pd and Pt surfaces. The surfaces considered are cut from a crystalline bulk phase to form atomically flat, well-defined crystal planes. The chosen plane, for reasons of stability is defined by its Miller indices [37] as described below. Both group 10 metals adopt a *fcc* structure in which each atom has 12 nearest neighbours; a (111) plane was used throughout the course of this research.

### 3.3.2. Miller Indices

The system used to denote a given crystal plane is the Miller index. Three integers ( $h, k, l$ ) are assigned to materials adopting either a bulk cubic (simple cubic (*sc*), *fcc*, body-centred cubic (*bcc*)) lattice, whereas four integers ( $w, h, k, l$ ) are used for *hcp* structures. Other less common crystallographic forms exist which can also be identified using Miller indices. In the example provided in figure 3.1, three mutually perpendicular Cartesian axes labelled  $x, y$ , and  $z$  are used to define a *fcc* lattice of lattice constant  $a$ . The shaded area represents the crystallographic plane to be labelled.

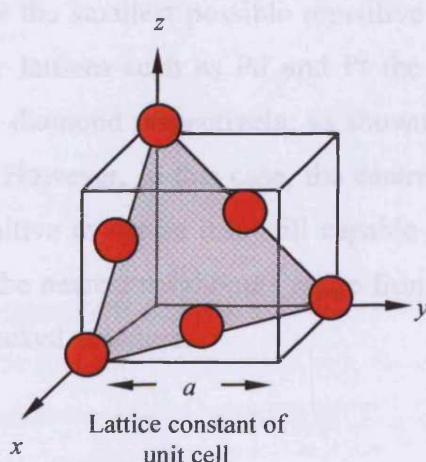


**Figure 3.1:** The (111) Miller index plane of a *fcc* lattice.

The Miller index of the plane is determined by firstly finding the interception of the plane on the  $x$ -,  $y$ - and  $z$ -axes in multiples of the unit-cell dimension,  $a$ . For the case above, this is written as (1, 1, 1) as clearly the plane intercepts all three axes at  $a$ . The indices are then defined by taking the reciprocal values of these intercepts and are expressed in round brackets with the commas removed *i.e.* (111). The three low indexed faces, (100), (110) and (111) common to surface studies of a *fcc* metal such as Pd and Pt are illustrated in figure 3.2.

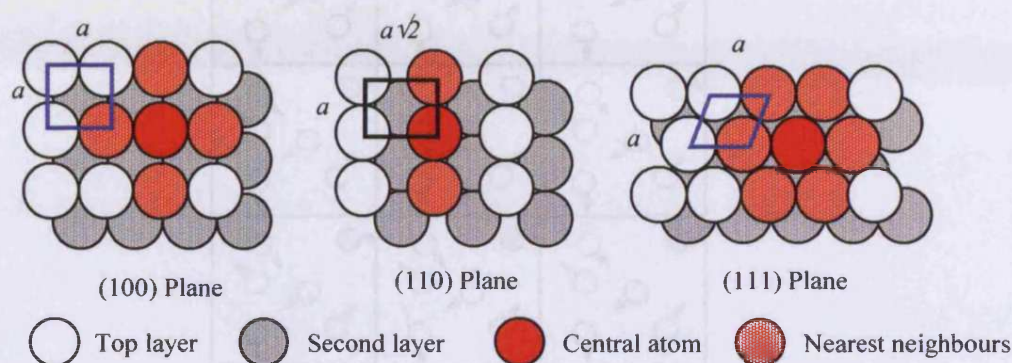


**Figure 3.2:** Plan views of the most common faces studied in surface science. The primitive surface unit mesh (blue lines) and centred rectangle unit cell (black lines) associated with each plane are shown.  $a$  is defined as in figure 3.1.

The crystal planes shown in figure 3.2 have the most ordered structures and offer the smallest numbers of sites for adsorption and are therefore considered as providing the simplest systems for analysis.

The primitive unit cell is the smallest possible repetitive unit necessary to generate the surface lattice. For *fcc* lattices such as Pd and Pt the (100) and (111) primitive surface cell is a square and diamond respectively, as shown in figure 3.2, whereas for the (110) it is a rectangle. However, in this case, the centred rectangle is taken as the unit cell, although not primitive in nature it is still capable of reproducing the surface lattice. For these surfaces the nearest neighbours range from 4 to 2 to 6 with the (111) face being the most close-packed structure.

### 3.3.3. Periodic Supercells

The supercell method is the ubiquitous approach for the study of solid-state periodic boundary conditions. In this approach a primitive unit cell of the solid is replicated in

space in three-dimensions up to the desired unit cell size, creating a supercell. An artificial periodicity (PBC) is then imposed onto this supercell, so that the simulation to be performed uses only a small number of particles in such a way that the particles experience forces as if they were in the bulk. An example of a cubic box of particles replicated in two-dimensions to give a periodic array is illustrated in figure 3.3.

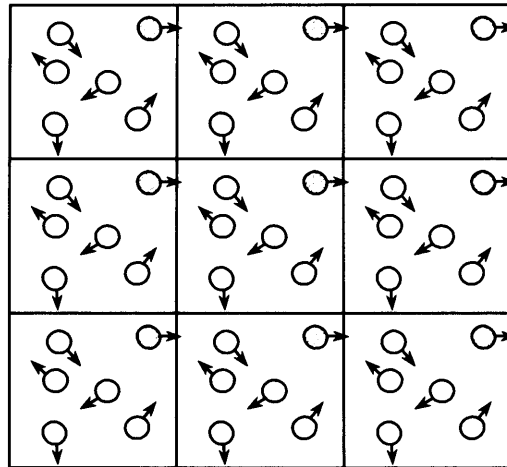


**Figure 3.3:** *Periodic boundary conditions in two-dimensions. Figure obtained from reference 20.*

In this example, each box is surrounded by eight nearest neighbours, which would increase to twenty-six in a three-dimensional array. It is simple to compute the coordinates of the particles in the image boxes as the integral multiples of the box sides are either added or subtracted. If a particle were to leave the supercell during the simulation, then under PBC it would be replaced by another image particle entering from the opposite side (figure 3.3), so as to keep the number of particles within the cell constant.

#### 3.3.4. Limitations to Periodic Boundary Conditions

Although widely used in computer simulations, PBC do have some limitations. One of the most detrimental is the fact that the periodic cell cannot achieve fluctuations that have a wavelength greater than the length of the cell. For a further discussion consult reference 21.



### 3.3.5. Bloch's Theorem

The main advantage in quantum chemistry of imposing PBC relates to Bloch's theorem, which states that in a periodic system each electronic wavefunction can be written as a product of a cell-periodic part  $f_i(r)$  and a wave like part,  $\exp[ik \cdot r]$  with wavevector  $k_i$ :

$$\Psi_i(r) = \exp[ik \cdot r] f_i(r) \quad (\text{Equation 3.38})$$

Of the electronic wavefunction, the cell-periodic part can easily be expanded with the use of a basis set. The most suitable basis set is comprised of a discrete set of plane-waves, the vectors of which are reciprocal lattice vectors of the crystal:

$$f_i(r) = \sum_G c_{i,G} \exp[iG \cdot r] \quad (\text{Equation 3.39})$$

Here, the Bloch wave coefficient is represented by the term  $c_i$  and the reciprocal lattice vectors are denoted by  $G$ , which in turn are given by  $G \cdot l = 2\pi m$  for all  $l$ , where  $l$  is a lattice vector of the crystal and  $m$  an integer. Thus, allowing each electronic wavefunction to be expressed as a sum of plane-waves:

$$\Psi_i(r) = \sum_G c_{i,k+G} \exp[i(k+G) \cdot r] \quad (\text{Equation 3.40})$$

### 3.3.6. Brillouin Zone and K-Point Sampling

For bulk solids it is the application of periodic boundary conditions that determine a set of  $k$ -points for the electronic states. The volume of the solid unit cell always determines the allowed density of  $k$ -points for the bulk. An infinite number of  $k$ -points are used to represent the infinite number of electrons in the solid, however each  $k$ -point is occupied by only a finite number of electronic states. With the introduction of  $k$ -points the Bloch theorem simplifies the problem of calculating an infinite number of electronic wavefunctions to a condition where a finite number of electronic wavefunctions at finite number of  $k$ -points are calculated. This can be achieved because for  $k$ -points that are close together it is inevitable that the wavefunctions will be almost indistinguishable. For this reason it is possible to use the wavefunctions at a single  $k$ -

point to describe the entire electronic wavefunctions over a region of  $k$ -space. This approach simplifies the computation of the total-energy of the solid as the electronic potential is calculated from the electronic states at only a finite number of  $k$ -points.

Since the '70s and early '80s many methods have been available to try and obtain accurate approximations to the electronic potential as well as the contribution to the total-energy from a filled electronic band (*i.e.* from calculating the electronic states at special sets of  $k$ -points in the Brillouin zone) [38]. With the use of these methods the electronic states at a small number of  $k$ -points can be calculated providing an accurate estimate for the electronic potential, which in turn is sufficient to yield precise total-energies for either an insulator or a semi-conductor.

Difficulties are experienced in trying to calculate the electronic potential and the total-energy for metallic systems because the Fermi surface requires a dense set of  $k$ -points. Inadequate  $k$ -point sampling can lead to errors in the total-energy however; this can easily be amended with the use of a denser set of  $k$ -points. The computed total-energy will converge as the density of the  $k$ -points increases reducing the error in the sampling to zero and so the required accuracy can be achieved systematically. The exact method used to obtain  $k$ -points in our calculations is the Mönkhorst-Pack scheme [38].

### 3.3.7. Mönkhorst-Pack Special Points

The Mönkhorst-Pack scheme is one of the most popular methods for generating  $k$ -points and was devised in 1976, and then modified a year later to accommodate hexagonal systems [39]. It produces a uniform grid of  $k$ -points along the three axes in reciprocal space. The resulting grid is then defined by three integers,  $q_i$  where  $i = 1, 2$  and 3, specifying the number of divisions along each of the axes. The integers then generate a sequence of numbers according to the following:

$$u_r = \frac{(2r - q_i - 1)}{2q_i} \quad (\text{Equation 3.41})$$

in which  $r$  varies from 1 to  $q_i$ .

The Mönkhorst-Pack grid is obtained by substituting the above sequences into the expression below:

$$k_{prs} = u_p b_1 + u_r b_2 + u_s b_3 \quad (\text{Equation 3.42})$$

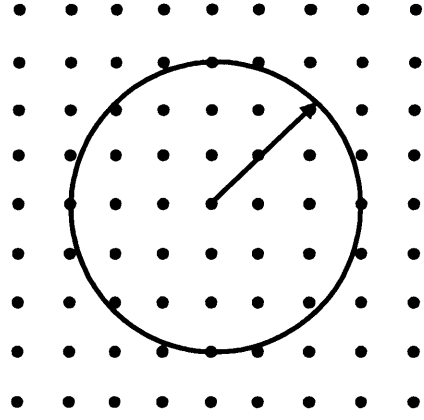
This set of  $q_1 q_2 q_3$  distinct points is further symmetrised and weights are assigned according to the number of symmetry images of a given point in the symmetrised set. Before the set is symmetrised it is possible to add a constant shift to all of the points, when applied to hexagonal symmetry systems, the points along the  $a$  and  $b$  axes are given by:

$$u_p = \frac{(p-1)}{q_i} \quad (\text{Equation 3.43})$$

where  $p$  varies from 1 to  $q_i$  [39].

### 3.3.8. Plane-Wave Basis Sets

Bloch's theorem implies that the electronic wavefunctions at each  $k$ -point can be expanded in terms of a discrete plane-wave basis set. Theoretically, for this to occur an infinite number of plane-waves would be required. In any real application the basis set must be truncated to allow the calculation to be performed. This can be done systematically by referring to the kinetic energy of the plane-waves:  $(\hbar^2/2m) |k+G|^2$ . Since the wavevector is proportional to the reciprocal of the wavelength, short-range features require large  $k$ -vectors and so large energy plane-waves. Hence if an electron density contains features that vary over a short range we will require high-energy waves to represent the density correctly. Put another way, the plane-wave basis set can be truncated to include only plane-waves that have kinetic energies that are smaller than some particular cutoff energy,  $E_{cut}$ , as illustrated in figure 3.4. To obtain the best  $E_{cut}$  for a particular problem its value is increased gradually and the total-energy plotted against  $E_{cut}$  to identify the point at which convergence occurs.



$$E_{cut} = \frac{1}{2} G^2 \max \quad (\text{Equation 3.44})$$

**Figure 3.4:** Schematic representation of the cutoff energy concept.

If Bloch theorem wasn't applied then regardless of how small the cutoff energy was, an infinitely large plane-wave basis set would be required to expand the electronic wavefunctions, rather than the discrete set of plane-waves imposed by the theorem. The truncation of the basis set at a finite cutoff energy will lead to an error in the computed total-energy and its derivatives. To reduce the magnitude of this error, the cutoff energy of the plane-waves could be systematically increased. In theory, the cutoff energy should only be increased until the calculated total-energy has converged within the required tolerance, although it is possible to perform computations at lower cutoff energies.

One of the drawbacks of using plane-wave basis sets is that the number of basis states changes discontinuously with cutoff energy. Discontinuities in the plane-wave basis set are also found when the size and shape of the unit cell changes under a fixed-energy cutoff. By using denser  $k$ -point sets the weight attached to any specific plane-wave basis state can be reduced serving to lessen the degree of the discontinuities present. Nevertheless, even with the use of very dense  $k$ -point sets the problem of discontinuities is never actually resolved. It can be treated approximately by using a correction factor, which accounts for the difference between the number of states in a basis set and an infinitely large number of  $k$ -points and the number of basis states actually used in the calculation [40].



### 3.3.9. Plane-Wave Representation of Kohn-Sham Equations

One of the major advantages of using plane-waves as a basis set for the electronic wavefunctions, is the fact that the Kohn-Sham equations are simplified:

$$\sum_{G'} \left[ \frac{\hbar^2}{2m} |k + G|^2 \delta_{GG'} + V_{ion}(G - G') + V_H(G - G') + V_{xc}(G - G') \right] c_{i,k+G'} = \epsilon_i c_{i,k+G} \quad (\text{Equation 3.45})$$

In this expression, the kinetic energy is diagonal and the electron-ion, Hartree and exchange-correlation potentials are described in terms of their Fourier transforms. The use of a plane-wave basis set also reduces the computational effort required to calculate derivatives of the total-energy with respect to atomic displacements such as stresses and forces. This allows efficient geometry optimisation and molecular dynamics schemes to be implemented. It is also simple to improve the convergence of plane-wave basis set calculations as there is a schematic way of adding more basis functions.

### 3.3.10. Non-Periodic Systems

Bloch's theorem cannot be applied to systems lacking periodicity in three-dimensions such as isolated molecules, defects in solids, and surfaces *etc.* In surface computations, the desired plane-wave basis set would be one that would be discrete in the plane of the surface yet continuous in the direction perpendicular to the surface. For this an infinite number of plane-wave basis states would be required regardless of the size of the cutoff energy for the basis set. Plane-wave basis set calculations can only be performed on the non-periodic systems above, if they are represented as periodic supercell geometries.

In a surface calculation the supercell is represented by a crystal slab and a vacuum region (figure 3.5), which is repeated over all space to obtain the periodicity.

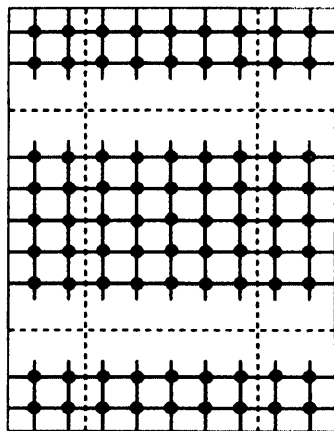


**Figure 3.5:** Schematic illustration of a supercell geometry for a surface of a bulk solid. The supercell is the area enclosed by the dashed lines. Figure obtained from reference 3.

The total-energy is then calculated over the whole crystal slab array. For accurate energies to be obtained two conditions must be fulfilled (i) the vacuum gap should be wide enough to prevent the faces of the adjacent crystal slabs from interacting with each other and (ii) the crystal slab should be sufficiently thick so as to eliminate artificial interactions arising between the surfaces of the individual crystal slabs through the bulk crystal. Isolated molecules can also be simulated in a similar fashion [41] (figure 3.6) on the basis that the supercells are large enough to ignore the interactions between them.

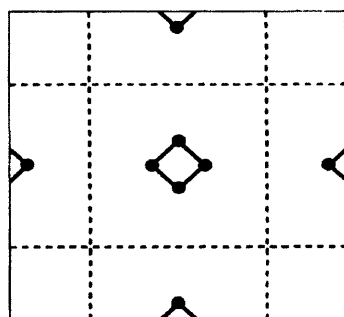


**Figure 3.6:** Schematic illustration of a supercell geometry for a molecule, convention as in figure 3.5. Figure obtained from reference 3.

### 3.3.11. Pseudopotential Approximation

Earlier it was shown that the solution to the Kohn-Sham equations for infinite crystalline systems is tractable with the use of careful  $k$ -point sampling and a plane-wave energy cutoff in the Fourier expansion of the wavefunction (sections 3.3.6 and

3.3.8) implemented within Bloch's theorem (section 3.3.5). However, the use of a plane-wave basis set alone is not ideal for the expansion of the electronic wavefunctions of heavy elements because a very large number are required to accurately describe the rapidly oscillating wavefunctions of the electrons in the core region.

To overcome such difficulties the pseudopotential approximation was introduced. Based on the observation that most physical properties are determined by the valence electrons, the approximation removes the core electrons and combines the interaction between the core and valence electrons and the strong nuclear valence electron interaction into a pseudopotential [42].

Within the core region, the valence wavefunctions are replaced by smoother nodeless pseudo-wavefunctions that are identical to the real wavefunctions outside the core region, as illustrated in figure 3.7.

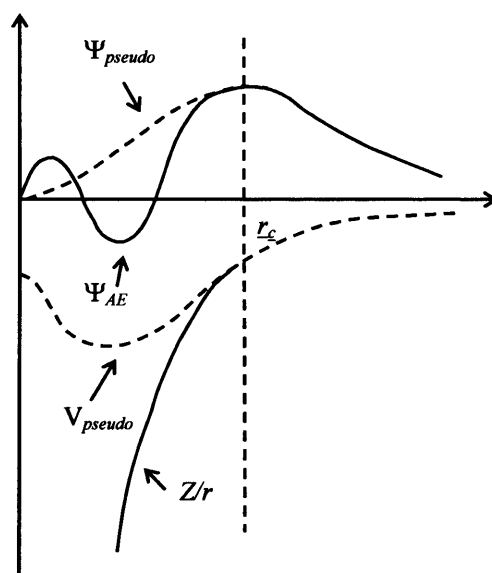


**Figure 3.7:** An illustration of the full all-electron wavefunction ( $\Psi_{AE}$ ) and electronic potential (solid lines) plotted against distance,  $r$ , from the atomic nucleus. The corresponding pseudo-wavefunction ( $\Psi_{pseudo}$ ) and potential ( $V_{pseudo}$ ) is plotted (dashed lines). Outside a given radius  $r_0$ , the all-electron and pseudo electron values are identical. Figure obtained from reference 43.

By doing so, the complexity of the problem is reduced in a number of ways. Initially, by removing the core electrons a fewer number of wavefunctions need to be calculated as well as the number of plane-waves required to describe the valence wavefunctions, as primarily the potential no longer diverges toward  $-\infty$  and the valence wavefunctions are smoother within the core region.



For a pseudopotential calculation to reproduce the same energy differences as an all-electron calculation, the pseudo-wavefunctions must be identical to the all-electron wavefunctions outside the core. This is referred to as the “norm-conservation” condition.

There are a number of different schemes for generating a pseudopotential, the two methods used for this work include the most common Vanderbilt or ultrasoft pseudopotentials (US-PP) [44] and the novel Projector Augmented-Wave (PAW) potentials [45,46]. Typically, all pseudopotentials are generated following a standard method, which usually involves specifying a cutoff distance for the core, an exchange-correlation potential and a general form for the pseudopotential. The most common form used is:

$$V_{pp} = \sum_{lm} Y_{lm}(\theta, \phi) V_l(r) Y_{lm}^*(\theta, \phi) \quad (\text{Equation 3.46})$$

where  $Y_{lm}(\theta, \phi)$  are spherical harmonics and  $V_l(r)$  is the pseudopotential for the  $l^{\text{th}}$  angular momentum component. An all-electron calculation is then performed, followed by the computation of eigenvalues and wavefunctions for an initial chosen set of parameters for the pseudopotential. The resulting eigenvalues and wavefunctions are then compared to those found from the all-electron calculation. Only once these values are equal has a self-consistent pseudopotential been generated. Otherwise a new set of parameters is chosen and the above process is repeated.

Generally, crystalline and non-periodic systems such as molecules [47] are studied with the use of a combination of plane-wave basis sets with pseudopotentials. As specified in Chapter 4, section 4.3 this Pseudopotential-Plane-wave method [48] is chosen to simulate the surface adsorption studies key to this research.

### 3.3.12. Limitations to Pseudopotential Approximation

Although, the use of pseudopotentials overcomes the initial problem of using large plane-wave basis sets for the treatment of periodic systems, one of the main disadvantages is the amount of computer time required to perform such calculations. At present, systems containing a few atoms in the unit cell are computationally expensive, and this expense increases as the number of atoms rises. To reduce such costs total-

energy pseudopotentials for larger systems are made efficient with the use of numerical algorithms, such as those employed for geometry optimisation discussed in the following section, (section 3.4).

### 3.4. Geometry Optimisation

The previous sections highlighted the theoretical aspects of minimising the electronic energies of molecular systems within the framework of *ab initio* and semi-empirical quantum mechanical methods. Although iterative methods were briefly covered to find solutions to determine the electronic energies, the actual process of conducting a geometry optimisation was ignored.

To find an optimised geometry *i.e.* a stable configuration for a molecule or periodic system, energy minimisation (geometry optimisation) calculations are performed to construct a PES. The procedure involves sampling this surface repeatedly until a potential energy minimum is obtained corresponding to a configuration where the forces on all the atoms are zero. For an initial configuration, the energy is first determined and then the atoms (and cell parameters for a periodic system) are altered to find a lower energy configuration by using the potential energy derivatives. The method is repeated until defined tolerances for the energy difference and derivatives between successive steps are achieved.

The stable states of the system correspond to the minimum points on the PES surface, and thus, moving away from this minimum would result in a configuration with a higher energy state. The lowest point on this surface represents the structure with the lowest energy and is referred to as the global energy minimum. The saddle point refers to the highest point on the pathway between two minima with the configuration of the atoms representing the transition state structure. On the PES both the minima and saddle points are stationary points, where the first derivative of the energy function is zero with respect to all coordinates. The only way to identify minimum-energy structures is to scan the PES by using a minimisation algorithm. The common features associated with the energy surface are shown in figure 3.8.

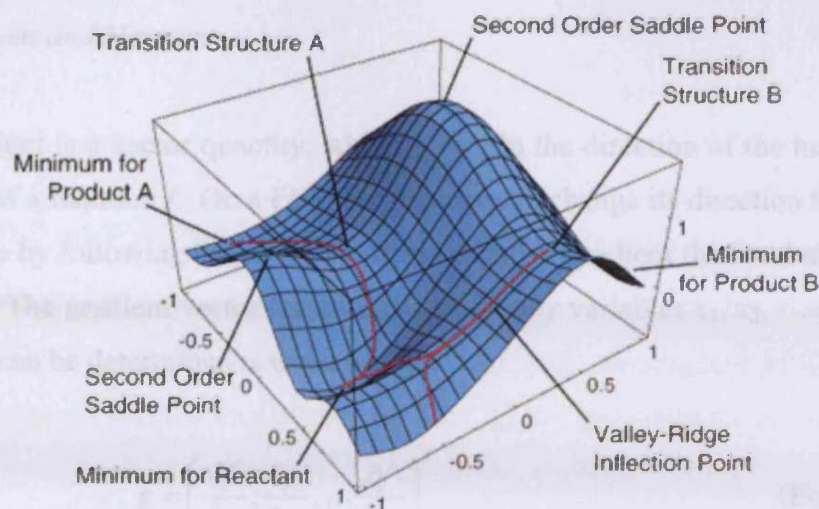


**Figure 3.8:** Schematic illustration of the features of a PES. Figure obtained from reference 49.

For complex systems local energy minima are more likely to be found rather than the true global energy minimum. To ensure that the global energy minimum structure is obtained either multiple initial configurations or more advanced modelling techniques are required. At present there are several well-known energy minimisation algorithms used to address such problems. These approaches range from simple line searches and steepest gradient methods, to the more advanced efforts of conjugate gradient (CG) and Newton-Raphson. These techniques can be used either independently or together to obtain the lowest energy configuration. Leach [50] provides a detailed review of the various energy minimisation techniques available. Of these approaches the following have been used to perform optimisations within this thesis: eigenvector following (EF) routine combined with the quadratic approximation (QA) algorithm, Berny optimisation algorithm, Broyden-Fletcher-Goldfarb-Shannon algorithm (BFGS), CG and quasi-Newton methods.

#### 3.4.1. Optimisation Techniques

The job of an optimiser is to alter the atomic coordinates to minimise the energy function. To achieve this most schemes employ the derivatives of the energy with respect to coordinates as well as the energy itself.

### 3.4.2. Gradient and Hessian

The gradient is a vector quantity, which points in the direction of the maximum rate of increase of a function  $f$ . On a PES the gradient can change its direction from point to point, and so by following the direction of the negative gradient the local minimum can be reached. The gradient vector for a function of many variables  $x_1, x_2, \dots$  etc for which a minimum can be determined is expressed as:

$$\underline{g} = \left( \frac{\partial f}{\partial x_1}, \frac{\partial f}{\partial x_2}, \dots, \frac{\partial f}{\partial x_n} \right)^T \quad (\text{Equation 3.47})$$

In most sophisticated minimisation methods knowledge of the second derivatives are required and these are collected into a matrix  $\underline{G}$ , known as the Hessian:

$$\underline{G} = \begin{pmatrix} \frac{\partial^2 f}{\partial x_1^2} & \frac{\partial^2 f}{\partial x_1 \partial x_2} & \cdots & \frac{\partial^2 f}{\partial x_1 \partial x_n} \\ \frac{\partial^2 f}{\partial x_2 \partial x_1} & \frac{\partial^2 f}{\partial x_2^2} & \cdots & \frac{\partial^2 f}{\partial x_2 \partial x_n} \\ \vdots & \vdots & \ddots & \vdots \\ \frac{\partial^2 f}{\partial x_n \partial x_1} & \frac{\partial^2 f}{\partial x_n \partial x_2} & \cdots & \frac{\partial^2 f}{\partial x_n^2} \end{pmatrix} \quad (\text{Equation 3.48})$$

Full Newton-Raphson methods [51] depend on the calculation of  $\underline{g}$  and  $\underline{G}$  at each step of the minimisation, but since this is expensive in computer time it is rarely used for large systems in computational chemistry. However, much simpler approaches have been developed which require only  $\underline{g}$  and occasional calculations of  $\underline{G}$ .

When the gradient is zero a stationary point is reached, true minima arise when this condition is fulfilled and the eigenvalues of the second derivative matrix are all positive. For a transition state the second derivatives are all positive except for one, which is negative. Such a state is investigated by calculating the eigenvalues and eigenvectors of the Hessian matrix.

### 3.4.3. Steepest Descent Approach

The majority of the iterative methods available for optimisation are based on the steepest descent method, which is commonly used for finding local minimum. In this approach the gradient at the starting geometry is followed downhill until the energy starts to rise. At this point an approximate local minimum is calculated using the last three points. The procedure continues by re-evaluating the gradient at this minimum until the energy once again begins to rise again. This reassessment of the gradient is repeated until the gradient reaches zero within some tolerance.

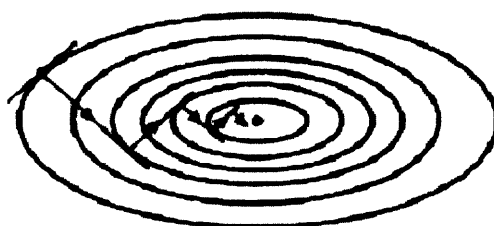


**Figure 3.9:** Schematic illustration of convergence to the centre of an anisotropic harmonic potential, using the steepest descent method. Figure obtained from reference 3.

The method is advantageous because it will always reach a minimum and the energy will always be lowered. On a practical basis only the gradient is required and so the computer storage required is low. However, due to its simple nature the local minimum will be approached slowly as the steepest descent will crawl toward it with ever decreasing speed. The method cannot go “uphill” and so as a consequence cannot be used to locate transition states. As a result the method is used typically for quick relaxation of geometries as well as cases in which a backup algorithm is required if more sophisticated techniques are unable to lower the function value.

### 3.4.4. Conjugate Gradient Method

This is a slightly more advanced version of the steepest descent approach, as it uses the gradient information at the previous points to correct the gradient direction of the current step. In this minimising procedure, the first step is carried out using the steepest descent direction. The minimum point is then located by performing a line search [52] along a direction that is made of the current negative gradient and the previous search direction.



It is an ideal method because the set of directions produced do not show the oscillatory behaviour of the steepest descent approach in narrow valleys and so better convergence is achieved. For a simple two-dimensional well the CG method locates the exact minimum of the function in just two steps as illustrated in figure 3.11. As the approach is based on steepest descents, CG can only locate local minimum and thus cannot proceed “uphill”, the method requires storage of previous gradients as well as the current gradient.

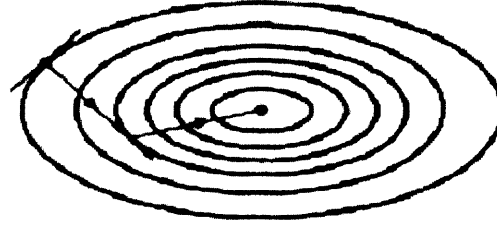


**Figure 3.10:** Schematic illustration of convergence to the centre of an anisotropic harmonic potential, using the conjugate gradient method. Figure obtained from reference 3.

#### 3.4.5. Quasi-Newton Methods

Quasi-Newton methods are efficient for finding minima particularly when inexpensive gradients *i.e.* first derivatives are available. In these algorithms the PES is represented as a quadratic model [53], which takes a series of steps in converging towards a minimum. The step to the stationary point known as the quasi-Newton or Newton-Raphson step ( $s^{NR}$ ) is:

$$s^{NR} = \underline{G}^{-1} f \quad (\text{Equation 3.49})$$

where  $f$  represents the force (negative of the gradient) calculated at the stationary point.

The optimisation starts by employing an approximate Hessian matrix ( $\underline{G}$ ) that has the required structure, which is then updated at each iteration step of the procedure using the computed gradients. The updated inverse Hessian is represented as  $\underline{G}^{-1}$  in the above expression. A number of methods have been developed to improve the stability and rate of convergence of the quasi-Newton algorithm. Those specific to the optimisations performed in this work include the Berny and BFGS methods.

In the BFGS method only the new and previous point are used to update the inverse Hessian. However, in order to give better convergence properties more of the previous points from further back in the optimisation are used to construct the Hessian (and so the  $\underline{G}^{-1}$ ) in the Berny algorithm. The method also uses a quartic polynomial, which guarantees just one local minimum in the line search. The full Berny algorithm is provided in reference [54]. The BFGS algorithm based on a different formula for the update of the  $\underline{G}^{-1}$  is particularly successful for minimisation because it ensures that the Hessian remains positive definite (the eigenvalues are all positive in the matrix). The BFGS formula is published in references [55-58].

#### 3.4.6. Eigenvector Following Routine

The procedures followed in the eigenvector follower optimiser are closely related to Newton-Raphson minimisation methods [51]. The combined optimisation routine of the EF [59,60] and the QA algorithm [61] is complicated but is generally based on the second order Taylor expansion of the energy around the current point. At this point the energy, the gradient and some estimate of the Hessian is available. Using this information the EF initially calculates the vibrational modes of the system and then uses these as the coordinate system to optimise with respect to.

The best method for performing the next geometry step is then determined by a number of test criteria, the first involves parameterising the step by applying a shift factor to ensure the geometry step length is within or on the hypersphere. If the Hessian has the correct structure then a pure Newton-Raphson step is performed and the shift factor is set to zero, however, if the step is longer than the trust radius (*i.e.* the maximum allowed step size) then a partitioned rational function optimisation (P-RFO) [59] step is attempted. Once again, if this is too long then the QA formula is used to carry out the optimisation step on the hypersphere. Only once the geometry step has been determined can the new energy and gradient be evaluated. If the values are within the tolerance specified by the user then the routine is terminated otherwise the process is repeated. This approach is good for determining transition states as it is more than likely that the maximised reaction coordinate is one of the vibrational mode eigenvectors.

Note that figure 3.11 summarises the process of optimisation and highlights the order in which the aforementioned optimisers proceed in the chain of steps involved during the procedure.

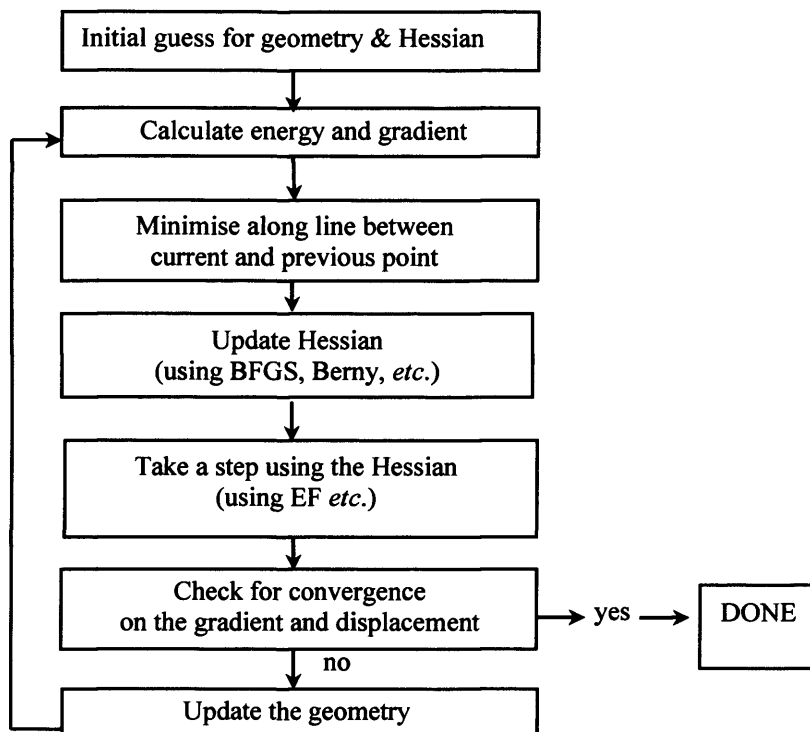


**Figure 3.11:** Flow diagram illustrating the steps involved during an optimisation procedure, i.e. locating a minimum on a PES. Figure obtained from reference 49.

### 3.5. Transition State Searches

Transition state searches for periodic adsorbed structures require a special optimisation algorithm. For periodic calculations using plane-wave methods it is well known that accurate evaluation of the Hessian is difficult due to the use of grids. As a result, the nudged elastic band (NEB) [62] method implemented within the VASP code is ideal for the calculation of minimum-energy reaction paths (MEP(s)) because it uses a non-Hessian based approach. As an improved version of the original plain elastic band (PEB) method, the NEB optimiser evaluates the potential energy and first derivatives only (*i.e.* gradients) allowing the MEP to converge within a well-defined limit. In the following sections the principles behind the algorithms are summarised, however for a thorough review of the approach and its implementation refer to the work of Jónsson *et al.* [63].

### 3.5.1. Plain Elastic Band Method

In the PEB method fixed reactant and product coordinates obtained from relaxed calculations are used. These start and end configurations are denoted as  $R_0$  and  $R_p$ , respectively in figure 3.12. Note that the coordinates comprise of the  $3N$  component vectors, in which  $N$  represents the number of atoms. To define a suitable path between the reactant and product, a series of “images” between them are obtained *via* an interpolation technique in coordination space and these are defined as  $R_1$ - $R_4$  in figure 3.12.

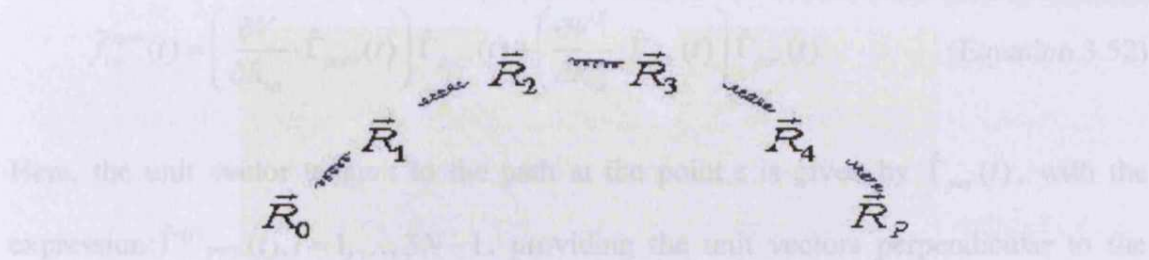


**Figure 3.12:** Schematic illustration of equidistant images separated by a spring constant in a PEB calculation. Figure obtained from reference 64.

A constrained minimisation is then performed so that the images descend in energy to the MEP. To prevent the images from collapsing to either the reactant or the product a spring force is set between them. The object function,  $f$ , which includes the spring force is expressed as:

$$f(\bar{R}_1, \bar{R}_2, \dots, \bar{R}_{P-1}) = \sum_{i=1}^{P-1} V(\bar{R}_i) + V^s \quad (\text{Equation 3.50})$$

where

$$V^s = \sum_{i=1}^P \frac{kP}{2} (\bar{R}_i - \bar{R}_{i-1})^2 \quad (\text{Equation 3.51})$$

One of the major drawbacks of this method is the fact that spring forces cause “corner cutting”, *i.e.* the algorithm does not converge to an accurate MEP on the PES. Convergence is found to be worst in the region of the saddle point (figure 3.8) since the density of the images are lowest near the highest points of the MEP.

### 3.5.2. Nudged Elastic Band Method

The NEB algorithm overcomes the resolution and “corner cutting” problems associated with the PEB method by setting the spring force in directions perpendicular to the path equal to zero. By setting the true forces along the path to zero the images are prevented from descending towards the endpoints as well as improving the density of images near the transition state. The new object function to be minimised with respect to  $3N(P-1)$  coordinates is expressed as:

$$\bar{f}_{i\alpha}^{new}(t) = \left( \frac{\partial V}{\partial R_{i\alpha}} \cdot \hat{\Gamma}_{perp}(t) \right) \hat{\Gamma}_{perp}(t) + \left( \frac{\partial V^s}{\partial R_{i\alpha}} \cdot \hat{\Gamma}_{par}(t) \right) \hat{\Gamma}_{par}(t) \quad (\text{Equation 3.52})$$

Here, the unit vector tangent to the path at the point  $t$  is given by  $\hat{\Gamma}_{par}(t)$ , with the expression:  $\hat{\Gamma}_{perp}^{(l)}(t), l = 1, \dots, 3N-1$ , providing the unit vectors perpendicular to the path at  $t$ . The forces acting on the images are redefined in the algorithm so that they zero out both the perpendicular component of the net spring force as well as the parallel component of the true interaction potential.

The NEB method is a desirable approach for finding MEP(s) of transitions because of its many advantages, which include, (i) its ability to converge to a MEP once a sufficient number of images are included in the chain. (ii) To only require evaluation of the interaction energy and the first derivative of the energy with respect to the coordinates. (iii) Convergence to the MEP is decoupled from the discrete representation of the path, making the former robust and the latter flexible. (iv) A continuous path can still be provided by the method even when multiple MEP(s) exist, and finally (v) the algorithm can be performed on either parallel computers or a linked cluster of workstations as it involves parallel calculations in which little communication is required between the computing nodes. However, on the downside, the computations are time consuming and the expense increases as more and more images are specified in the chain.

## 3.6. References

- [1] MOPAC 7, Public Domain Copy, J. J. P. Stewart, Colorado Springs CO, (1993).  
M. J. S. Dewar, E. G. Zoebisch, E. F. Healy and J. J. P. Stewart, *J. Am. Chem. Soc.*, **107**, 3902 (1985).
- [2] GAUSSIAN '98 and '03, M. J. Frisch, G. W. Trucks, H. B. Schlegel, G. E. Scuseria, M. A. Robb, J. R. Cheeseman, J. A. Montgomery, Jr., T. Vreven, K. N. Kudin, J. C. Burant, J. M. Millam, S. S. Iyengar, J. Tomasi, V. Barone, B. Mennucci, M. Cossi, G. Scalmani, N. Rega, G. A. Petersson, H. Nakatsuji, M. Hada, M. Ehara, K. Toyota, R. Fukuda, J. Hasegawa, M. Ishida, T. Nakajima, Y. Honda, O. Kitao, H. Nakai, M. Klene, X. Li, J. E. Knox, H. P. Hratchian, J. B. Cross, C. Adamo, J. Jaramillo, R. Gomperts, R. E. Stratmann, O. Yazyev, A. J. Austin, R. Cammi, C. Pomelli, J. W. Ochterski, P. Y. Ayala, K. Morokuma, G. A. Voth, P. Salvador, J. J. Dannenberg, V. G. Zakrzewski, S. Dapprich, A. D. Daniels, M. C. Strain, O. Farkas, D. K. Malick, A. D. Rabuck, K. Raghavachari, J. B. Foresman, J. V. Ortiz, Q. Cui, A. G. Baboul, S. Clifford, J. Cioslowski, B. B. Stefanov, G. Liu, A. Liashenko, P. Piskorz, I. Komaromi, R. L. Martin, D. J. Fox, T. Keith, M. A. Al-Laham, C. Y. Peng, A. Nanayakkara, M. Challacombe, P. M. W. Gill, B. Johnson, W. Chen, M. W. Wong, C. Gonzalez, and J. A. Pople, Gaussian, Inc., Pittsburgh PA, (2001 and 2003).
- [3] CASTEP 4.2, Academic Version, Licensed under the UKCP-MSI Agreement (1999), M. C. Payne, M. P. Teter, D. C. Allan, T. A. Arias and J. D. Joannopoulos, *Rev. Mod. Phys.*, **64**, 1045, (1992).
- [4] VASP 4.5, G. Kresse and J. Furthmüller, Vienna, Austria, (2003). G. Kresse and J. Furthmüller, *Comput. Mater. Sci.*, **6**, 15, (1996). G. Kresse and J. Furthmüller, *J. Phys. Rev. B*, **54**, 11169, (1996).
- [5] P. Hohenberg and W. Kohn, *Phys. Rev.*, **136**, 864B, (1964).
- [6] W. Kohn and L. J. Sham, *Phys. Rev.*, **140**, 1133A, (1965).
- [7] A. R. Leach, in “*Molecular Modelling, Principles and Applications*”, 2<sup>nd</sup> Ed., Pearson Education, Prentice Hall, England, (2001).
- [8] C. J. Cramer, in “*Essentials of Computational Chemistry, Theories and Models*”, John Wiley & Sons, Chichester, West Sussex, (2003).
- [9] A. Hinchliffe, in “*Modelling Molecular Structures*”, 2<sup>nd</sup> Ed., John Wiley & Sons, Chichester, West Sussex, (2000).

- [10] P. W. Atkins, in *"Physical Chemistry"*, 5<sup>th</sup> Ed., Oxford University Press, Oxford, England, (1994).
- [11] <http://www.msg.ameslab.gov/GAMESS/GAMESS.html>
- [12] A. R. Leach, in *"Molecular Modelling, Principles and Applications"*, 2<sup>nd</sup> Ed., Pearson Education, Prentice Hall, England, 111, (2001).
- [13] A. R. Leach, in *"Molecular Modelling, Principles and Applications"*, 2<sup>nd</sup> Ed., Pearson Education, Prentice Hall, England, 114, (2001).
- [14] C. J. Cramer, in *"Essentials of Computational Chemistry, Theories and Models"*, John Wiley & Sons, Chichester, West Sussex, 211, (2003).
- [15] A. R. Leach, in *"Molecular Modelling, Principles and Applications"*, 2<sup>nd</sup> Ed., Pearson Education, Prentice Hall, England, 93, (2001).
- [16] <http://www.semichem.com/ampac.html>
- [17] <http://www.cvc.mun.ca/software/HyperChem/hyperchem.html>
- [18] <http://comp.chem.umn.edu/Zindo-mm>
- [19] A. R. Leach, in *"Molecular Modelling, Principles and Applications"*, 2<sup>nd</sup> Ed., Pearson Education, Prentice Hall, England, 156, (2001).
- [20] A. R. Leach, in *"Molecular Modelling, Principles and Applications"*, 2<sup>nd</sup> Ed., Pearson Education, Prentice Hall, England, 317, (2001).
- [21] A. R. Leach, in *"Molecular Modelling, Principles and Applications"*, 2<sup>nd</sup> Ed., Pearson Education, Prentice Hall, England, 142, (2001).
- [22] P. W. Atkins, in *"Physical Chemistry"*, 5<sup>th</sup> Ed., Oxford University Press, Oxford, England, A31, (1995).
- [23] U. von Barth, in *"Many Body Phenomena at Surfaces"*, D. Langreth *et al.* (Editors), Academic, New York, 3, (1984).
- [24] R. M. Dreizler and J. da Providencia, in *"Density Functional Methods in Physics"*, Plenum, New York, (1985).
- [25] R. O. Jones and O. Gunnarsson, *Rev. Mod. Phys.*, **61**, 689, (1989).
- [26] E. S. Kryachko and E. V. Ludena, in *"Energy Density Functional Theory of Many Electron Systems"*, Kluwer Academic, Boston, (1990).
- [27] J. F. Janak, *Phys. Rev. B*, **18**, 7165, (1978).
- [28] J. P. Perdew, R. G. Parr, M. Levy and J. L. Balduz, Jr., *Phys. Rev. Lett.*, **49**, 1691, (1982).
- [29] E. P. Wigner, *Trans. Faraday Soc.*, **34**, 678, (1938).
- [30] L. Hedin and B. Lundqvist, *J. Phys. C*, **4**, 2064, (1971).

- [31] S. H. Vosko, L. Wilk and M. Nusair, *Can. J. Phys.*, **58**, 1200, (1980).
- [32] J. P. Perdew and A. Zunger, *Phys. Rev. B*, **23**, 5048, (1981).
- [33] J. P. Perdew, J. A. Chevary, S. H. Vosko, K. A. Jackson, M. R. Pederson, D. J. Singh and C. Fiolhais, *Phys. Rev. B*, **46**, 6671, (1992).
- [34] A. D. Becke, *J. Chem. Phys.*, **98**, 5648, (1993).
- [35] C. Lee, W. Yang and R. G. Parr, *Phys. Rev. B*, **37**, 785, (1988).
- [36] P. J. Stevens, J. F. Devlin, C. F. Chabalowski and M. J. Frisch, *J. Phys. Chem.*, **98**, 11623, (1994).
- [37] G. Attard and C. Barnes, in “*Surfaces*”, Oxford University Press, Oxford, England, (1998).
- [38] H. J. Monkhorst and J. D. Pack, *Phys. Rev. B*, **13**, 5188, (1976).
- [39] J. D. Pack and H. J. Monkhorst, *Phys. Rev. B*, **16**, 1748, (1977).
- [40] G. P. Francis and M. C. Payne, *J. Phys. Condens. Matter*, **17**, 1643, (1990).
- [41] J. D. Joannopoulos, P. Bash and A. Rappe, *Chemical Design Automation News*, **6**, 8, (1991).
- [42] M. T. Yin and M. L. Cohen, *Phys. Rev. B*, **25**, 7403, (1982).
- [43] <http://cmt.dur.ac.uk/sjc/thesis/thesis/node20.html>
- [44] D. Vanderbilt, *Phys. Rev. B*, **41**, 7892, (1990).
- [45] P. E. Blöchl, *Phys. Rev. B*, **50**, 17953, (1994).
- [46] G. Kresse and D. Joubert, *Phys. Rev. B*, **59**, 1758, (1999).
- [47] J. Crain and S. J. Clark, in “*Calculation of Structure and Dynamical Properties of Liquid Crystal Molecules in Liquid Crystals I*”, D. M. P. Mingos (Editor), Springer-Verlag, Berlin, **94**, 1, (1999).
- [48] M. D. Segall, P. J. D. Linden, M. J. Probert, C. J. Pickard, P. J. Hasnip, S. J. Clark and M. C. Payne, *J. Phys. Condens. Matter*, **14**, 2717, (2002).
- [49] [http://www.gaussian.com/g\\_ur/b\\_proglimits.htm](http://www.gaussian.com/g_ur/b_proglimits.htm)
- [50] A. R. Leach, in “*Molecular Modelling, Principles and Applications*”, 2<sup>nd</sup> Ed., Pearson Education, Prentice Hall, England, 253, (2001).
- [51] A. R. Leach, in “*Molecular Modelling, Principles and Applications*”, 2<sup>nd</sup> Ed., Pearson Education, Prentice Hall, England, 267, (2001).
- [52] A. R. Leach, in “*Molecular Modelling, Principles and Applications*”, 2<sup>nd</sup> Ed., Pearson Education, Prentice Hall, England, 262, (2001).
- [53] Ö. Farkas and H. B. Schlegel, *J. Chem. Phys.*, **111**, 10806, (1999).
- [54] H. B. Schlegel, *J. Comput. Chem.*, **3**, 214, (1982).



- [55] C. G. Broyden, *J. Inst. Math. Appl.*, **6**, 76, (1970).
- [56] R. Fletcher, *Comput. J.*, **13**, 317, (1970).
- [57] D. Goldfarb, *Math. Comp.*, **24**, 23, (1970).
- [58] D. F. Shanno, *Math. Comp.*, **24**, 647, (1970).
- [59] A. Banerjee, N. Adams, J. Simons and R. Shepard, *J. Phys. Chem.*, **89**, 52, (1985).
- [60] J. Baker, *J. Comp. Chem.*, **7**, 385, (1985).
- [61] P. Culot, G. Dive, V. H. Nguyen and J. M. Ghuysen, *Theo. Chim. Acta.*, **82**, 189, (1992).
- [62] G. Mills, H. Jonsson and G. K. Schenter, *Surf. Sci.*, **324**, 305, (1995).
- [63] H. Jónsson, G. Mills and K. W. Jacobsen, in “*Classical and Quantum Dynamics in Condensed Phase Simulations*”, B. J. Berne, G. Ciccotti and D. F. Coker (Editors), World Scientific, (1998).
- [64] <http://www.pitt.edu/~jordan/neb.html>

## ***Chapter 4***

### ***Computational Methods and Parameters***

## 4.0. Introduction

As described in the previous Chapter, a number of computational methods based on quantum mechanical techniques such as *ab initio*, semi-empirical, DFT and pseudopotential theory have been employed to study isolated gas-phase reaction molecules as well as surface adsorbed hydrogenation intermediates. The desired computations have been performed using four different packages available to the Cardiff computational group: MOPAC [1], GAUSSIAN [2], CASTEP [3] and VASP [4] using a variety of external and internal computational resources. The following subsections of this Chapter will systematically describe the exact computational procedure as well as the parameters used to generate the desired results of this research (Chapters 5-7). Where necessary a justification of the parameters will also be provided as well as a brief description of the software used and its general capabilities.

### 4.1. Semi-Empirical Optimisations

#### 4.1.1. Method and Parameters Used in Cinchonidine Calculations

The semi-empirical work of this thesis is carried out using the MOPAC software [1]. MOPAC standing for Molecular Orbital PACkage created by James J. P. Stewart in 1993 and now a cooperative development is basically a general-purpose semi-empirical molecular orbital package, which enables the study of chemical structures and reactions. Its capabilities include the use of semi-empirical Hamiltonians MNDO, MINDO/3, AM1, and PM3 in the electronic part of the calculation to obtain molecular orbitals, the heat of formation and its derivatives with respect to molecular geometry. Using these results MOPAC can calculate the vibrational spectra, thermodynamic quantities, isotopic substitution effects and force constants for molecules, radicals, ions, and polymers. Some of the quantum theory and mathematical foundations MOPAC draws upon are discussed in the previous Chapter, although a more thorough account of the background can be found in the relevant theory section of the manual [5].

Within this environment, explicit geometry optimisation calculations (Chapter 5, section 5.2.1) for the conformational analysis of CD were performed using the HF method in conjunction with the PM3 (third parameterisation of MNDO) Hamiltonian [6]. The optimiser used within MOPAC is a combination of the EF algorithm [7,8] and

the QA algorithm [9]. Both use the Hessian for computing changes in the geometry to make the gradients vanish when a minimum-energy is reached.

To control the precision of the stages involved in the SCF iterations as well as the geometry optimisation parts of the computation the “PRECISE” criteria was specified. In doing so the convergence for the SCF calculation is stopped only when the change in energy on successive iterations is less than the adjustable parameter “SCFCRT” set at  $0.1 \times 10^{-5}$  kcal mol<sup>-1</sup>. The geometry optimisation part of the calculation is terminated once a number of different test criteria have been met simultaneously and these are: (i) “Test on X Satisfied” (“TOLERX”), the projected change in geometry must be less than the “TOLERX” value of  $0.1 \times 10^{-3}$  Å; (ii) “Herbert’s Test Satisfied” (“DELHOF”), the projected decrease in energy ought be less than 0.001 kcal mol<sup>-1</sup>; (iii) “Test on Gradient Satisfied” (“TOLERG”), the gradient norm in kcal mol<sup>-1</sup> Å<sup>-1</sup> should be less than 0.2 multiplied by the square root of the number of coordinates to be optimised; (iv) “Heat of Formation Test Satisfied” (“TOLERF”), the calculated heats of formation on two successive cycles must differ by less than 0.002 kcal mol<sup>-1</sup>; (v) the absolute value of the largest component of the gradient must be less than the default “TOL2” value of 0.01; (vi) the square root of the ratio of the projected change in the geometry to the actual geometry must be less than “TOLS1”,  $1 \times 10^{-12}$  and finally (vii) every component of the gradient should be 0.2 and less. Additional information regarding SCF and optimisation criterion can be found in the subsequent “criteria” section of the MOPAC manual [5]. Note that care should be taken with precision criteria as increasing the criterion can potentially introduce infinite SCF loops whilst decreasing criterion can lead to unacceptably imprecise results.

The semi-empirical calculations of Chapter 5 were performed using the 7<sup>th</sup> release of the MOPAC software [1] and executed in serial mode on Alpha Dec workstations (500 au) available at Cardiff.

## 4.2. *Ab Initio* Optimisations

### 4.2.1. Method and Parameters Used in Cinchonidine and Cinchonidine-Reactant Complex Calculations

The GAUSSIAN [2] code has been employed to study all *ab initio* optimisations. Originally developed by John Pople and co-workers in 1987, it comprises of a series of electronic structure programs, designed to model a broad range of molecular systems under a variety of conditions. By performing molecular orbital calculations based on the laws of quantum mechanics, the code can predict energies, molecular structures and vibrational frequencies and their associated molecular properties either in the gas- or solution-phase and in both their ground and excited states. Semi-empirical and *ab initio* calculations including the capabilities of (i) predicting the one- and two-electron integrals over *s*, *p*, *d*, and *f* contracted gaussian functions as well as (ii) using Mulliken population analysis, multipole moments, and electrostatic fields to evaluate various one-electron properties of the HF wavefunction and (iii) performing correlation energy calculations using configuration interaction using either all double excitations or all single and double excitations can be computed within GAUSSIAN under a variety of theory levels, ranging in accuracy and corresponding computational cost. The software is sophisticated in the sense that chemical phenomena such as substituent effects, reaction mechanisms and electronic transition states can be explored.

Superior optimisations can be achieved by using a higher level of theory, such as DFT together with a sufficiently large basis set of orbitals to provide a good description of the molecular wavefunction. The basis functions used in GAUSSIAN are referred to as Gaussian Type Orbitals (GTO), and can be characterised by (i) its size *i.e.* by the number of functions in the minimal basis set (single-zeta basis), such that doubling and tripling the functions would result in a double-zeta and triple-zeta basis, (with or without polarisation) and (ii) by the level of frozen core approximation.

The HF method combined with the density functional hybrid method of B3LYP [10] (Chapter 3, section 3.2.20) with the 6-31G(d) basis set was applied to calculate the structure optimisations of CD, CDH<sup>+</sup> and its complexation with EtPy and butane-2,3-dione. The basis set employed is classified as a split valence triple-zeta basis set with polarisation functions on the heavy (*i.e.* non-hydrogen) atoms, 6 gaussian functions are used to describe the inner shell with 3 contracted functions and 1 diffuse function for

the valence shell. With use of the Berny optimisation algorithm [11] the DFT calculations were solved self-consistently ensuring that all degrees of freedom were fully optimised to a gradient of less than  $4.5 \times 10^{-4}$  hartree bohr<sup>-1</sup>.

Two different versions of the GAUSSIAN code *i.e.* the '98 and '03 suite of programs [2] were used to perform the *ab initio* calculations. The computations were executed using the same workstations as specified for the semi-empirical work as well as the Helix supercomputer facility at Cardiff [12]. Once again, the previous Chapter discusses the theoretical concepts behind GAUSSIAN, however an excellent reference is the accompanying manual by J. Foresman and Æ. Frisch [13].

### 4.3. Periodic Optimisations

The concluding results of this thesis are generated with the use of two alternative plane-wave periodic codes CASTEP [3] and VASP [4]. CASTEP standing for Cambridge Sequential Total Energy Package, was originally developed in the Theory of Condensed Matter Group at Cambridge University in the UK [14]. It consists of a suite of programs enabling advanced quantum mechanical calculations to be executed for chemicals and materials research. Based upon the plane-wave pseudopotential Car-Parrinello method, DFT is the default *ab initio* theory supporting LDA, GGA, and their spin unrestricted equivalents (LSDA and GGS respectively). With the use of molecular dynamics (MD), efficient matrix diagonalisation schemes and an efficient Pulay mixing, an exact evaluation of the instantaneous electronic ground state at each MD or optimisation step can be assessed. CASTEP can easily calculate forces and stress, used to relax atoms and unit cell parameters to their instantaneous groundstate. To describe the interactions between ions and electrons a range of local and non-local Vanderbilt and norm-conserving pseudopotentials are available. Symmetrisation of the wavefunction is available to speed up calculations for symmetric systems.

VASP (Vienna *Ab Initio* Simulation Package)/VAMP developed by Juergen Hafner, George Kresse and co-workers on the other hand is slightly more advanced than CASTEP. Although the approach implemented within the program is similar to that of CASTEP, it has the same roots as the CASTEP/CETEP (parallel processing equivalent) 1989 code, VASP offers the use of additional pseudopotentials of the type generated by the PAW method.

The underlying principles behind the two codes are discussed in the previous Chapter, however, the relevant sections within the program manuals are also very useful [15,16]. The exact programs used in our calculations include version 4.2 for CASTEP [3] and version 4.4.5 for VASP [4]. The subsequent periodic DFT computations of Chapter 6 were performed using the external Turing [17] and Mott [18] Beowulf clusters located at Daresbury and Rutherford Appleton laboratories, whilst the most recent work of Chapter 7 used the Helix supercomputer.

The initial CASTEP and VASP computations performed in Chapters 6 and 7 are used as a comparative study against reference VASP work conducted by Watson *et al.* [19]. For this series of work no prior testing of computational parameters for energy convergence (to be discussed later) were conducted as the methodology used in the reference work was shown to adequately yield adsorption data in agreement with the available thermodynamic data. However, due to recommendations specified in the VASP manual, the extent of electron smearing was tested on this system. A full discussion is provided in section 4.3.3. The exact computational procedure used in this comparative study is the same as discussed in reference 19 and is outlined in the following section.

Note that all periodic optimisations specified in this work are performed without constraints as all degrees of freedom are allowed to relax. Initially the periodic systems are optimised so that all cell parameters vary to simulate constant pressure conditions so that no net stress remains on the simulation cell boundaries. This is achieved by setting P1 symmetry for the simulation cells, so that no symmetry is imposed on the atomic positions (other than translational symmetry) and allows all six cell parameters to vary. This implies for surfaces cell vectors are allowed to relax but they are not as they are kept fixed.

#### 4.3.1. Method and Parameters Used in Comparative Study of Ethene Adsorption on Pt(111)

In this work the (111) surface of Pt was represented as a slab of material, in which a vacuum gap was employed perpendicularly to the surface in a 3-dimensional periodic cell. A  $p(2 \times 2)$  surface unit cell of 3 Pt layers thick with a vacuum gap of 9.2 Å was employed. Upon this surface the adsorption of ethene was found to give rise to a

nearest intermolecular H-H distance of approximately 3 Å (shorter distance measured in CASTEP compared to VASP). The same surface coverage had been used in previous analogous periodic simulations conducted by Ge and King [20].

The DFT calculations were set-up with the exchange and correlation energies described by GGA with Perdew *et al.*'s '91 parameterisation (PW91) [21]. Periodic boundary conditions were employed to allow the crystal wavefunctions to be expanded in terms of a basis set. By doing so this enables CASTEP and VASP to calculate the forces on the atoms with the Hellmann-Feymann theorem [22] allowing a BFGS [23-26] (CASTEP) and either a CG [27] or quasi-Newton [28] (VASP) relaxation to be performed.

With the use of a plane-wave basis set no basis set superposition error (BSSE) [29] occurs. Essentially, this error arises when a molecule with the use of a localised basis set, lowers its energy by allowing its electron density to be represented by basis set functions assigned to another molecule or alternatively in this case assigned to the surface. As a result, the comparison of a gas-phase molecule with a surface adsorbed molecule as required for the calculation of adsorption energy (refer to Chapter 6, equation 6.2) would yield an error due to changes in the basis set arising from different atom positions. However, this does not occur for systems using plane-wave basis sets as both the gas-phase and adsorbed state molecule is represented by the same basis set which is dependent only on the cell volume and plane-wave KE cutoff.

To improve efficiency of the calculations Vanderbilt US-PPs [30] (CASTEP) and novel PAW-PPs [31,32] (VASP) were employed with a cutoff energy set at 300 eV. The extended electronic states of the surface were represented by phase factors substituted into the wavefunctions, specified as a series of *k*-points measured in reciprocal space. A Monkhorst-Pack [33] *k*-point sampling of  $9 \times 9 \times 1$  was used, as it was previously shown to converge the adsorption energy to within approximately 3 kJ mol<sup>-1</sup> [19]. This difference is within the present accuracy of the DFT methodology. The extent of electron smearing for the Pt surface was adequately described with use of second-order Methfessel-Paxton smearing [34] set at a width of 0.1 eV.

Geometry optimisation calculations were carried out allowing the full relaxation of the surface and adsorbing molecule. For CASTEP, the optimisation procedure is only stopped when all four of the following default criteria for the system atoms are satisfied, (i) root mean square (RMS) displacement tolerance is 0.001 Å or below, (ii) RMS force



tolerance is  $0.05 \text{ eV } \text{\AA}^{-1}$  or below (iii) RMS stress tolerance is  $0.1 \text{ eV}$  or below and (iv) the change of energy between successive configurations is less than the “ETOT\_TOL” (minimiser for tolerance for total energy) value of  $0.2 \times 10^{-4} \text{ eV}$  per atom. In the VASP procedure the electronic degrees of freedom are stopped once the free energy change ( $\Delta G$ ) and the band structure energy change (“change of eigenvalues”) between two steps are both smaller than the “EDIFF” value of  $10^{-4} \text{ eV}$ . In other words this is the error allowed in the calculated total energy.

#### *4.3.2. Method and Parameters Used in Formaldehyde and Acetone Adsorption on Pd and Pt(111)*

For the investigation of the adsorption of formaldehyde and acetone intermediates on the (111) surface of Pd and Pt, periodic DFT calculations analogous to those specified in the above section were employed. Both CASTEP and VASP were used to study the energetics and the corresponding results are discussed in Chapters 6 and 7. To accommodate the larger adsorbates the size of the original cell was increased to the dimensions of  $p(3 \times 3)$ , incorporating 27 metal atoms in total (3-layer slab), of which 9 represented the substrate plane. The model corresponds to an adsorbate surface coverage of 56%.

Although, experimentally the adsorption energies and geometries of the aldehyde and ketone intermediates are thought to be coverage-dependent, it is computationally expensive to examine the energetics and all possible modes of adsorption at various coverages. As a compromise only the most favourable structural conformations, as determined by surface science techniques and previous theoretical modelling (Chapter 2, section 2.6) are investigated in this work.

#### *4.3.3. Justification and Convergence Tests of Parameters Used in Periodic Optimisations*

Generally, for realistic surface calculations to be performed three different steps to ensure convergence of the system must be fulfilled. The first involves modelling an accurate bulk energy, this is achieved by using a finite temperature method for electron

smearing and increasing the number of  $k$ -points and KE cutoff until the calculation converges to a required accuracy.

For reasons discussed in Chapter 6, *i.e.* the modelling of an inaccurate substrate due to the type of US-PPs used in CASTEP, the VASP program is found to be most suitable for the simulation of surface adsorbed species. Based on this all convergence tests illustrated here unless otherwise stated are performed using this program. To decide upon the  $k$ -points and cutoff energy most suitable to provide accurate energetic and structural information for the adsorption of formaldehyde and acetone, various optimisations testing 10 different  $k$ -point grid sizes and 5 different cutoff values were performed on the bulk Pt. The corresponding energies for these bulk cells are summarised in figure 4.1.

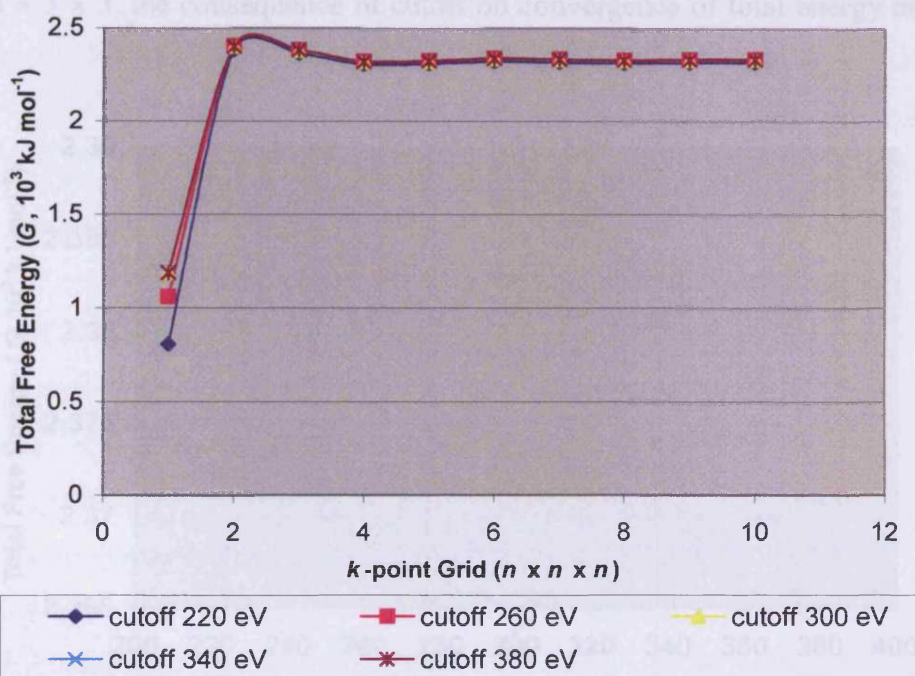


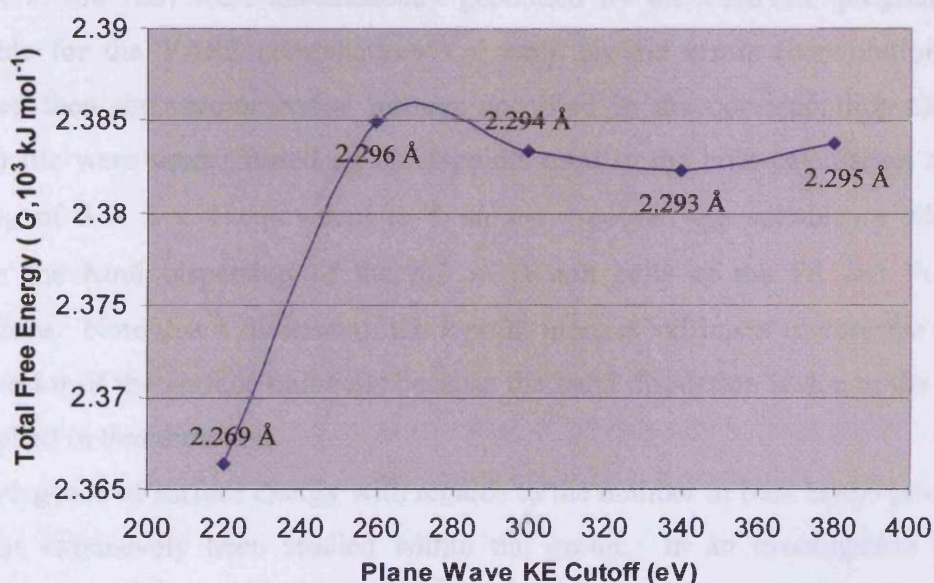
**Figure 4.1:** The effect of  $k$ -points and cutoff energies on the convergence of the bulk Pt energy. DFT calculations performed using VASP with theory level specified at GGA-PW91.

It is evident from the correlation above that as the cutoff value is increased from 220 to 380 eV a significant stabilisation of the bulk Pt cell is observed upon optimisation. The total energy of the bulk Pt is found to be at a minimum when 1  $k$ -point is used, although only small differences in energy with the other cutoffs are observed. With regards to  $k$ -points, a grid density of  $3 \times 3 \times 3$  (4 unique  $k$ -points) is sufficient to converge the bulk energy within the limits of error for DFT. However, convergence of

the energy within  $1 \text{ kJ mol}^{-1}$  is obtained with higher grid densities equivalent to 35  $k$ -points.

Although it is evident that increasing the  $k$ -point sampling leads to more accurate total energy calculations, a compromise between accuracy and computational cost has to be made. Energy convergence with regards to the “mixed” approach of a high cutoff (380 eV) and a low number of  $k$ -points (4 for the bulk) is more than adequate for the calculations of this work. This is verified by the calculation of the lattice constant (*i.e.* interlayer spacing of the bulk).

The aim in this work is to try and obtain a theoretical lattice constant in good agreement with experimental and previous modelling work for which accurate adsorption data has been generated. For calculations incorporating the chosen  $k$ -point grid of  $3 \times 3 \times 3$ , the consequence of cutoff on convergence of total energy and lattice



constant is illustrated in figure 4.2.

**Figure 4.2:** The effect of cutoff energies on the convergence of the bulk Pt energy and lattice constant. Calculations performed using VASP at DFT theory level GGA-PW91.

In the reference work of Watson *et al.* [19] the lattice constant obtained by VASP for the bulk Pt was an atom interlayer spacing of  $2.30 \text{ Å}$  with the experimental LEED value quoted at  $2.26 \text{ Å}$  [35]. From the above 4  $k$ -point calculations, cutoff energies of 260 eV and 380 eV are found to adequately converge the total energy of the bulk to a minimum for a lattice constant of approximately  $2.30 \text{ Å}$ . The analogous methodology for



CASTEP also provided a bulk with the desired lattice constant and this is discussed in Chapter 6, section 6.1.

Similar convergence tests for the bulk Pd energy were previously conducted as part of an M. Sc. project at Cardiff [36]. With the use of CASTEP, the parameters best found to be suitable for the convergence energy of bulk Pd were a  $k$ -point sampling of  $3 \times 3 \times 3$  (4  $k$ -points) with a KE cutoff value of 380 eV. These parameters are in agreement with those determined for the Pt case, figures 4.1 and 4.2.

Once sufficient parameters for the bulk calculation have been determined, the second stage usually involves finding suitable Fast Fourier Transform (FFT)-meshes and  $k$ -points for the surface calculation. This is typically followed by the third step, which tests the number of bulk and vacuum layers required to obtain a reasonable surface energy.

Initially the FFT-meshes specified in the surface calculations (ranging between  $48\text{-}54 \times 48\text{-}54 \times 108\text{-}126$ ) were automatically generated by the CASTEP program and if unsuitable for the VASP computations *i.e.* wrap around errors (convolutions) were generated then the recommended settings specified in the corresponding OUTCAR (results) file were used. Based on the  $k$ -points used in the bulk calculation a  $k$ -point sampling of  $3 \times 3 \times 1$  equivalent to 5 unique  $k$ -points was suitable to adequately describe the band dispersion of the  $p(3 \times 3)$  unit cells of the Pd and Pt surface calculations. Note that 1 division of the  $k$ -point mesh is sufficient to describe the long lattice vector of the surface unit cells because the band dispersion is due to the vacuum zero applied in that direction.

Convergence of surface energy with regards to the number of bulk layers prior to this work has extensively been studied within the group. In an investigation into the adsorption and diffusion of H over Group 10 (111) surfaces, 3- and 5-layer slabs were tested [37]. Only slight differences in the adsorption energies were observed, with greater stabilisation favoured over the relaxed 3-layer slab. As with the case of ethene adsorption over Pt(111), the resulting adsorption energies obtained with surface cells incorporating 3 bulk layers were found to compare well against the available thermodynamic data and analogous theoretical models [19]. These studies justify the use of such surface slabs in our periodic calculations.

Initially, the CASTEP surface cells were modelled using a 10 Å vacuum gap, however upon optimisation of an  $\eta^1(\text{O})$  (endon) acetone species over a Pd(111) surface

an attraction of the periodic image of the lower layer of the Pd slab with the methyl groups of the acetone was observed. This resulted in the overbinding of the adsorbate with the surface. On increasing the vacuum gap by a further 5 Å, the adsorption energy was found to reduce by approximately 10 kJ mol<sup>-1</sup> [36]. Based on this, a vacuum gap of 15 Å is best suited for the surface calculations of this work.

Another important parameter tested was the level of electron smearing. Smearing allows fractional occupation of the closely-spaced levels within a given change in energy ( $\Delta E$ ) of the  $E_F$  level of a metal. This improves convergence of the SCF procedure by allowing orbitals to relax more rapidly. The character of the virtual orbitals can be more effectively mixed into the occupied space, since the orbitals will be fractionally occupied.

Watson *et al.* [19] showed sufficient convergence of adsorption energies for ethene with the use of second-order Methfessel-Paxton smearing of width 0.1 eV. In VASP the level of Methfessel-Paxton can be altered from first- to second-order and the width of the smearing can be increased from 0.1 to 0.2 eV. For relaxations in metals the VASP manual recommends the width of the smearing to be 0.2 eV. Based on this argument all available levels of smearing were tested for convergence. A further parameter introduced into the calculations as recommended by the program manual for transition metals is the “VOSKOWN” tag.

Usually VASP uses the standard interpolation for the correlation part of the exchange correlation functional. If the “VOSKOWN” tag is switched on then the interpolation formula according to Vosko Wilk and Nusair [38] is used. By enhancing the magnetic moments and magnetic energies, this interpolation is usually applied in the context of gradient corrected functionals and VASP suggests this to be used whenever the PW91 functional is applied, as is the case here. Bearing these factors in mind a combination of relaxations were performed with and without “VOSKOWN” specified using different magnitudes of Methfessel-Paxton smearing, the resulting Pt bulk structures are analysed as illustrated in table 4.1.

Calculation Method	Relaxed Lattice Constant, $a$ , (Å)	Interlayer Spacing (Å)	Total Free Energy, $G$ , ( $10^3$ kJ mol $^{-1}$ )
Ismear = 1, Sigma = 0.1	3.9806	2.2982	2.3316
Ismear = 1, Sigma = 0.2	3.9812	2.2985	2.3317
Ismear = 2, Sigma = 0.1	3.9806	2.2982	2.3316
Ismear = 2, Sigma = 0.2	3.9808	2.2983	2.3315

**Table 4.1:** VASP calculations to test the width and level of electron smearing with and without the Vosko Wilk and Nusair interpolation formula for the PW91 functional required for adequate bulk relaxation of Pt. Ismear represents the level of Methfessel-Paxton smearing i.e. 1 and 2 equate to first- and second-order and determines how the partial occupancies  $f_{nk}$  are set for each wavefunction, whilst for the finite temperature LDA sigma indicates the magnitude of the smearing in eV. DFT relaxations performed using parameters as discussed in section 4.3.1 and reference 19 i.e. 41 k-points and 300 eV cutoff radius.

Surprisingly, whether the “VOSKOWN” tag is switched on or off in the relaxation makes no difference to the overall lattice vectors, as both set of computations result in the same bulk cells. However, as mentioned earlier “VOSKOWN” is recommended for the application of all transition metals, so it must be made clear that it has no effect specifically on the relaxed structure of Pt although it could for the other groups of the transition series.

Varying the level of electron smearing also appears to have a very small effect, which in reality is negligible on the bulk Pt cells. In this case no one method is better than the other at relaxing the bulk. However, since the modelling of a reasonable surface is crucial to the calculations of this study, the same convergence test was performed on the  $p(2 \times 2)$  Pt surface, in this series of calculations the “VOSKOWN” tag was switched off (default in VASP) for reasons discussed above.

Calculation Method	Interlayer Spacing (Å)	Surface Energy (J m $^{-2}$ )	CPU Time (mins)
Ismear = 1, Sigma = 0.1	2.3238	1.50	53
Ismear = 1, Sigma = 0.2	2.3254	1.49	56
Ismear = 2, Sigma = 0.1	2.3227	1.50	49
Ismear = 2, Sigma = 0.2	2.3257	1.50	53

**Table 4.2:** VASP calculations to test the same electron smearing parameters as defined in table 4.1. DFT relaxations were performed on a  $p(2 \times 2)$  Pt (111) surface as modelled using the computational method and parameters discussed in section 4.3.1 and reference 19. Surface energies calculated using the

expression:  $E_{\text{surface}} = \frac{E_{\text{slab}} - \frac{n}{n'} E_{\text{bulk}}}{2A}$  where  $E$  represents the electronic energy,  $\frac{n}{n'}$  is the stoichiometric

*ratio of the number of surface atoms over the number of bulk atoms in the fcc cube and  $A$  denotes the surface area. The expression is further explained in section 6.1, Chapter 6.*

As expected similar Pt surfaces are optimised when either one of the four electron smearing settings is specified in the calculation. No great difference is observed in either the energies (in this case translated as the surface energy) or the interlayer spacings of the surfaces. However, electron smearing helps the SCF procedure to converge, which is essential as this ultimately helps to reduce the computational expense of the calculations. In this series the method of electron smearing which converges the quickest is the second-order smearing with a width of 0.1 eV, as illustrated in table 4.2. Note that these calculations were all performed in parallel mode using 8 processors of the external Mott facility [18].

By running the above calculations not only is the level of electron smearing chosen for all periodic calculations of this research justified but they also help to confirm the procedure used in the initial comparative study of ethene adsorption over Pt(111) with the VASP program (Chapter 7). In the literature, the reference state for the adsorption energy of ethene is a fully relaxed Pt slab that has an interlayer spacing of 2.32 Å compared to the calculated bulk spacing of 2.30 Å [19]. The calculations on the analogous bulk and surface confirm this to be the case for the computations in which second-order Methfessel-Paxton smearing with a width of 0.1 eV is specified (tables 4.1 and 4.2), as used in the reference work [19].

Based on the above justifications the parameters used within the DFT calculations specified at theory level GGA-PW91 to best model the effects of surface adsorption of formaldehyde and acetone over Pd and Pt were as follows: 3-layer surface slabs incorporating a 15 Å vacuum gap, 5 Monkhorst-Pack special  $k$ -points equivalent to a  $3 \times 3 \times 1$  grid, 380 eV KE cutoff and second-order Methfessel-Paxton smearing with a width of 0.1 eV. As with the ethene study, Vanderbilt US-PPs and PAW-PPs were used in the CASTEP and VASP calculations respectively. All optimisations were performed using the CG approach.

#### 4.3.4. Method and Parameters Used in Transition State Searches for the Adsorption Modes of Formaldehyde and Acetone on Pd and Pt(111)

The NEB approach [39,40] implemented within the VASP code was used to identify transition states. Calculations were performed to investigate the energy barriers between the transformations of the stable  $\eta^1(\text{O})$  to  $\eta^2(\text{C},\text{O})$  adsorption modes of formaldehyde and acetone, as well as the corresponding  $\eta^1(\text{C})$  acetone enolate to the di- $\sigma$ ,  $\eta^2(\text{C},\text{O})$  adsorption mode on the (111) surface of Pd and Pt (Chapter 7). As outlined in Chapter 3, sections 3.5.1 and 3.5.2, the transition search was initiated by interpolating either 5 or 10 images of the system respectively, between the optimised reactant and product states. Each image was then optimised in parallel to map the minimum-energy reaction path. The calculations were performed using the latest release of VASP, version 4.4.6 and executed on the Helix supercomputer at Cardiff with either 10 or 12 processors allocated per image of the NEB calculation. To maintain the spacing between adjacent images to a constant a spring interaction of  $-5$  as recommended by the program manual was added to the calculations. The overall parameters used to perform the elastic band calculations were the same as used to originally optimise the start and end configurations, as summarised in the previous section.



## 4.4. References

- [1] MOPAC 7, Public Domain Copy, J. J. P. Stewart, Colorado Springs CO, (1993).  
M. J. S. Dewar, E. G. Zoebisch, E. F. Healy and J. J. P. Stewart, *J. Am. Chem. Soc.*, **107**, 3902 (1985).
- [2] GAUSSIAN '98 and '03, M. J. Frisch, G. W. Trucks, H. B. Schlegel, G. E. Scuseria, M. A. Robb, J. R. Cheeseman, J. A. Montgomery, Jr., T. Vreven, K. N. Kudin, J. C. Burant, J. M. Millam, S. S. Iyengar, J. Tomasi, V. Barone, B. Mennucci, M. Cossi, G. Scalmani, N. Rega, G. A. Petersson, H. Nakatsuji, M. Hada, M. Ehara, K. Toyota, R. Fukuda, J. Hasegawa, M. Ishida, T. Nakajima, Y. Honda, O. Kitao, H. Nakai, M. Klene, X. Li, J. E. Knox, H. P. Hratchian, J. B. Cross, C. Adamo, J. Jaramillo, R. Gomperts, R. E. Stratmann, O. Yazyev, A. J. Austin, R. Cammi, C. Pomelli, J. W. Ochterski, P. Y. Ayala, K. Morokuma, G. A. Voth, P. Salvador, J. J. Dannenberg, V. G. Zakrzewski, S. Dapprich, A. D. Daniels, M. C. Strain, O. Farkas, D. K. Malick, A. D. Rabuck, K. Raghavachari, J. B. Foresman, J. V. Ortiz, Q. Cui, A. G. Baboul, S. Clifford, J. Cioslowski, B. B. Stefanov, G. Liu, A. Liashenko, P. Piskorz, I. Komaromi, R. L. Martin, D. J. Fox, T. Keith, M. A. Al-Laham, C. Y. Peng, A. Nanayakkara, M. Challacombe, P. M. W. Gill, B. Johnson, W. Chen, M. W. Wong, C. Gonzalez, and J. A. Pople, Gaussian, Inc., Pittsburgh PA, (2001 and 2003).
- [3] CASTEP 4.2, Academic Version, Lincensed under the UKCP-MSI Agreement (1999), M. C. Payne, M. P. Teter, D. C. Allan, T. A. Arias and J. D. Joannopoulos, *Rev. Mod. Phys.*, **64**, 1045, (1992).
- [4] VASP 4.4.5 and 4.4.6, G. Kresse and J. Furthmüller, Vienna, Austria, (2003).  
G. Kresse and J. Furthmüller, *Comput. Mater. Sci.*, **6**, 15, (1996). G. Kresse and J. Furthmüller, *J. Phys. Rev. B*, **54**, 11169, (1996).
- [5] <http://www.chm.tu-dresden.de/edv/mopac7/mirror/mopac.html>
- [6] A. R. Leach, in “*Molecular Modelling, Principles and Applications*”, 2<sup>nd</sup> Ed., Pearson Education, Prentice Hall, England, 98, (2001).
- [7] A. Banerjee, N. Adams, J. Simons and R. Shepard, *J. Phys. Chem.*, **89**, 52, (1985).
- [8] J. Baker, *J. Comp. Chem.*, **7**, 385, (1985).
- [9] P. Culot, G. Dive, V. H. Nguyen and J. M. Ghuysen, *Theo. Chim. Acta.*, **82**, 189, (1992).

- [10] P. J. Stevens, J. F. Devlin, C. F. Chabalowski and M. J. Frisch, *J. Phys. Chem.*, **98**, 11623, (1994).
- [11] H. B. Schlegel, *J. Comput. Chem.*, **3**, 214, (1982).
- [12] <http://www.helix.cf.ac.uk/contact.html>
- [13] J. Foresman and Æ. Frisch, in “*Exploring Chemistry with Electronic Structure Methods*”, 2<sup>nd</sup> Ed., Gaussian Inc., (1995).
- [14] <http://www.tcm.phys.cam.ac.uk>
- [15] [http://www.cse.clrc.ac.uk/cmng/NETWORKS/UKCP/Castep\\_guide\\_2.0ps](http://www.cse.clrc.ac.uk/cmng/NETWORKS/UKCP/Castep_guide_2.0ps)
- [16] [http://www.ctm.uhp\\_nancy.fr/CherCheurs/Janos.Angyan/VaspManual/vasp.html](http://www.ctm.uhp_nancy.fr/CherCheurs/Janos.Angyan/VaspManual/vasp.html)
- [17] <http://www.cse.clrc.ac.uk/cmng/CRYSTAL/BenchmarksMPP/MPPmachines/tuning.html>
- [18] <http://www.cse.clrc.ac.uk/disco/dl-beowulfs.shtml#loki>
- [19] G. W. Watson, R. P. K. Wells, D. J. Willock and G. J. Hutchings, *J. Phys. Chem. B*, **104**, 6439, (2000).
- [20] Q. Ge and D. A. King, *J. Chem. Phys.*, **110**, 4699, (1999).
- [21] J. P. Perdew, J. A. Chevary, S. H. Vorto and K. A. Jackson, M. R. Pedersen, D. J. Singh and C. Frohais, *Phys. Rev. B*, **46**, 6671, (1992).
- [22] A. R. Leach, in “*Molecular Modelling, Principles and Applications*”, 2<sup>nd</sup> Ed., Pearson Education, Prentice Hall, England, 121, (2001).
- [23] C. G. Broyden, *J. Inst. Math. Appl.*, **6**, 76, (1970).
- [24] R. Fletcher, *Comput. J.*, **13**, 317, (1970).
- [25] D. Goldfarb, *Math. Comp.*, **24**, 23, (1970).
- [26] D. F. Shanno, *Math. Comp.*, **24**, 647, (1970).
- [27] A. R. Leach, in “*Molecular Modelling, Principles and Applications*”, 2<sup>nd</sup> Ed., Pearson Education, Prentice Hall, England, 262, (2001).
- [28] A. R. Leach, in “*Molecular Modelling, Principles and Applications*”, 2<sup>nd</sup> Ed., Pearson Education, Prentice Hall, England, 268, (2001).
- [29] A. R. Leach, in “*Molecular Modelling, Principles and Applications*”, 2<sup>nd</sup> Ed., Pearson Education, Prentice Hall, England, 121, (2001).
- [30] D. Vanderbilt, *Phys. Rev. B*, **41**, 7892, (1990).
- [31] G. Kresse and D. Joubert, *Phys. Rev. B*, **59**, 1758, (1999).
- [32] P. E. Blöchl, *Phys. Rev. B*, **50**, 17953, (1994).
- [33] H. J. Monkhorst and J. D. Pack, *Phys. Rev. B*, **13**, 5188, (1976).

- [34] M. Methfessel and A. Paxton, *Phys. Rev. B*, **49**, 3616, (1989).
- [35] G. A. Somorjai, in “*Surface Chemistry and Catalysis*”, John Wiley & Sons, New York, (1994).
- [36] W. J. van Rensburg, M. Sc. Dissertation, Cardiff University, Park Place, Cardiff, S. Wales, (2002).
- [37] G. W. Watson, R. P. K. Wells, D. J. Willock and G. J. Hutchings, *J. Phys. Chem. B*, **105**, 4889, (2001).
- [38] S. H. Vosko, L. Wilk and M. Nusair, *Can. J. Phys.*, **58**, 1200, (1980).
- [39] G. Mills, H. Jonsson and G. K. Schenter, *Surf. Sci.*, **324**, 305, (1995).
- [40] H. Jonsson, G. Mills and K. W. Jacobsen, in “*Classical and Quantum Dynamics in Condensed Phase Simulations*”, B. J. Berne, G. Ciccotti and D. F. Coker (Editors), World Scientific, (1998).

## ***Chapter 5***

*A Semi-Empirical and Ab Initio Study of the  
Conformational Behaviour of Cinchonidine  
and its Interaction with Ethyl Pyruvate  
and Butane-2,3-dione*

## 5.0. Introduction

Chapter 2 (section 2.2) of this thesis illustrated the continuing efforts by various groups over the past years to try and understand the enantioselectivity achieved in the hydrogenation of  $\alpha$ -ketoesters in the presence of platinum modified by cinchona alkaloids, first reported by Orito *et al.* [1]. It is well documented that in several reactions using either Pt-cinchona [2] or Pd-cinchona [3] catalysts, characteristically high *ees* (90-95%) have been observed accompanied with an initial enhancement in the rate of reaction. Consequently, the high yields and optical activities observed have resulted in the reaction being viewed as a model for heterogeneous enantioselective hydrogenation catalysis.

The most important parameters affecting *ee* (Chapter 1, equation 1.1) have been identified and reported in a number of studies [4,5]. With respect to the origin of *ee*, it is widely accepted that in these catalyst systems the cinchona alkaloids provide the source of chirality and are strongly adsorbed to form a chiral environment on the metal surface for the hydrogenation reaction to proceed. However, it is trying to understand the actual nature of the *ed* on the metal surface that is emerging to be the most challenging aspect of this system and as a result a full mechanistic description of the reaction has yet to be achieved.

With reference to either Mt- or EtPy hydrogenation reactions a number of mechanistic models have been proposed to interpret the metal-reactant-chiral modifier interaction responsible for the *ee* and rate enhancement (Chapter 2, section 2.2.7). Recent studies suggest that good enantioselectivity is only achieved once the adsorption mode of the reactant and the cinchona alkaloid appropriately interact during the hydrogen uptake process in the enantio-discriminating step. With regards to this mechanism, the enantioselection cannot be deduced from *in situ* adsorption studies and as a result extensive surface science and H/D exchange experiments have been conducted to shed light on the adsorption mode of CD [6-9] and its “anchoring” quinoline moiety [8,10,11] on Pt surfaces.

At present, the most widely accepted mode of adsorption for CD on Pt surfaces is a parallel orientation of the quinoline group with the surface in a  $\pi$ -bonded species, as evident from *in situ* attenuated total reflection infrared (ATR-IR) investigations [12]. Recently, a combined *ab initio* and NMR spectroscopic investigation of CD in different

solvents highlighted the stability of four different conformers of CD and found that the Open(3) (Chapter 2, section 2.2.12, figure 2.8, structure A2) structure is energetically favoured [13]. Based on these two pieces of evidence it is thought that the Open(3) form of the modifier is the most likely conformation on the surface of the active catalyst. With respect to the origin of *ed* a number of studies have systematically varied the structure of the CD to illustrate that the quinuclidine N functionality is most crucial, with the O-H group displaying only a marginal effect [4,5].

The adsorption mode of  $\alpha$ -ketoesters on metal surfaces have been deduced by various techniques, two distinct modes exist either an “upright mode” significant on clean surfaces or a “tilted” orientation under an atmosphere of hydrogen (Chapter 2, section 2.2.15). As with CD,  $\alpha$ -ketoesters can easily interconvert and adsorb either in their *s-cis* or *s-trans* conformations (figure 5.1) [14].

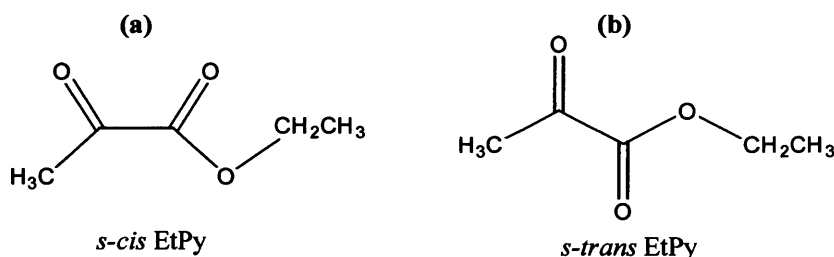


**Figure 5.1:** Geometric isomers of EtPy: (a) *s-cis* and (b) *s-trans*.

In response to the large body of experimental data, a number of different mechanisms have been hypothesised to explain the enantio-differentiating complex formed between the  $\alpha$ -ketoesters and the cinchona alkaloids [15,16] (Chapter 2, sections 2.2.7-2.2.11). One of the most significant and adaptable models is that proposed by Baiker *et al.* [17] (Chapter 2, section 2.2.11), which essentially predicts the chirality of the main product by calculating the relative stability of bi-molecular reactant-modifier complexes to predict the preference for (*R*)- or (*S*)-products. One of the main features of the model, crucial for *ed* is the direction from which the hydrogen approaches the *keto* C of the  $\alpha$ -ketoester during the uptake process. In common with the template model [18] it is assumed that H approaches from the Pt surface side, in common with mechanistic beliefs for the hydrogenation reactions of ethylene and acetylene on Ni [19].

Although the above model appears to interpret the *ed* observed in the hydrogenation of  $\alpha$ -ketoesters and related reactions [20] a definitive mechanism is still not resolved,

partly because, on a molecular level the system is still not fully understood. Since the enantioselective reaction is highly complex it is extremely difficult to gain such information experimentally. As a result the desired molecular information can only be gained by the use of theoretical calculations. In order for the calculations to be feasible a number of approximations are included as it would be uneconomical to model the whole system *i.e.* the supported Pt/CD catalyst flushed with hydrogen and reactant under the desired solvent, as many degrees of freedom would be involved.

The majority of the theoretical studies have focussed on the specific interactions between the reactant and modifier and modelled the resulting complexes in the gas-phase and in solution. An example of this is the work conducted by Baiker *et al.* [21], which used *ab initio* methods to investigate the interaction complexes between  $\text{CDH}^+$  and MtPy involved in hydrogenation over Pt catalysts (Chapter 2, section 2.2.11).

In view of the above study and the relevance of the approximate structures of the enantio-differentiating intermediate complexes proposed in the mechanistic models (Chapter 2, sections 2.2.8-2.2.11), the present work also focuses on molecular modelling of the substrate-modifier interactions involved in the enantioselective hydrogenation of EtPy over CD modified Pt and extends this modelling to butane-2,3-dione hydrogenation. As the structure of the intermediate complexes are determined by the modifier and pyruvate conformations, their adsorption modes and their interaction on the Pt surface, our calculations are first performed in isolation to analyse the conformational behaviour of CD. The most stable configurations are then protonated to form  $\text{CDH}^+$  species which then interact *via* hydrogen bonding with the EtPy in either the *s-cis* and *s-trans* conformations (as indicated by Baiker's earlier work [21]) to form the diastereomeric complexes. Upon geometry optimisation the stability of the reactive complexes on the proposed flat Pt(111) surface and whether they preferentially favour either the (*R*)- or (*S*)-product lactates are identified.

The enantioselective hydrogenation of butane-2,3-dione over the same modified catalyst system as  $\alpha$ -ketoesters is a relatively unexplored system, and thus, it is not surprising then to find a lack of mechanistic studies reported in the literature (Chapter 2, section 2.3). Due to the experimental similarities between EtPy and butane-2,3-dione, Wells *et al.* [22] have proposed the same complex formation between CD and the diketone to account for the enantio-discrimination, particularly, towards the first hydrogenated products of (*R*)- and (*S*)-3-hydroxybutan-2-one. With regards to this

view, the appropriate substrate-modifier complexes under acidic solvents are simulated in this work using the same methodology as proposed for the analogous EtPy structures.

### 5.1. Theoretical Calculations

As it is clearly evident that four or more stable conformers of CD exist, our conformational analysis is conducted using the method specified in reference 23 *i.e.* starting geometries of CD for optimisation are constructed with the rigid quinoline and quinuclidine parts specified in the corresponding Closed and Open configurations. These geometries were constructed and visualised using the graphical Cerius<sup>2</sup> interface [24]. Starting structures for the 44 atom CD conformers were produced using the “CLEAN” function for the Cerius<sup>2</sup> models prior to higher theory level geometry optimisation calculations. CLEAN produces structure with standard bond lengths and angles. Initial gas-phase CD conformers were obtained by performing calculations using MOPAC [25].

The initial geometries of the CD conformers (as with all other calculations in this thesis) were specified in Cartesian coordinates. The PM3 Hamiltonian was used in conjunction with the EF and QA routine to search for the minimum geometry in the optimisation [26]. All calculations were carried out with the “PRECISE” criteria specified. Refer to Chapter 4, section 4.1 for a full discussion of the computational parameters used in the MOPAC calculations.

The MOPAC optimised structures of the conformers were then used as the start point for *ab initio* calculations, which were performed using the GAUSSIAN [27] software. Two versions of the program, GAUSSIAN98 [28] and '03 [29] were used for the computations. The level of theory applied to calculate the structure optimisations was HF combined with the DFT exchange-correlation functional of B3LYP [30,31] with the 6-31G(d) basis set. The DFT calculations were solved self-consistently ensuring that all degrees of freedom were fully optimised. A thorough account of the methodology applied is provided in Chapter 4, section 4.2.

With the resulting GAUSSIAN optimised CD conformers at their minimum-energy, a set of complexes between protonated CD and EtPy were completely optimised using the same calculation parameters as above. No corrections were made for the basis set superposition error (BSSE) [32], as it has recently been shown that for hydrogen-bonded complexes calculated at the HF level using medium sized basis sets such as 6-



31G(d,p) the BSSE and the correlation correction to the binding energy cancel quite evenly [33].

The 1:1 complexes were designed so that the main proposed interaction between the two molecules *i.e.* hydrogen bonding *via*  $\text{N}^+-\text{H}\cdots\text{O}$  interaction (Baiker [17,34]) would be favoured. For the two Closed and two Open CD conformers, four complexes each were optimised, one starting with the *s-trans* EtPy in an arrangement that would lead to the pro (*R*) complexes (*keto* carbonyl of the pyruvate directed towards aromatic moiety of CD, figure 5.2(a)) and another with an arrangement which would lead to the pro (*S*) complexes (ester carbonyl of the pyruvate directed towards aromatic moiety of CD), refer to figure 5.2(b). A further two complexes arise when the EtPy is modelled in the equivalent *s-cis* configurations.

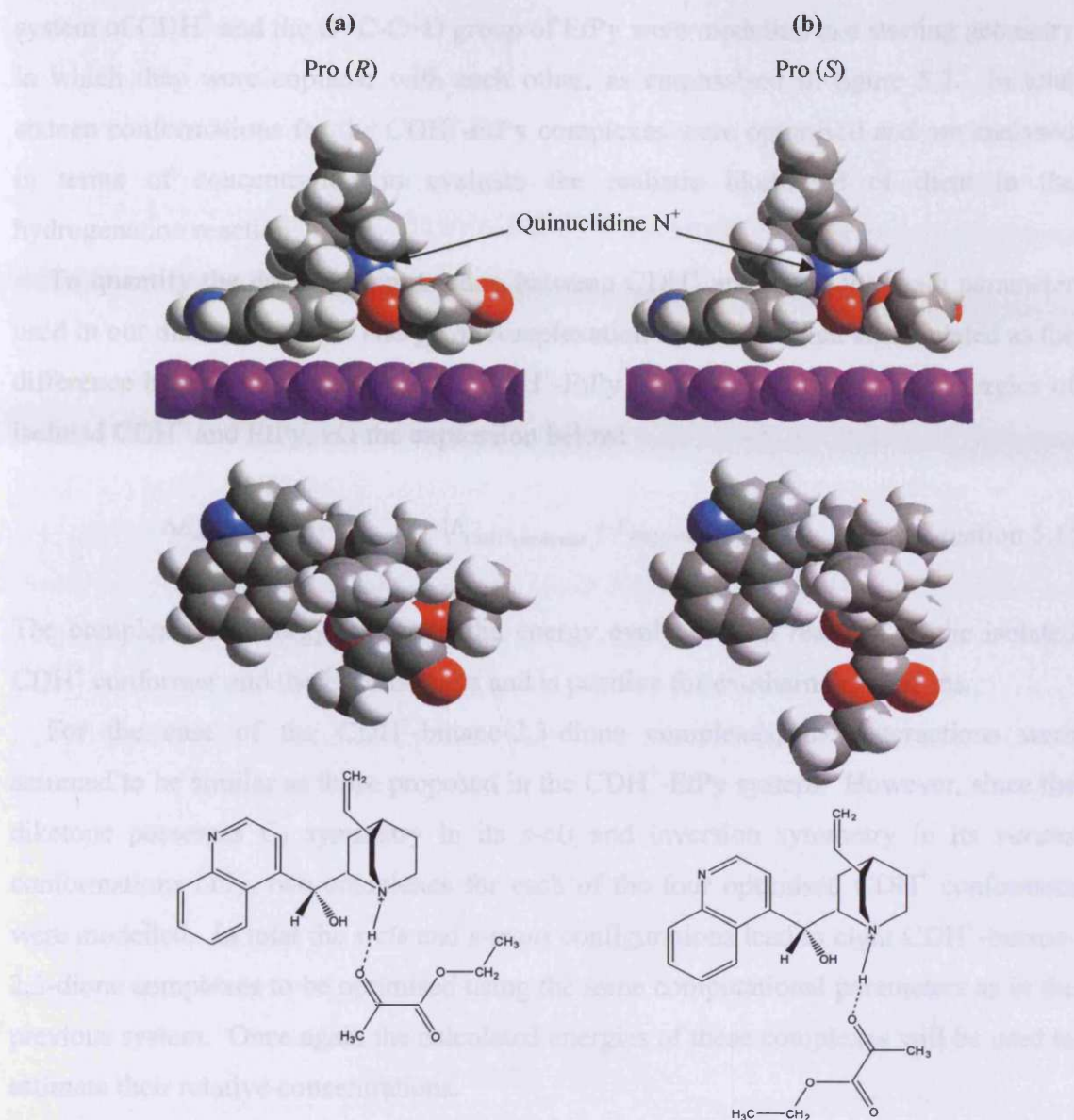


**Figure 5.2:** Space filling models for the proposed diastereomeric complexes between Open(3) CDH<sup>-</sup> EtPy leading to (a) R- and (b) S-lactate on hydrogenation. Note that the corresponding complexes involving the *s*-cis conformation of EtPy, can yield the same products. Models represent the starting configurations for geometry optimisation calculations and are illustrated from two different angles. The first depicts a side view of the complex over an “ideal” Pt(111) surface, which is included only for illustration and is not present in the calculations. Note that CD adsorbs via  $\pi$ -bonding of the quinoline ring on the metal surface. The second illustrates the top view of the complex and the chemical drawing representations at the bottom of the figure are provided for clearer definition of the attractive interaction between the modifier and the reactant. Molecular atoms are colour coded: Pt purple, H white, C grey, O red and N blue.

To simulate the steric constraints imposed by the Pt surface *i.e.* to assume parallel adsorption as implied by Wells *et al.* [18] and Baiker *et al.* [16], the quinoline ring

system of  $\text{CDH}^+$  and the  $\text{O}=\text{C}-\text{C}=\text{O}$  group of EtPy were modelled in a starting geometry in which they were coplanar with each other, as emphasised in figure 5.2. In total sixteen conformations for the  $\text{CDH}^+$ -EtPy complexes were optimised and are analysed in terms of concentration to evaluate the realistic likelihood of them in the hydrogenation reaction.

To quantify the degree of interaction between  $\text{CDH}^+$  and EtPy, the main parameter used in our discussion is the energy of complexation/reaction, which is calculated as the difference between the energy of the  $\text{CDH}^+$ -EtPy complex and the sum of energies of isolated  $\text{CDH}^+$  and EtPy, *via* the expression below:

$$\Delta E_{\text{complexation}} = - \left( E_{\text{complex}} - (E_{\text{CDH}^+ \text{ conformer}} + E_{\text{EtPy isomer}}) \right) \quad (\text{Equation 5.1})$$

The complexation energy is simply the energy evolved upon reaction of the isolated  $\text{CDH}^+$  conformer and the EtPy isomers and is positive for exothermic reactions.

For the case of the  $\text{CDH}^+$ -butane-2,3-dione complexes, the interactions were assumed to be similar as those proposed in the  $\text{CDH}^+$ -EtPy system. However, since the diketone possesses  $\text{C}_2$  symmetry in its *s-cis* and inversion symmetry in its *s-trans* conformations only, two complexes for each of the four optimised  $\text{CDH}^+$  conformers were modelled. In total the *s-cis* and *s-trans* configurations lead to eight  $\text{CDH}^+$ -butane-2,3-dione complexes to be optimised using the same computational parameters as in the previous system. Once again the calculated energies of these complexes will be used to estimate their relative concentrations.

## 5.2. Results

### 5.2.1. Conformational Analysis of Cinchonidine

As emphasised earlier (Chapter 2, section 2.2.12), CD (figure 5.3(a)) shows a rich conformational behaviour. Conformational calculations using a combination of HF and DFT approaches performed by Bürgi and Baiker [13] illustrate how the gross conformation of the cinchona alkaloids is determined by the two torsional angles  $\tau_1$ :  $\text{C}_3-\text{C}_4-\text{C}_9-\text{C}_8$  and  $\tau_2$ :  $\text{C}_4-\text{C}_9-\text{C}_8-\text{N}_1$ , which defines the spatial relationship between the quinoline and quinuclidine ring systems. Other important degrees of freedom were found to include the orientation of the O-H and the vinyl groups and the left- or right-

handed screw of the quinuclidine ring with respect to the quinoline moiety, which ultimately determines the conformations: Closed(1), Closed(2) *etc.* The stable conformers were calculated to be those with the hydroxyl H pointing away from the quinuclidine ring, which itself adopts a left-handed screw. The conformer in which the C=C double bond of the vinyl group (of the quinuclidine) was present in the *s-cis* arrangement with the C<sub>3'</sub>-H bond was found to agree with the crystal structure of CD [35].

The conformational analysis of CD, following the methodology described earlier (section 5.1) resulted in four fully optimised minimum-energy structures for both MOPAC and GAUSSIAN calculations. The optimised geometries of the GAUSSIAN98 (Open(3) and (4)) and '03 (Closed(1) and (2)) CD conformers are shown in figure 5.3(b). As expected the Closed conformers possess the lone pair of the quinuclidine N pointing towards the quinoline ring and the Open structures have this lone pair pointing away. Table 5.1 compares the semi-empirical and *ab initio* relative energies and dihedral angles as defined in figure 5.3(a), for these CD conformations.

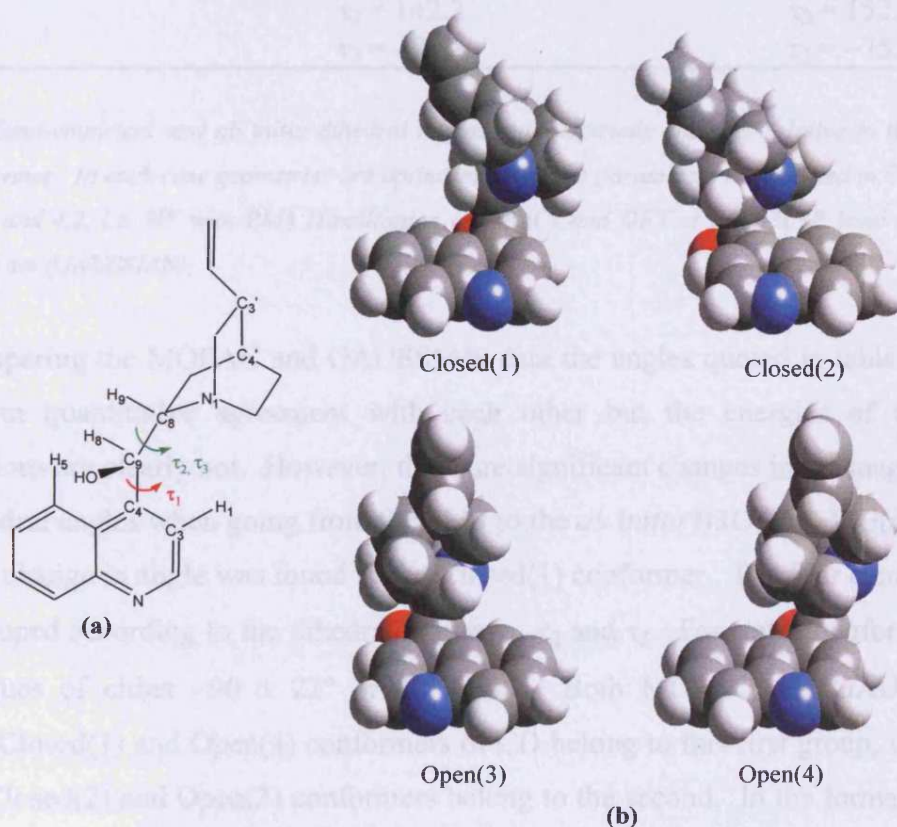


**Figure 5.3:** (a) Atom labelling of CD and definition of  $\tau_1$ ,  $\tau_2$ , and  $\tau_3$  dihedral angles. (b) Space filling representation of the four most stable conformers of CD. Geometries are fully optimised at the DFT level



as specified in Chapter 4, section 4.2 using a 6-31G(d) basis set in GAUSSIAN98 and '03 software. Molecular atoms are colour coded: H white, C grey, O red and N blue.

Conformation of CD	MOPAC7		GAUSSIAN98 & '03	
	Relative Energy (kJ mol <sup>-1</sup> )	Dihedral Angle (°) $\tau_1 = \text{C}_3\text{-C}_4\text{-C}_8\text{-C}_9$ $\tau_2 = \text{C}_4\text{-C}_9\text{-C}_8\text{-N}_1$ $\tau_3 = \text{H}_1\text{-C}_9\text{-C}_8\text{-H}_2$	Relative Energy (kJ mol <sup>-1</sup> )	Dihedral Angle (°) $\tau_1 = \text{C}_3\text{-C}_4\text{-C}_8\text{-C}_9$ $\tau_2 = \text{C}_4\text{-C}_9\text{-C}_8\text{-N}_1$ $\tau_3 = \text{H}_1\text{-C}_9\text{-C}_8\text{-H}_2$
Closed(1)	0.0	$\tau_1 = -68.1$ $\tau_2 = 35.2$ $\tau_3 = -150.5$	6.7	$\tau_1 = -105.7$ $\tau_2 = 57.8$ $\tau_3 = -175.9$
Closed(2)	2.4	$\tau_1 = 67.7$ $\tau_2 = 64.7$ $\tau_3 = -172.7$	9.5	$\tau_1 = 83.4$ $\tau_2 = 68.5$ $\tau_3 = -168.4$
Open(3)	11.5	$\tau_1 = 75.2$ $\tau_2 = 169.4$ $\tau_3 = -64.5$	0.0	$\tau_1 = 102.1$ $\tau_2 = 152.5$ $\tau_3 = -79.1$
Open(4)	16.6	$\tau_1 = -97.7$ $\tau_2 = 142.2$ $\tau_3 = -88.4$	11.2	$\tau_1 = -87.3$ $\tau_2 = 152.1$ $\tau_3 = -75.4$

**Table 5.1:** Semi-empirical and ab initio dihedral angles and electronic energies relative to the lowest energy conformer. In each case geometries are optimised using the parameters as specified in Chapter 4, sections 4.1 and 4.2, i.e. HF with PM3 Hamiltonian (MOPAC) and DFT at the B3LYP level with a 6-31G(d) basis set (GAUSSIAN).

On comparing the MOPAC and GAUSSIAN data the angles quoted in table 5.1 are generally in quantitative agreement with each other but the energies of the CD conformations are clearly not. However, there are significant changes in the magnitudes of the dihedral angles when going from the PM3 to the *ab initio* B3LYP 6-31G(d) level, the largest change in angle was found in the Closed(1) conformer. The four conformers can be grouped according to the dihedral angles  $\tau_1$ ,  $\tau_2$  and  $\tau_3$ . For stable conformers  $\tau_1$  adopts values of either  $-90 \pm 22^\circ$  or  $82 \pm 20^\circ$ . Both MOPAC and GAUSSIAN optimised Closed(1) and Open(4) conformers of CD belong to this first group, whereas the other Closed(2) and Open(3) conformers belong to the second. In the former group conformations, the O-H functionality is directed towards the quinoline ring H<sub>5</sub> atom, while the latter structures possess the O-H towards the H<sub>1</sub> atom. With regards to the optimised geometries of both theoretical methods four minima are found in  $\tau_2$  at  $57 \pm$

22° and correspond to the Closed conformers, whilst the angle for the Open conformers are at  $154 \pm 15^\circ$ . The calculated  $\tau_3$  angles for the minima are observed at  $-77 \pm 12^\circ$  for the Open structures whereas the largest values of  $-92 \pm 84^\circ$  are evident for the Closed(1) and (2) conformations.

On comparing the MOPAC and GAUSSIAN structures against each other it appears that the greatest discrepancies between the geometries exist in the Closed(1) conformer as all three dihedral angles are grossly underestimated by the semi-empirical calculation. The largest difference in the three dihedral angles for this conformation was found to be  $-37.6^\circ$  for  $\tau_1$ . However, the geometries for the Closed(2) structure agree reasonably well, as the  $\tau_2$  and  $\tau_3$  angles differ by no more than  $4.3^\circ$  with  $\tau_1$  differing by approximately  $16^\circ$  indicating the C<sub>4</sub>-C<sub>9</sub>-C<sub>8</sub> backbone of the CD connecting the quinuclidine part with the quinoline ring to be more “upright” in the GAUSSIAN structure than in the MOPAC model. For the Open conformers, the MOPAC Open(4) geometry is in better agreement with that predicted by the GAUSSIAN program than the Open(3) structure as the differences between the three structure determining angles are less.

Conformation of CD	Literature Values	
	Relative Energy (kJ mol <sup>-1</sup> )	Dihedral Angle (°) $\tau_1 = \text{C}_3\text{-C}_4\text{-C}_8\text{-C}_9$ $\tau_2 = \text{C}_4\text{-C}_9\text{-C}_8\text{-N}_1$ $\tau_3 = \text{H}_1\text{-C}_9\text{-C}_8\text{-H}_2$
Closed(1)	(1) = 6.0	$\tau_1 = -107.0$
	(2) = 4.6	$\tau_2 = 57.5$
	(3) = 5.3	$\tau_3 = -176.8$
Closed(2)	(1) = 9.0	$\tau_1 = 80.4$
	(2) = 7.7	$\tau_2 = 65.3$
	(3) = 7.7	$\tau_3 = -172.5$
Open(3)	(1) = 0.0	$\tau_1 = 101.4$
	(2) = 0.0	$\tau_2 = 153.6$
	(3) = 0.0	$\tau_3 = -78.3$
Open(4)	(1) = 13.9	$\tau_1 = -89.3$
	(2) = 13.8	$\tau_2 = 150.1$
	(3) = 11.6	$\tau_3 = -77.5$

**Table 5.2:** Literature electronic energies and dihedral angles are calculated relative to the stable Open(3) CD conformer at the ab initio HF level using a (1) 6-31G\*\* and (2) 6-31+G\* basis set,

respectively, and at the density functional level (B3LYP) using a (3) 6-31+G\* basis set employed in GAUSSIAN94, as specified in reference 13.

To further validate the structures of the CD conformers, comparison is made against angles quoted in the literature. One of the best studies to date is the combined NMR and *ab initio* investigation of the conformational behaviour of CD in different solvents by Bürgi and Baiker [13]. Their calculations of the gas-phase structure revealed that in the two-dimensional conformational subspace of  $\tau_1$  and  $\tau_2$ , six minima corresponding to six conformers of CD exist on the PES [36]. Each of these structures were fully optimised at the *ab initio* HF level using the 6-31G\*\* basis set. Four of these conformations were found to be considerably more stable than the other two: Closed(1) and (2) and Open(3) and (4) and thus, their calculated dihedral angles (table 5.2) previously found to be in qualitative agreement with earlier values predicted by the MM2 force field and *ab initio* HF 3-21G method [37,38], are used for comparison.

Thus, on evaluating the CD conformers presented here against the torsional angles measured in the above study, it generally appears that the GAUSSIAN angles for all conformations compare well, whereas the MOPAC angles vary considerably. For the GAUSSIAN models the three dihedral angles measured to the nearest degree are within  $\pm 1^\circ$  for Closed(1),  $\pm 4^\circ$  for Closed(2),  $\pm 1^\circ$  and  $\pm 2^\circ$  for the Open(3) and (4), respectively compared to the corresponding literature angles. These values are considerably smaller than those of MOPAC differences of  $\pm 39^\circ$  (due to the large  $\tau_1$  difference) and  $\pm 13^\circ$  for the Closed structures and  $\pm 26^\circ$  and  $\pm 11^\circ$  for the Open forms. From this geometry analysis it appears that the GAUSSIAN98 and '03 Open(3) followed by the Closed(1), Open(4) and Closed(2) conformers of CD are best modelled against the equivalent literature GAUSSIAN94 structures.

To determine the order of stability of the four CD conformers the energies of the structures are analysed, obviously the conformation possessing the largest negative energy would represent the most stable structure. Thus, the relative energies in relation to this structure are calculated in the MOPAC and GAUSSIAN series and are provided in table 5.1. The first thing to note is the difference in the order of stability of the conformers predicted by the two computational methods. MOPAC predicts the Closed(1) structure to be most stable followed by Closed(2) and Open(3) with the Open(4) CD the least thermodynamically stable. The Closed structures differ by 2.4 kJ mol<sup>-1</sup> whereas the energy gap is much larger at 5.1 kJ mol<sup>-1</sup> for the Open conformers.

In contrast, the order of stability calculated by GAUSSIAN follows the trend Open(3), Closed(1), Closed(2) and Open(4). In agreement with the MOPAC relative energies, the Closed conformers differ by  $2.8 \text{ kJ mol}^{-1}$  whereas the stabilisation of the Open(3) is calculated at  $11.2 \text{ kJ mol}^{-1}$  compared to the alternative Open geometry. Although the two methods predict a different order of stability, the Open(4) structure is found to be the least stable conformer of CD by both techniques.

As with the geometry, the stability trends of our conformations are verified against literature models. A recent study by Aranda *et al.* [39] (Chapter 2, section 2.2.12) used the same PM3 model as in the MOPAC calculations to highlight the stability of four major conformers of CD from nine minima located on its PES. The four most stable conformers found were in the order Closed(2), Closed(3), Open(3) followed by Closed(1). (Note that the Closed(3) structure is another Closed conformation ignored in our calculations as earlier studies using a higher level of theory have optimised this as an unstable high-energy geometry [40]). Although the absolute trend does not correlate with our MOPAC results (order of stability Closed(1), Closed(2), Open(3) and Open(4)), the Closed structures in both cases are found to be more stable than the Open forms.

Referring back to the work of Bürgi and Baiker [13], the GAUSSIAN98 and '03 energies for the CD conformers can be confirmed, as not only were the same four conformations optimised using the earlier GAUSSIAN code (GAUSSIAN94) but in addition to the degree of theory mentioned earlier (HF 6-31G\*\*), the authors investigated the influence of diffuse basis functions by performing single-point calculations using a 6-31+G\* basis set. As with our calculations, they also tested the density functional hybrid method introduced by Becke [30] where the non-local correlation is provided by the LYP expression [31], thus making it an ideal study for comparison against our work. The relative calculated electronic energies converted from  $\text{kcal mol}^{-1}$  (units employed by the authors) into  $\text{kJ mol}^{-1}$  for the four CD conformers modelled using theory levels HF 6-31G\*\*, HF 6-31+G\* and B3LYP 6-31+G\* are provided in table 5.2.

Regardless of the level of theory used the literature energies predict the same order of stability that is, the Open(3) is most stable followed by the Closed(1), Closed(2) and lastly Open(4) as observed in the GAUSSIAN calculations presented here. The relative energies highlight the fact that increasing the basis sets or changing from HF to DFT has only minor effects on the gas-phase relative energies. Note that only the



corresponding conformers 1-3 have been observed in NOESY experiments for some quinine and quinidine derivatives [41].

On comparison, the energy of our Closed(1) structure relative to the Open(3) was found to be  $1.4 \text{ kJ mol}^{-1}$  greater than the corresponding literature value, for Closed(2) the difference was larger at  $1.8 \text{ kJ mol}^{-1}$  and for the Open(4) conformer the difference was relatively insignificant at  $0.4 \text{ kJ mol}^{-1}$ . One possible reason to account for these differences, is the fact that a slightly different basis set incorporating a diffuse function is used in the reference work (6-31+G\*) compared to the 6-31G(d) basis set used in this study.

Despite these minor differences our GAUSSIAN calculations have managed to quantitatively and structurally model the four most stable conformers of CD and highlight the thermodynamic importance of the Open(3) structure. As a consequence, the results of the more sophisticated *ab initio* DFT calculations demonstrate how the semi-empirical method of PM3 is good for predicting rough estimates for a geometry but that accuracy is sacrificed for CPU time, thus, justifying its use for generating refined starting structures for the higher level calculations.

All of the optimised CD conformations *i.e.* the Closed(1)-(2) and Open(3)-(4) can be involved in the formation of the modifier-substrate complex, as emphasised by the modifier-MtPy complex modelling studies of Margitfalvi *et al.* [40]. In the following section the corresponding EtPy complexes involving the  $\text{CDH}^+$  conformers are investigated with particular emphasis on the Open(3) structures.

### 5.2.2. Interaction Between Cinchonidine and Ethyl Pyruvate

The interaction between CD and EtPy was studied by calculation of sixteen different complexes between these two molecules. We first identified the possible *s-cis* and *s-trans* conformation of EtPy and then distinguished the possible structures that would lead to the pro (*R*) and pro (*S*) complexes (figure 5.2). In each case the quinuclidine N atom of all four CD conformers was protonated, and then the EtPy either in its *s-cis* or *s-trans* conformation and with the *keto* carbonyl group ( $-\text{COCH}_3$ ) of EtPy facing either towards (pro (*R*)) or away (pro (*S*)) from the quinoline ring of the modifier was docked, in a position where the most relevant interactions assumed to act between them would be strengthened.

For the complexes involving the Closed  $\text{CDH}^+$  conformers the pro (*R*) was distinguished from the pro (*S*) by the way in which the EtPy was orientated, for Closed(1) $\text{H}^+$  the pro (*R*) has the *keto* carbonyl docked over the carbon 6-ring of the quinoline of the  $\text{CDH}^+$ , whereas in the pro (*S*) it is orientated over the quinoline N atom of the  $\text{CDH}^+$ , the vice versa of this labels the pro (*R*) and pro (*S*) complexes involving the Closed(2) conformer of  $\text{CDH}^+$ .

Once protonated the quinuclidine N can act as an electrophile otherwise it can interact *via* nucleophilic attack with the half-hydrogenated state of the reactant as proposed under solvent conditions such as toluene [42]. The formation of a reactant-modifier 1:1 complex is supported by all proposed models *i.e.* Wells *et al.* [18], Baiker *et al.* [5], Augustine *et al.* [43] and Margitfalvi *et al.* [44], however, the actual  $\text{N}^+\text{-H}\cdots\text{O}$  type interaction (H-bond) between the protonated CD species and the *keto* carbonyl O atom of the pyruvate ester was first devised by Baiker *et al.* [17,34].

In the complexes presented here we assume the parallel adsorption of CD (favoured in all models [45] with the exception of Margitfalvis' work [40,46]) and EtPy onto a Pt surface so that H uptake for *ed* could occur from the surface side (theorised by Wells *et al.* [18] and defended by Baiker *et al.* [37]). (Referring back to figure 5.2(a), the starting geometry for the complex clearly depicts the EtPy to be coplanar with the CD quinoline ring moiety, so as to accommodate this proposed parallel adsorption).

Once the complexes were modelled in the desired orientations they were fully optimised at the B3LYP 6-31G(d) level, and their resulting energies analysed to identify their relative thermodynamic stabilities as well as their relative concentrations in low dielectric solvents.

### 5.2.3. Analysis of Diastereomeric Complexes of Protonated Cinchonidine and Ethyl Pyruvate

By changing the dihedral angle  $\text{O}=\text{C}-\text{C}=\text{O}$  EtPy can adopt either the *s-cis* or *s-trans* conformation (figure 5.1). Our DFT optimisation calculations of both molecules showed how in the gas-phase ( $\epsilon_r = 1.0$ ) the energy difference between them is relatively small at roughly  $6.5 \text{ kJ mol}^{-1}$  with the *s-trans* conformer being slightly more stable. These results are in excellent agreement with the *ab initio* study of Ferri, Bürgi and Baiker [14], which calculated this difference to be approximately  $6.8 \text{ kJ mol}^{-1}$  with the

relative abundance of the *s-trans* to be 93.9% in relation to the *s-cis* EtPy. Note that the discrepancies in the values correspond to the accuracy employed in the calculations, the literature calculations were performed at the DFT level (B3PW91) using a 6-31++G(d,p) basis set, with the introduction of a second polarisation function the theory level is slightly more sophisticated than the level of DFT used in these calculations (B3LYP 6-31G(d)).

As with the conformation of CD (Chapter 2, section 2.2.12), solvent effects can greatly influence the distribution of the geometric isomers of EtPy. In the aforementioned study it was stated that at room temperature both conformers coexist with the *s-trans* conformer being predominant in apolar solvents (as reinforced by our results). However, under conditions of polar solvents, such as acetone, the stability of *s-cis* EtPy increases due to its larger dipole moment (4.99 vs. 1.54 D) and thus increases its resulting fraction making it comparable to the *s-trans* EtPy. The addition of H-bonding with alcoholic solvents is also thought to stabilise the *s-cis* conformer.

In our calculations the CD conformers are initially protonated to simulate the resulting influence of a polar solvent such as acetic acid (in which the highest optical yield for  $\alpha$ -ketoester hydrogenation has been reported [45]), and as a consequence one of the aims of the work is to establish if the *s-cis* (as predicted in the isolated solvent study above [14]), is stabilised in contrast to the *s-trans* EtPy when interacting with the  $\text{CDH}^+$  modifier.

Table 5.3 gives the calculated complex energies for all sixteen modifier-EtPy combinations. The gas-phase energies of the isolated complexes are calculated relative to the most thermodynamically stable complex labelled the pro (*R*) structure in which the Open(3) conformer of  $\text{CDH}^+$  interacts with the EtPy in its *s-cis* form. The configuration of this diastereomeric complex is analogous to the structure illustrated in figure 5.2(a), and for this analysis is appropriately referenced to zero energy. The corresponding complexation energies for the modifier-EtPy intermediates are calculated using equation 5.1, for which the appropriate energy of the protonated CD conformer and isomer of EtPy is used. Note that the same proton affinity is assumed for all conformations of CD. Using the equations of the kinetic model provided in Appendix A, the complexation energies can be used to theoretically calculate the relative concentrations of the species in a given sample, and thus, the energetic difference

between the two most populated/concentrated diastereomeric complexes (represented as  $[A]$  and  $[B]$  in equation 5.2) used to predict the expected  $ee$ .

$$ee = \frac{([A] - [B])}{([A] + [B])} \times 100 \quad (\text{Equation 5.2})$$

Reactant Components and Diastereomeric Complex	Gas-Phase Relative Energy (kJ mol <sup>-1</sup> )	Absolute Complexation Energy (kJ mol <sup>-1</sup> )	Concentration of Reactant Components and Diastereomeric Complex
Closed(1) CD	6.7		0.06
Closed(2) CD	9.5		0.02
Open(3) CD	0.0		0.91
Open(4) CD	11.2		0.01
Closed(1) CDH <sup>+</sup>	2.9		0.22
Closed(2) CDH <sup>+</sup>	6.7		0.05
Open(3) CDH <sup>+</sup>	0.0		0.72
Open(4) CDH <sup>+</sup>	10.6		0.01
<i>s-cis</i> EtPy	6.5		0.07
<i>s-trans</i> EtPy	0.0		0.93
Pro ( <i>R</i> ) Closed(1)H <sup>+</sup> - <i>s-cis</i> EtPy	10.2	99.4	8.72×10 <sup>14</sup>
Pro ( <i>S</i> ) Closed(1)H <sup>+</sup> - <i>s-cis</i> EtPy	12.9	96.7	2.94×10 <sup>14</sup>
Pro ( <i>R</i> ) Closed(1)H <sup>+</sup> - <i>s-trans</i> EtPy	31.8	71.4	1.53×10 <sup>11</sup>
Pro ( <i>S</i> ) Closed(1)H <sup>+</sup> - <i>s-trans</i> EtPy	35.1	68.0	4.02×10 <sup>10</sup>
Pro ( <i>R</i> ) Closed(2)H <sup>+</sup> - <i>s-cis</i> EtPy	15.7	97.7	1.39×10 <sup>14</sup>
Pro ( <i>S</i> ) Closed(2)H <sup>+</sup> - <i>s-cis</i> EtPy	17.7	95.6	6.09×10 <sup>13</sup>
Pro ( <i>R</i> ) Closed(2)H <sup>+</sup> - <i>s-trans</i> EtPy	38.2	68.6	1.68×10 <sup>10</sup>
Pro ( <i>S</i> ) Closed(2)H <sup>+</sup> - <i>s-trans</i> EtPy	38.1	68.8	1.79×10 <sup>10</sup>
Pro ( <i>R</i> ) Open(3)H <sup>+</sup> - <i>s-cis</i> EtPy	0.0	106.7	2.33×10 <sup>17</sup>
Pro ( <i>S</i> ) Open(3)H <sup>+</sup> - <i>s-cis</i> EtPy	1.7	105.0	1.18×10 <sup>17</sup>
Pro ( <i>R</i> ) Open(3)H <sup>+</sup> - <i>s-trans</i> EtPy	23.5	76.7	1.90×10 <sup>13</sup>
Pro ( <i>S</i> ) Open(3)H <sup>+</sup> - <i>s-trans</i> EtPy	25.5	74.8	8.76×10 <sup>12</sup>
Pro ( <i>R</i> ) Open(4)H <sup>+</sup> - <i>s-cis</i> EtPy	11.8	105.5	1.61×10 <sup>15</sup>
Pro ( <i>S</i> ) Open(4)H <sup>+</sup> - <i>s-cis</i> EtPy	11.7	105.5	1.66×10 <sup>15</sup>
Pro ( <i>R</i> ) Open(4)H <sup>+</sup> - <i>s-trans</i> EtPy	36.2	74.6	9.15×10 <sup>10</sup>
Pro ( <i>S</i> ) Open(4)H <sup>+</sup> - <i>s-trans</i> EtPy	37.9	72.9	4.62×10 <sup>10</sup>
<i>ee</i>	33%		

**Table 5.3:** Relative energies of CD, CDH<sup>+</sup> conformers, EtPy isomers and resultant diastereomeric complexes upon reaction of these reactants. Absolute complexation energies calculated using equation

5.1 and relative concentrations deduced from the model presented in Appendix A. In the *pro* (R) complex the CH<sub>3</sub> group of the keto carbonyl of the pyruvate is directed towards the aromatic ring of the modifier whereas in the *pro* (S) the group is directed away from the ring. *ee* calculated using equation 5.2 for which the concentrations of the most populated species indicated in red font were substituted into the calculation. DFT calculations performed at the B3LYP level with a 6-31G(d) basis set using methodology specified in Chapter 4, section 4.2.1 and executed with GAUSSIAN03 software.

The trend in the relative energies of the CD conformers were previously discussed in section 5.2.1, when the energetics are translated in terms of concentrations in a given molecular sample, the Open(3) form is calculated to be the dominant species constituting 91% of the sample. In relation to this, only trace amounts of the other CD conformers are calculated. The Closed(2) and Open(4) conformers, as reflected by their large energies are found to occupy no more than 2% of a CD sample and the Closed(1) roughly about 6%. Upon protonation of the quinuclidine N atom of the CD the concentration of the conformers are found to modify. The greatest change is found for the Closed1 form as it stabilises relative to the Open(3) as it occupies 22% of the mixture. The concentration of the Closed(2) increases to 5% and the Open(3) CD falls to 72%. The stability of the Open(4) is not affected and under acidic media is expected to constitute 1% of a CD mixture. The stabilisation of the *s-trans* EtPy is also verified, in agreement with *ab initio* calculations of reference 14, the relative abundance of the *s-trans* is found to be 93% in relation to the *s-cis* EtPy.

However, the relation between the energies of the diastereomeric complexes and their theoretical concentrations is not as simple as the case of the isolated reactants above. In this case, the concentrations of the intermediate dimers are calculated based accordingly to the actual concentrations of the CD and EtPy conformers (refer to Appendix A) and not the concentrations of the Closed and Open CDH<sup>+</sup> structures for which the optimised energies are used to calculate the overall energy of the reaction *i.e.* the complexation energy.

The optimised diastereomeric complexes involving the *s-cis* EtPy are found to be lower in energy and hence, stabilised in the gas-phase compared to the *s-trans* EtPy complexes. Within this trend, a further pattern emerges as in each case with the exception of the Closed(2)H<sup>+</sup>-*s-trans* EtPy complexes, the configurations labelled as the *pro* (R) intermediates are generally, very slightly stabilised in comparison to the alternative *pro* (S) complexes. For the pairs of diastereomeric complexes *i.e.* *pro* (R), *pro* (S) Closed(1)H<sup>+</sup>-*s-cis* EtPy, Closed(1)H<sup>+</sup>-*s-trans* EtPy *etc* (following the order in

table 5.3) the differences in the energies are calculated at 2.7, 3.3, 2, 2 and 1.7 kJ mol<sup>-1</sup>, respectively. However, the energies of the corresponding complexes for the Closed(2)H<sup>+</sup>-*s-trans* EtPy and Open(4)H<sup>+</sup>-*s-cis* EtPy configurations are optimised to be iso-energetic in nature, implying that both the pro (*R*) and (*S*) geometries are theoretically in thermodynamic equilibrium with each other if there is only a small barrier to their inter-conversion.

The two most stable complexes are the pro (*R*) and pro (*S*) pair of the form Open(3)H<sup>+</sup>-*s-cis* EtPy (figure 5.4), for which the former is stabilised by 1.7 kJ mol<sup>-1</sup>. This finding is in accordance with the *ab initio* calculations of Bürgi and Baiker for which MtPy was the reactant [21]. For the stabilisation of the next complex an energy of 10.2 kJ mol<sup>-1</sup> is afforded for the pro (*R*) Closed(1)H<sup>+</sup>-*s-cis* EtPy complex. From this point onwards, the rest of the CDH<sup>+</sup>-*s-cis* complexes are stabilised relative to the pro (*R*) Open(3)H<sup>+</sup>-*s-cis* EtPy complex by energies ranging from 12 (pro (*S*) Closed(1)H<sup>+</sup>-*s-cis* EtPy) to 18 kJ mol<sup>-1</sup> (pro (*S*) Closed(2)H<sup>+</sup>-*s-cis* EtPy). In contrast, the relative energies for the complexes involving the *s-trans* isomer of EtPy are much larger ranging from 32 (pro (*R*) Closed(1)H<sup>+</sup>-*s-trans* EtPy) to 38 kJ mol<sup>-1</sup> (pro (*R*) and (*S*) Closed(2)H<sup>+</sup>-*s-trans* EtPy). The latter structures are thus, optimised in this data set to be the least stable complexes.

The stability of the different diastereomeric complexes is reflected in the energy afforded to complete the reaction between the CDH<sup>+</sup> and the EtPy to form the complex. For stable complexes, the complexation energy is most positive, implying in this case, exothermic reaction (equation 5.1). For the stable Open(3)H<sup>+</sup>-*s-cis* EtPy intermediates, the complexation energies are quite similar at 106.7 and 105 kJ mol<sup>-1</sup> for the pro (*R*) and pro (*S*) pair. The least favourable reaction occurs between the alternative configurations of the Closed(2) CDH<sup>+</sup> conformer and *s-trans* EtPy, as the energy released on formation of the complex is no more than roughly 69 kJ mol<sup>-1</sup>, these structures have previously been identified as the least stable intermediates. Surprisingly, the reaction between the Open(4) CDH<sup>+</sup> and *s-cis* EtPy is favoured (105.5 kJ mol<sup>-1</sup>), as in their isolated gas-phase states both the reactants are energetically unstable compared to their counterparts.

On interpreting the complexation energies in terms of concentrations, the actual realistic presence of the diastereomeric complexes as hydrogenation reaction intermediates can be assessed. The most populated intermediates are the complexes involving the Open(3) form of CDH<sup>+</sup> and the *s-cis* isomer of EtPy. This result is expected, especially for the Open(3) CD as this is calculated to be the most abundant



conformation of CD, however under standard conditions the *s-trans* EtPy is the abundant isomer. The results imply that upon reaction with the protonated CD, the *s-cis* isomer is stabilised. The Open(3)H<sup>+</sup>-*s-cis* EtPy complex in its pro (*R*) configuration (figure 5.4(a)) is calculated to be twice as abundant as the alternative pro (*S*) intermediate (figure 5.4(b)), as the relative concentrations at room temperature are 2.33 and 1.18, respectively. The differences in the relative concentrations of these species (equation 5.2) correspond to a theoretical *ee* of 33% in favour of the pro (*R*) product.

The relative abundances of the other complexes can be considered to be negligible as the next pair of populated species for example, are the Open(4)H<sup>+</sup>-*s-cis* EtPy structures which are 100 times less likely to form than the stable Open(3)H<sup>+</sup>-*s-cis* EtPy complexes. However, consistent with the trend observed in the energetics the least abundant complexes are those, which involve the *s-trans* isomer of EtPy.

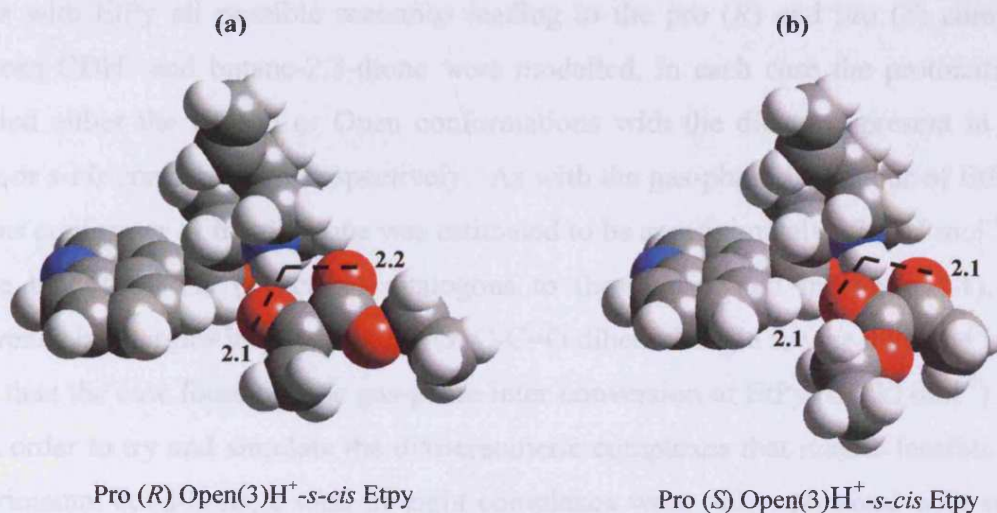


**Figure 5.4:** Space filling, minimum-energy structures of CDH<sup>+</sup>-EtPy complexes: (a) structure of the most abundant complex leading to the (*R*)- and (b) (*S*)-EtLt, respectively upon hydrogenation from the Pt side, i.e. from below. N<sup>+</sup>-H...O distances measured in Å. DFT calculations performed at the B3LYP level with a 6-31G(d) basis set using methodology specified in Chapter 4, section 4.2.1 and executed with GAUSSIAN03 software. Molecular atoms are colour coded: H white, C grey, O red and N blue.

The stabilities of the Open(3)H<sup>+</sup>-*s-cis* EtPy complexes are found to arise from their coordination geometries. As illustrated in figure 5.4, a bifurcated hydrogen bond with the N<sup>+</sup>-H binding to the two-carbonyl O atoms is exhibited. In both complexes the N<sup>+</sup>-H...O distances are identical, for the pro (*R*) case the values are 2.1 and 2.2 Å whereas the bonds are measured at 2.1 Å for the pro (*S*). In the pro (*R*) complex the distance to the *keto* carbonyl O is slightly shorter than the distance to the ester carbonyl O. This

partially helps to explain why the complexation energy for this complex is  $1.7 \text{ kJ mol}^{-1}$  lower than the alternative pro (*S*) structure, although the fact that the methyl of the *keto* carbonyl end of the pyruvate is less sterically hindered compared to the ester functionality of the pyruvate in the pro (*S*) complex is perhaps a better argument. The optimised geometry of the EtPy in both complexes is bound to the modifier in a relatively flat mode although not entirely coplanar with the aromatic ring of the CD. The configuration of the *s-cis* conformation appears to imply that it is capable of bonding to a metal surface *via* a  $\pi$ -bonding adsorption mode, as indicated by *in situ* XANES data collected in an atmosphere of hydrogen (Chapter 2, section 2.2.15).

#### 5.2.4. Interaction Between Cinchonidine and Butane-2,3-dione

As with EtPy all possible scenarios leading to the pro (*R*) and pro (*S*) complexes between  $\text{CDH}^+$  and butane-2,3-dione were modelled, in each case the protonated CD adopted either the Closed or Open conformations with the diketone present in the *s-trans* or *s-cis* configuration, respectively. As with the gas-phase behaviour of EtPy, the *s-trans* conformer of the diketone was estimated to be approximately  $27.6 \text{ kJ mol}^{-1}$  more stable than the *s-cis* (structures analogous to those presented in figure 5.1). The difference in energies implies that the  $\text{O}=\text{C}-\text{C}=\text{O}$  dihedral angle for the diketone is more rigid than the case found for the gas-phase inter-conversion of EtPy ( $6.5 \text{ kJ mol}^{-1}$ ).

In order to try and simulate the diastereomeric complexes that maybe feasible under experimental conditions, a total of eight complexes were fully optimised with starting structures biased towards geometries in which the proposed  $\text{N}^+-\text{H}\cdots\text{O}$  H-bonding could be reinforced. As mentioned earlier with respect to the mechanistic models drawn for the hydrogenation of  $\alpha$ -ketoesters (Chapter 2, sections 2.2.7-2.2.11) it is the  $\text{Open}(3)\text{H}^+$ -diketone complexes, which are of most interest.

#### 5.2.5. Analysis of Diastereomeric Complexes of Protonated Cinchonidine and Butane-2,3-dione

Since our conformational analysis of CD illustrated the relevance of the Closed(1), Closed(2) and Open(4) conformers it seems appropriate to briefly discuss their interactions with the *s-cis* and *s-trans* diketones. The energies for these complexes are



provided in table 5.4 and are specified relative to the pro (*R*) Open(3)H<sup>+</sup>-*s-cis* diketone complex, thought to yield the initial (*R*)-3-hydroxybutan-2-one which further hydrogenates into the (*R,R*)-butan-2,3-diol (Chapter 2, section 2.3). Unlike the EtPy case, for which the pro (*R*) and pro (*S*) structures were identified based on the effects of steric hindrance, it is not so easy to distinguish the structures for the diketone complexes. In this case, only the complexes that are sufficiently populated are termed the pro (*R*) and pro (*S*) species.

Reactant Components and Diastereomeric Complex	Gas-Phase Relative Energy (kJ mol <sup>-1</sup> )	Absolute Complexation Energy (kJ mol <sup>-1</sup> )	Concentration of Reactant Components and Diastereomeric Complex
<i>s-cis</i> Diketone	27.6		0.07
<i>s-trans</i> Diketone	0.0		0.93
Pro ( <i>S</i> ) Closed(1)H <sup>+</sup> - <i>s-cis</i> Diketone	7.9	99.0	1.65×10 <sup>11</sup>
Closed(1)H <sup>+</sup> - <i>s-trans</i> Diketone	24.2	55.1	2.42×10 <sup>8</sup>
Closed(2)H <sup>+</sup> - <i>s-cis</i> Diketone	12.1	98.5	4.45×10 <sup>10</sup>
Closed(2)H <sup>+</sup> - <i>s-trans</i> Diketone	28.6	54.4	6.04×10 <sup>7</sup>
Pro ( <i>R</i> ) Open(3)H <sup>+</sup> - <i>s-cis</i> Diketone	0.0	104.0	1.79×10 <sup>13</sup>
Open(3)H <sup>+</sup> - <i>s-trans</i> Diketone	12.8	63.5	1.04×10 <sup>11</sup>
Pro ( <i>S</i> ) Open(4)H <sup>+</sup> - <i>s-cis</i> Diketone	11.2	103.3	1.54×10 <sup>11</sup>
Open(4)H <sup>+</sup> - <i>s-trans</i> Diketone	34.5	52.4	1.36×10 <sup>07</sup>
<i>ee</i>	98%		

**Table 5.4:** Energies of diketone isomers and resultant CDH<sup>+</sup>-diketone diastereomeric complexes relative to the minimum-energy structures. Absolute complexation energies calculated using equation 5.1 appropriately substituted for the energies of the diketone isomer and energies of the CDH<sup>+</sup> conformers specified in table 5.3. Relative concentrations deduced from the model presented in Appendix A and using the CD concentrations specified in table 5.3. *ee* calculated using equation 5.2 for which the concentrations of the most populated species indicated in red font were substituted into the calculation. DFT calculations performed at the B3LYP level with a 6-31G(d) basis set using methodology specified in Chapter 4, section 4.2.1 and executed with GAUSSIAN03 software.

The energies presented in the above table are found to follow the same trend as observed in the CDH<sup>+</sup>-EtPy case (section 5.2.3), *i.e.* the *s-cis* diketone complexes are more stable than their alternative *s-trans* structures. For the Closed(1)H<sup>+</sup> and Closed(2)H<sup>+</sup> complexes the *s-cis* vs. *s-trans* diketone energy gap is roughly the same

averaging at  $16.4 \text{ kJ mol}^{-1}$ , with a difference of  $0.2 \text{ kJ mol}^{-1}$  calculated for the latter structures. This gap is reduced to  $12.8 \text{ kJ mol}^{-1}$  for the  $\text{Open}(3)\text{H}^+$  pair of complexes and nearly doubled in the case of the  $\text{Open}(4)\text{H}^+$  structures. Once again the results illustrate the concept of how  $\text{CDH}^+$  stabilises the *s-cis* diketone on interaction more so than the *s-trans*.

As with the EtPy isomers, the *s-cis* diketone conformer has a considerably larger dipole moment than the *s-trans* ( $5.4$  vs.  $0.0 \text{ D}$ ) [47], for which the two polar carbonyl groups are oriented antiparallel. The degree of dipole moment is expected to affect the stabilisation of the conformers, as clearly emphasised in reference 14, where the *s-cis* conformer of EtPy was found to significantly stabilise relative to the *s-trans* on increasing solvent polarity. The diketone conformers are expected to display the same characteristics as above with regards to the effect of solvents as experimentally (as with the hydrogenations of  $\alpha$ -ketoesters), solvents with low dielectric constants are found to result in the highest enantioselectivities (with the exception of acetic acid [45]) [48].

The most thermodynamically stable structure is the complex involving the  $\text{Open}(3)\text{CDH}^+$  with the diketone optimised in its *s-cis* geometry (figure 5.5(a)), this affords an energy of  $104 \text{ kJ mol}^{-1}$ . Subsequently, with the  $\text{Open}(3)$  form being the most populated conformation of CD, the relative concentration of this complex is calculated to be the most abundant at room temperature of all the diastereomeric complexes optimised in this data set. The  $\text{Open}(3)\text{H}^+$ -*s-cis* diketone structure is proposed to yield the (*R*)-product of the first hydrogenation step of the overall reaction (Chapter 2, section 2.3, figure 2.11) and is analogous to the minimum-energy structure found in the  $\text{CDH}^+$ -EtPy case. The second most abundant species is the analogous  $\text{Closed}(1)\text{H}^+$  complex (figure 5.5(b)), which possesses a higher energy of approximately  $8 \text{ kJ mol}^{-1}$  and costs an extra  $5 \text{ kJ mol}^{-1}$  to form than the reference  $\text{Open}(3)\text{H}^+$ -*s-cis* diketone structure. Note that the differences between the magnitudes of the relative concentrations of these abundant species is a factor of 100 in favour of the  $\text{Open}(3)\text{H}^+$  complex. The calculated abundance of the  $\text{Closed}(1)\text{H}^+$ -*s-cis* diketone implies that this structure could indeed be responsible for generating the experimentally observed low yield (*S*)-3-hydroxybutan-2-one product of the hydrogenation reaction. The calculated difference in the relative abundance pro (*R*)/pro (*S*) (equation 5.2) at room temperature corresponds to a theoretical *ee* of 98% in favour of the (*R*)-product.

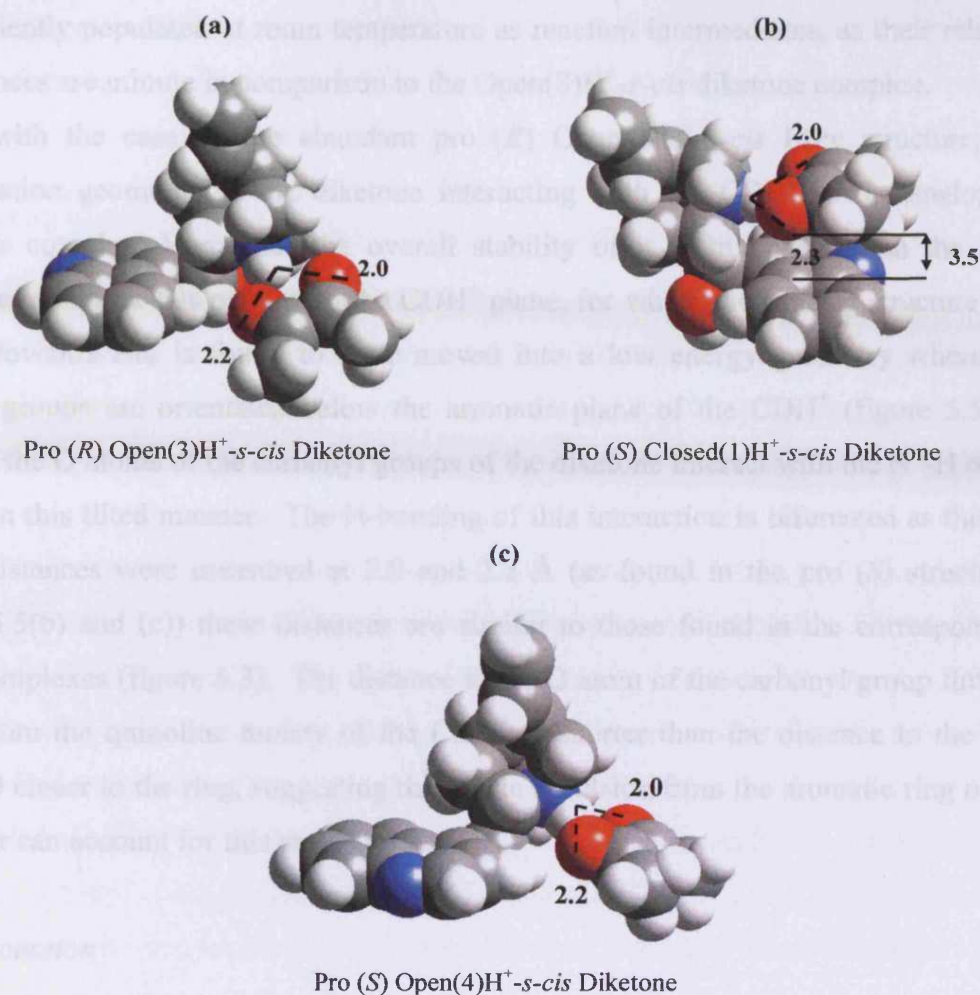


**Figure 5.5:** Space filling, minimum-energy structures of CDH<sup>+</sup>-diketone complexes: (a) structure of the most abundant complex leading to the (R)-hydroxybutanone with (b) the second most abundant intermediate and (c) the structure leading to the (S)-hydroxybutanone, respectively upon hydrogenation from the Pt side, i.e. from below. N<sup>+</sup>-H<sup>+</sup>...O distances measured in Å. DFT calculations performed at the B3LYP level with a 6-31G(d) basis set using methodology specified in Chapter 4, section 4.2.1 and executed with GAUSSIAN03 software. Molecular atoms are colour coded: H white, C grey, O red and N blue.

However, a third complex, Open(4)H<sup>+</sup>-s-cis diketone (figure 5.5(c)) is also found to be sufficiently stabilised by 11.2 kJ mol<sup>-1</sup> relative to the Open(3)H<sup>+</sup>-s-cis diketone structure, affording a complexation energy of 103.3 kJ mol<sup>-1</sup>. The calculated relative abundance of this species is virtually the same as measured for the Closed(1)H<sup>+</sup>-s-cis diketone. This implies that either one of the complexes or possibly a mixture of them both are capable of yielding the (S)-3-hydroxybutan-2-one product. The other CDH<sup>+</sup>-diketone complexes, with the exception of the Open(3)H<sup>+</sup>-s-trans diketone (relative abundance of 1.0, comparable to the above two complexes) can be considered to be



insufficiently populated at room temperature as reaction intermediates, as their relative abundances are minute in comparison to the Open(3)H<sup>+</sup>-*s-cis* diketone complex.

As with the case of the abundant pro (*R*) Open(3)H<sup>+</sup>-*s-cis* EtPy structure, the coordination geometry of the diketone interacting with the CDH<sup>+</sup> in the analogous diketone complex determines the overall stability of it. On optimisation the *s-cis* diketone no longer lies parallel to the CDH<sup>+</sup> plane, for which the starting structure was biased towards and is found to have moved into a low energy geometry where the methyl groups are orientated below the aromatic plane of the CDH<sup>+</sup> (figure 5.5(a)). Both of the O atoms of the carbonyl groups of the diketone interact with the N<sup>+</sup>-H of the CDH<sup>+</sup> in this tilted manner. The H-bonding of this interaction is bifurcated as the N<sup>+</sup>-H...O distances were measured at 2.0 and 2.2 Å (as found in the pro (*S*) structures, figure 5.5(b) and (c)) these distances are similar to those found in the corresponding EtPy complexes (figure 5.3). The distance to the O atom of the carbonyl group furthest away from the quinoline moiety of the CDH<sup>+</sup> is shorter than the distance to the *keto* group O closer to the ring, suggesting that steric repulsion from the aromatic ring of the modifier can account for this trend.

### 5.3. Discussion

#### 5.3.1. The Conformation of Cinchonidine

In the gas-phase, semi-empirical and *ab initio* calculations at different levels of theory have identified the stability of the two Open and two Closed conformations of CD, suggesting relative populations of them in an equilibrated mixture at room temperature. The relative stability of these conformers is greatly influenced by the repulsive interaction between the quinoline, quinuclidine, and the O-H parts of the molecule. On measuring the O...H<sub>5</sub> distance (figure 5.3(a)) for the optimised GAUSSIAN Closed(1) and Open(4) conformers we find the value to be shorter by approximately 0.17 Å compared with the equivalent O...H<sub>1</sub> distance (figure 5.3(a)) in the Closed(2) and Open(3) forms. This suggests a greater H-bonding interaction stabilising the latter two complexes. In support of this, Bürgi and Baiker [13] calculated the Gibbs free energies for the same CD conformers (similar theory level as specified in our calculations) and compared them against the corresponding energies for deoxyCD (supporting information in reference 13), which is a derivative of the alkaloid in which

the O-H group of CD is replaced with a H atom. Thus, as expected the repulsion between the corresponding H<sub>1</sub> and H<sub>5</sub> and the substituted H atom in deoxyCD was less than that found between the same atoms and the O-H group of the CD. Such an effect was found to stabilise the Closed(1) conformer by about 2.9 kJ mol<sup>-1</sup> relative to the Open(3), when going from CD to deoxyCD.

Although our DFT studies clearly emphasised Open(3) to be the most stable conformation, in agreement with the crystallographic structure found by Margitfalvi and Tfirst [40], the Closed(1) has become closer in energy than in Baiker's calculations albeit a relative difference of 6.7 kJ mol<sup>-1</sup>. Note that the PM3 method had given the Closed(1) to be most stable. The theoretical importance of the Closed(1) is valid as NOESY experiments of Dijkstra and co-workers conducted for deoxyCD in benzene [41] found amounts as high as 40% besides the more abundant Open(3). The stabilities of the Open(3) and Closed(1) CD conformers are reflected in their relative abundances. Using the GAUSSIAN energies, the Open(3) is the most abundant conformer of CD with a calculated relative abundance of 91% at room temperature. This compares to the population of 74% derived by Bürgi and Baiker [13] when performing analogous *ab initio* calculations. In contrast, the populations of the Closed(1) and (2) conformers at 13% in this study are found to be twice as abundant for our Closed(1) structure (6%) and 11% greater for the Closed(2). However, in agreement with the earlier authors, the contribution of the Open(4) is negligible at roughly 1%. The discrepancies in the values exist as the authors added an extra diffuse function to the 6-31G(d) basis set, which was used in our calculations.

Under experimental conditions, the use of solvents can affect the observed trend in the gas-phase stability of the CD conformers (Chapter 2, section 2.2.12). In the reference study above [13], the analysis of CD in various solvents found the Closed conformers to become more stable relative to the Open(3) as the polarity of the solvent increased. This stability of the Closed forms in relation to the Open(3) was also observed in our calculations for which the quinuclidine N atom of the CD was protonated to mimic the effect of acidic media. The abundances of the conformations of the modifier altered to give 72% Open(3), 22% Closed(1) and 5% Closed(2). Roughly the same population of the Closed(1) was found in calculations incorporating a solvent of dielectric constant 4.8 [13]. At the same time the population of the Closed(2) was derived to be the same at 21% and the Open(3) was 58% [13]. As in our calculations, the stability of the Open(4) was not found to be affected by the presence of solvent [13].

The strength of the interaction between the solvent and the solute is determined by the dipole moment of the CD and this is affected by its actual conformation. Therefore, according to Bürgi and Baiker [13] the actual stabilisation of the conformers should in fact correlate to their dipole moments. Note that, despite solvation having a considerable effect on the relative stability of the CD conformers the actual geometries of them are not much altered from their optimised gas-phase structures [13].

### 5.3.2. The Approximate Intermediate Complexes of Cinchonidine-Ethyl Pyruvate and Cinchonidine-Butane-2,3-dione

To date the mechanistic models for trying to understand the *ee* at the CD modified Pt surface for hydrogenation reactions are limited to the chiral induction in  $\alpha$ -ketoesters (Chapter 2, sections 2.2.7-2.2.11). One of the most prominent models is that proposed by Baiker *et al.* (Chapter 2, section 2.2.11), which principally argues the fact that it is the different stabilities of the diastereomeric complexes which would lead to the (*R*)- and (*S*)-products, respectively upon hydrogenation from the surface side. The adsorbed modifier and the reactant are assumed to interact *via* an inter-molecular H-bond, which leads to the initial discrimination for adsorption of the reactant on one of the two enantiofaces. In other words, the relative populations of the competing intermediate complexes determine the reaction *ee*. Unlike the other models proposed (Chapter 2, sections 2.2.8-2.2.10), this model has proven to be effective in not only predicting the absolute configuration of the reaction product and the enantio-differentiating power of cinchona alkaloids [5] but also several other synthetic modifiers [21,49].

Therefore, rationalising the populations of our optimised diastereomeric complexes against this model, a theoretical *ee* of 33% is obtained from the pro (*R*) and pro (*S*) Open(3)H<sup>+</sup>-*s-cis* EtPy complexes (figure 5.4). However, the experimental *ee* achieved under optimised conditions for the hydrogenation of Mt- and EtPy over CD modified Pt is reported to be 95% and above [50]. There are a number of factors, which can explain the low predicted *ee* value, the most obvious is the fact that the populations have been derived from gas-phase energies.

In an analogous investigation conducted by Bürgi and Baiker [21], the relative stability calculated for the pro (*R*) and pro (*S*) complexes between the protonated Open(3) and *s-trans* MtPy was found to correspond to an *ee* of 92% in favour of the (*R*)

lactate. This *ee* is in excellent agreement with that achieved in acetic acid [50]. The analogous complexes involving the *s-cis* MtPy were found to predict a theoretical yield of only 17%. These values, unlike the *ee* estimated in our calculations are comparable with experiment because the diastereomeric complexes were modelled in an environment of acetone ( $\epsilon_r = 20.7$ ) using a self-consistent reaction field model in GAUSSIAN94 [27]. In this case, the reported theoretical *ees* imply that the *s-trans* conformation of the MtPy is effectively more reactive than the *s-cis* isomer.

For butane-2,3-dione, two intermediates were found to be equally populated and both are expected to yield the (*S*)-hydroxybutanone. The relative concentrations of the pro (*R*) Open(3)H<sup>+</sup>-*s-cis* diketone and either one of the pro (*S*) Closed(1)H<sup>+</sup>-*s-cis* diketone or Open(4)H<sup>+</sup>-*s-cis* diketone was found to yield an *ee* of 98% for (*R*)-3-hydroxybutan-2-one. The actual experimental *ee* recorded for the hydrogenation of the diketone over Pt modified CD is 50% in dichloromethane [22] and 10% in favour of the (*S*)-hydroxybutanone with CN. As with the case of the EtPy, the comparison of the magnitude of the *ee* is not good but the correct sense of the selectivity is obtained. Initially the *ee* is derived from the concentrations of gas-phase complexes mimicking the effect of low dielectric constants and not actually optimised solvent energies.

Thus, it must be noted that perhaps our calculations are not accurate enough to draw qualitative predictions of *ee*, as obviously the effects of solvent and most importantly the presence of the Pt surface have been ignored (because of computational expense). One would expect the relative stability of the complexes to alter as well as the geometries in which they are stabilised in under the influence of either or both of these parameters, as observed in the isolated cases of the CD and EtPy (Chapter 2, sections 2.2.12-2.2.15). However, in both reactions we have successfully shown that the dimer model energetics can account for the sign of the observed selectivity.

Nevertheless, the *ab initio* calculations highlight the importance of the *s-cis* complexes with respect to the *s-trans*, as they are stabilised on interaction with the CDH<sup>+</sup>. Besides the obvious strength of the H-bonding in the CDH<sup>+</sup>-reactant complexes, the largest contribution to the complexation energy is the charge-dipole interaction, which favours the *s-cis* over *s-trans*. When considering the effect of the Pt surface the *s-cis* complexes are expected to be more stable than the *s-trans*, as the *s-cis* conformer with the larger dipole moment is thought to enhance the dipole-induced dipole interaction on the metal. Such a scenario has been indicated by a vibrational

spectroscopic study for MtPy on Ni(111) under UHV conditions, for which the *s-cis* conformer was found in abundance [51].

Further support of *s-cis* stabilisation is found when the resulting  $N^+-H\cdots O=C$  H-bonding interaction between *s-cis* EtPy and a trimethyl ammonium (TMA) ion is stronger than the *s-trans* complex [14]. When comparing the optimised geometries of this work, it is interesting to note a similar trend in the way in which the structure is hydrogen bonded, for example, in the most favourable H-bonded *s-trans* EtPy-TMA complex the  $N^+-H$  points inbetween the *keto* and ester carbonyl O with distances of 1.87 and 2.90 Å. These values correspond well to those found in the *s-trans*, pro (*R*) and pro (*S*)  $CDH^+$ -EtPy complexes (figure 5.6(a) and (b)) *i.e.* at 1.8 and 2.9 Å respectively, (the stronger H-bond was also evident in the corresponding *s-trans* diketone complexes).

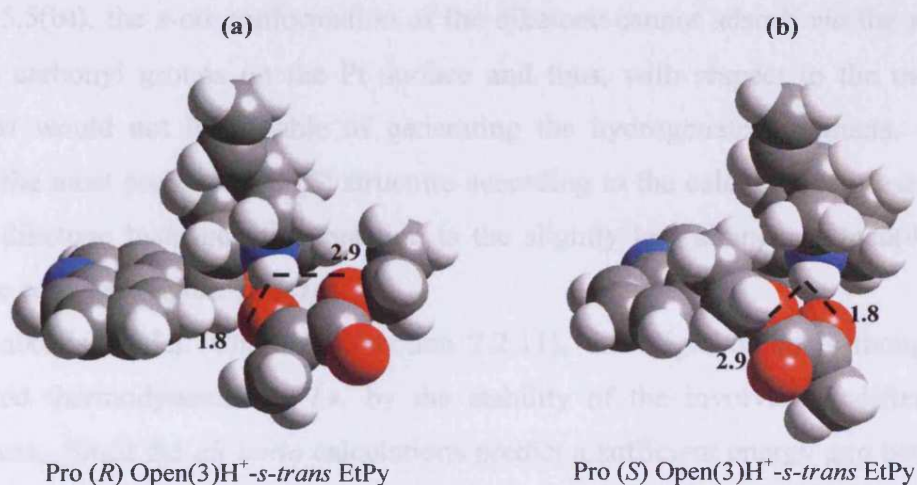


**Figure 5.6:** Space filling, minimum-energy structures of Open(3) $H^+$ -*s-trans* EtPy complexes potentially leading to: (a) (*R*)- and (b) (*S*)-EtLt, respectively upon hydrogenation from the Pt side, *i.e.* from below.  $N^+-H\cdots O$  distances measured in Å. DFT calculations performed at the B3LYP level with a 6-31G(d) basis set using methodology specified in Chapter 4, section 4.2.1 and executed with GAUSSIAN03 software. Molecular atoms are colour coded: H white, C grey, O red and N blue.

The interaction of the *s-cis* conformers of EtPy and diketone with  $CDH^+$  were found to be analogous to the bonding observed in the reference *s-cis* EtPy-TMA complex [14], as the optimal arrangement was *via* a bifurcated hydrogen bond in which the  $N^+-H$  proton interacted with the lone pairs of both carbonyl groups through distances measuring 2.04 and 2.20 Å, respectively. As illustrated in figure 5.4, the same bifurcated hydrogen bond was observed in the *s-cis*, pro (*R*) and pro (*S*) EtPy complexes with bond lengths measured at 2.1 and 2.2 Å for the former and 2.1 Å for the latter



complex. Similar measurements were recorded for the *s-cis* diketone complexes (figure 5.5).

The origin in the energy difference between the two complexes in favour of the pro (*R*) can be explained in terms of steric hindrance or the repulsive interaction between the EtPy and the quinoline ring of  $\text{CDH}^+$ , as the ester portion of the pyruvate in the pro (*S*) clashes with and is pushed away from the optimal hydrogen bonding arrangement found in the pro (*R*) complex. A similar analogy can be applied to the butane-2,3-dione case as the adsorption of the pro (*R*) complex in which the methyl groups are clearly unhindered by the alkaloid (figure 5.5(a)) is energetically more favourable than the pro (*S*) complexes (figure 5.5(b) and (c)).

In the latter example, *i.e.* the complex involving the Closed(1) conformer of  $\text{CDH}^+$  (figure 5.5(b)), the *s-cis* conformation of the diketone cannot adsorb *via* the  $\pi$ -systems of both carbonyl groups on the Pt surface and thus, with respect to the mechanism proposed would not be capable of generating the hydrogenated products. For this reason, the most probable pro (*S*) structure according to the calculations presented here for the diketone hydrogenation reaction is the slightly less abundant Open(4) $\text{H}^+$ -*s-cis* diketone complex (figure 5.5(c)).

In Baiker's model (Chapter 2, section 2.2.11), the origin of *ed* is thought to be controlled thermodynamically *i.e.* by the stability of the involved modifier-reactant complexes. Since the *ab initio* calculations predict a sufficient energy gap between the pro (*R*) and pro (*S*) complexes for the *s-cis* conformation of EtPy ( $1.7 \text{ kJ mol}^{-1}$ ) and for butane-2,3-dione ( $11.2 \text{ kJ mol}^{-1}$ ) the model is reinforced. However, in contrast to this a similar theoretical approach involving Open(3) $\text{H}^+$ -MtPy complexes saw the *s-cis* conformation of MtPy fail to predict a considerable energy difference between the pro (*R*) and pro (*S*) complexes, leading the authors to question the origin of *ed* [21].

Thermodynamics alone could not account for the observations found in the aforementioned complexes and so it was proposed that the *ed* in this case could be kinetically dictated by the different hydrogenation rates of the pro (*R*) and pro (*S*) complexes. It was suggested that the reaction rate could be influenced by the hydrogen bond formed between the  $\text{N}^+\text{-H}$  and the *keto* group of the pyruvate, which is ultimately hydrogenated. For the Open(3) $\text{H}^+$ -*s-cis* MtPy complexes, in particular the pro (*R*), the consequence of a shorter distance measured between the quinuclidine N and the *keto* O compared to the pro (*S*) complex could be responsible for the enhancement of the rate of

reaction for the pro (*R*). Similarly, it was proposed that the *s-trans* could be kinetically favoured over the *s-cis* complexes, since the quinuclidine N-*keto* O distance was found to be shorter for the former (as observed in the analogous EtPy and diketone complexes modelled here).

At the time of the above study [21] there was no microscopic information available to support the argument of the kinetic concept, however, a few years later Vargas within Baiker's research group managed to illustrate how the mechanistic model could indeed account for *ed* as well as the *ra* induced by the modifier, with different rates predicted for the pathways to (*R*)- and (*S*)-products [52]. The experimental and theoretical methods rationalised the concept of how the more stable interaction complex within a diastereomeric couple is hydrogenated the fastest. This was deduced from the correlation between the hydrogenation rate and the stability of the carbonyl  $\pi$  orbitals of the reactant.

Finally, it should be noted that the energetic considerations of the approximate intermediates in this work were carried out in isolation, assuming no effect from other coadsorbed species such as solvent and product. If coadsorbates were present, then one would expect the surface population of the diastereomeric complexes to be affected, which would ultimately challenge the calculated relative stability versus surface coverage correlation.

With regards to accuracy and reliability the complexes modelled in this study are perhaps not necessarily the minimum-energy complexes expected if to assume the presence of a flat Pt surface, as clearly figure 5.6 illustrates the EtPy molecule optimised in space with the neglect of this assumption. In an ideal situation, constraints to keep the CDH<sup>+</sup> and reactant coordinates in a common plane should have been imposed in the starting geometries, thus allowing the other degrees of freedom to optimise, as specified in the parallel study of Baiker *et al.* [21]. Therefore, due to the possible number of different configurations of the CDH<sup>+</sup>-reactant complexes it appears that single calculations of geometry optimised structures may not identify the true minima, or indeed sample the available minima well, for reliable conclusions to be drawn. Certainly a more accurate approach to this investigation would have been a systematic search of the PES, employing sampling techniques so that the average difference between the many alternative routes across the PESs could have been taken into account. However, the number of dimer structures and the requirement to use high-

level DFT calculations to obtain accurate results precluded this approach due to inevitable restrictions on computer time.

#### 5.4. Conclusions

The most widely accepted mechanistic model for the enantioselective hydrogenation of activated ketones over chirally modified heterogeneous catalysts is Baiker's model [42]. The model is used to explain the *ra* and the *ed* observed in the hydrogenation of EtPy and the *ed* in the first hydrogenation step of butan-2,3-dione. *Ab initio* HF calculations were performed to study the conformational stability of CD. The calculations illustrated CD to be stable in four different conformations: two each of the Open and Closed forms. The structures and stabilities were found to compare well against *ab initio* HF calculations of Bürgi and Baiker [13]. The semi-empirical CD structures obtained with the MOPAC code were best used as the start point geometries for the more computationally expensive *ab initio* calculations. The higher theory level calculations revealed the important conformations of CD in the gas-phase: the Open(3) and the Closed(1), which are illustrated in figure 5.3(b) (Chapter 5, section 5.2.1). Concentrations of the CD conformers were calculated from their electronic energies. 91% of a CD mixture will constitute the Open(3) form whereas the Closed(1) form represents 6%. Only trace amounts were calculated for the Open(4) and Closed(2) structures. In acidic media the quinuclidine N atom of the CD is found to be protonated [21]. *Ab initio* HF calculations for the protonated CD conformers found the Closed forms to stabilise relative to the Open(3) as the populations of the Closed(1) and Closed(2) increased to 22% and 5% whilst the Open(3) fell to 72%. The stability of the Open(4) did not alter on protonation.

Optimisation of the intermolecular interaction between the CD conformers and the activated ketones relevant to the Baiker model were obtained by performing *ab initio* HF calculations. One of the key points revealed was that the conformation of the ketone was just as important as the conformation of the CD, as both were found to affect the stereochemical outcome of the reaction. The complex yielding the (*R*)-ethyl lactate upon hydrogenation is one in which the protonated CD adopts the Open(3) conformation and the EtPy, the *s-cis* geometry. This dimer is calculated to be more stable than the pro (*S*) complex by 1.7 kJ mol<sup>-1</sup> and corresponds to a 33% *ee*. The experimental *ee* achieved under optimised conditions for the hydrogenation of  $\alpha$ -

ketoesters over CD modified Pt is reported to be 95% and above [50]. The stability of the complexes is accounted for by the extent of steric repulsion felt between the EtPy and the anchoring group of the modifier. The calculations show that the effect of this plays an important role for *ed*. For the pro (*S*) complex the calculation models the ester functionality of the EtPy to be sterically hindered against the quinoline ring of the CD whereas in the pro (*R*) complex the methyl of the *keto* carbonyl is less hindered.

For the case of butan-2,3-dione this explanation does not help to discriminate between the pro (*R*) and pro (*S*) complexes, as the substituents on the two carbonyl groups are the same. The calculations show that the more stable pro (*R*) complex yielding (*R*)-3-hydroxybutan-2-one upon hydrogenation is analogous to that modelled for EtPy hydrogenation. The pro (*S*) complex is taken to be one in which the protonated Open(4) CD is H-bonded to the *s-cis* butan-2,3-dione. The pro (*R*)/pro (*S*) energy difference corresponds to a 98% *ee* and is larger than the experimental value of 50% recorded for dichloromethane [22].

The calculated *ees* for the hydrogenation of EtPy and butan-2,3-dione are poorly modelled against their experimental values. We expect this to arise from our model provided in Appendix A, as a small error in the energy of the complex will lead to a large error in the calculated *ee* as the *ee* is exponentially related to the calculated energies.

*S-cis* EtPy and butan-2,3-dione forms a bifurcated hydrogen bond to the quinuclidine H of protonated CD involving the O atoms of both carbonyl groups. On average, for the EtPy the hydrogen bond distance to the *keto* group is slightly shorter for the pro (*R*) complex, which could favour hydrogen addition to this complex in the case of *s-cis* EtPy. The complexes involving the Closed conformations of CD are not suitable intermediates as their concentrations in solution are calculated to be negligible. Geometrically, these complexes are constrained as both the modifier and the reactant cannot simultaneously interact with one another whilst assuming a parallel interaction with the surface: they do not fulfil the steric requirements imposed in the model [42].

In conclusion the calculations have been shown to provide a detailed description of the stable conformations the modifier and reactants adopt in the gas-phase and the maximum interaction in which both stabilise to form the surface dimer proposed by Baiker [42]. To improve the calculations we suggest imposing steric constraints on the anchoring group of CD and the O=C-C=O section of the  $\alpha$ -ketoester so as to impose

parallel adsorption with the catalyst surface as well as incorporate solvent effects. Such modifications have been applied to analogous calculations involving MtPy as the reactant [21]. In the literature, the energy difference between the *s-cis* complexes was found to completely vanish and the stability of them reduced with respect to the *s-trans* complexes. An *ee* of 92% was calculated from the pro (*R*)/pro (*S*) *s-trans* complexes and found to be in full agreement with experiment [21]. On changing the conformation of the EtPy in our calculations into the *s-trans*, the energy difference between the pro (*R*) and pro (*S*) complexes increases to 2 kJ mol<sup>-1</sup> and results in a 37% *ee*, showing an already improved *ee*. Clearly this is the direction in which the calculations should be heading. However, our results demonstrate that molecular modelling with *ab initio* calculations is a powerful tool to give quantitative data for the substrate-modifier interactions taking place in the liquid phase.

### 5.5. Future Work

Chapter 2, section 2.2.3, briefly highlighted literature ideas regarding the implications of Pd modified catalysts in enantioselective hydrogenation reactions [53,54]. In 1996, Wells *et al.* through deuteration experiments for the case of hydrogenation of  $\alpha$ -ketoesters with Pd/Al<sub>2</sub>O<sub>3</sub> illustrated how the major route to product was conversion to adsorbed *enol*, with the CD chemisorbed onto the metallic surface before attachment of the substrate to be hydrogenated [55].

In view of this, it seems apparent that all of the literature examined neglected the possibility of the *enol* pyruvate forming a stable diastereomeric complex with the CD, despite the concept being known for a while. The recent combined theoretical and experimental investigations focussed purely on the conformational behaviour of the CD and the pyruvate in the resulting diastereomeric complexes.

As assessed in this present work and reinforced by the *ab initio* calculations, sufficient data exists in understanding the role of the approximate intermediates, *i.e.* how the complexes of Open(3) CDH<sup>+</sup> with pyruvate in the *s-cis* and *s-trans* conformations can account for the *ed* and *ra* observed. However, it must be made clear that the role of the *enol* could alter these conclusions as no real study to date has modelled the CD N<sup>+</sup>-H<sup>+</sup>...O *enol* pyruvate interaction.

A good insight into the role of the *enol* is by initially analysing the gas-phase *keto-enol* equilibrium. Both the *s-cis* and *s-trans* conformer of EtPy can interconvert into the corresponding *enol* forms, illustrated in figure 5.7. Table 5.5 provides the ground state energies for the resulting *s-cis keto* and *enol* and *s-trans enol* EtPy gas-phase structures, measured relative to the *s-trans keto* EtPy. The corresponding data relative to the *s-trans* butane-2,3-dione is also supplied.

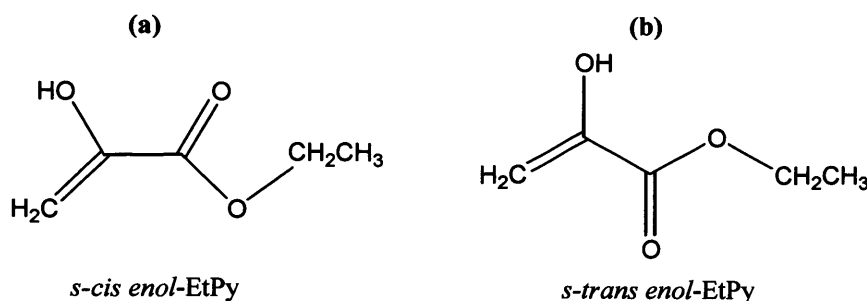


**Figure 5.7:** Enol tautomers of EtPy derived from: (a) *s-cis* and (b) *s-trans* EtPy (figure 5.1).

<i>Keto-Enol Tautomers</i>	Gas-Phase ( $\epsilon_r = 1.0$ ) Relative Energy (kJ mol <sup>-1</sup> )
<i>s-cis keto</i> EtPy	27.6
<i>s-cis enol</i> EtPy	60.9
<i>s-trans keto</i> EtPy	0.0
<i>s-trans enol</i> EtPy	73.1
<i>s-cis keto</i> diketone	6.5
<i>s-cis enol</i> diketone	59.7
<i>s-trans keto</i> diketone	0.0
<i>s-trans enol</i> diketone	62.9

**Table 5.5:** Energies for the *s-cis* and *s-trans* keto and enol gas-phase structures for EtPy and butane-2,3-dione. In each case the energies are measured relative against the *s-trans keto* structures, as this is the conformation thought to favour the (*R*)-products in the corresponding hydrogenation reactions. Calculations were performed at the DFT B3LYP level using 6-31G(d) basis set.

The calculations above clearly illustrate the unstable nature of the gas-phase *enols* for both EtPy and butane-2,3-dione, as it stands the *s-trans* are more stable than the *s-cis* which in turn are more stable than the *enol*. However, on interaction with the CD the order of stability could clearly alter, as our calculations previously estimated the *s-cis* complexes to be energetically favourable over the corresponding *s-trans* complexes. One would thus expect the *enols* in particular the *s-cis* derived molecules with the larger dipole moments to stabilise on interaction with the Pt metal, as dipole-induced dipole

interactions would maximise. Stabilisation of the *enols* on contact with Pd and Pt surfaces have been verified with the use of periodic models presented in Chapters 6 and 7.

In fact, when considering the *s-trans* and *s-cis* EtPy *enols*, the  $\pi$ -electrons are higher in energy (−10.03 and −10.02 eV, respectively) [56], more polarisable and therefore more likely to complex to Pt than the corresponding low energy electrons of the pyruvate carbonyls of the most stable twisted ( $\theta = \sim 95^\circ$ ), *s-trans* and *s-cis* coplanar EtPy conformations [58] (−13.38, −13.34 and −13.33 eV, respectively) [56], suggesting that the *enol* is more reactive towards hydrogenation.

This partly justifies the hydrogenation mechanism of EtPy, under acetic acid over CD modified Pt/Al<sub>2</sub>O<sub>3</sub> outlined by Solladié-Cavallo *et al.* [58]. Here, the modifier is thought to activate the pyruvate through the formation of a faster reacting *enol* species (figure 5.8(a)) (acceleration part of reaction) and is in equilibrium with the CD ammonium acetate (CDH<sup>+</sup>/OAc<sup>−</sup>) which associates *via* H-bonding to EtPy in a complex similar to that of figure 5.8(a) (responsible for higher reactivity). In this mechanism the pK<sub>a</sub> (acid dissociation constant) of the CD is suitable to provide enough *enol* and then to liberate the corresponding hydroxyester once hydrogenation is over [59].

With regards to this study, it would be interesting to model the corresponding *s-trans* and *s-cis* EtPy *enol* CD complexes as implied in figure 5.8(a), and to analyse the stability and energetics of them over the relevant *s-trans* and *s-cis* CDH<sup>+</sup> diastereomeric complexes, so as to comment on their true nature as to whether they exist in equilibrium with the product inducing, higher reactivity complexes *i.e.* reinforce the arguments of Wells *et al.* [55] and Solladié-Cavallo *et al.* [58]. Similarly, to extend the scope of the mechanistic work on the butane-2,3-dione reaction, the analogous *enol* CD complexes (figure 5.8(b)) would be worth considering. The specific implications of the effect of surface adsorption of the *enol* are examined in the following Chapters.

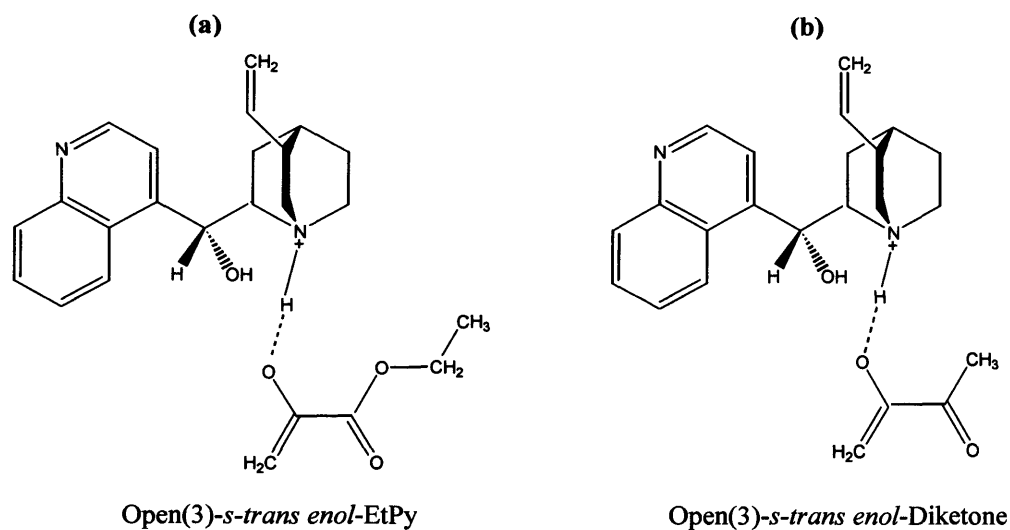


**Figure 5.8:** Formula models for the proposed **(a)** CD-s-trans enol-EtPy and **(b)** CD-s-trans enol-butane-2,3-dione complexes, note that the corresponding s-cis reactants may also form the enol complexes as above.



## 5.6. References

- [1] Y. Orito, S. Imai and S. Niwa, *Nippon Kagaku Kaishi*, 1118, (1979).
- [2] Y. Orito, S. Imai and S. Niwa, *J. Chem. Soc. Jpn.*, 1118, (1979).
- [3] Y. Nitta, Y. Ueda and T. Imanaka, *Chem. Lett.*, 1095, (1994).
- [4] P. B. Wells and A. G. Wilkinson, *Topics Catal.*, **5**, 39, (1998).
- [5] A. Baiker, *J. Mol. Catal. A: Chem.*, **115**, 473, (1997).
- [6] K. E. Simons, A. Ibbotson, P. Johnston, H. Plum and P. B. Wells, *J. Catal.*, **150**, 321, (1994).
- [7] G. Bond and P. B. Wells, *J. Catal.*, **150**, 329, (1994).
- [8] A. F. Carley, M. K. Rajumon, M. W. Roberts and P. B. Wells, *J. Chem. Soc. Faraday Trans.*, **91**, 2167, (1995).
- [9] T. Evans, A. P. Woodhead, A. Gutierrez-Sosa, G. Thorton, T. J. Hall, A. A. Davis, N. A. Young, P. B. Wells, R. J. Oldman, O. Plashkevych, O. Vahtras, H. Agren and V. Carravetta, *Surf. Sci.*, **436**, L691, (1999).
- [10] J. M. Bonello and R. M. Lambert, *Surf. Sci.*, **498**, 212, (2002).
- [11] J. M. Bonello, R. Lindsay, A. K. Santra and R. M. Lambert, *J. Phys. Chem. B*, **106**, 2672, (2002).
- [12] D. Ferri, T. Bürgi and A. Baiker, *Chem. Commun.*, 1172, (2001).
- [13] T. Bürgi and A. Baiker, *J. Am. Chem. Soc.*, **120**, 12920, (1998).
- [14] D. Ferri, T. Bürgi and A. Baiker, *J. Chem. Soc., Perkin Trans. 2*, 221, (2000).
- [15] H. -U. Blaser, H. P. Jalett, M. Müller and M. Studer, *Catal. Today.*, **37**, 441, (1997).
- [16] A. Baiker, T. Mallat, B. Minder, O. Schwalm, K. E. Simons and J. Weber, in *"Chiral reactions in heterogeneous catalysis"* (G. Jannes and V. Dubois, Eds.), 1995, Plenum Press, New York and London, p. 95.
- [17] O. Schwalm, B. Minder, J. Weber and A. Baiker, *Catal. Lett.*, **23**, 271, (1994).
- [18] K. E. Simons, P. A. Meheux, S. P. Griffiths, I. M. Sutherland, P. Johnston, P. B. Wells, A. F. Carley, M. K. Rajumon, M. W. Roberts and A. Ibbotson, *Rec. Trav. Chim. Pays-Bas.*, **113**, 465, (1994).
- [19] K. L. Haug, T. Bürgi, T. R. Trautman and S. T. Ceyer, *J. Am. Chem. Soc.*, **120**, 8885, (1998).
- [20] A. Roucoux, I. Suisse, M. Devocello, J. -F. Carpentier, F. Agbossou and A. Mortreux, *Tetrahedron Asym.*, **7**, 379, (1996).

- [21] T. Bürgi and A. Baiker, *J. Catal.*, **194**, 445, (2000).
- [22] J. A. Slipszenko, S. P. Griffiths, P. Johnston, K. E. Simons, W. A. H. Vermeer and P. B. Wells, *J. Catal.*, **179**, 267, (1998).
- [23] J. L. Margitfalvi, P. Marti, A. Baiker, L. Botz and O. Sticher, *Catal. Lett.*, **6**, 281, (1990).
- [24] [www.accelrys.com](http://www.accelrys.com)
- [25] [www.cachesoftware.com/mopac/](http://www.cachesoftware.com/mopac/)
- [26] A. Banerjee, N. Adams, J. Simons and R. Shepard, *J. Phys. Chem.*, **89**, 52, (1985). J. Baker, *J. Comp. Chem.*, **7**, 385, (1986). P. Culot, G. Dive, V. H. Nguyen and J. M. Ghuysen, *Theo. Chim. Acta*, **82**, 189, (1992).
- [27] [www.gaussian.com](http://www.gaussian.com)
- [28] [www.msi.uma.edu/software/gaussian98/details.html](http://www.msi.uma.edu/software/gaussian98/details.html)
- [29] [www.gaussian.com/g03.htm](http://www.gaussian.com/g03.htm)
- [30] A. D. Becke, *J. Chem. Phys.*, **98**, 5648, (1993).
- [31] C. T. Lee, W. T. Yang and G. R. Parr, *Phys. Rev. B*, **37**, 785, (1988).
- [32] M. A. Spackman and A. S. Mitchell, *Phys. Chem. Chem. Phys.*, **3**, 1518, (2001).
- [33] T. Bürgi, T. Droz and S. Leutwyler, *Chem. Phys. Lett.*, **246**, 291, (1995).
- [34] O. Schwalm, J. Weber, J. Margitfalvi and A. Baiker, *J. Mol. Struct.*, **297**, 285, (1993).
- [35] B. J. Oleksyn, *Acta Crystallogr.*, **B38**, 1832, (1982).
- [36] F. I. Carrol, P. Abraham, K. Gaetano, S. W. Mascarella, R. A. Wohl, J. Lind and K. Petzoldt, *Chem. Soc., Perkin Trans. 1*, **1**, 3017, (1991).
- [37] M. Schürch, O. Schwalm, T. Mallat, J. Weber and A. Baiker, *J. Catal.*, **169**, 275, (1997).
- [38] M. Schürch, N. Künzle, T. Mallat, J. Weber and A. Baiker, *J. Catal.*, **176**, 569, (1998).
- [39] D. A. G. Aranda, J. W. M. Carneiro, C. S. B. Oliveira, F. B. Passos, P. R. N. Souza and O. A. C. Antunes, *Braz. J. Chem. Eng.*, **18**, 3, (2001).
- [40] J. L. Margitfalvi and E. Tfirst, *J. Mol. Catal. A: Chemical*, **139**, 81, (1999).
- [41] G. D. H. Dijkstra, R. M. Kellogg and H. Wynberg, *J. Org. Chem.*, **55**, 6121, (1990).
- [42] A. Baiker, *J. Mol. Catal. A*, **163**, 205, (2000).
- [43] R. L. Augustine and S. K. Tanielyan, *J. Mol. Catal. A*, **112**, 93, (1996).

- [44] J. L. Margitfalvi, E. Tálás, E. Tfirst, C. V. Kumar and A. Gergely, *Appl. Catal. A*, **191**, 177, (2000).
- [45] M. von Arx, T. Mallat and A. Baiker, *Topics Catal.*, **19**, 1, 75, (2002).
- [46] J. L. Margitfalvi, M. Hegedüs and E. Tfirst, *Stud. Surf. Sci. Catal.*, **101A**, 241, (1996).
- [47] A. Rochefort and P. McBreen, *J. Phys. Chem. A*, **105**, 1320, (2001).
- [48] R. P. K. Wells, N. R. McGuire, X. Li, R. L. Jenkins, P. J. Collier, R. Whyman and G. J. Hutchings, *Phys. Chem. Chem. Phys.*, **4**, 2839, (2002).
- [49] A. Vargas, T. Bürgi and A. Baiker, *J. Catal.*, **197**, 378, (2000).
- [50] H. -U. Blaser, H. P. Jalett and J. Wiehl, *J. Mol. Catal.*, **68**, 215, (1991).
- [51] M. Castonguay, J. -R. Roy, A. Rochefort and P. H. McBreen, *J. Am. Chem. Soc.*, **122**, 518, (2000).
- [52] A. Vargas, T. Bürgi and A. Baiker, *New J. Chem.*, **26**, 807, (2002).
- [53] K. Borszeky, T. Mallat, A. Baiker, *Catal. Lett.*, **59**, 95, (1999).
- [54] T. Mallat, S. Szabo, M. Schürz, U. W. Göbel and A. Baiker, *Catal. Lett.*, **47**, 221, (1997).
- [55] T. J. Hall, P. Johnston, W. A. H. Vermeer, S. R. Watson and P. B. Wells, *Stud. Surf. Sci. Catal.*, **101**, 221, (1996).
- [56] Calculations have been carried out using PM3 on a CAChe Worksystem [73]
- [57] R. Partasarathy, J. Ohrt, A. Horeau, J. P. Vigneron and H. Kagan, *Tetrahedron*, **26**, 4705, (1970).
- [58] A. Solladié-Cavallo, C. Marsol, F. Hoernel and F. Garin, *Tetrahedron Lett.*, **42**, 4741, (2001).
- [59] K. P. C. Vollhardt, *Organic Chemistry*, WH Freeman and Company, New York. (1987).

## ***Chapter 6***

*A Comparative Density Functional Theory  
Study of the Adsorption of Ethene and  
Simple Ketones Over Group 10 Metal  
Surfaces, Using Two Alternative Plane-  
Wave Codes*

## 6.0. Introduction

Earlier in Chapter 2, the possibilities of ketones to rearrange *via* proton movement into vinyl alcohols through the process of *keto-enol* tautomerism were discussed. As implied in Chapter 5 and referenced in the available literature, the *enol* and corresponding enolate species (evidenced by surface RAIRS on Ni(111) [1]) could play a significant role as surface adsorbed intermediates in the enantioselective hydrogenation of  $\alpha$ -ketoesters and related structures. At present most mechanistic arguments for the model reactants ignore this concept (Chapter 2, sections 2.2.8-2.2.11).

To investigate the possible surface adsorbed intermediates and spectator species under experimental conditions in the hydrogenation reaction over Pd and Pt(111) surfaces, periodic DFT slab calculations were employed. This plane-wave approach has been chosen for the study of molecular adsorption [2] over the alternative DFT cluster method, as generally a better description of the electronic structure of the metals close to the actual experimental catalytic surfaces can be modelled, thus yielding adsorption data comparable to experimental values. This holds true for the adsorption of simple molecules such as H<sub>2</sub> [3,4], CO [5,6], NO [7,8], O<sub>2</sub> [9] and hydrocarbons: CH<sub>4</sub> [10] and C<sub>2</sub>H<sub>4</sub> [11].

Since simulation of the pyruvate structures using periodic techniques are computationally expensive the chemisorption of smaller *keto* containing molecules are studied. The simplest *keto* group containing molecule is formaldehyde, which with the addition of 2C and 4H atoms builds up to acetone. For acetone *keto-enol* tautomerism is possible, with the equilibrium favouring the *keto* form under acid and base catalysed conditions.

Two leading programs used routinely in computational chemistry for catalytic surface studies are the plane-wave periodic codes CASTEP and VASP, which were briefly reviewed in Chapter 4. Initially, in this work simulations for the effect of formaldehyde adsorption and the tautomerism of acetone on both Pd and Pt surfaces are performed using the CASTEP code. However, prior to this an investigation into the energetics of ethene over Pt(111) is used as a model system for a comparative study of VASP and CASTEP. Such a study will hopefully identify the most suitable programme to be used in further simulations of periodic intermediates in this thesis.

At present, extensive literature is available for the different theoretical approaches used to study chemisorption such as periodic vs. cluster, but comparison between different codes which essentially perform the same types of calculations is much more limited.

Throughout this work and where necessary all adsorption data will be compared to experimental and theoretically derived adsorption energies from the literature.

### 6.1. The Adsorption of Ethene on Pt(111)

The interaction of ethene with the (111) surface of Pt was chosen as a model system for the comparative study between the two codes because, firstly, the size of the molecule is representative of the molecules of the *keto* group to be explored in this work and secondly, it is a well researched area due to its importance in many catalytic processes, such as hydrogenation/dehydrogenation and isomerisation. The main study to be used as reference is the VASP work conducted by Watson *et al.* [12]. Using the computational procedure outlined in the reference and discussed in Chapter 4, section 4.3.1, periodic DFT calculations were performed to investigate six adsorption modes of ethene (bridge, *fcc* and *hcp* hollow, atop-bridge and -hollow and cross bridge (refer to figure 6.3 for the most stable sites) on Pt(111). The corresponding adsorption energies were found to compare well against experimentally derived values [12] and are presented in table 6.2.

These calculations were repeated using the CASTEP program. Initially the bulk *fcc* Pt unit cell (obtained from the Cerius<sup>2</sup> [13] resource library) was first optimised and then built up and cleaved using the Cerius<sup>2</sup> modules visualiser [14] and surface builder [15] to form a (111) index 3-layer Pt slab of dimensions  $p(2 \times 2)$ , with a 9.2 Å vacuum gap. The computations were performed under the same settings as specified in the reference work [12] *i.e.* a 300 eV plane-wave cutoff energy and a *k*-point sampling of  $9 \times 9 \times 1$  accelerated to convergence with the use of Methfessel-Paxton electron smearing [16]. Full relaxation of the adsorbing ethene and all of the atoms in the Pt slab were specified.

Prior to the introduction of ethene onto the surface, a comparison between the fully equilibrated bulk Pt cell against the corresponding VASP cell is essential to verify the

optimisation procedure in CASTEP. A comparison of the CASTEP derived bulk parameters against the literature values are provided in table 6.1.

Bulk Pt Models	Lattice Constant, $a$ , (Å)	Interlayer Pt Spacing (Å)
Cerius <sup>2</sup> experimental cell	3.9239	2.27
CASTEP	3.9755	2.30
VASP <sup>a</sup>	3.9837	2.30

**Table 6.1:** Relaxed lattice constants and interlayer surface atom spacing of bulk Pt. CASTEP computation performed using bulk modified periodic DFT parameters as specified in Chapter 4, section 4.3.1. <sup>a</sup>Data obtained from reference 12.

Relaxation results in the expansion of the bulk cell as a slight lengthening of the lattice constant is observed when compared against the corresponding experimental cell. For CASTEP, this translates to an expansion of 1.3% in both the lattice constant and the interlayer Pt spacings, when compared against the original experimental XRD cell obtained from the Cerius<sup>2</sup> library. However, Watson *et al.* [12] do not quote the dimensions of the experimental cell used in their study and so in comparison with the above cell, the lattice constant is found to enlarge by roughly 0.06 Å. These differences in lattice constant between the CASTEP and VASP bulk cells are within the expected error from DFT theory. There is no deviation between the measured interlayer spacings of the Pt planes in the two theoretically derived models, and consequently it appears that both programs are consistent in optimising the bulk. Most importantly, both models show excellent agreement with the LEED derived bulk Pt spacing of 2.26 Å [17], which helps to verify the theoretical method used. To ensure accuracy in adsorption energies the CASTEP derived lattice constant is used as the lattice constant in the surface calculations with CASTEP.

Surfaces are composed of atoms which do not have a full complement of neighbours, each surface atom in the (111) *fcc* plane of Pt and similar transition metals have 9 nearest neighbours compared with their normal coordination number of 12 in the bulk. The loss of 3 nearest neighbour bonds in the formation of the surface results from the “removal” of a layer of bulk atoms, as illustrated in figure 6.1.

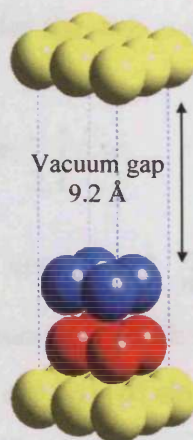


**Figure 6.1:** The CASTEP  $p(2 \times 2)$  Pt(111) surface used in the ethene adsorption studies, computed with the periodic DFT parameters as specified in Chapter 4, section 4.3.1. The surface atoms have lower coordination numbers than the related bulk atoms. The surface is formed by effectively removing a plane of bulk atoms. Surface layers are colour coded: first layer blue, second layer red, third layer and periodic image yellow.

In order for the surface to compensate for the “loss” of bonding, it may undergo “surface relaxation” in the form of an oscillatory change in the interlayer spacing, measured as a difference in the  $z$  coordinates of the highest-lying and lowest-lying metal atoms in the surface layer ( $\Delta z$ ), as shown in figure 6.4. In this process, to regain coordination, the first layer atoms tend to contract towards the second layer, to compensate the over coordination in this layer the third layer atoms respond by expanding away. The oscillation in  $\Delta z$  continues to further, penetrate deeper into the surface until, eventually the effect is completely damped. Consequently, this effect is found to affect the energy and morphology of the resulting surfaces. The effect of adsorption-induced surface corrugation is described in the appropriate results section.

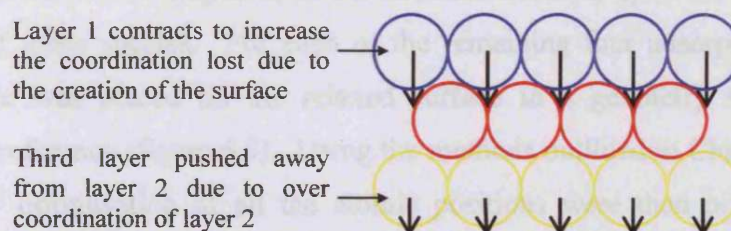


**Figure 6.2:** The effects of surface relaxation on atomic layers. Figure obtained from reference 18.

On relaxation of the  $p(2 \times 2)$  Pt surface the crystallographic structure was found to be different from that of the bulk as the interlayer spacing at  $2.27 \text{ \AA}$  was contracted by  $0.03$



Å. The CASTEP surface energy for the slab was calculated at 1.52 J m<sup>-2</sup> using the expression below:

$$E_{\text{surface}} = \frac{E_{\text{slab}} - \frac{n}{n'} E_{\text{bulk}}}{2A} \quad (\text{Equation 6.1})$$

where  $E$  represents the electronic energy and  $\frac{n}{n'}$  is the stoichiometric ratio of the number of surface atoms over the number of bulk atoms in the *fcc* cube.  $A$  denotes the surface area and is calculated from  $A = |\underline{a}| |\underline{b}| \sin 60^\circ$  measured in Å<sup>2</sup>. Both  $\underline{a}$  and  $\underline{b}$  are the unit cell dimensions in Å. The surface energy is originally obtained in units of eV Å<sup>-2</sup> and is converted *via* a series of steps into the common units of J m<sup>-2</sup>.

The surface energy of the reference slab is approximately 1.50 J m<sup>-2</sup> (as calculated from analogous VASP computations, Chapter 4, section 4.3.3) and is sufficiently lower compared to the CASTEP energy implying a more stable plane with enhanced surface atom coordination. For this surface an expansion in the interlayer spacing from the bulk value of 2.30 to 2.32 Å for the slab was observed, in good agreement with the expansion indicated by LEED experiments for the surface layer of a Pt(111) single crystal [17]. However, the CASTEP surface contradicts this behaviour as a 1.3% contraction is calculated. The fully relaxed Pt slab has an interlayer spacing of 2.27 Å compared to the calculated bulk spacing of 2.30 Å.

At this stage it is evident that the computer codes have produced different surfaces, which in theory should be identical. These differences are expected to carry on through into the estimation of adsorption energies for ethene, but to what extent, and the origin of them, is the concern of the following discussion.

Of the original six adsorption modes investigated by Watson *et al.* [12] the *fcc* and *hcp* hollow sites were not computed, as the authors remarked upon the uncertainty of the existence of these species. For each of the remaining four adsorption modes an ethene molecule was placed on the relaxed surface in a geometry similar to that obtained in the reference (figure 6.3). Using the methods outlined in Chapter 4, section 4.3.1, geometry optimisation of all the atomic positions were then performed using CASTEP.

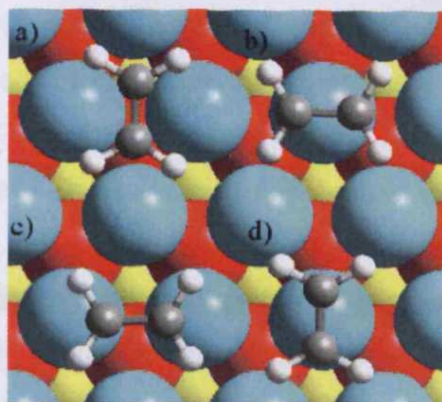


**Figure 6.3:** Schematic illustration of the four adsorption modes of ethene investigated: (a) cross bridge, (b) atop-bridge, (c) bridge and (d) atop-hollow. Surface layers and molecular atoms are colour coded: first layer blue, second layer red, third layer yellow, H white and C grey.

The calculation of adsorption energy,  $\Delta E_{ads}$  is used to measure the strength of the interaction of the molecule with the surface, and is provided by the expression:

$$\Delta E_{ads} = -(E_{adsorbate/surface} - (E_{surface} + E_{adsorbate})) \quad (\text{Equation 6.2})$$

Here the energy of the adsorbed molecule,  $E_{adsorbate/surface}$  is compared with that of the free surface,  $E_{surface}$  and the gas-phase molecule,  $E_{adsorbate}$ . The adsorption energy is simply the energy evolved on adsorption and is positive for exothermic adsorption. The resulting adsorption energies for the CASTEP ethene configurations are provided in table 6.2, with the corresponding reference values stated for comparison.

Coordination Geometry	Adsorption Energy ( $\text{kJ mol}^{-1}$ )	
	VASP <sup>a</sup>	CASTEP
Atop-bridge ( $\pi$ )	85.8	105.7
Atop-hollow ( $\pi$ )	84.8	103.9
Bridge (di- $\sigma$ )	127.3	143.3
Cross bridge	9.2	11.0

**Table 6.2:** Theoretical adsorption energies of ethene on Pt(111) calculated using equation 6.2. Computations performed using periodic DFT specified at theory level GGA-PW91 using computational parameters as specified in Chapter 4, section 4.3.1. <sup>a</sup>Literature values obtained from reference 12.

Both programs predict the same ordering in the relative adsorption energies. The cross bridge adsorbs ethene equidistant from two surface Pt atoms with the C-C bond parallel to the surface and perpendicular to the Pt-Pt direction (figure 6.3(a)). This

arrangement has ethene only weakly adsorbed with a binding energy of around  $10 \text{ kJ mol}^{-1}$ . The alternative  $\pi$  adsorbed modes, in which the molecule is coordinated to a single Pt atom, differ only in the orientation of the C-C bond relative to the neighbouring Pt atoms. For the atop-bridge alignment occurs with the bridge sites (figure 6.3(b)) whereas in the atop-hollow the molecule aligns with the hollow sites (figure 6.3(d)). Both programs point towards the iso-energetic nature of the two modes suggesting that realistically the orientation of the ethene in an atop site would not be fixed. The most favourable site for ethene is binding to the surface through the bridging mode where the two carbon atoms interact with separate Pt atoms forming di- $\sigma$  bonded species (figure 6.3(c)). A stronger adsorption *i.e.* a difference of  $16 \text{ kJ mol}^{-1}$  is given by CASTEP than VASP for this coordination. In fact, throughout the dataset CASTEP values appear to be much larger, although to varying degrees, than the corresponding VASP adsorption values. The largest discrepancies, up to 23%, are modelled in the two  $\pi$  adsorbed modes.

Upon chemisorption, it is typical for a molecular geometry to distort from its free gas-phase state into a new geometry, which accommodates the electronic influence of the surface. A number of geometric parameters are used to measure the extent of this distortion, and these are briefly summarised in figure 6.4.

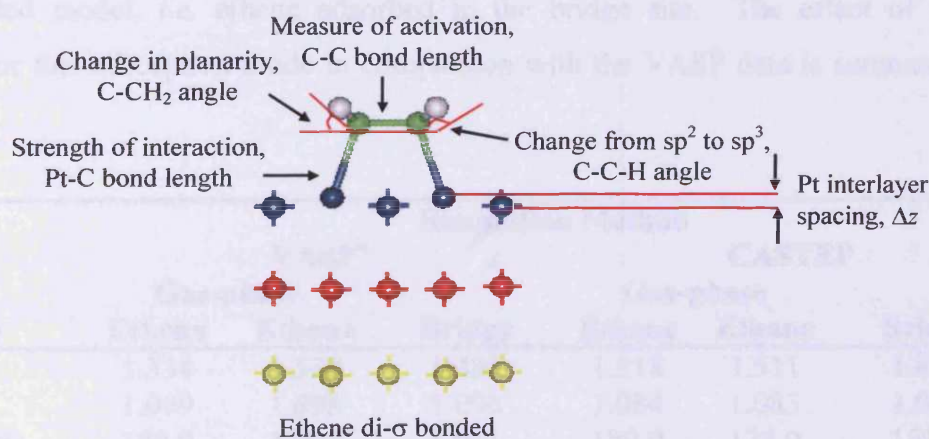


**Figure 6.4:** Schematic representation of the geometric parameters used to measure the extent of molecular distortion of a Pt adsorbed ethene molecule. Surface layers and molecular atoms are colour coded: first layer dark blue, second layer red, third layer yellow, H grey and C green.

Using ethene as the example, the C-C bond length is used to measure the degree of activation of the molecule as it indicates the extent of double bond character. This is expected to vary from the CASTEP gas-phase calculated values of  $1.318 \text{ \AA}$  for the



double bond of ethene and 1.511 Å for the single bond of ethane. These bond lengths, although slightly shorter, are found to be in agreement with the corresponding theoretical bond lengths from VASP (1.334 and 1.527 Å) [12] and the experimental values of 1.337 and 1.541 Å [19], respectively. Moving from double to single bond character can result in the planar nature of the molecule changing, by measuring the angle between the C-C bond and each of the CH<sub>2</sub> planes (the C-CH<sub>2</sub> angles) this can be monitored. For ethene, the degree of distortion away from the planar structure should range between 180° (gas-phase ethene) to 128.1° (gas-phase ethane). Accompanying this is the change in the C-C-H bond angle, which signifies the change from sp<sup>2</sup> to sp<sup>3</sup> hybrid geometries of the carbon atoms. The range this bond angle is expected to change by on adsorption is 10.7°, as the angles take the values of 122.2° for ethene and 111.5° for ethane. Finally, as an indication of the strength of the interaction of the molecule with the surface atoms, the Pt-C distance is measured, the stronger the interaction the shorter the distance.

Earlier, clear differences between the calculated adsorption energies for the four adsorption sites of ethene (table 6.2) were observed when compared with the corresponding VASP data. To investigate the effect on the structure of the adsorbed species, the geometric parameters discussed above were calculated for the most stable di-σ bonded model, *i.e.* ethene adsorbed in the bridge site. The effect of surface bonding for this adsorption mode in comparison with the VASP data is summarised in table 6.3.

Property	Simulation Method					
	VASP <sup>a</sup>			CASTEP		
	Gas-phase			Gas-phase		
	Ethene	Ethane	Bridge	Ethene	Ethane	Bridge
C-C (Å)	1.334	1.527	1.485	1.318	1.511	1.472
C-H (Å)	1.099	1.098	1.096	1.084	1.083	1.090
C-CH <sub>2</sub> <sup>b</sup> (°)	180.0	128.1	138.1	180.0	128.0	103.2
C-C-H (°)	122.2	111.5	112.1	122.0	111.3	114.6
Pt-C (Å)			2.117			2.099
Δz (Pt) <sup>c</sup> (Å)			0.235 (×2)			0.252/0.250
Pt interlayer spacing <sup>d</sup> (Å)			2.238			2.246

**Table 6.3:** Theoretical geometries of adsorbed ethene on Pt(111) as modelled by CASTEP and VASP using the computational parameters as specified in Chapter 4, section 4.3.1. <sup>a</sup>Literature values obtained

from reference 12. <sup>b</sup>Angle of C-C bond to CH<sub>2</sub> plane. <sup>c</sup>Displacement of coordinated Pt atoms from the surface plane. <sup>d</sup>Spacing between the first and second Pt layers of the surface.

In each case the C-C bond appears to be elongated from its gas-phase measurements in the adsorbed states. Greater lengthening of the bond is observed in the CASTEP simulated molecule compared with the VASP model, as the differences between the C-C bond lengths of the gas-phase structure with the adsorbed state is measured at 0.154 and 0.151 Å, respectively. As the extent of elongation indicates the di-σ nature of the bond, both VASP and CASTEP C-C bonds at 1.485 and 1.472 Å display a significant reduction in the double bond character and are closer to the bond length in ethane than ethene. Compared against the gas-phase data both adsorbed states display a considerable amount of distortion away from the original planar structures, at C-CH<sub>2</sub> angles of 138.1° (VASP) and 103.2° (CASTEP), the ethene molecules can be considered to begin mimicking the properties typical to gas-phase ethane (C-CH<sub>2</sub> angle of 128.1°). This distortion is accompanied by a change in the C-C-H bond angle and both adsorbed states clearly illustrate a marked change from sp<sup>2</sup> to sp<sup>3</sup> hybrid geometries of the carbon atoms (the trend being more apparent in the CASTEP system).

Overall the geometries from the two programs show general agreement and certainly lead to the same conclusions regarding the change of molecular geometry compared to the corresponding gas-phase data. However, the stronger interaction from CASTEP results leads to shorter Pt-C distances (2.099 Å) and a slightly more pronounced movement of the coordinated Pt atoms out of the surface plane (0.252/0.250 Å). This extraction of surface atoms causes a rumpling effect, as the rest of the surface layer contracts to reduce the interlayer spacing. The movement of the surface Pt atoms suggests that some repulsion occurs between the molecule and the surface, which is relieved by the directly coordinated Pt atom moving out of the surface. By doing so, the effective density of the surface layer is reduced which in turn lowers the strain of the surface by relaxing toward the bulk. However, contrary to the adsorption data this effect is more prominent for the VASP model as the Pt interlayer spacing is reduced from the reference surface value of 2.320 to 2.238 Å, whereas for CASTEP the corresponding layer spacings are 2.270 and 2.246 Å, respectively.

In summary, the degree of distortion of the geometry of ethene ties in well with the observation that the adsorption energies calculated by CASTEP are consistently greater than the corresponding values from VASP.

## 6.2. The Adsorption of Formaldehyde on Pd and Pt(111)

Experimentally, the chemisorption modes identified for formaldehyde are the two geometries termed the  $\eta^1$  or endon, in which the O lone pair of the molecule couples to the surface in a tilted or vertical fashion (figure 6.5(a)) and the  $\eta^2$  or di- $\sigma$  mode in which, similar to the ethene molecule, the C and O atom each interact with a separate surface atom with the C=O bond axis parallel to the surface plane (figure 6.5(b)). Recently, a variety of theoretical chemisorption models have confirmed these adsorption modes and a full discussion of the available literature is presented in Chapter 2, section 2.6.1.

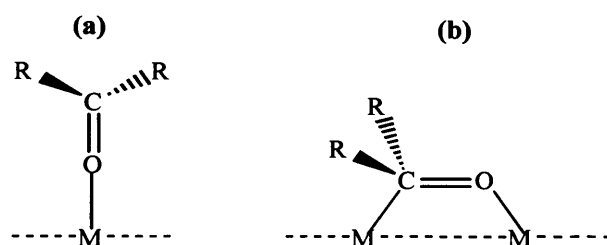


**Figure 6.5:** Surface bonding configurations of keto groups: (a)  $\eta^1(O)$  (endon) and (b)  $\eta^2(C,O)$  (di- $\sigma$ ).  $R = H$  or  $CH_3$  to give formaldehyde and acetone, respectively.  $M$  = surface metal atom.

Although, theoretically the dimensions of the unit cell used for the previous ethene calculations are sufficient to accommodate the chemisorption of formaldehyde, it lacks adequate metal sites for the adsorption of acetone and its *enol* tautomer. As the aim of this work is to collect a comparable dataset of adsorption energies for *keto* group functionalities, a new set of surfaces representing the (111) plane of Pd and Pt were generated.

As specified in Chapter 4, section 4.3.2, the new 3-layer surface slabs were increased to dimensions of  $p(3 \times 3)$ , so as to minimise the interaction of adsorbates with their periodic images. Sufficient convergence of the total-energies for these surface cells were found with the use of 5 Mönkhorst-Pack special  $k$ -points and a KE cutoff of 380 eV. The width of the vacuum gap was increased to 15 Å for reasons discussed in Chapter 4, section 4.3.3. As with the ethene surface, both the Pd and Pt surfaces were initially constructed using the surface builder module within the Cerius<sup>2</sup> interface and cleaved from their corresponding fully relaxed bulk *fcc* unit cells. Geometry

optimisations were performed as specified in Chapter 4, section 4.3.3, *i.e.* using the same DFT parameters as employed in the ethene study.

For these surfaces, the reference state used for the calculation of adsorption energies include fully relaxed Pd and Pt slabs that have an interlayer spacing of 2.28 Å and 2.29 Å compared to their calculated bulk spacings of 2.26 and 2.30 Å, respectively. The corresponding experimental values for the single (111) crystals determined by LEED experiments [17], show expansions of 1.3% from the bulk value of 2.246 to 2.276 Å for the surface layer of Pd and 0.9% from 2.26 to 2.28 Å for Pt. The optimised surface energies for the  $p(3 \times 3)$  Pd and Pt slabs were estimated at 1.20 and 1.57 J m<sup>-2</sup>, respectively, and were derived using equation 6.1.

The investigation into the adsorption of formaldehyde over these surfaces was conducted by copying the optimised gas-phase structure of the molecule into the periodic surface region and manipulating the structure so that it resembled firstly, the  $\eta^1$  mode and secondly, the  $\eta^2$  coordination as discussed earlier (refer to figure 6.5). In each calculation a good starting structure was modelled by closely associating the reacting adsorbate atoms with the corresponding surface atoms. These interactions were based loosely on the optimised Pt-C distances recorded for the ethene models (table 6.3). As with ethene, the calculations were set-up to allow full relaxation of the surface and the adsorbate. The optimised geometric and adsorption data for formaldehyde over the (111) surface of each metal is provided in table 6.4 and the corresponding structures are illustrated in figure 6.6.

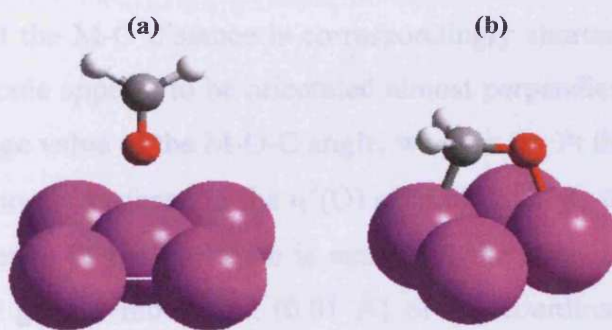


**Figure 6.6:** CASTEP adsorption geometries of formaldehyde: (a)  $\eta^1$ (O) and (b)  $\eta^2$ (C,O) on Pd(111). Most of the metal atoms have been removed for clarity. Geometry optimisations performed using periodic DFT specified at theory level GGA-PW91 using computational parameters as discussed in Chapter 4, sections 4.3.2 and 4.3.3. Note that the configurations on the Pt(111) surface are similar to those found for the Pd case but with only slight differences in the geometry (table 6.4) and so for this reason are not provided here. Molecular atoms are colour coded: Pd purple, H white, C grey and O red.

Property	Gas-Phase Formaldehyde	Surface Adsorption States			
		M = Pd		M = Pt	
		$\eta^1(\text{O})$	$\eta^2(\text{C,O})$	$\eta^1(\text{O})$	$\eta^2(\text{C,O})$
$\Delta E_{\text{ads}}$ (kJ mol <sup>-1</sup> )		13.2	60.3	41.2	77.6
C=O (Å)	1.210	1.228	1.347	1.215	1.304
O-CH <sub>2</sub> <sup>a</sup> (°)	180	180	148	180	137
M-C (Å)		3.527	2.117	3.007	2.107
M-O (Å)		2.320	2.040	2.149	2.039
M-O-C (°)		172	111	123	111
$\Delta z$ (M) <sup>b</sup> (Å)		0.059	0.120(C) 0.083(O)	0.068	0.155(C) 0.119(O)
Pt interlayer spacing <sup>c</sup> (Å)		2.242	2.236	2.860	2.300

**Table 6.4:** CASTEP adsorption energies and geometries of adsorbed formaldehyde on Pd and Pt(111). Periodic DFT computations performed using parameters and methodology as specified in Chapter 4, sections 4.3.2 and 4.3.3. <sup>a</sup>Angle between CO bond and CH<sub>2</sub> plane. <sup>b</sup>Displacement of coordinated metal (M) atom(s) from the surface plane. <sup>c</sup>Spacing between the first and second Pt layers of the surface.

Upon optimisation both the  $\eta^1$  and  $\eta^2$  adsorption modes are observed in both systems. The data implies that the oxygen atom of the formaldehyde in the  $\eta^1$  configuration is weakly coordinated to a single M atom compared to the alternative  $\eta^2$  mode. On adsorption in the  $\eta^1$  mode the molecular geometry of the formaldehyde remains almost planar with very little affect on the C=O bond length or the O-CH<sub>2</sub> angle. The distortion of the C=O bond from the gas-phase data (*i.e.* C=O 1.210 Å) is more pronounced on the Pd surface. The adsorption energy on Pt is 28 kJ mol<sup>-1</sup> greater than that for Pd and the M-O distance is correspondingly shorter by 0.171 Å. In the case of Pd the molecule appears to be orientated almost perpendicular to the surface, as evidenced by the large value of the M-O-C angle, whereas for Pt the C=O bond makes a much smaller angle to the surface. In the  $\eta^1(\text{O})$  adsorption mode the perturbation of the surface by the presence of the molecule is small but the stronger interaction with Pt results in a slightly greater movement (0.01 Å) of the coordinated metal out of the surface plane.

The optimised structures for the  $\eta^2$  adsorption geometries were found to be reminiscent of di- $\sigma$  bonded ethene. In these structures the molecular plane of the formaldehyde was found to be parallel to the surface. This was indicated by the O-CH<sub>2</sub> angles and the M-C and M-O interactions taking up the additional coordination sites for



each C and O atom. In this adsorption state the more electronegative oxygen atom tends to form shorter bonds than the carbon atom to the surface. As in the  $\eta^1$  case, the adsorption was found to be greater on Pt than on Pd for the  $\eta^2$  adsorbed states by 17.3 kJ mol<sup>-1</sup>. This was accompanied with greater movement of the coordinated surface atoms out of the surface plane. However, the extension in the C=O bond compared to the gas-phase bond length was more apparent in the Pd case than the more strongly adsorbed Pt state.

To summarise the Pt metal appears to be more reactive than the Pd surface as in each calculation greater adsorption energies with generally, shorter and stronger interactions are observed. Of the two adsorption modes greater stability of the formaldehyde in the  $\eta^2(\text{C},\text{O})$  configuration far exceeds the  $\eta^1(\text{O})$  mode. For Pd, the difference between the adsorption energies of each species equates to 47.1 kJ mol<sup>-1</sup>, whereas for Pt the gap reduces to 36.4 kJ mol<sup>-1</sup> because of its more reactive nature.

### 6.3. The Adsorption of Acetone on Pd and Pt(111)

The adsorption of acetone on metal surfaces is an interesting topic, with regard to the adsorbate as a possible intermediate in hydrogenation catalysis all possible adsorption modes must be investigated. As discussed in Chapter 2, section 2.6.3, either acid or base catalysed conditions can trigger *keto-enol* tautomerism, in which rearrangement of a single proton yields a vinyl alcohol. Such isomeric forms are well known for acetone (figure 6.7) and studies investigating the equilibrium are well documented [20-22].

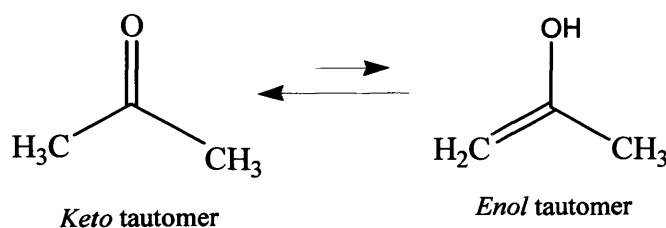


**Figure 6.7:** *Keto-enol* tautomerism for acetone.

Prior to surface calculations, it is important to comment upon the energies of the *keto* and *enol* isomers of acetone, in the gas-phase the equilibrium is known to strongly favour the *keto* form with less than 0.1% of a given sample to be occupied by the *enol*

structure [23]. The energetics modelled by CASTEP will theoretically illustrate the direction in which the equilibrium lies.

Optimisations of the gas-phase structures were performed using the same computational parameters as used in the formaldehyde study. Each calculation was performed using the same size periodic box to be used in the corresponding surface calculations, although with no metal atoms present, as consistency is imperative to obtain accurate results. In the gas-phase, the DFT calculations estimate the *keto-enol* energy difference to be just under  $51 \text{ kJ mol}^{-1}$  favouring the ketone form.

The bias of the equilibrium towards the *keto* isomer implies that there are two possible scenarios for surface adsorption, as summarised in figure 6.8. In the first situation the *enol* may well have a higher adsorption energy than the *keto* isomer but if the energy does not overcome the gas-phase difference then the ketone remains the thermodynamically favoured species on the surface (figure 6.8(a)). However, if the *enol* adsorption energy is sufficiently greater than the ketone to overcome the gas-phase difference, then the *enol* will become the thermodynamically preferred adsorbed state, refer to figure 6.8(b).

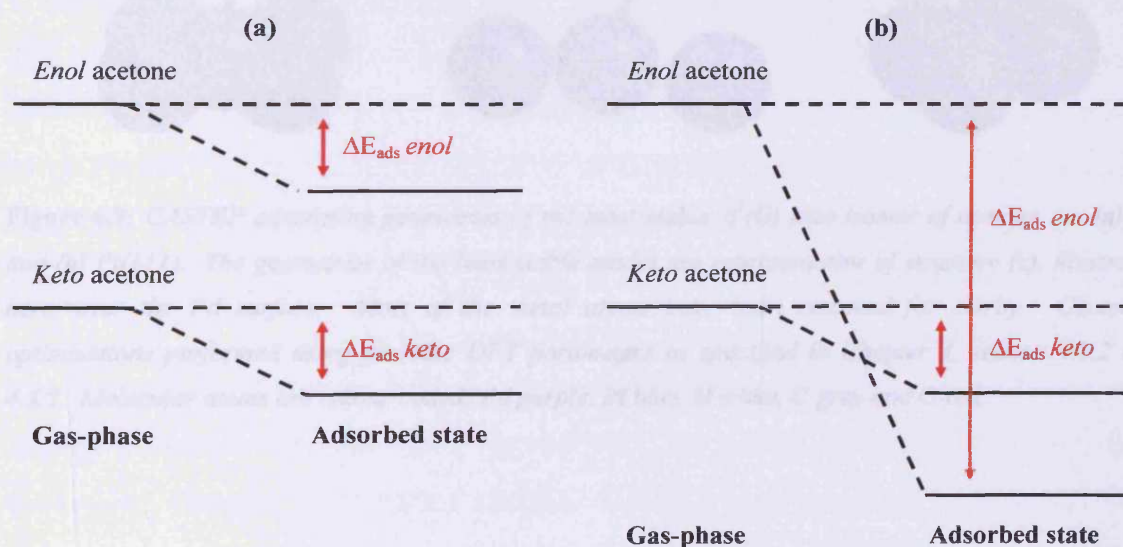


**Figure 6.8:** Possible scenarios for the adsorption of the keto-enol energetics of acetone: (a) keto isomer and (b) enol isomer preferred adsorbed states. Energy profiles not drawn to scale.

For acetone, surface calculations are performed for three different adsorption modes, as with formaldehyde the corresponding  $\eta^1$  and  $\eta^2$  coordinations are investigated as well as the *enol* species. The *enol* is expected to interact with the surface in a manner similar to that of the  $\eta^2$  state observed for formaldehyde, *i.e.* upon chemisorption, the C

atoms of the C=C bond should attain an  $sp^3$ -like hybridised geometry implying a single C-C bond bridged over two adjacent metal atoms.

All calculations were performed in an analogous fashion to that specified in the formaldehyde investigation (refer to section 6.2) using the computational parameters outlined in Chapter 4, sections 4.3.2 and 4.3.3. To obtain a complete dataset for the adsorption of acetone the investigation was carried out over Pd and Pt(111) surfaces. The resulting optimised geometry and binding data for the *keto* isomer of acetone adsorbed on both metals is provided in table 6.5. Of the adsorption modes investigated only the most stable species on the alternative metals are provided in figure 6.9, however the structure of the  $\eta^1(O)^a$  species on Pd is included to illustrate the differences between the optimised geometries.

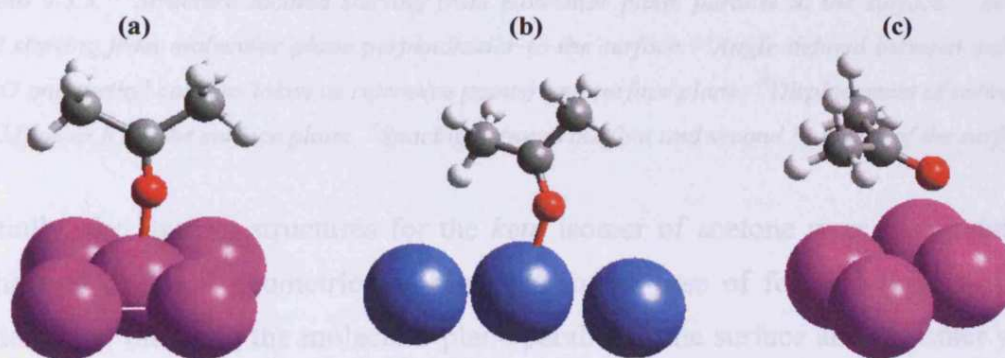


**Figure 6.9:** CASTEP adsorption geometries of the most stable  $\eta^1(O)$  keto isomer of acetone on: (a) Pd and (b) Pt(111). The geometries of the least stable modes are representative of structure (c), illustrated here, over the Pd surface. Most of the metal atoms have been removed for clarity. Geometry optimisations performed using periodic DFT parameters as specified in Chapter 4, section 4.3.2 and 4.3.3. Molecular atoms are colour coded: Pd purple, Pt blue, H white, C grey and O red.

Property	Gas-Phase <i>Keto Acetone</i>	Surface Adsorption States			
		M = Pd		M = Pt	
		$\eta^1(\text{O})^a$	$\eta^1(\text{O})^b$	$\eta^1(\text{O})^a$	$\eta^1(\text{O})^b$
$\Delta E_{\text{ads}}$ (kJ mol <sup>-1</sup> )		18.8	20.8	12.9	42.9
C=O (Å)	1.222	1.237	1.226	1.233	1.241
O-Me <sub>2</sub> /M <sup>c</sup> (°)		29	87	29	89
M-C (Å)		3.126	3.367	3.302	3.257
M-O (Å)		2.353	2.154	2.655	2.198
M-O-C (°)		134	169	141	142
$\Delta z$ (M) <sup>d</sup> (Å)		0.114	0.052	0.042	0.154
Pt interlayer spacing <sup>e</sup> (Å)		2.236	2.239	2.302	2.308

**Table 6.5:** CASTEP adsorption energies and geometries of adsorbed keto isomer of acetone on Pd and Pt(111). Periodic DFT computations performed using parameters as specified in Chapter 4, sections 4.3.2 and 4.3.3. <sup>a</sup>Structure located starting from molecular plane parallel to the surface. <sup>b</sup>Structure located starting from molecular plane perpendicular to the surface. <sup>c</sup>Angle defined between molecular plane (O and methyl carbons taken as reference points) and surface plane. <sup>d</sup>Displacement of coordinated metal (M) atom from the surface plane. <sup>e</sup>Spacing between the first and second Pt layers of the surface.

Initially, the starting structures for the *keto* isomer of acetone were manipulated so that the two different geometries as observed in the case of formaldehyde would be considered *i.e.* one with the molecular plane parallel to the surface and the other with it perpendicular. However, for acetone both of these alternatives lead to a  $\eta^1(\text{O})$  or endon optimised final geometry, the di- $\sigma$  bonding mode was not observed. For both metals the final geometries differ in the orientation of the molecular plane with respect to the surface with the parallel starting point leading to a smaller O-Me<sub>2</sub>/M angle. In the Pt case the optimise structures differ in adsorption energy by 30 kJ mol<sup>-1</sup> even though both are best described as  $\eta^1$  adsorption geometries. The greatest geometric difference is in the O-Me<sub>2</sub>/M angle, in the higher adsorption energy structure this is close to 90° with one methyl group closer to the surface than the other (figure 6.9(b)). The lower energy structure has the O-Me<sub>2</sub>/M angle close to 30° and the methyl groups similar distances from the surface (figure 6.9(c), shows the analogous structure over Pd). A similar preference can be seen for the Pd calculations although the energy difference is less pronounced (figures 6.9(a) and (c)).

The strength of the molecular adsorptions are reflected in the movement of the bonding metal atoms pulled out of the surface planes, this is more apparent in the Pt



case as a difference of 0.112 Å is noted for the two  $\eta^1$  modes. Due to the similarities in the adsorptions over the Pd metal, similar adsorbate induced surface corrugations are observed (average interlayer spacing for the two surfaces, 2.238 Å), whereas the differences are more apparent in the Pt case. The interlayers of the Pt surface are very slightly more contracted in the weakly adsorbed  $\eta^1(\text{O})^a$  adsorption compared to the  $\eta^1(\text{O})^b$  species, as the corresponding  $\Delta z$  values are 2.302 and 2.308 Å, respectively.

However, upon adsorption a significant change in the length of the C=O double bond is observed for all species. Initially, upon binding with the surface the C=O bond of the molecule is found to expand, implying stabilisation of the acetone through electron donation from the oxygen lone pair orbital. The largest expansion compared to the gas-phase C=O bond length of 1.222 Å is observed in the  $\eta^1(\text{O})^b$  adsorption on the Pt surface, which ties in well with the observed adsorption energy.

To summarise, the *keto* acetone is found to remain planar on adsorption on both metal surfaces, and the bonding is thought to occur *via* a weak interaction between the oxygen lone pair and a single metal atom. For the  $\eta^1(\text{O})^b$  endon species the Pt surface appears to be much more reactive than the Pd one, this trend is reversed for the alternative  $\eta^1(\text{O})^a$  adsorption mode.

For the adsorption of the *enol* isomer the acetone was found to optimise through the expected  $\eta^2(\text{C,C})$  on the Pd(111) surface (figure 6.10(a)). However, this geometry was not achieved on the corresponding Pt surface as the molecule ended in a structure reminiscent of the endon configuration of the *keto* isomer (figure 6.10(b)). A summary of the calculated adsorption energies and geometric data of the *enol* isomer investigated on both metals is provided in table 6.6.

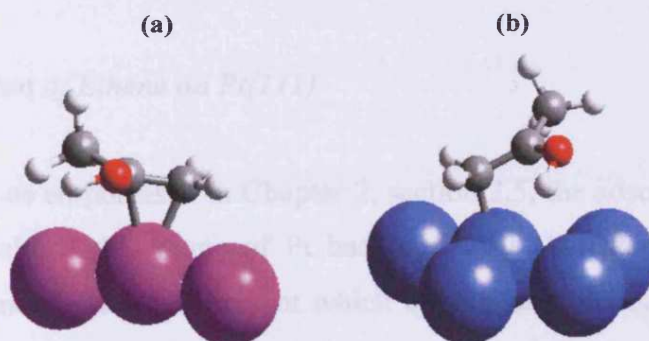


**Figure 6.10:** CASTEP adsorption geometries of the *enol* isomer of acetone on: (a) Pd and (b) Pt(111). Most of the metal atoms have been removed for clarity. Geometry optimisations performed using

periodic DFT parameters as specified in Chapter 4, section 4.3.2 and 4.3.3. Molecular atoms are colour coded: Pd purple, Pt blue, H white, C grey and O red.

Property	Surface Adsorption States	
	M = Pd $\eta^2(\text{C,C})^a$	M = Pt $\eta^1(\text{C})$
$\Delta E_{\text{ads}}$ (kJ mol <sup>-1</sup> )	71.1, {21.1} <sup>b</sup>	117.5, {66.5} <sup>b</sup>
C-OH (Å)	1.362	1.304
C-CH <sub>2</sub> <sup>c</sup> (°)	156	139
C-CCO <sup>c</sup> (°)	163	176
M-C (Å)	2.180/2.312	2.130/2.804
M-C-C (°)	77	103
$\Delta z$ (M) <sup>d</sup> (Å)	0.286	0.190
Pt interlayer spacing <sup>e</sup> (Å)	2.233	2.306

**Table 6.6:** CASTEP adsorption energies and geometries of adsorbed enol isomer of acetone on Pd and Pt(111). Periodic DFT computations performed using parameters as specified in Chapter 4, section 4.3.3. <sup>a</sup>Both atoms coordinate to a single Pd atom. <sup>b</sup>Adsorption energy relative to the gas-phase keto isomer of acetone shown in braces. <sup>c</sup>Angle formed by the plane of three atoms and the bond indicated by dash. <sup>d</sup>Displacement of coordinated metal (M) atom from the surface plane. <sup>e</sup>Spacing between the first and second Pt layers of the surface.

In the case of Pd the adsorption energy relative to the ketone gas-phase isomer is close to the favoured endon adsorption of the *keto* isomer from table 6.5. This suggests that both *keto* and *enol* isomers will be present on the Pd surface at thermodynamic equilibrium. From the calculated adsorption energy of the *enol* and *keto* isomers on the Pt surface it appears that the *enol* form should be strongly favoured on Pt(111).

## 6.4. Discussion

### 6.4.1. The Adsorption of Ethene on Pt(111)

Experimentally, as emphasised in Chapter 2, section 2.5, the adsorption behaviour of ethene over the stable (111) plane of Pt has been well characterised [24]. At low temperatures,  $\pi$ -bonded ethene is present which upon heating transforms to a strongly chemisorbed di- $\sigma$  mode, the formation of which is considered to be an activated process. This temperature dependence is reflected extremely well in the calculated adsorption energies. The most stable mode investigated was the di- $\sigma$  adsorption at a

bridge site followed by the  $\pi$  mode adsorbed at the two atop sites. The difference in stability equates to around  $38 \text{ kJ mol}^{-1}$ . The iso-energetic behaviour of the two top sites implies that experimentally the orientation of the  $\pi$ -bonded ethene would not be fixed. The least stable site, the cross bridge, in which ethene is found to very weakly interact using a combination of both  $\pi$  and di- $\sigma$  electron density (*i.e.*  $\pi$  interaction with the second layer Pt atom of the *hcp* hollow site directly beneath the plane of the molecule and di- $\sigma$  stabilisation with the surrounding first layer Pt atoms, figure 6.3(a)) is very unlikely to be observed experimentally.

On comparison against experimental data the calculated adsorption energies of  $104.8 \text{ kJ mol}^{-1}$  (average) for the  $\pi$  adsorption and  $143.3 \text{ kJ mol}^{-1}$  for the di- $\sigma$  are within the upper limit of  $203 \text{ kJ mol}^{-1}$  obtained from collision-induced desorption studies [25]. However, these values are much higher than those estimated by VASP calculations, as the corresponding energies are  $85.8 \text{ kJ}$  and  $127.3 \text{ kJ mol}^{-1}$ , respectively [12]. Closer agreement is found to exist between the CASTEP data and the microcalorimetric energies of  $136 \text{ kJ mol}^{-1}$  for the di- $\sigma$  and  $120 \text{ kJ mol}^{-1}$  for a mixture of  $\pi$  and di- $\sigma$  adsorbed ethene on the more reactive (110) surface [26], and the measured value of  $120 \text{ kJ mol}^{-1}$  for a mixed  $\pi$ /di- $\sigma$  adsorption on Pt powders [27,28].

The optimised geometries of the adsorbed ethene are also in agreement with the available surface science results. EELS [29], UPS [30] and NEXAFS data [31,32] all point towards a “bridging” adsorption mode, with a C-C bond length of approximately  $1.50 \text{ \AA}$ . The corresponding bond length of  $1.472 \text{ \AA}$  (refer to table 6.3) calculated by the CASTEP program for the di- $\sigma$  mode is in excellent agreement with the experimental value and found to be closer to the gas-phase ethane ( $1.541 \text{ \AA}$ ) than ethene ( $1.337 \text{ \AA}$ ).

The observed elongation of the C=C bond, implies a reduction of the bond order and strengthening of the surface-adsorbate bonds in the di- $\sigma$  mode which can be explained in terms of a simple bonding model. In this coordination, ethene chemisorbs onto the Pt surface by forming two Pt-C dative  $\sigma$  bonds with associated loss of the initial  $\pi$  bond. Since ethene is a weak base the bonds are stabilised by an additional bonding contribution *i.e.* back-donation of electron density from the metal to the ethene. This occurs with electron transfer into the molecular  $\pi^*$  orbital which has the right symmetry for effective overlap with occupied Pt *d*-orbitals. The net result of this back-donation of electron density, known as the Dewar-Chat-Duncanson model [33] is the significant change in the structural geometry of the adsorbed molecule. The stabilisation of the

atop mode of ethene can be explained in terms of this model by a simultaneous back-donation and  $\pi$ -donation of electron density.  $\pi$ -Donation implies the transfer of electron density from the  $\pi$  orbitals of the C-C double bond into an empty Pt  $d$ -orbital. In the atop case donation/back-donation must be much weaker since molecular planarity is not lost.

Although much of the data implies that the di- $\sigma$  adsorption of ethene on the bridge site of the Pt(111) surface is the most stable of the alternatives considered, it is important to be aware of the fact that recent diffuse LEED data at 200 K, suggests the di- $\sigma$  molecule to be preferentially adsorbed on the *fcc* hollow site with a C-C bond length of  $1.56 \pm 0.5$  Å. Whether this is a realistic adsorption mode is a matter of debate as the uncertainty in the atom positions in the experimental study were large.

However, with use of the theoretical model referenced in Chapter 4, section 4.3.1, Watson *et al.* [12] investigated the *fcc* hollow adsorption along with the alternative at the *hcp* hollow site. The calculated adsorption energies were quoted as 74.7 and 71.7 kJ mol<sup>-1</sup>, respectively. Although, not as stable as the bridge mode or the  $\pi$ -bonded atop sites significant stabilisation compared to the cross-bridge site is observed (table 6.2).

The uncertainty of the presence of the adsorption at the hollow sites lead to a neglect of them in this work, by simplifying the investigation it was decided that the energetics of adsorption at the remaining four sites of Watson's study (figure 6.3) were enough to help discriminate the differences between the two similar codes, CASTEP and VASP.

Although the same, periodic DFT method as used by Watson *et al.* [12] was applied to the CASTEP investigation of ethene, significant differences between the CASTEP and VASP adsorption energies were noted. Both programs were consistent in predicting the same trend in adsorption *i.e.* the bridge site more stable than the atop followed by the cross bridge (table 6.2). However, the binding energies of ethene were found to be consistently overestimated by between 10 and 20% by CASTEP, compared to the analogous VASP energies, which were previously shown to be in good agreement (considering the error associated with DFT) with the available thermodynamic data [12]. Since the calculated adsorption energy depends on the adsorbate structure and on the reference states of the free surface and free molecule the observed difference may be due of any or all three of these calculations.

Both programs are consistent in relaxing the bulk *fcc* unit cell of Pt to a degree in which the interlayer atom spacings are identical (refer to table 6.1). However this is not



the case for the optimisation of the surface slab. Upon relaxation, a contraction of the interlayer spacing is observed for the CASTEP  $p(2 \times 2)$  Pt surface whereas the analogous VASP slab gives an expansion of the interlayer spacing. The loss of surface expansion was noted to contradict the surface LEED experiments carried out on a single Pt(111) crystal [17]. The contraction of the surface is symptomatic of a general overbinding in the CASTEP results. This is also evident from the general trend for shorter molecular bonds in the CASTEP results for both the adsorbed structures and reference gas-phase calculations (table 6.3).

Although the origin of the difference in the calculated data has been deduced, the root of the problem was not initially evident. Theoretically, both programs perform the surface calculations in the same way, *i.e.* the system is modelled by using the supercell approach with PBC. The periodic calculations then take advantage of calculation in  $k$ -space through FFT techniques employed in expansions of both the electronic wavefunctions, expressed in terms of a plane-wave basis set, and the potential generated by the nuclei. The theoretical concepts behind this calculation procedure are discussed in Chapter 3.

The main source of error in the energies can be linked to differences in the norm-conserving pseudopotentials (NC-PP) [34] used. In each set of calculations, Vanderbilt US-PPs [35] were employed to represent the interaction of the valence electrons with the ionic core. The advantage of using the US-PPs is to reduce the plane-wave cutoff needed for elements that would be described by hard NC-PPs. As essentially it is difficult to generate NC-PPs for first row elements such as O, N, F and transition metals as very large plane-wave basis sets are required to accurately represent the contracted  $p$  and  $3d$  orbitals, respectively. To yield sufficiently converged results, the PP require cutoffs of more than 70 Ry.

In Vanderbilt's "ultrasoft" approach the normalised charge density is the sum of the two terms: a soft part represented in terms of smooth orbitals and a hard part which is treated as an augmented charge. For a concise summary of the parallel implementation of the Car-Parrinello scheme [36] using US-PPs used in both programs consult reference [37,38].

Although, initially the same type of PP were used in both sets of calculations, they are found to differ in the way in which they are derived and treated within the calculations. In the CASTEP case, standard US-PPs used to describe the Pt, C and H

atoms were obtained from the Cerius<sup>2</sup> CASTEP library [39]. They were originally generated for CASTEP version 3.2 and were used in this case with the 4.2 academic version of the code. The US-PPs for the atoms were generated with the settings suggested by Prof. Lee's group [40] (refer to Appendix B) and were shown to adequately converge the lattice constants and bond lengths of a number of systems using GGA corrected DFT calculations with the "PRECISE" cutoff value of 300 eV. Validation tests for the Pt US-PP showed a deviation of 1.2% in the lattice constant  $a$  when compared against the experimental unit cell of Pt. This expansion is in agreement with the 1.3% modelled in our calculations, refer to table 6.1. However, larger discrepancies were observed in the analogous calculations performed to test the C US-PP, a difference of 4.5% in the lattice constant  $c$  was observed for graphite. This is not unexpected as the dispersion forces, which hold together graphite sheets are poorly represented in DFT.

As evident from the calculations performed in this work, the systematic inconsistency noted at the validation procedure for the CASTEP US-PPs is found to continue through into subsequent GGA surface calculations. Irrespective of user selection of LDA or GGA functionals, the PP's are generated using LDA. For GGA calculations, problems arise because essentially the core is modelled using LDA.

Although LDA is well known to accurately model structural properties such as bulk moduli, bond lengths and lattice constants for crystalline compounds, it overestimates cohesion energies [41] *i.e.* the energy of the solid with respect to infinitely separated constituent atoms. Consequently, LDA generally overbinds atoms in most types of model systems and causes the bond energies to be exaggerated. The reasons for this are quite simple, while LDA is successful in describing regions of high electron density near the core it fails to properly describe the decay of the electron density in the low region, *i.e.* wavefunction tails. As a result, tightly bonded systems such as solids are treated well whereas weakly interacting particles and surface adsorbed systems are not.

To correct the deficiency in LDA, *i.e.* calculation of bonds that are too short, the GGA functional is used. By incorporating a dependence on the gradient of the electron density, the exponential decay in the low density region can be more accurately described. In theory, the use of the GGA should help to improve and possibly overshoot the calculated bond energies (resulting in too long bonds). However, although it is fairly well established that gradient corrected methods are superior to

LDA for surface applications and systems with H-bonded components, it appears that in this case the results are unacceptable.

In principle, when GGA is used in solid-state systems with LDA-generated pseudopotentials (referred to here as a “mixed” approach), the GGA correction should be smaller than calculations employing GGA and GGA-generated pseudopotentials, as employed in the VASP calculations conducted by Watson *et al.* [12]. The latter fact helps to explain why most of the time the “mixed” approach works better than either methods employing LDA and LDA-generated PPs or GGA and GGA-generated PPs. The derived energies and bond lengths are estimated somewhere in the middle range between the two limits and is often observed to be closer to experiment. Although, this is expected, it appears that, in this case, the estimation of bonds in molecules with use of the GGA and GGA-generated PPs (Watson *et al.* [12]) works much better than the “mixed” approach of GGA and LDA-generated PPs employed in the CASTEP calculations, as the results are pulled towards the LDA overbinding. This overestimation is not good as the CASTEP results of ethene adsorption are clearly in poor agreement with the available experimental and VASP data.

In an attempt to try and improve the accuracy of surface calculations with CASTEP, our initial findings were reported to the program developers. Correspondence *via* Krokidis [42] (PI-IMI representative), lead to a series of test calculations performed by his colleague Milman [43]. With the use of a later version of CASTEP a repeat of the Pt calculations were carried out. When calculations were performed with GGA-PPs, Milman found CASTEP to model the bulk Pt (3.959 Å) much better than VASP (3.984 Å), which pointed towards “underbinding”. However, with the use of an all electron method *i.e.* no PPs, relaxation correctly showed an expansion from the bulk value of 2.286 to 2.312 Å for the surface layer of Pt(111) in accordance with the 0.9% expansion reported in LEED experiments [17] and the VASP study [12]. This expansion contradicts the contraction modelled in our calculations *i.e.* from 2.297 to 2.267 Å, when using LDA-PPs, which is clearly wrong. In principle, these test calculations prove the ability of the CASTEP code to model surface applications within the limits of DFT.

However, to amend the problem of overbinding in our data, since the GGA-PPs as used by Milman are not implemented within the program version available, he does suggest using a different approach to model the surface. As used in the test calculations, a 6-layer slab to represent the surface with the two bottom layers held

fixed is recommended. However, earlier work within the group (discussed in Chapter 4, section 4.3.3) tested the number of surface layers as well as the protocol of fixing the slab bottom and found that a fully relaxed slab employing 3-layers was sufficient to give adsorption data comparable to experimental values [44]. For this reason, and for advantages of simplification of the calculations, such a surface was employed in our calculations.

Although, a good comparison between the two periodic models for ethene adsorption has been provided here, it is perhaps necessary to compare the CASTEP data with corresponding cluster models, as this will put into context where the CASTEP results lie. With the use of a 10-atom cluster simulated using DFT with the B3LYP exchange and correlation functional, Watwe *et al.* [45] calculated the adsorption energies of the di- $\sigma$  and  $\pi$  modes to be 149 and 103 kJ mol<sup>-1</sup>. Surprisingly, excellent agreement between these values and the corresponding CASTEP energies exist, with calculated differences of 5.7 and 2.7 kJ mol<sup>-1</sup>, respectively. Obviously, a clear overestimation in the values are observed when compared against the more respectable periodic energies calculated by Watson *et al.* [12].

The large adsorption energies derived from the cluster calculations were rationalised in terms of the ethene interacting directly with Pt atoms from the cluster edge, which are considered to be more reactive than those of an extended (111) crystal surface. However, further calculations by the same group [28] illustrated how cluster size affects adsorption energies as a larger cluster of 19-atoms was found to reduce the energies of the two adsorbed species to 116 and 71 kJ mol<sup>-1</sup>, making them more comparable against periodic calculations in which the substrate is better modelled.

One of the major outcomes of Watson's study [12] was the effect  $k$ -point sampling and surface relaxation has on the convergence of energy. Low  $k$ -point sampling and insufficient relaxation was found to model the metal band structure poorly, which ultimately causes the adsorption energies to be overestimated. With this in mind it is fair to comment on the possible nature of periodic calculations to behave like cluster models if the above two factors apply. Clearly, such an explanation could account for the observed similarity between the CASTEP results and the cluster energies of Watwe *et al.* [28,45].

#### 6.4.2. The Adsorption of Formaldehyde on Pd and Pt(111)

Unlike ethene, it is extremely difficult to experimentally characterise the adsorption of formaldehyde on transition metals because the species are highly reactive and either decompose at roughly 170 K *via* C-H bond cleavage to produce adsorbed CO and surface H or polymerise to form paraformaldehyde [46]. However, the available literature has clearly emphasised two stable adsorption modes for formaldehyde, the  $\eta^1$  (endon) and the  $\eta^2$  (di- $\sigma$ ) (as discussed earlier, section 6.2).

Upon optimisation both modes of adsorption were found to be stabilised on both the Pd and Pt(111) surfaces. In both cases the  $\eta^2$  formaldehyde resembled the di- $\sigma$  adsorption mode found for ethene on Pt(111), with both the C and O atoms interacting with single separate surface atoms in a bridged geometry. This adsorption mode was significantly stabilised compared to the  $\eta^1$  on both metals. There is a stronger attraction of the formaldehyde to the Pt(111) surface than the analogous Pd plane. The adsorption energy of the di- $\sigma$  formaldehyde over Pd and Pt was calculated to be 60.3 and 77.6 kJ mol<sup>-1</sup>. These values appear to be greater than those derived from TPD experiments. The estimated adsorption energy of formaldehyde on Pd(111) is 51 kJ mol<sup>-1</sup> [46], which is similar to the value derived for the analogous Pt surface, at 52 kJ mol<sup>-1</sup> [47]. Closer agreement between the theoretically derived value and the experimental data exists for the Pd surface as the difference in the overestimation translates to 18%, which is 31% smaller than the Pt case. However, for Pt, the CASTEP adsorption energy for the  $\eta^1$  mode is closer at 41.2 kJ mol<sup>-1</sup> to the TPD estimate than the stable  $\eta^2$  geometry.

Although, experimental data for formaldehyde adsorption is lacking, sufficient theoretical data is available for comparison (refer to Chapter 2, section 2.6.1 for details). However, most studies investigate formaldehyde in the context of adsorbed intermediates for the dehydrogenation of methanol. One in particular, is the periodic DFT investigation carried out by Desai *et al.* [48]. With the use of the VASP program, the di- $\sigma$  adsorption energies for formaldehyde over Pd and Pt(111) were estimated at 54 and 49 kJ mol<sup>-1</sup>. These values are found to be in excellent agreement with the available TPD estimates, and clearly emphasise the overbinding of formaldehyde with CASTEP.

Despite the significant differences in the calculated adsorption energies, the geometries of the adsorbed  $\eta^2$  species on the Pt(111) surface modelled by the two programs are well matched. Both codes optimise the formaldehyde with the carbonyl

group orientated roughly parallel to the metal surface with the hydrogen atoms directed away from the surface. The resulting Pt-C and Pt-O bonds in the CASTEP model are measured at 2.107 and 2.039 Å, respectively, which correlate well, although slightly shorter against Desai's analogous lengths of 2.12 and 2.06 Å [48].

The full effect of surface binding is reflected in the extent of surface corrugation. For the di- $\sigma$  adsorbed formaldehyde on Pt, the interlayer spacing calculated by CASTEP is 2.3 Å whereas the analogous separation simulated in the VASP model is much smaller at 0.11 Å, implying a higher degree of surface contraction due to a larger surface-adsorbate repulsion. This observation ties in well with the calculated adsorption energies *i.e.* di- $\sigma$  binding estimated to be stronger in the CASTEP model by approximately 29 kJ mol<sup>-1</sup>. A similar scenario is observed in the Pd case, the stronger CASTEP adsorbed di- $\sigma$  species contract the surface layer by roughly 0.03 Å more than the analogous weakly adsorbed VASP state, which has an adsorption energy of 53.9 kJ mol<sup>-1</sup> (Chapter 7, section 7.2).

The overestimation in the CASTEP formaldehyde adsorption energies further confirms that the CASTEP GGA calculations incorporating US-PPs generated at the LDA level lead to overbinding. Desai *et al.* [48] employed US scalar relativist PPs implemented within VASP, as previously cited by Watson *et al.* for ethene [12].

Realistically, a fair comparison between the two sets of data cannot be drawn for a number of reasons. Firstly, the adsorption energies and geometries of formaldehyde are thought to be coverage dependent. In the CASTEP calculations a  $p(3 \times 3)$  unit cell was used representing an adsorbate surface coverage of 56%. Desai *et al.* [48] on the other hand, employed a much smaller surface of dimensions  $p(2 \times 2)$  which was equivalent to one-quarter monolayer. This was modelled using a 3 Pt layer slab as in the CASTEP calculations but with a smaller vacuum gap measuring 11 Å (CASTEP employed a vacuum gap of 15 Å). Convergence was optimum with a larger  $k$ -point grid of  $5 \times 5 \times 1$  and a smaller cutoff of 330 eV compared to the CASTEP system ( $3 \times 3 \times 1$   $k$ -points and 380 eV cutoff).

Although, the use of low  $k$ -point sampling is known to overestimate adsorption energies by reducing the repulsion between the extended electronic states of the surface and the C=O double bond electron density, the effect of surface relaxation can also influence the energetics. To allow likely changes in the surface structure upon adsorption of formaldehyde, only the first two layers of the Pt(111) slab were fully

relaxed during optimisation in Desai's model with the third layer atoms held fixed at their bulk positions [48]. In contrast all Pt atom layers were allowed to fully relax in the CASTEP surface. If full relaxation was incorporated in Desai's surface an increase in the adsorption energies for formaldehyde are anticipated. However, Desai's model in practice is satisfactory as close agreement between experimental data is observed [48].

Finally, as with the ethene case, the periodic values of formaldehyde adsorption can also be compared against cluster models. Recently, Kua *et al.* [49] and Ishikawa *et al.* [50] independently reported calculations on the dehydrogenation of methanol for which formaldehyde was an adsorbed state. Their DFT calculations incorporated clusters containing between 8-10 metal atoms. The adsorption energy of the di- $\sigma$  bound formaldehyde was reported to be within 74.9 kJ mol<sup>-1</sup> over Pd(111) [49-50] and is roughly 15 kJ mol<sup>-1</sup> larger than the analogous adsorption energy calculated by CASTEP.

Delbecq and Sautet also examined the adsorption of formaldehyde at various sites on Pd and Pt using extended Hückel theory [51]. Two different cluster models containing 49 and 114 atoms were used to represent a flat and stepped (111) surface. In agreement with the CASTEP data, their analysis also implied the stability of formaldehyde in the di- $\sigma$ , bridged site on both metals. On Pd<sub>49</sub> and Pt<sub>49</sub> the  $\eta^1$  and  $\eta^2$  adsorptions were calculated at 43.1, 133.1, 46 and 95.8 kJ mol<sup>-1</sup>, respectively. Generally, these values are found to be poorly modelled against the CASTEP values (table 6.4). Similarity arises only in the  $\eta^1$  formaldehyde over Pt<sub>49</sub> as the adsorption energies differ by only 4.8 kJ mol<sup>-1</sup> as the CASTEP value is calculated at 41.2 kJ mol<sup>-1</sup>. Comparison between the CASTEP adsorption energies and those calculated at the Pt<sub>114</sub> terrace lead to the same conclusions. Here the corresponding adsorptions for the  $\eta^1$  and  $\eta^2$  adsorbed species were calculated at 38.9 and 95.8 kJ mol<sup>-1</sup>, respectively. In this case the adsorption energy of the endon formaldehyde on the Pt<sub>114</sub> cluster is better matched to the CASTEP value than the adsorption measured on the Pt<sub>49</sub> cluster. The differences in adsorption energies over these cluster models can be attributed to the same reasons as discussed for ethene *i.e.* due to cluster-size effects, the poor representation of the band structure of the metal and the reactive nature of edge atoms.

### 6.4.3. The Adsorption of Acetone on Pd and Pt(111)

As with formaldehyde, and especially at low temperatures, surface science studies have clearly distinguished the endon and the di- $\sigma$  geometries of acetone to be stabilised upon adsorption on metal surfaces. Generally, as the multilayer phase develops the  $\eta^1$  species disappear and are replaced by  $\eta^2$  acetone, the conversion below temperatures of 200 K is more rapid on the Pt(111) surface [52,53] compared to the equivalent Pd surface [54]. A full review of the available literature is presented in Chapter 2, sections 2.6.2 and 2.6.3 of this work.

On Ni(111), with the use of RAIRS, Sim *et al.* [1] proposed the adsorption of acetone through an enolate intermediate. Since acetone is known to undergo *keto-enol* tautomerism, the effect was investigated with CASTEP. The gas-phase difference between the two isomers was calculated to be roughly 51 kJ mol<sup>-1</sup> with the equilibrium in favour of the more stable *keto* species. This value is in good agreement with the experimental range of 46.9-58.2 kJ mol<sup>-1</sup> [20,21] and the best theoretical estimate of 51.9 kJ mol<sup>-1</sup> [22].

The adsorption of *keto* acetone on both surfaces was found to optimise primarily through the  $\eta^1(\text{O})$  geometry and the di- $\sigma$  coordination was not observed, despite the starting structure of the calculation being a modified version of the optimised di- $\sigma$  adsorbed formaldehyde. The two  $\eta^1$  adsorption modes were labelled  $\eta^1(\text{O})^a$  and  $\eta^1(\text{O})^b$  with  $\eta^1(\text{O})^b$  having the higher adsorption energies for both metals.

Experimentally, TDS studies have measured the heats of adsorption of the di- $\sigma$  and endon modes to be 52.3 and 48.1 kJ mol<sup>-1</sup> with multilayer acetone at 33.5 kJ mol<sup>-1</sup> on Pt(111) [55]. The CASTEP  $\eta^1(\text{O})^b$  species over the analogous surface is found to be in agreement with the corresponding TDS value [56] as well as with the earlier adsorption energy predicted by Avery *et al.* (48.5 kJ mol<sup>-1</sup>) [52].

The experimental Pd(111) adsorptions are found to be similar to those of the above study on the analogous Pt surface. In particular, the  $\eta^1$  coordinations are identical whereas the di- $\sigma$  is strongly adsorbed by roughly 16.7 kJ mol<sup>-1</sup> [54]. On Pd, the CASTEP adsorptions of  $\eta^1(\text{O})^a$  and  $\eta^1(\text{O})^b$  are closely matched (average adsorption energy, 19.8 kJ mol<sup>-1</sup>) and as a result neither one of these energies show the same degree of stabilisation as observed by Davis *et al.* [54].



On comparison with other theoretical models, a good reference to use is the cluster study conducted by Delbecq *et al.* [57]. Already discussed in context of formaldehyde adsorption, the results of acetone over a Pt<sub>49</sub> cluster contradict the experimental TDS observations *i.e.* the  $\eta^1$  is stabilised over the  $\eta^2$ , whereas for the corresponding Pd cluster the same trend of di- $\sigma$  stabilisation is observed. The periodic energy of the  $\eta^1(\text{O})^b$  over the Pd surface at 42.9 kJ mol<sup>-1</sup> is found to be in excellent agreement with the cluster result of 43.1 kJ mol<sup>-1</sup>. This trend runs through into the Pt results, CASTEP models the same adsorption mode at 42.9 kJ mol<sup>-1</sup> which is 3.1 kJ mol<sup>-1</sup> lower than the cluster value. Although a suitable di- $\sigma$  adsorption mode has not been successfully modelled on either metal in this set of calculations, the energies from the cluster approach were 25.5 and 79.9 kJ mol<sup>-1</sup> for Pt and Pd(111). Note that acetone chemisorbed on a Pt<sub>114</sub> terrace predicts  $\eta^1$  and  $\eta^2$  geometries with adsorption energies of 38.5 and 20.9 kJ mol<sup>-1</sup> [57]. The arguments presented in the ethene and formaldehyde discussion stand for the differences observed in the cluster and periodic adsorption energies for acetone.

Unfortunately, comparison against a suitable periodic model for the investigation of acetone adsorption could not be made as there is a lack of literature available. However, analogous periodic calculations performed using the VASP program (Chapter 7, section 7.3) indicated the presence of both  $\eta^1$  and  $\eta^2$  geometries of the *keto* isomer of acetone on both metals. The CASTEP  $\eta^1(\text{O})^a$  adsorption energy was found to be in excellent agreement with the VASP endon species on Pd(111), as the difference in energy was found to be 0.4 kJ mol<sup>-1</sup> greater in the CASTEP value. However, for the Pt(111) case, the corresponding VASP adsorption energy was found to lie in between the range of the CASTEP  $\eta^1(\text{O})^a$  and  $\eta^1(\text{O})^b$  modes at 28.3 kJ mol<sup>-1</sup>. The VASP adsorption energies for the di- $\sigma$  acetone species were roughly estimated at 9 and 19 kJ mol<sup>-1</sup> on the Pd and Pt(111) surfaces.

In addition to the adsorption of endon and di- $\sigma$  acetone the *enol* species was investigated over both metals, however, an appropriate structure was only found to be stabilised on the Pd surface with both C atoms of the double bond interacting with a single metal atom. The structure was found to be stabilised in a similar manner to that found for the atop mode of ethene over Pt, *i.e.* via the donation of electron density from the  $\pi$  orbital into an empty Pd *d*-orbital. The adsorption energy was found to be much higher than either of the previous two adsorption modes ( $\eta^1(\text{O})^{a,b}$ ) and at 71.1 kJ mol<sup>-1</sup>

closely resembled the experimental and theoretical values gained for the di- $\sigma$  *keto* acetone species. On Pt the adsorption was not stabilised in the expected mode but *via* the  $\eta^1(\text{C})$  alkyl mode and at 117.5 kJ mol<sup>-1</sup> was found to be significantly stabilised compared to the *keto* adsorbed states identified by the experimental and theoretical work discussed above.

Note that the *enol* adsorbed structures in the analogous VASP study (Chapter 7, section 7.3) were found to bind to both metals *via* the stabilising  $\eta^2(\text{C,C})$  geometries bridged over two single metal atoms as in the case of the CASTEP formaldehyde di- $\sigma$  coordination. For Pd, the adsorption for the *enol* species was slightly weaker compared to the Pt mode, which was calculated to be approximately 125 kJ mol<sup>-1</sup>. The VASP *enol* Pd adsorption energy at 81.5 kJ mol<sup>-1</sup> is close to the CASTEP  $\eta^2(\text{C,C})$  value of 71.1 kJ mol<sup>-1</sup> on the analogous surface.

Although, the interaction of the *enol* is expected on both Pd and Pt(111), the stabilities of the CASTEP structures can be improved upon as illustrated by the VASP models. As with the case of the previous ethene and *keto* containing molecules, the problems associated with the use of LDA pseudopotentials as well as 5 *k*-points to represent the electronic structure of the metals within the calculations still exist.

## 6.5. Conclusions

The calculations indicate that the most favourable adsorption mode for ethene on the Pt(111) surface is the di- $\sigma$  adsorption site and is in agreement with experimental EELS, UPS and NEXAFS data [29-32]. The  $\pi$  adsorption mode is stabilised in the atop-bridge and atop-hollow sites with respect to gas-phase ethene, although less stable than the di- $\sigma$ . The calculations indicate that the adsorption energies of the two orientations are practically the same implying that the orientation of the ethene in the atop sites would not be fixed under experimental conditions. The cross bridge mode has been shown to be only weakly adsorbed and is very unlikely to be observed experimentally. The trend in adsorption of ethene to Pt(111) is modelled in accordance with that calculated by Watson *et al.* [12], although the adsorption energies are overestimated by between 10-20% in our calculations. The adsorption energies for the di- $\sigma$  and the  $\pi$  adsorption mode are modelled reasonably well against the values derived from microcalorimetric studies on Pt(110) [26] and Pt powders [27,28] but the values can be improved upon.

The adsorption energies calculated in the literature were derived with the VASP program and are in better agreement with the available thermodynamic data [12].

The over estimation in the adsorption energies in our calculations derives from the Vanderbilt US-PPs employed in CASTEP. The US-PPs employed in the VASP program have the core of the atoms generated at the GGA level whereas in CASTEP they are calculated with the LDA functionality. The calculations show that differences in electronic energies are obtained when these different PP's are combined with gradient corrected DFT. In CASTEP the LDA PP's are found to overestimate the cohesion energies and is responsible for the over binding of the atoms resulting in increased bond lengths and energies. The GGA corrections to the calculations are supposed to rectify the problem, but for CASTEP the effect of LDA is prominent. The problem associated with the PP's will always be consistent for CASTEP calculations as user selection of the choice of PP's is restricted within the code. It is clear from the literature that it is better to use the VASP code than CASTEP for surface calculations as GGA US-PP's are available which when combined with GGA DFT calculations give more promising adsorption energies which are comparable to experimental data [12]. However, our adsorption energies for the di- $\sigma$  and  $\pi$  adsorbed ethene are in good agreement with cluster calculations of Watwe *et al.* [45].

For the interaction of formaldehyde to a Pd and Pt(111) surface, two adsorption modes identified as the di- $\sigma$ ,  $\eta^2(\text{C},\text{O})$  and the endon,  $\eta^1(\text{O})$  were stabilised. The most energetically favoured mode on both metals is the di- $\sigma$  adsorption site and the corresponding adsorption energies were calculated at 60.3 and 77.6 kJ mol<sup>-1</sup> on Pd and Pt(111) respectively. This result, however, contradicts TPD experiments which indicates the adsorption to be iso-energetic on both surfaces at 51-52 kJ mol<sup>-1</sup> [46,47] and the periodic calculations of Desai *et al.* in which the di- $\sigma$  mode at 54 kJ mol<sup>-1</sup> is stabilised by 5 kJ mol<sup>-1</sup> to the Pd(111) surface [48]. Our calculations show that by increasing the size of the unit cells of the surfaces by one unit cell and allowing each layer of the slab to relax the strength of the adsorption is increased. The TPD assignment is most likely the formyl ( $\text{H}-\text{C}=\text{O}$ ) adsorbed species and not molecular formaldehyde as modelled in our calculations, as this is the known species in which formaldehyde reacts with Pd and Pt(111) [46,47]. The preference for the stabilisation of the di- $\sigma$  mode onto the Pd(111) surface is also demonstrated by the extended Hückel calculations of Delbecq and Sautet [51].

For the adsorption of acetone to Pd and Pt(111) the *keto* and *enol* isomeric forms were considered, as were the orientations in which formaldehyde was found to interact. The gas-phase calculations showed the ketone to be considerably more stable than the *enol* form implying that the first step in any adsorption process would begin with the ketone interacting with the surface. For the *keto* isomer only the endon configuration was stabilised and the adsorption to the Pt surface was stronger by roughly  $22 \text{ kJ mol}^{-1}$  than that to Pd(111). The  $\eta^2(\text{C},\text{O})$  adsorption mode did not form even if the starting geometry was biased towards it, which suggests that there is a barrier to the formation of the di- $\sigma$  bonded molecule. The calculations show that the strength of the adsorption of acetone to the Pt surface is similar to the corresponding mode for formaldehyde but on the Pd surface the adsorption of the acetone is much stronger. Our results for the adsorption energy for acetone on the Pt surface is in good agreement with the experimental value derived from TDS [52,55]. The adsorption energies also agree with the cluster calculations of Delbecq *et al.* [57].

The *enol* isomer was found to adsorb in a  $\eta^2(\text{C},\text{C})$  geometry on Pd(111) and in a much stronger  $\eta^1(\text{C})$  alkyl alcohol mode on Pt(111). In both cases the adsorption energy in the *enol* form is sufficient to compensate for the gas-phase energy difference between the *keto* and *enol* isomers, suggesting that thermodynamically the *enol* form will be favoured on both metals. The energetics of acetone adsorption on both the metals is summarised in figure 6.11.

Our results confirm the model of molecular adsorption proposed by Watson *et al.* [12]. We find adsorption to be a balance between attraction, which results from localised bond formation, and repulsion, which is due to the interaction between the extended electronic states of the surface and the molecule's electron density. With the adsorption energies agreeing well with cluster models it appears that the extended electronic states of the Pd and Pt surfaces are underestimated in the low  $k$ -point calculations and results in stronger bonding to the surface as the repulsion is underestimated, causing the values to be overestimated. Ultimately this effect will depend on the strength of the localised bonding. However, in our calculations the effect of poorly treated extended electronic states only partially contributes to the overestimation observed as the greatest contribution is from the use of LDA derived US-PPs in GGA calculations.

To improve the CASTEP results, so that the effect of over binding is reduced, we propose two different methods to model the substrate. Firstly, the slab thickness can be increased from three to six metal layers and secondly, working with the original slab the coordinates of the two bottom layers can be fixed to their bulk values. In either case, energy convergence with regards to unit cell size,  $k$ -point density, KE plane-wave cutoffs *etc* would have to be tested.

To conclude, our calculations clearly illustrate the inadequacies of the US-PPs incorporated within CASTEP to predict realistic adsorption energies. In this work, CASTEP is deduced as a good theoretical tool for qualitative investigation of surface adsorption as the electronic structure of the metals are poorly represented. The quantitative nature of the alternative plane-wave code VASP, as employed by Watson *et al.* [12], has been shown to better model the energies of surface adsorbed species. A repeat of this investigation with use of the VASP code is provided in the following results chapter. Efforts towards finding activation barriers for the formation of the *enol* or the possibility of an enolate ion are also presented.

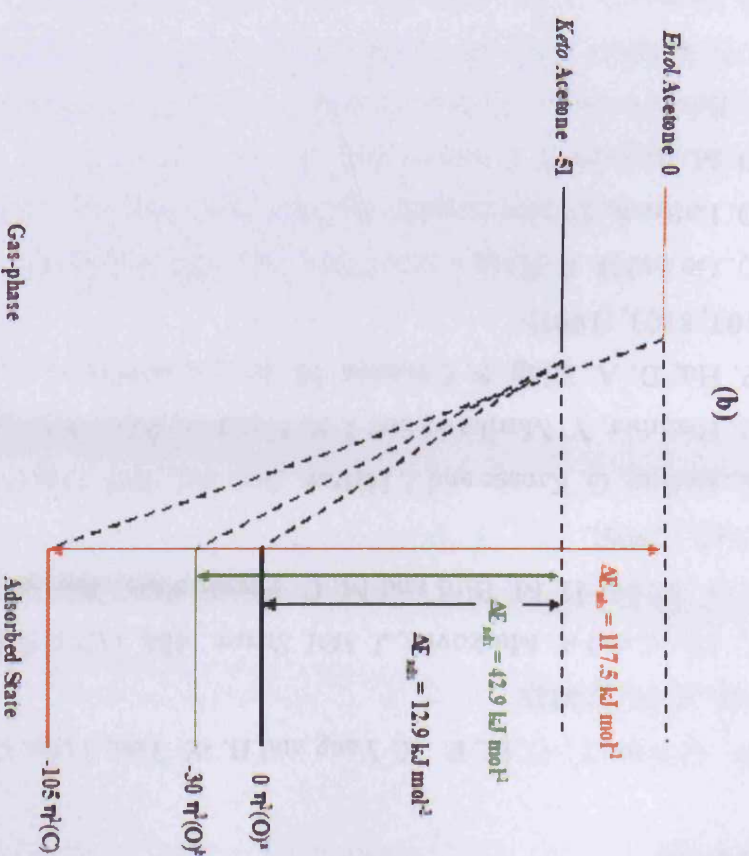
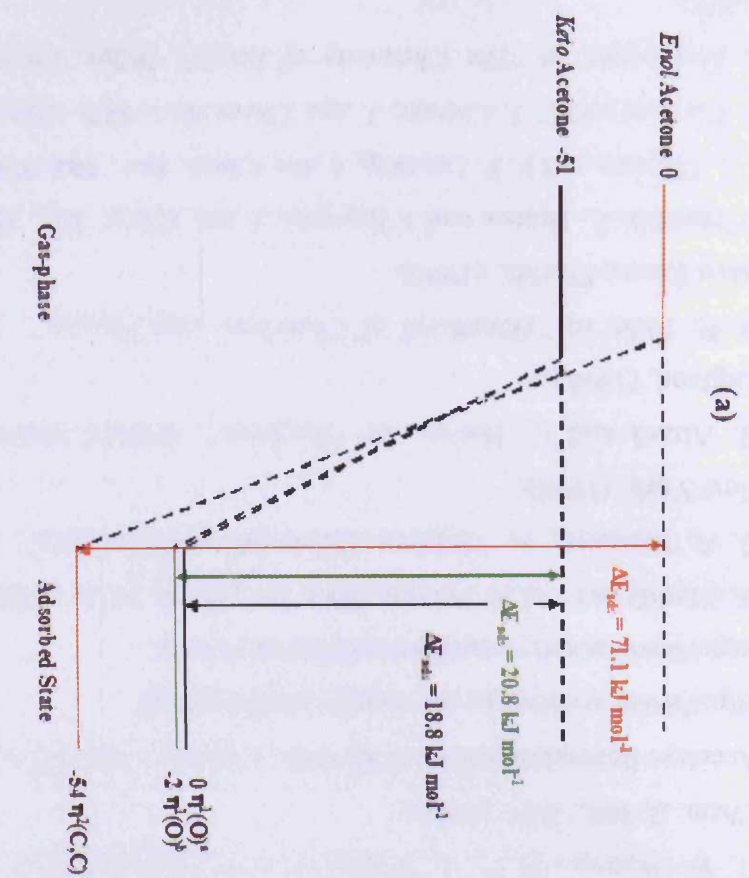


**Figure 6.11:** Energy profiles summarizing the CASTEP data for the surface adsorbed acetone intermediates on (a) Pd and (b) Pt(111). Profiles not drawn to scale. Energetics derived from periodic DFT calculations using parameters as specified in Chapter 4, sections 4.3.2 and 4.3.3.

## 6.6. References

- [1] W. -S. Sim, T. -C. Li, P. -X. Yang and B. -S. Yeo, *J. Am. Chem. Soc., Commun.*, **124**, 4970, (2002).
- [2] C. Minot and A. Markovits, *J. Mol. Struct.*, **424**, 119, (1998).
- [3] J. A. White, D. M. Bird and M. C. Payne, *Phys. Rev. B: Condens. Matter*, **53**, 1667, (1996).
- [4] A. Eichler, G. Kresse and J. Hafner, *Surf. Sci.*, **397**, 116, (1988).
- [5] B. Hammer, Y. Morikawa and J. K. Nørskov, *Phys. Rev. Lett.*, **76**, 2141, (1996).
- [6] P. Hu, D. A. King, S. Cramoin, M. H. Lee and M. C. Payne, *J. Chem. Phys.*, **107**, 8103, (1997).
- [7] Q. Ge and D. A. King, *Chem. Phys. Lett.*, **285**, 15, (1998).
- [8] D. Loffreda, D. Simon and P. Sautet, *Chem. Phys. Lett.*, **291**, 15, (1998).
- [9] D. M. Bird and P. A. Gravil, *Surf. Sci.*, **377**, 555, (1997).
- [10] F. Besenbacher, I. Chorkendorff, B. S. Clausen, B. Hammer, A. M. Molenbroek, J. K. Nørskov and I. Stensgaard, *Science*, **279**, 1913, (1998).
- [11] Q. Ge and D. A. King, *J. Chem. Phys.*, **110**, 4699, (1999).
- [12] G. W. Watson, R. P. K. Wells, D. J. Willock and G. J. Hutchings, *J. Phys. Chem. B*, **104**, 6439, (2000).
- [13] Accelrys licensed software, <http://www.accelrys.com/cerius2>
- [14] <http://www.accelrys.com/cerius2/visualizer.html>
- [15] <http://www.accelrys.com/cerius2/builders.html>
- [16] M. Methfessel and A. Paxton, *Phys. Rev. B*, **49**, 3616, (1989).
- [17] G. A. Somorjai, in “*Surface Chemistry and Catalysis*”, John Wiley & Sons, New York, (1994).
- [18] G. Attard and C. Barnes, in “*Surfaces*”, Oxford University Press, Oxford, England, (1998).
- [19] D. R. Lide, in “*Handbook of Chemistry and Physics*”, 77<sup>th</sup> Ed., CRC Press, Boca Raton, Florida, (1996).
- [20] F. Tureček, L. Brabee and J. Korvola, *J. Am. Chem. Soc.*, **110**, 7984, (1988).
- [21] J. L. Holmes and F. P. Lossing, *J. Am. Chem. Soc.*, **104**, 2648, (1982).
- [22] F. Tureček and C. J. Cramer, *J. Am. Chem. Soc.*, **117**, 12243, (1995).
- [23] Z. Rappoport, in “*The Chemistry of Enols*”, Wiley, Chichester, West Sussex, (1990).

- [24] P. S. Cremer and G. A. Somorjai, *J. Chem. Soc., Faraday Trans.*, **91**, 3671, (1995).
- [25] G. Szulczewski and J. R. Lewis, *J. Am. Chem. Soc.*, **118**, 3521, (1996).
- [26] A. Stuck, C. E. Wartnaby, Y. Y. Yeo and D. A. King, *Phys. Rev. Lett.*, **74**, 578, (1995).
- [27] B. E. Spiewak, R. D. Cortright and J. A. Dumesic, *J. Catal.*, **176**, 405, (1998).
- [28] J. Shen, J. M. Hill, M. Watwe, B. E. Spiewak and J. A. Dumesic, *J. Phys. Chem. B*, **103**, 3923, (1999).
- [29] H. Steininger, H. Ibach and S. Lehwald, *Surf. Sci.*, **117**, 685, (1982).
- [30] T. E. Fetter and W. H. Weinberg, *Surf. Sci.*, **103**, 265, (1981).
- [31] J. Stohr, F. Sette and A. L. Johnson, *Phys. Rev. Lett.*, **53**, 1684, (1984).
- [32] J. A. Horsley, J. Stohr and J. R. Koestner, *J. Chem. Phys.*, **83**, 3146, (1985).
- [33] M. Bochmann, in “*Organometallics 1 and 2*”, Oxford University Press, Oxford, England, (1996).
- [34] D. R. Hamann, M. Schlüter and C. Chiang, *Phys. Rev. Lett.*, **43**, 1494, (1979).
- [35] D. Vanderbilt, *Phys. Rev. B*, **41**, 7892, (1990).
- [36] A. R. Leach, in “*Molecular Modelling, Principles and Applications*”, 2<sup>nd</sup> Ed., Pearson Education, Prentice Hall, England, 616, (2001).
- [37] P. Giannozzi, F. D. Angelis and R. Car, *J. Chem. Phys.*, **120**, 13, 5903, (2004).
- [38] K. Laasonen, A. Pasquarello, R. Car, C. Lee and D. Vanderbilt, *Phys. Rev. B*, **47**, 10142, (1993).
- [39] <http://www.accelrys.com/cerius2/castep.html>
- [40] <http://mbe.ee.nctu.edu.tw/mbe/index.php>
- [41] R. O. Jones and O. Gunnarsson, *Rev. Mod. Phys.*, **61**, 689, (1989).
- [42] X. Krokidis, Accelrys, Barnwell Road, Cambridge, England.
- [43] V. Milman, Accelrys, Barnwell Road, Cambridge, England.
- [44] G. W. Watson, R. P. K. Wells, D. J. Willock and G. J. Hutchings, *J. Phys. Chem. B*, **105**, 4889, (2001).
- [45] R. M. Watwe, B. E. Spiewak, R. D. Cortright and J. A. Dumesic, *J. Catal.*, **180**, 184, (1998).
- [46] J. L. Davies and M. A. Barteau, *J. Am. Chem. Soc.*, **111**, 1782, (1989).
- [47] N. M. Abbas and R. J. Madix, *Appl. Surf. Sci.*, **7**, 241, (1981).
- [48] S. K. Desai, M. Neurock and K. Kourtakis, *J. Phys. Chem. B*, **106**, 2559, (2002).
- [49] J. Kua and W. A. Goddard, *J. Am. Chem. Soc.*, **121**, 10928, (1999).



- [50] Y. Ishikawa, M. Liao and C. Cabrera, *Surf. Sci.*, **463**, 66, (2000).
- [51] F. Delbecq and P. Sautet, *Langmuir*, **9**, 197, (1993).
- [52] N. R. Avery, *Surf. Sci.*, **125**, 771, (1983).
- [53] A. B. Anton, N. R. Avery, B. H. Toby and W. H. Weinberg, *J. Am. Chem. Soc.*, **108**, 1684, (1986).
- [54] J. L. Davis and M. A. Barteau, *Surf. Sci.*, **208**, 383, (1989).
- [55] M. A. Vannice, W. Erley and H. Ibach, *Surf. Sci.*, **254**, 1, (1991).
- [56] N. R. Avery, W. H. Weinberg, A. B. Anton and B. H. Toby, *Phys. Rev. Lett.*, **51**, 682, (1983).
- [57] F. Delbecq and P. Sautet, *Surf. Sci.*, **295**, 353, (1993).

## ***Chapter 7***

*A Repeat of the Density Functional Theory  
Study of the Adsorption of Ethene and  
Simple Ketones Over Group 10 Metal  
Surfaces, Using the VASP Code*

## 7.0. Introduction

The previous Chapter highlighted the shortfall of the available CASTEP Vanderbilt US-PPs [1] to predict adequate surface energies and heats of adsorption for ethene, formaldehyde and acetone over group 10 transition metals, in particular, when applied to periodic DFT GGA corrected surface calculations. However, the use of the alternative version of the CASTEP code, VASP used by Watson *et al.* [2] illustrated the successful application of the computational methodology in calculating the adsorption data for the interaction of ethene on Pt(111), as the calculated values were found to be in excellent agreement with the available thermochemical data. Thus, to be able to correctly quantify and examine the effects of the *keto-enol* adsorption of acetone (Chapter 6, figure 6.7) on the clean (111) surface of Pd and Pt it was decided that the VASP code would be employed.

In an attempt to extend our previous quantum chemical calculations and turn the effective qualitative approach of CASTEP (Chapter 6) into a more quantitative one, VASP has been used to explore all of the possible adsorption geometries of formaldehyde and isomeric forms of acetone as well as to determine the most stable structures. Preliminary work on the adsorption characteristics of butane-2,3-dione over both metals is also provided. With reference to the initial VASP US-PPs [1] used to describe ethene adsorption a new set of potentials derived by the projector augmented-wave (PAW) method [3,4] are introduced.

To gain insight into the kinetics, that is, to estimate the rates of reaction and understand the mechanism of adsorption, the latter part of this work will focus on the application of the VASP interfaced nudged elastic band (NEB) method (Chapter 3, section 3.5.2) used to calculate activation barriers, where the potential energy maximum along the MEP is determined. This has been applied to the case of the transformation of the endon adsorbed molecule into the di- $\sigma$  adsorbed species, which for acetone extends to the formation of a possible enolate ion.

As with the CASTEP results, the VASP adsorption energies will be verified against earlier experimental and theoretical data reviewed in Chapter 2. The system of nomenclature for the adsorption energies are drawn from the concept of hapticity used in organometallic chemistry and is consistent with that reported in the literature and the previous work. However, in addition to the earlier structures of type  $\eta^1(\text{O})$  and

$\eta^2(\text{C},\text{O})$ , the symbol  $\mu_n$  will be used to indicate that the adsorbate is bridging  $n$  surface metal atoms.

It is the aim of this work to use computer modelling to consider the adsorption modes of ketone molecules on Pd and Pt(111), and to discuss the implications of them for models of the enantioselective hydrogenation of  $\alpha$ -ketoesters.

### 7.1. The Adsorption of Ethene on Pt(111)

To check the validity of the VASP program available to the Cardiff theoretical group the surface adsorption calculations of ethene interacting with Pt(111) presented in the previous Chapter were repeated. The periodic computations were constructed and performed using the same methodology as stated in Chapter 6, section 6.1, and set to those parameters used in the reference study of Watson *et al.* [2]. However, the original Vanderbilt US-PPs (Appendix B) were substituted with the use of novel PAW-PPs (Appendix C) implemented within the recent release of the VASP code, of which version 4.4.5 was employed [5].

As with the CASTEP simulations of the Pt surface (Chapter 6, section 6.1), the corresponding lattice parameters for the optimised VASP bulk Pt cell against the experimental cell (obtained from the Cerius<sup>2</sup> [6] database of XRD structures) and the reference cell [2] are provided in table 7.1.

Bulk Pt Models	Lattice Constant, $a$ , (Å)	Interlayer Pt Spacing (Å)
Cerius <sup>2</sup> experimental cell	3.9239	2.27
VASP	3.9806	2.30
VASP <sup>a</sup>	3.9837	2.30

**Table 7.1:** Relaxed lattice constants and interlayer surface atom spacing of bulk Pt. VASP computation performed using bulk modified periodic DFT parameters as specified in Chapter 4, section 4.3.1. <sup>a</sup>Data obtained from reference 2.

In agreement with the findings outlined in the corresponding section of the previous Chapter, the bulk Pt cell is found to expand by 1.5% upon relaxation, as the lattice constant lengthens from the experimental value by approximately 0.06 Å. The dimensions of the relaxed cell are consistent with those calculated for the reference cell of Watson *et al.* [2], in which different PPs were employed in the calculation to those used in this study: refer to section 7.4.1 for a full discussion. The expansion in the cell

is also consistent with experimental LEED data for which the interlayer Pt spacing is reported to be 2.26 Å for the bulk (111) single crystal [7]. To ensure accuracy in the calculations the relaxed lattice constant is used to build the subsequent  $p(2 \times 2)$  surface to which ethene is adsorbed. The surface energy of the 3-layer slab analogous to the CASTEP model presented in Chapter 6, figure 6.1 is calculated to be  $1.50 \text{ J m}^{-2}$ . The energy is determined with the use of the appropriately substituted form of equation 6.1; refer to Chapter 6, section 6.1. The interlayer spacing is calculated to be 2.32 Å and the 0.9% expansion from the bulk corresponds to the expansion from 2.26 to 2.28 Å (0.9%) observed for the surface layer of a Pt(111) single crystal [7].

To this surface a single molecule of ethene was positioned in the adsorption modes illustrated in figure 6.3 (Chapter 6, section 6.1). Following the method outlined in Chapter 4, section 4.3.1 geometry optimisation of all the atomic positions were then performed using VASP. The adsorption energy of the ethene molecule interacting with the surface was calculated using the expression defined as equation 6.2 in the previous Chapter. The calculated energies for the ethene adsorption modes are provided in table 7.2 and are compared against the reference values of Watson *et al.* [2].

Coordination Geometry	Adsorption Energy ( $\text{kJ mol}^{-1}$ )	
	VASP <sup>a</sup>	VASP
Atop-bridge ( $\pi$ )	85.8	85.3
Atop-hollow ( $\pi$ )	84.8	84.9
Bridge (di- $\sigma$ )	127.3	132.0
Cross bridge	9.2	9.0

**Table 7.2:** Theoretical adsorption energies of ethene on Pt(111) calculated relative to the clean surface and gas-phase molecule using the appropriately substituted form of equation 6.2 (Chapter 6, section 6.1). Computations performed using periodic DFT specified at theory level GGA-PW91 using computational parameters as specified in Chapter 4, section 4.3.1. <sup>a</sup>Literature values obtained from reference 2.

The recent VASP simulations are found to compare well against those previously modelled, as not only are the adsorption energies in excellent agreement with each other but the same ordering of stability of adsorption modes is achieved. As with the previous case *i.e.* the CASTEP models, the cross bridge site is the least stable mode of interaction of ethene on Pt(111) followed by the iso-energetic sites of atop-bridge and atop-hollow. With a strong adsorption measuring  $132 \text{ kJ mol}^{-1}$  the bridge site with ethene bonded to the surface in a di- $\sigma$  fashion is the most stable mode of binding.

Since the adsorption energies are estimated within roughly 4% accuracy of each other, (largest discrepancy observed in the di- $\sigma$  adsorbed states), the effect of distortion of the geometry of the molecule upon binding will not be discussed to avoid repetition. Firstly, most of the comments will be similar to those discussed in Chapter 6, section 6.1 but obviously the geometric data will be less exaggerated as the CASTEP program was found to overestimate adsorption and secondly a good discussion is provided in the reference work [2]. At this stage the analysis of the adsorption energies is good enough to deduce that reliable data can be achieved with the available VASP program, as comparison with thermochemical data is good: refer to section 7.4.

## 7.2. The Adsorption of Formaldehyde on Pd and Pt(111)

For reasons discussed in Chapter 6, section 6.2 a larger surface unit cell of dimensions  $p(3 \times 3)$  was used to model the stable adsorption modes of formaldehyde on the (111) plane of Pd and Pt. These surfaces were constructed using the same methodology as stated in the aforementioned Chapter and geometry optimised to allow full relaxation of the metal atom coordinates. The relaxed surfaces used as the reference states for the calculation of adsorption energy include 3-layer slabs of Pd and Pt that possess an interlayer atom spacing of 2.29 and 2.33 Å compared to their calculated bulk spacings of 2.26 and 2.30 Å, respectively. These values are comparable to the CASTEP data presented in Chapter 6, section 6.2. In comparison, experimental LEED data showed expansions of 1.3% and 0.9% in the surface layer of a Pd and Pt(111) single crystal [7]. With the use of equation 6.1 (Chapter 6, section 6.1) the energies of the VASP surfaces were calculated at  $1.17 \text{ J m}^{-2}$  for Pd and  $1.55 \text{ J m}^{-2}$  for Pt, implying the high reactivity of the latter surface.

As with the previous CASTEP calculations the endon and di- $\sigma$  adsorption modes of formaldehyde were investigated using the same modelling procedure, schematically these surface bonding configurations are illustrated in figure 6.5 (Chapter 6, section 6.2). The corresponding VASP optimised adsorption energies and geometric data is provided in table 7.3. The actual optimised configurations of the molecule are shown in figure 7.1 and vary slightly to those obtained from the CASTEP calculations (figure 6.6, Chapter 6, section 6.2). The most significant difference is the direct bonding observed in the VASP models for the interaction of formaldehyde in the  $\eta^1(\text{O})$  geometry.

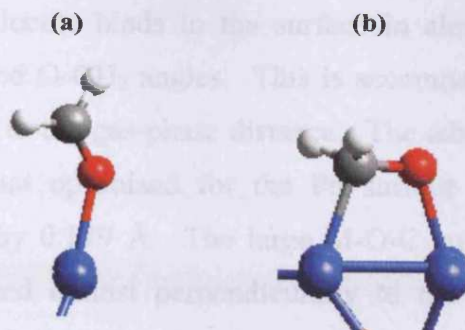


**Figure 7.1:** VASP adsorption geometries of formaldehyde: (a)  $\eta^1(\text{O})$  and (b)  $\eta^2(\text{C},\text{O})$  on Pt(111). Most of the metal atoms have been removed for clarity. Geometry optimisations performed using periodic DFT specified at theory level GGA-PW91 using computational parameters as discussed in Chapter 4, sections 4.3.2 and 4.3.3. Note that the configurations on the Pd(111) surface are similar to those found for the Pt case but with only slight differences in the geometry (table 7.3) and so for this reason are not provided here. Molecular atoms are colour coded: Pt blue, H white, C grey and O red.

Property	Gas-Phase Formaldehyde	Surface Adsorption States			
		M = Pd		M = Pt	
		$\eta^1(\text{O})$	$\eta^2(\text{C},\text{O})$	$\eta^1(\text{O})$	$\eta^2(\text{C},\text{O})$
$\Delta E_{\text{ads}}$ (kJ mol <sup>-1</sup> )		11.7	53.9	17.1	69.5
C=O (Å)	1.217	1.223	1.316	1.232	1.363
O-CH <sub>2</sub> <sup>a</sup> (°)	180	180	148/212	180	136/224
M-C (Å)		3.459	2.132	3.142	2.111
M-O (Å)		2.323	2.080	2.144	2.036
M-O-C (°)		153.3	111.9	135.4	111.1
$\Delta z$ (M) <sup>b</sup> (Å)		0.111	0.113(C) 0.102(O)	0.197	0.173(C) 0.168(O)

**Table 7.3:** VASP adsorption energies and geometries of adsorbed formaldehyde on Pd and Pt(111). Adsorption energies calculated relative to the clean surface and gas-phase formaldehyde molecule using the appropriately substituted form of equation 6.2 (Chapter 6, section 6.1). Periodic DFT computations performed using parameters and methodology as specified in Chapter 4, sections 4.3.2 and 4.3.3. <sup>a</sup>Angle between CO bond and CH<sub>2</sub> plane. <sup>b</sup>Displacement of coordinated metal (M) atom(s) from the surface plane.

Formaldehyde was found to bind to the two metal surfaces in the manner expected, as clearly the two distinct adsorption modes in which the starting structure was biased towards were observed. The effect of adsorption on formaldehyde geometry is similar to those observations made in the analogous CASTEP calculations (Chapter 6, section 6.2). Characteristically, in the endon mode only the O atom is closely coordinated to the surface and weakly interacts with a single metal atom (M) in a  $\eta^1(\text{O})$  configuration.

On both metals, the molecule binds to the surface in almost a planar geometry, as indicated by the calculated O-CH<sub>2</sub> angles. This is accompanied by the lengthening of the C=O bond compared to the gas-phase distance. The adsorption energy on Pt is 5.4 kJ mol<sup>-1</sup> greater than that optimised for the Pd surface and the M-O distance is correspondingly shorter by 0.179 Å. The large M-O-C angle of 153.3° suggests that formaldehyde is orientated almost perpendicularly to the Pd surface, whereas it is slightly more tilted towards the Pt, as the corresponding angle is measured to be 135.4°. As indicated by the movement of the coordinated metal atom out of the surface plane the more strongly bound endon molecule on Pt is found to disrupt the surface geometry more so than the weakly bound Pd formaldehyde.

The di-σ adsorption was found to be similar to that modelled for the stable geometry of ethene over Pt(111) *i.e.* parallel coordination to the surface with the molecule bridged over two separate surface atoms. As with the analogous CASTEP models (Chapter 6, section 6.2), the O atom formed a slightly shorter bond than the C to the alternative surfaces and the effect was more pronounced in the Pt system. This was accompanied by an observed elongation in the C=O bond length and in accordance with the calculated adsorption energy of 69.5 kJ mol<sup>-1</sup>, this was greater for the Pt adsorbed formaldehyde than that of the Pd molecule, which has a lower adsorption energy at 53.9 kJ mol<sup>-1</sup>.

Experimentally, at a temperature of 170 K, HREELS and TPD studies have provided evidence for the adsorption of formaldehyde in the η<sup>2</sup> configuration as an intermediate species in the decomposition process of methanol on Pd and Pt(111) [8,9]. The η<sup>1</sup>(O) adsorption mode has been difficult to isolate experimentally due to the reactive nature of the formaldehyde but evidence for the stabilisation of the intermediate comes from the modelling work of the previous Chapter (Chapter 6) and the theoretical calculations of Delbecq and Sautet [10,11].

Since the presence of these surface intermediates on Pd and Pt have been demonstrated, barrier calculations have been performed to understand in more detail the transformation of the endon, η<sup>1</sup>(O) formaldehyde to the stable di-σ, η<sup>2</sup>(C,O) adsorption mode. The calculations on Pd and Pt(111) have been executed using the elastic band method [12]. The method involves using fixed start (endon formaldehyde) and end (di-σ formaldehyde) points from the relaxed surface adsorbed calculations. With the use of a linear interpolation technique a series of structures from the start and end point are



obtained, these are then used in a parallel computer simulation in which the end points are fixed. To prevent the structures from “collapsing” into one another the calculation is performed using a constraint to keep the structures equidistant from its neighbour. As a result the chain of structures behave like an elastic band that is stretched and bent until the lowest energy pathway is found. The theory behind the method is discussed in detail in Chapter 3, sections 3.5.1 and 3.5.2 and the parameters used in the calculation are summarised in Chapter 4, section 4.3.4.

The elastic band calculations of  $\eta^1(\text{O})$  to  $\eta^2(\text{C},\text{O})$  formaldehyde are summarised in figure 7.2 and shows the adsorption energy as a function of the reaction coordinate. It is clearly indicated by the two peaks that a small energy barrier of around 2 and 6 kJ mol<sup>-1</sup> to this transformation exists on Pd and Pt(111), respectively.

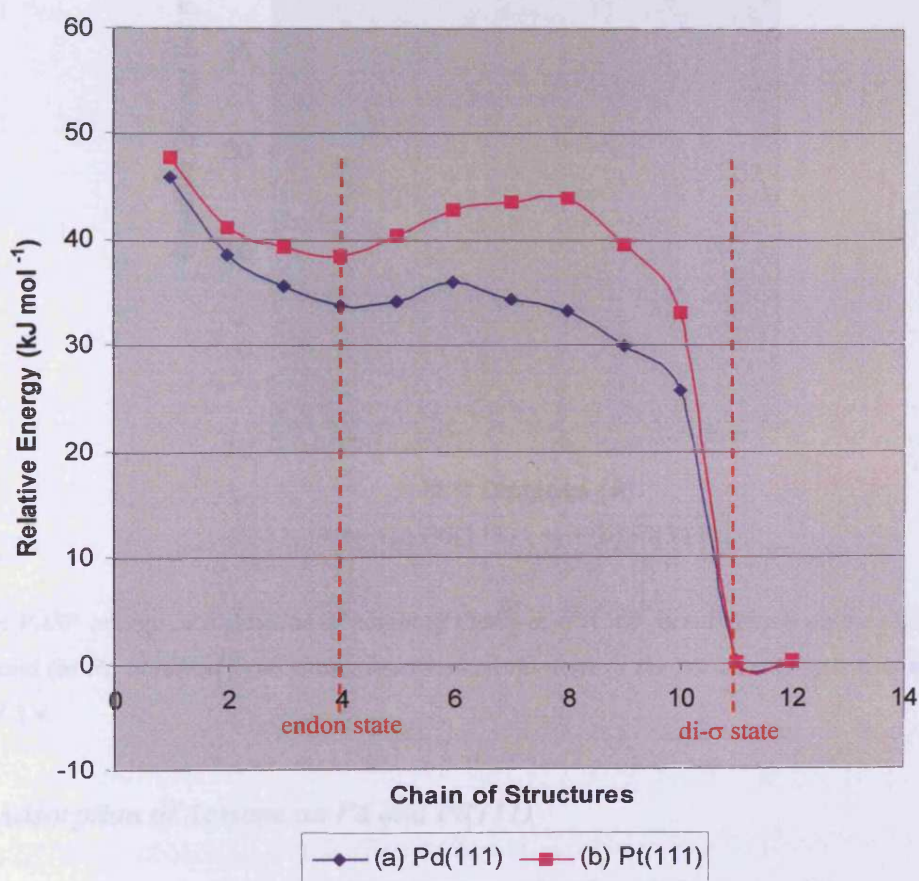


**Figure 7.2:** VASP energy as a function of reaction coordinate for the transformation of endon,  $\eta^1(\text{O})$  to di- $\sigma$ ,  $\eta^2(\text{C},\text{O})$  formaldehyde on the (111) surface of: (a) Pd and (b) Pt, obtained from elastic band calculations set to the parameters specified in Chapter 4, section 4.3.4. NB. Structures 1 and 12 represent the fixed start and end points for the elastic band calculations. On relaxing the chain of structures the original endon and di- $\sigma$  states further minimise into adsorbed states 4 and 11 and these structures are used to calculate the energy barrier for the inter-conversion.

As the calculations indicate the di- $\sigma$  adsorption mode of formaldehyde to be most stable, the energy as a function of the height of the molecule from the surface *i.e.* the M-C distance was recorded as the chain of structures converged to their MEPs. These pathways are illustrated in figure 7.3, and are consistent with the previous calculations in the sense that the same energy barriers exist for adsorption in the di- $\sigma$  mode on Pd and Pt(111).

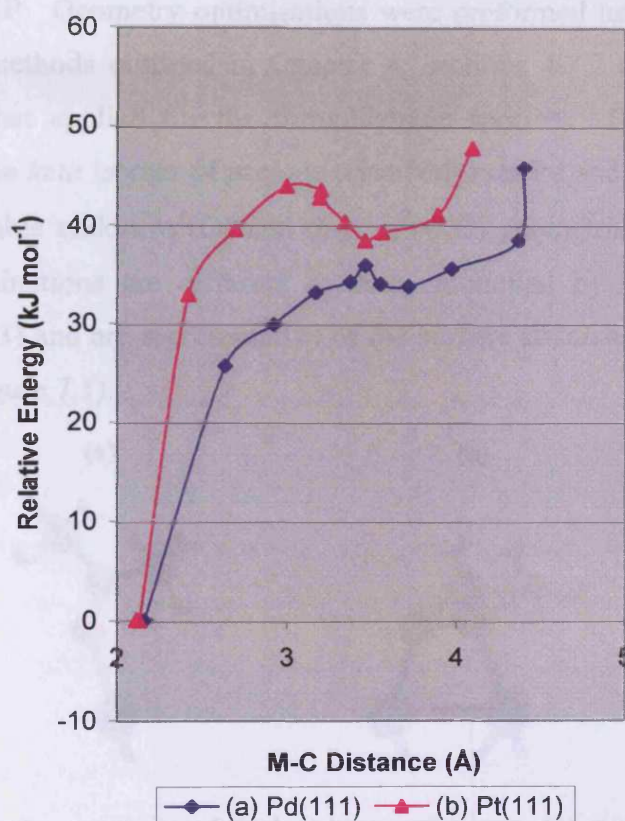


**Figure 7.3:** VASP energy as a function of height of the di- $\sigma$ ,  $\eta^2(\text{C},\text{O})$  formaldehyde on the (111) surface of: (a) Pd and (b) Pt, obtained from elastic band calculations set to the parameters specified in Chapter 4, section 4.3.4.

### 7.3. The Adsorption of Acetone on Pd and Pt(111)

The importance of the *keto-enol* tautomerism of acetone illustrated in figure 6.7 (Chapter 6, section 6.3) was briefly discussed in the previous Chapter (section 6.3). As with the CASTEP calculations the gas-phase equilibrium was calculated using VASP. However, greater care than the previous simulations were taken to derive accurate energies, as the gas-phase molecules were relaxed in the empty  $p(3 \times 3)$  simulation cells of Pd and Pt to be used in the surface calculations. For the Pt system the gas-phase



difference is measured to be  $50 \text{ kJ mol}^{-1}$  whereas for the Pd case the difference is slightly larger at  $53 \text{ kJ mol}^{-1}$ . The calculations point towards the stability of the ketone form, in agreement with the earlier CASTEP work (Chapter 6, section 6.3). The importance of the *keto-enol* energetics of acetone with regards to surface adsorption were summarised in figure 6.8 (Chapter 6, section 6.3).

The same adsorption modes for acetone as presented in Chapter 6, section 6.3 were modelled using VASP. Geometry optimisations were performed using the parameters and computational methods outlined in Chapter 4, sections 4.3.2 and 4.3.3 and in a similar fashion to that applied for the formaldehyde species. Table 7.4 gives the calculated data for the *keto* isomer of acetone adsorbed over Pd and Pt(111) and figure 7.4 illustrates the stable endon,  $\eta^1(\text{O})$  and di- $\sigma$ ,  $\eta^2(\text{C},\text{O})$  geometries of the molecule. Note that the coordinations are different to those modelled by CASTEP (refer to Chapter 6, section 6.3) and are representative of the surface stabilised species observed for formaldehyde (figure 7.1).

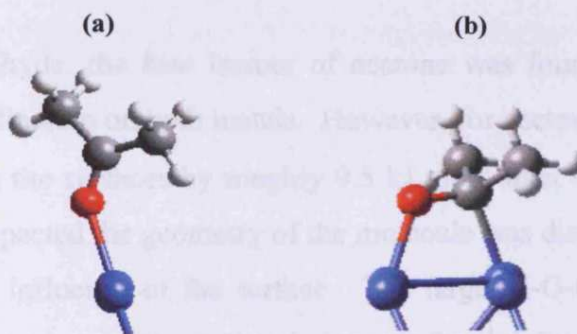


**Figure 7.4:** VASP adsorption geometries of the keto isomer of acetone: (a)  $\eta^1(\text{O})$  and (b)  $\eta^2(\text{C},\text{O})$  on Pt(111). Most of the metal atoms have been removed for clarity. Geometry optimisations performed using periodic DFT specified at theory level GGA-PW91 using computational parameters as discussed in Chapter 4, sections 4.3.2 and 4.3.3. Note that the configurations on the Pd(111) surface are similar to those found for the Pt case but with only slight differences in the geometry (table 7.4) and so for this reason are not provided here. Molecular atoms are colour coded: Pt blue, H white, C grey and O red.

Property	Gas-Phase <i>Keto Acetone</i>	Surface Adsorption States			
		M = Pd		M = Pt	
		$\eta^1(\text{O})$	$\eta^2(\text{C},\text{O})$	$\eta^1(\text{O})$	$\eta^2(\text{C},\text{O})$
$\Delta E_{\text{ads}}$ (kJ mol <sup>-1</sup> )		18.4	8.9	28.3	19.1
C=O (Å)	1.226	1.236	1.305	1.247	1.373
O-Me <sub>2</sub> /M <sup>a</sup> (°)	180	180	148/212	180	133/227
M-C (Å)		3.394	2.275	3.266	2.173
M-O (Å)		2.191	2.112	2.210	2.046
M-O-C (°)		163.6	119.6	140.2	115.1
$\Delta z$ (M) <sup>b</sup> (Å)		0.080	0.175(C) 0.114(O)	0.170	0.231(C) 0.152(O)

**Table 7.4:** VASP adsorption energies and geometries of adsorbed keto isomer of acetone on Pd and Pt(111). Adsorption energies calculated relative to the clean surface and gas-phase keto acetone molecule using the appropriately substituted form of equation 6.2 (Chapter 6, section 6.1). Periodic DFT computations performed using parameters and methodology as specified in Chapter 4, sections 4.3.2 and 4.3.3. <sup>a</sup>Angle defined between molecular plane (O and methyl Cs taken as reference points) and metal (M) surface plane. <sup>b</sup>Displacement of coordinated M atom(s) from the surface plane.

As with formaldehyde, the *keto* isomer of acetone was found to stabilise in both endon and di- $\sigma$  coordination on both metals. However, for acetone the  $\eta^1(\text{O})$  mode was strongly adsorbed on the surfaces by roughly 9.5 kJ mol<sup>-1</sup> than the alternative  $\eta^2(\text{C},\text{O})$  configuration. As expected the geometry of the molecule was distorted upon adsorption to accommodate the influence of the surface. The large M-O-C angles of the  $\eta^1(\text{O})$  mode indicate that the plane of the molecule is more “upright” *i.e.* perpendicular to the surface on Pd than Pt and by doing so this causes only a small disruption in the surface atom plane. Despite the fact that the  $\eta^1(\text{O})$  adsorption energy is 9.9 kJ mol<sup>-1</sup> greater for Pt than the Pd surface, the corresponding M-O distances are roughly measured to be the same and the C=O distances are not much altered from those measured in the gas-phase molecule.

For the weakly bound di- $\sigma$  acetones the adsorption energy on Pt was found to be twice as much as that calculated for the Pd(111) surface. Like formaldehyde, acetone adsorbs parallel to the surface but in each case the M-O bond is shorter than the M-C distance and as a result the C atom is found to withdraw the bonding metal atom out of the surface plane more so than the O atom. In contrast to the C=O bond lengths measured for the endon geometries, a significant expansion is observed in the di- $\sigma$

modes when compared to the gas-phase distance of the free acetone. This implies a significant change from double to single bond character upon adsorption.

Experimental observations have shown  $\eta^1(\text{O})$  adsorbed acetone to form at high coverage at 185 K on the (111) surface of Pt, which transforms to a low coverage di- $\sigma$  mode on heating to 220-240 K [13-15]. The conversion between these adsorbed states has been shown to occur rapidly on Pd(111) [16]. Since direct adsorption into the di- $\sigma$  mode at low temperature is prohibited by the stabilisation of the endon geometry a barrier to the transformation to it must exist, preventing it from forming. To investigate this barrier to the bridged  $\eta^2(\text{C},\text{O})$  mode, elastic band calculations, as summarised for the case of formaldehyde (section 7.2) were conducted for adsorption on both the Pd and Pt(111) surfaces. The resulting MEPs for the transformation from the endon to di- $\sigma$  states are illustrated in figure 7.5. For the Pd surface, the calculations show that there is no energy barrier to adsorption, and emphasise the preferential stabilisation of *keto* acetone in the endon geometry at low temperature. This corroborates with the conclusions drawn from the profile of di- $\sigma$  adsorption illustrated in figure 7.6(a), in which adsorption energy as a function of the height of the molecule from the surface is plotted. However, two distinct peaks indicating two energy barriers for the transformation are observed on the Pt surface (figure 7.5(b)). The first barrier (1) measuring a little over 1 kJ mol<sup>-1</sup> can be translated as a more stable  $\eta^1(\text{O})$  geometry of *keto* acetone than that specified as the fixed point *i.e.* starting configuration of the elastic band calculation. The second barrier (2) at roughly 10 kJ mol<sup>-1</sup> can be assumed to be the activation energy required for the endon geometry to convert into the di- $\sigma$  coordination. This energy barrier is also observed in figure 7.6(b), which shows the change in the M-C bond distance of the di- $\sigma$  *keto* acetone as the chain of structures relaxes to the MEP.

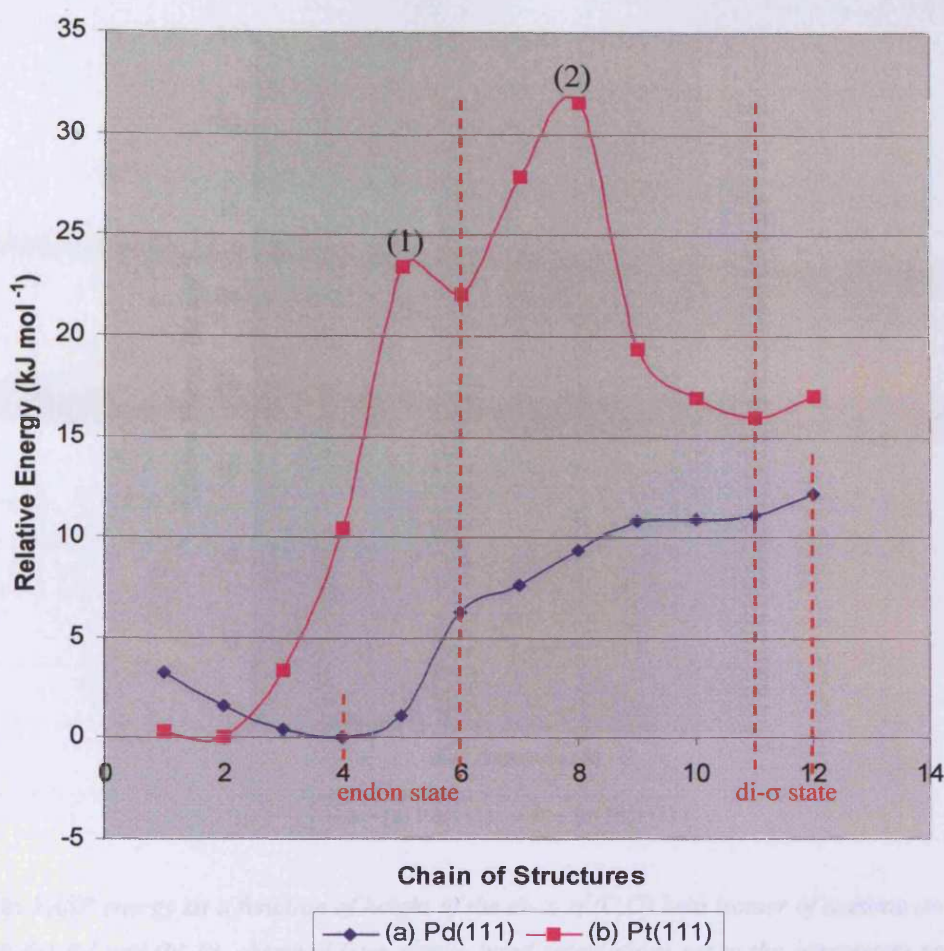


**Figure 7.5:** VASP energy as a function of reaction coordinate for the transformation of the endon,  $\eta^1(\text{O})$  keto isomer of acetone to di- $\sigma$ ,  $\eta^2(\text{C},\text{O})$  adsorption mode on the (111) surface of: (a) Pd and (b) Pt, obtained from elastic band calculations set to the parameters specified in Chapter 4, section 4.3.4. NB. Structures 1 and 12 represent the fixed start and end points for the elastic band calculations. On relaxing the chain of structures the original endon and di- $\sigma$  states further minimise into adsorbed states 6 and 11 on Pt and species 4 on the Pd surface. These structures are used to calculate the energy barrier for the inter-conversion.



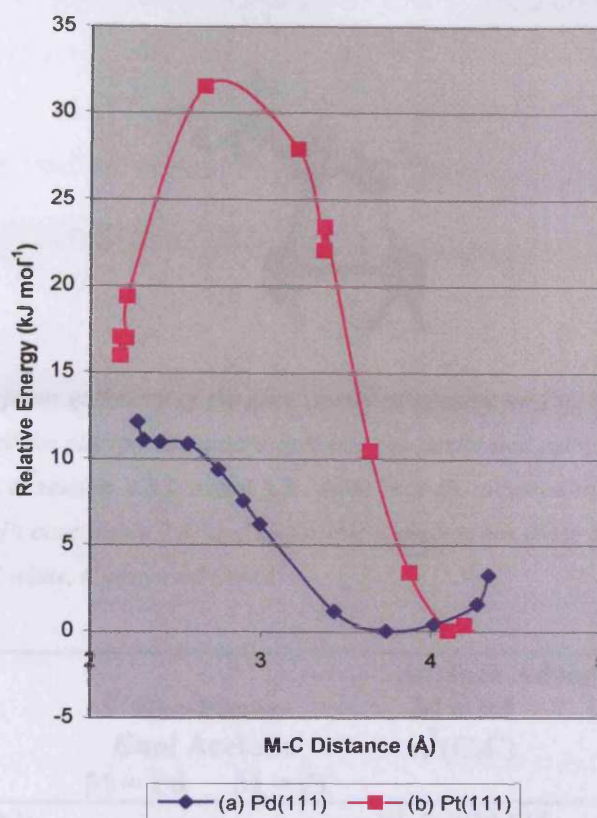


**Figure 7.6:** VASP energy as a function of height of the di- $\sigma$ ,  $\eta^2$ (C,O) keto isomer of acetone on the (111) surface of: (a) Pd and (b) Pt, obtained from elastic band calculations set to the parameters specified in Chapter 4, section 4.3.4.

Having observed the stabilisation of the *keto* isomer, the *enol* form of acetone was docked onto the surfaces in a geometry that would favour surface bonding and then optimised using the same parameters and methods as specified for the ketone. The resulting adsorption data is summarised in table 7.5 and the stabilised geometry is illustrated in figure 7.7, note that the surface coordination is significantly different to that modelled by the CASTEP code, refer to figure 6.10 (Chapter 6, section 6.3).

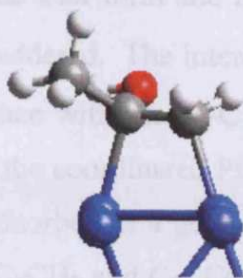


**Figure 7.7:** VASP adsorption geometry of the enol isomer of acetone on Pt(111). Most of the metal (M) atoms have been removed for clarity. Geometry optimisation performed using periodic DFT parameters as specified in Chapter 4, section 4.3.2 and 4.3.3. Note that the adsorption geometry on the Pd(111) surface is similar to the Pt case (table 7.5) and so for this reason is not illustrated. Molecular atoms are colour coded: Pt blue, H white, C grey and O red.

Property	Gas-Phase <i>Enol</i> Acetone		Surface Adsorption States	
			M = Pd	M = Pt
	M = Pd	M = Pt	$\eta^2(\text{C},\text{C})$	$\eta^2(\text{C},\text{C})$
$\Delta E_{\text{ads}}$ (kJ mol <sup>-1</sup> )			81.5, {28.5} <sup>a</sup>	124.6, {74.6} <sup>a</sup>
C-OH (Å)	1.384	1.377	1.393	1.399
C-CH <sub>2</sub> <sup>b</sup> (°)	180	180	217	226
C-CCO <sup>b</sup> (°)	180	180	143	135
M-C (Å)			2.117/2.155	2.101/2.151
M-C-C (°)			99.8/114.4	102.4/112.0
$\Delta z$ (M) <sup>c</sup> (Å)			0.184(C <sub>1</sub> ) 0.197(C <sub>2</sub> )	0.225(C <sub>1</sub> ) 0.216(C <sub>2</sub> )

**Table 7.5:** VASP adsorption energies and geometries of adsorbed enol isomer of acetone on Pd and Pt(111). Adsorption energies calculated relative to the clean surface and gas-phase enol and <sup>a</sup>keto isomer of acetone (shown in braces) using the appropriately substituted form of equation 6.2 (Chapter 6, section 6.1). Periodic DFT computations performed using parameters as specified in Chapter 4, sections 4.3.2 and 4.3.3. <sup>b</sup>Angle formed by the plane of three atoms and the bond indicated by dash. <sup>c</sup>Displacement of coordinated metal (M) atoms from the surface plane.

On both metals, *enol* acetone stabilised via a coordination in which the plane of the molecule was parallel to the surface with the C=C bond bridged over, and binding to two separate surface atoms in a di- $\sigma$  mode similar to that found for ethene over Pt(111) (figure 6.3(c), Chapter 6, section 6.1). The adsorption energies for the *enol* isomer are much larger than those measured for the *keto* acetone (table 7.4) implying that thermodynamically it is the preferred adsorbed state. The energies were explicitly



referenced against the gas-phase *keto* isomer so that it included the energy required to convert a gas-phase ketone into the *enol* form and thus, serves as a common reference state for all surface adsorbates considered. The interaction was found to be  $46.1 \text{ kJ mol}^{-1}$  stronger on Pt than the Pd surface with the M-C distances correspondingly shorter, resulting in a larger movement of the coordinated Pt atoms from the surface. The *enol*, unlike its gas-phase structure is adsorbed in a geometry that is non-planar in nature as emphasised by the change in the C-CH<sub>2</sub> and C-CCO angles, and the lengthening of the C-OH bond. The geometry of the adsorbate and structure of the metal is distorted in such a way as to maximise the attraction and yet minimise the effect of repulsion as well as satisfy the conditions of steric hindrance.

With the *enol* isomer stabilised on the metal surfaces it is reasonable to assume that the corresponding enolate could well play a role in the mechanism of hydrogenation of ketones and be present on the catalytic surface as an adsorbed intermediate. Recently, RAIRS experiments for the condensation of acetone over a clean and preoxidised Ni(111) surface have isolated such species [17]. The enolate is formally an anionic species generated by proton abstraction from the alcohol group of the *enol* isomer. To model the adsorption modes of the enolate, the abstracted hydrogen atom is also included and is docked onto the metal surface as far as possible from the enolate moiety in the simulation cell employed. The gas-phase calculation of the enolate ion, modelled in the Pd simulation box, shows the species to be roughly  $258 \text{ kJ mol}^{-1}$  higher in energy than the stable *keto* isomer of acetone. For the Pt simulated enolate, the gas-phase energy difference is slightly smaller at  $256 \text{ kJ mol}^{-1}$ .

Earlier, the *enol* was found to stabilise in a  $\eta^2(\text{C,C})$  bridging adsorption geometry, figure 7.7. For this adsorption mode the corresponding enolate ion was modelled on both the surfaces with the abstracted H atom positioned in the two most favourable sites for adsorption *i.e.* the *hcp* and *fcc* hollow sites (refer to Chapter 2, section 2.4 for relevant literature). The resulting adsorption energies for these species are presented in table 7.6 with the most stable geometry for the enolate illustrated in figure 7.8.

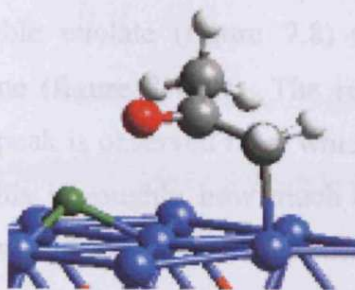


**Figure 7.8:** VASP adsorption geometry of the most stable enolate ion of acetone on Pt(111). The abstracted H atom is adsorbed onto an fcc hollow site. Most of the metal (M) atoms have been removed for clarity. Geometry optimisation performed using periodic DFT parameters as specified in Chapter 4, section 4.3.2 and 4.3.3, i.e. those used for the simulation of keto group molecules. The corresponding adsorption geometry on the Pd(111) surface is similar but weakly bound (table 7.6) and so for this reason is not illustrated. Molecular atoms are colour coded: Pt blue, H white, H-abstracted green, C grey and O red.

Property	Surface Adsorption States			
	Adsorption site of H atom			
	Hcp Hollow		Fcc Hollow	
	M = Pd $\eta^1(\text{C})$	M = Pt $\eta^1(\text{C})$	M = Pd $\eta^1(\text{C})$	M = Pt $\eta^1(\text{C})$
$\Delta E_{\text{ads}}$ (kJ mol <sup>-1</sup> )	41.3, {-11.7} <sup>a</sup>	62.5, {12.5} <sup>a</sup>	61.1, {8.1} <sup>a</sup>	84.2, {34.2} <sup>a</sup>

**Table 7.6:** VASP adsorption energies of adsorbed acetone enolate species on Pd and Pt(111). Adsorption energies calculated relative to the clean surface and gas-phase enolates and <sup>a</sup>keto isomer of acetone (shown in braces) using the appropriately substituted form of equation 6.2 (Chapter 6, section 6.1). Periodic DFT computations performed using parameters as specified in Chapter 4, sections 4.3.2 and 4.3.3, i.e. those used to model keto group molecules.

In contrast to the parallel coordination of the adsorbed *enol* species, the enolates were found to stabilise through a  $\eta^1(\text{C})$  alkyl mode, reminiscent of the CASTEP *enol* acetone geometry on Pt(111) (refer to figure 6.10, Chapter 6, section 6.3). The energies referenced to the gas-phase *keto* acetone indicate that the adsorption of the H atom in an *fcc* hollow site is thermodynamically more stable than the alternative *hcp* site. The adsorption on the Pt surface for the stable enolate is approximately 26 kJ mol<sup>-1</sup> stronger than that calculated for the Pd surface and when compared to their parent *enol* structures, for which the adsorption is preferred, the interactions are weaker by 40.4 and 20.4 kJ mol<sup>-1</sup> respectively.

For the Pt surface, elastic band calculations, set to the same specifications as commented upon earlier, were employed to investigate the energy barrier for the transformation from the stable enolate (figure 7.8) to the corresponding  $\eta^2(\text{C},\text{O})$  adsorbed state of *keto* acetone (figure 7.4(b)). The resulting profile is illustrated in figure 7.9 and from it a clear peak is observed from which a barrier of approximately 51 kJ mol<sup>-1</sup> can be derived. This is roughly how much energy the abstracted H atom, occupying an *fcc* hollow site would require to diffuse across the Pt(111) surface to react with the enolate to produce the di- $\sigma$  bound ketone. The energy barrier can also be seen in figure 7.10, which follows the reaction for the C-H bond formation *i.e.* between the abstracted H atom and the C atom of the adsorbed enolate to give the resulting methyl group of the acetone.

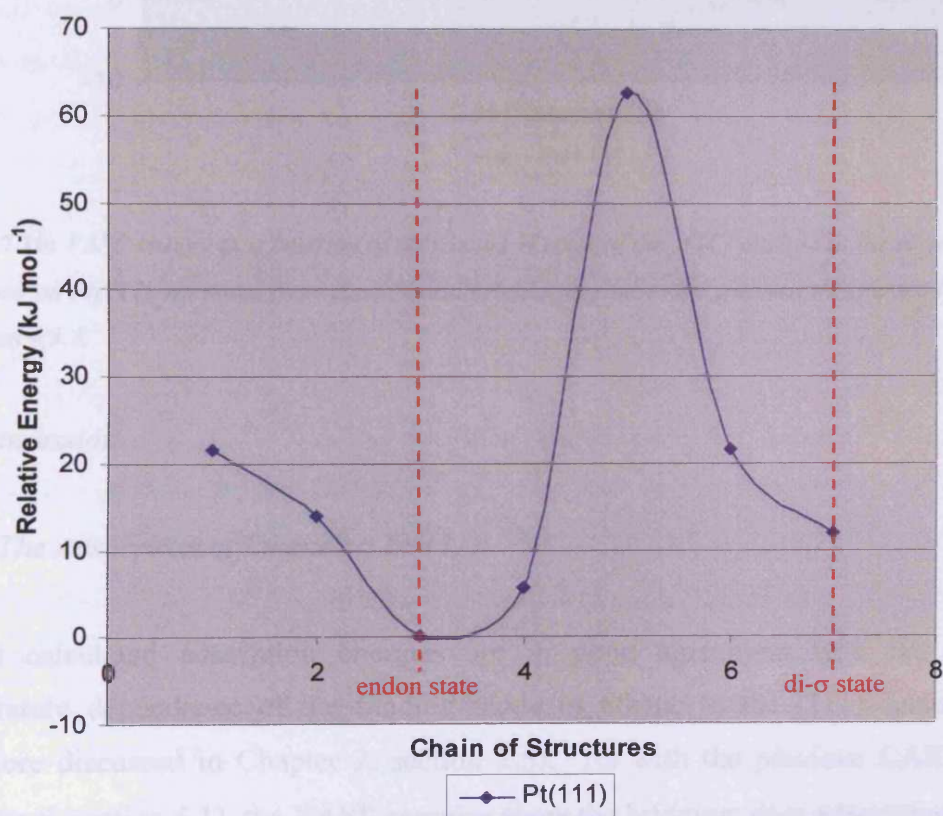


**Figure 7.9:** VASP energy as a function of reaction coordinate for the transformation of acetone enolate, adsorbed in a  $\eta^1(\text{C})$  geometry with the abstracted H atom occupying an *fcc* hollow site to the di- $\sigma$ ,  $\eta^2(\text{C},\text{O})$  adsorption mode on the (111) surface of Pt. Elastic band calculations set to the parameters specified in Chapter 4, section 4.3.4. NB. Structures 1 and 7 represent the fixed start and end points for the elastic band calculations. On relaxing the chain of structures the original endon state further minimises into adsorbed state 3. Structures 3 and 7 are used to calculate the energy barrier for the inter-conversion.



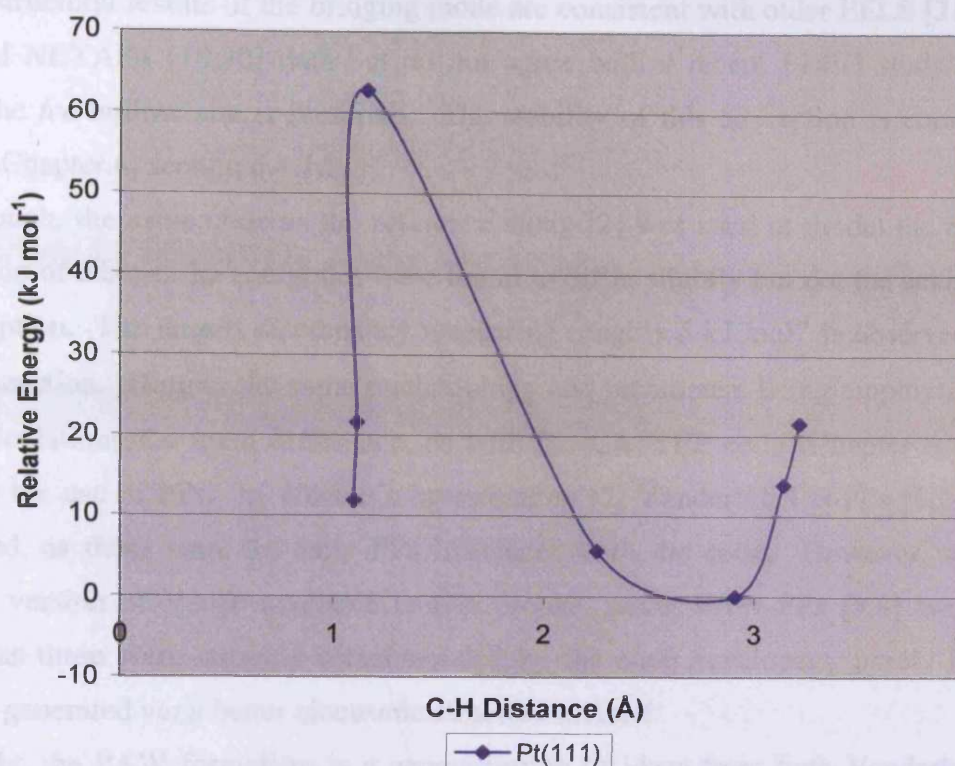


**Figure 7.10:** VASP energy as a function of abstracted H atom of the  $\eta^1(\text{C})$  enolate to the formation of di- $\sigma$  acetone on Pt(111), obtained from elastic band calculations set to the parameters specified in Chapter 4, section 4.3.4.

## 7.4. Discussion

### 7.4.1. The Adsorption of Ethene on Pt(111)

The calculated adsorption energies are in good agreement with the observed temperature dependence of the binding mode of ethene to the (111) surface of Pt, (literature discussed in Chapter 2, section 2.5). As with the previous CASTEP data (Chapter 6, section 6.1), the VASP energies show the bridging, di- $\sigma$  adsorption mode to be most stable followed by  $\pi$  adsorption at the alternative atop sites. The weak interaction of the cross bridge mode, indicated by its small adsorption energy ( $9 \text{ kJ mol}^{-1}$ ) implies the unlikely nature of this adsorbed species to be observed under experiment. The di- $\sigma$  adsorption at  $132 \text{ kJ mol}^{-1}$  is in good agreement with the microcalorimetric study of  $136 \text{ kJ mol}^{-1}$  for di- $\sigma$  and  $120 \text{ kJ mol}^{-1}$  for a mixed di- $\sigma$  and  $\pi$  adsorption measured on the Pt(110) surface [18] and Pt powders [19,20].

The structural results of the bridging mode are consistent with older EELS [21], UPS [19] and NEXAFS [10,20] data but do not agree with a recent LEED study [22] in which the *fcc* hollow site is preferred. The stability of this adsorption is commented upon in Chapter 6, section 6.4.1.

Although, the same code as the reference study [2] was used to model the periodic adsorption of ethene, the energetics were found to differ slightly but not the actual trend in adsorption. The largest discrepancy measuring roughly  $5 \text{ kJ mol}^{-1}$  is observed in the di- $\sigma$  adsorption. Despite the same methodology and parameters being employed in the DFT calculations the main difference, as with the CASTEP code (Chapter 6, section 6.4.1) is the use of PPs. In Watson's investigation [2] Vanderbilt US-PPs [1,23] were employed, as these were the only PPs interfaced with the code. However, with the updated version of VASP available to this project, novel PAW-PPs [3,4] were used instead as these were strongly recommended by the code developers, purely because they are generated *via* a better electronic structure method.

Briefly, the PAW formalism is a generalisation of ideas from both Vanderbilt-type US-PP and the linear augmented-plane-wave (LAPW) methods [24] and was first proposed by Blöchl [4]. Blöchl introduced a linear transformation from the soft pseudo- (PS) to the all-electron (AE) wavefunction and applied the derived PAW total-energy functional to the Kohn-Sham (KS) functional. Compared with the US-PP, the construction of the PAW datasets is much easier because the pseudization of the augmented charges is avoided as the PAW approach uses only the AE wavefunctions and potentials. The full derivation of the exact formal relationship between Vanderbilt-type US-PPs and Blöchl's PAW method, along with its implementation in the VASP code can be found in references 3 and 4.

Although, it has been illustrated that both approaches yield reasonably accurate total-energies, the PAW-PPs are considered to be more precise than the alternative US-PPs for two reasons: the first of which involves the size of the core radii, PAW possessing smaller radial cutoffs than the US-PPs, and the second involving the ability of the PAW to reconstruct the exact valence wavefunction with all nodes in the core region. Note that older US-PPs can be used if higher precision calculations are not required, as the smaller core radii of the PAW-PPs require larger energy cutoffs (*i.e.* basis sets). As an example, PAW-PPs used in the ethene adsorption calculations have been provided in Appendix C and their corresponding Vanderbilt US-PPs are specified in Appendix B.

In comparison with earlier DFT calculations, the VASP energetics and structures are in excellent agreement with the periodic study of Ge and King [25] for which adsorption energies of  $121.8 \text{ kJ mol}^{-1}$  for the di- $\sigma$  and  $53.4 \text{ kJ mol}^{-1}$  for the  $\pi$  modes were obtained. However, unlike the CASTEP results (Chapter 6, section 6.4.1), the periodic energies are not comparable to the cluster model of Watwe *et al.* [26], for which adsorption energy was found to be affected by the size of the cluster and the poor representation of the extended (111) state of the Pt surface.

Excellent agreement between the literature periodic work and in particular the reference study verifies the methodology employed to study surface calculations. Unlike the CASTEP code, for which the approximate error in ethene adsorption energy was calculated to be between 10-20%, VASP generated more reliable data. The actual difference between the energetics and that of the reference work is calculated to be up to 4% and is well within the acceptable limit for DFT calculations. For this reason, continuation to study the chemisorption characteristics of the ketone groups over Pd and Pt(111) with VASP was justified.

#### 7.4.2. The Adsorption of Formaldehyde on Pd and Pt(111)

Despite the fact that at low temperature the adsorbed species of formaldehyde cannot be easily characterised on Pd(111) [27] and Pt(111) [28,29] because of the reactive nature of the molecule, theoretical models have isolated the single adsorbed intermediates. In accordance with the CASTEP modelling (Chapter 6, section 6.2), VASP stabilised both the endon and di- $\sigma$  geometries of formaldehyde on both the (111) surfaces of Pd and Pt. Weaker interactions were calculated with the VASP program (table 7.3) than the CASTEP code (table 6.4, Chapter 6, section 6.2) as reflected in the calculated adsorption energies. In each case, the calculations show the di- $\sigma$  mode to be more strongly bound to the surface than the endon formaldehyde, in agreement with the dominant species observed experimentally [28].

A significant difference in energy between the two adsorption modes, measuring up to  $42$  and  $52 \text{ kJ mol}^{-1}$  on Pd and Pt was observed, prompting the barrier between the transformation from endon to di- $\sigma$  to be calculated. Elastic band calculations indicate small barriers of  $2$  and  $6 \text{ kJ mol}^{-1}$  for the transformation on the Pd and the Pt surface. This shows the origin of the stability of the endon mode at low temperature on Pt and

the rapid conversion between the adsorbed states on Pd(111), and ties in well with the literature *i.e.* formaldehyde adsorbed states decompose or polymerise rapidly. Note, also, that the conversion of the analogous  $\eta^1$  to the  $\eta^2$  adsorbed state of acetone has been shown to occur rapidly on Pd(111) above 200 K [16].

The adsorption energy of  $54 \text{ kJ mol}^{-1}$  for the di- $\sigma$  adsorption on Pd(111) is in excellent agreement with the TPD estimate of  $51 \text{ kJ mol}^{-1}$  of Davis and Barteau [27], whereas, for the Pt surface the interaction is stronger by roughly  $18 \text{ kJ mol}^{-1}$  than the TPD value characterised by Abbas *et al.* [28]. However, experimentally, the adsorption of the  $\eta^1(\text{O})$  mode has only been characterised on surfaces which have been modified with an oxygen adatom overlayer, and for this reason the corresponding data presented here is best compared against earlier theoretical work. The adsorption of the endon state on Pd and Pt(111) is roughly  $12$  and  $17 \text{ kJ mol}^{-1}$  and is found to disagree with the corresponding values of  $43$  and  $46 \text{ kJ mol}^{-1}$  calculated by Delbecq *et al.* [10,11]. Coincidentally, the predominant di- $\sigma$  species, with adsorption energies measuring  $95.8$  and  $133 \text{ kJ mol}^{-1}$  for the Pd and Pt(111) are also grossly exaggerated in the above study compared to the periodic values. The disparity is expected as extended Hückel calculations were used employing clusters of 49 metal atoms to represent the flat (111) surface of Pd and Pt. Although, the adsorption energy of the di- $\sigma$  on the defect surface of Pt<sub>114</sub> (step site) was observed to be lower than that measured on the (111) terrace [11], the values were still in poor agreement with those calculated by VASP. Generally, for surface calculations cluster models tend to neglect the extended states in the metal system, causing the adsorbates to over bind [30].

However, the adsorption energy of the di- $\sigma$  on the Pd(111) was modelled by VASP to be identical to the DFT value calculated by Desai *et al.* [31]. Unfortunately, the corresponding Pt value was overestimated by some  $20 \text{ kJ mol}^{-1}$ , which corresponded to the TPD estimates [28]. The difference in energy originates from the parameters used to represent the periodic models and these were discussed previously (Chapter 6, section 6.4.2) and not the program used. Note that the same computational parameters except the US-PPs in the CASTEP work were applied to the VASP models presented here.

Structurally, the results of the di- $\sigma$  correspond to the vibrations observed in HREELS spectra after Pt(111) is annealed to 240 K [8]. The distortion of the molecular geometry in the sense that the atoms sites are hybridised from  $sp^2$  to  $sp^3$  on coordination with the surfaces is analogous to that reported for aldehydes [10,27,32]. In the di- $\sigma$  case, the

C=O bond length is significantly increased from its gas-phase distance and is close to the value of 1.40-1.41 Å found in organometallic complexes such as  $\text{Pt}_2(1,5\text{-C}_8\text{H}_{12})_2\eta_2(\text{CF}_3)_2\text{CO}$  [33] and  $(\text{Cp}_2\text{ZrX})_2(\text{HRCO})$  [34].

#### 7.4.3. The Adsorption of Acetone on Pd and Pt(111)

VASP optimised two very different stable minima for the *keto* isomer of acetone on each of the (111) surfaces of Pd and Pt. These were found to correspond to the coordination modes reported in the literature, which were derived from experimental characterisation techniques [15,16]. The adsorbed structures were analogous to those determined for formaldehyde. Note that only the endon,  $\eta^1(\text{O})$  geometries were observed with CASTEP modelling (refer to figure 6.9 and table 6.5, Chapter 6, section 6.3). With the use of VASP, the stability of the endon coordination over the di- $\sigma$  was predicted on both surfaces and found to support the TDS and HREELS experiments of acetone on Pt single crystals, in which the  $\eta^1(\text{O})$  mode dominates the small quantity of  $\eta^2(\text{C,O})$  observed at defect sites [15]. The dominance of the endon mode is also confirmed by more recent RAIRS and HREELS experiments on almost defect free Pt(111) [35]. Note that recent vibrational studies performed by a colleague within the computational group at Cardiff, illustrates the incorrect assignment of this di- $\sigma$ ,  $\eta^2(\text{C,O})$  ketone to be representative of an adsorbed enolate species instead [36].

Experimentally, the results of TPD studies have been used to derive adsorption energies for the  $\eta^1(\text{O})$  acetone on Pd and Pt(111) using the Redhead equation [37]. The values are similar and between 48-49 kJ mol<sup>-1</sup> [15,16,35]. However, they do not correspond to the periodic calculations, as the adsorption energies are roughly 30 and 21 kJ mol<sup>-1</sup> greater in energy. Likewise, the corresponding adsorption energy of the di- $\sigma$  mode on Pd is 69 kJ mol<sup>-1</sup> and 52 kJ mol<sup>-1</sup> on Pt [16] and again is nowhere near the values optimised in VASP *i.e.* 19 and 9 kJ mol<sup>-1</sup>, respectively. In fact the theoretical calculations presented here contradict the energetic ordering determined by TPD and the earlier HREELS and TDS data of Vannice *et al.* [35]. This could possibly be due to the incorrect assignment to adsorbed states, as mentioned earlier.

However, the ordering, although not the absolute adsorption energies are comparable to the cluster model of Delbecq *et al.* [11], which was referenced earlier for the adsorption of formaldehyde (section 7.4.2). On the Pt<sub>49</sub> surface the endon adsorption



measured  $46 \text{ kJ mol}^{-1}$  and is found to be roughly twice the value calculated by the periodic model and in agreement with the TPD data above [15,35] whereas the di- $\sigma$  adsorption at  $26 \text{ kJ mol}^{-1}$  is stronger by  $7 \text{ kJ mol}^{-1}$ . On increasing the size of the Pt cluster to 114 atoms, the corresponding adsorption energies of binding onto the terrace of the step site was found to reduce to  $39 \text{ kJ mol}^{-1}$  for the  $\eta^1(\text{O})$  mode and  $21 \text{ kJ mol}^{-1}$  for the  $\eta^2(\text{C},\text{O})$  coordination. Despite this, the reverse ordering was observed on the  $\text{Pd}_{49}$  cluster as the di- $\sigma$  adsorption at  $80 \text{ kJ mol}^{-1}$  was found to be dominant over the endon geometry ( $43 \text{ kJ mol}^{-1}$ ). Note that previous DFT calculations based on a 2-layer Pt(111) surface slab with only adsorbate atoms geometry optimised, confirmed that, for acetone, the  $\eta^2(\text{C},\text{O})$  parallel adsorption geometry is less energetically favourable than the  $\eta^1(\text{O})$  endon structure [38], in agreement with the data presented here.

Initially, to study the adsorption of the  $\eta^2(\text{C},\text{O})$  acetone the starting structure of the calculation was set-up so that the molecular plane was configured parallel to the surface. By doing so the structure was found to relax to the endon adsorbed minimum. The actual di- $\sigma$  coordinations reported here were obtained by distorting the molecule so that the methyl groups were away from the surface prior to relaxation. Hence, elastic band calculations were performed to measure the energy barrier for the transformation from endon to parallel adsorption modes. From the adsorption data (table 7.4), the lower bound of the barrier on Pd is estimated to be  $9.5 \text{ kJ mol}^{-1}$  and for Pt  $9.2 \text{ kJ mol}^{-1}$ . However, no barrier to conversion was observed on Pd (figure 7.5(a)) whereas on Pt (figure 7.5(b)) an activation energy of  $10 \text{ kJ mol}^{-1}$  is required, indicating in both cases the origin of the stability of the observed  $\eta^1(\text{O})$  mode at low temperature. Nevertheless, if the conditions are favourable then the barrier on Pt could very easily be overcome to allow the stabilisation of the di- $\sigma$  geometry and thus, supports the evidence for the small concentration observed at defect sites [15]. Note that rapid conversion of the  $\eta^1$  to the  $\eta^2$  state has been observed above 200 K on Pd(111) [16].

The reverse energetic ordering of the adsorbed states for formaldehyde in comparison to the trend observed for the *keto* acetone implies that the steric interaction of the methyl groups with the (111) surface is responsible for destabilising the  $\eta^2(\text{C},\text{O})$  structure. In earlier DFT models the destabilisation was thought to be exaggerated due to the use of a fixed surface [38].

The adsorption of the *enol* isomer of acetone was investigated with VASP, the gas-phase equilibrium of the *keto-enol* tautomerism was found to lie between 50 and 53 kJ

$\text{mol}^{-1}$  in preference of the ketone for Pt and Pd, respectively. The discrepancy between the energy difference can be explained in terms of the size of the simulation box used. The dimensions for the Pt cell measured in Å are slightly larger at  $8.43 \times 8.43 \times 19.59$  than those for the Pd *i.e.*  $8.33 \times 8.33 \times 19.54$ , and thus contribute to the measured energies of the acetone isomers. The energies are consistent with our earlier DFT calculations (Chapter 6, section 6.3) and are in agreement with the experimental range of 46.9-58.2  $\text{kJ mol}^{-1}$  [39,40] and theoretical estimates of 51.9  $\text{kJ mol}^{-1}$  [41].

The adsorption geometry of the *enol* in the  $\eta^2(\text{C,C})$  coordination modelled on both surfaces is found to be close to that predicted by the CASTEP program for the Pd, in which both C atoms of the double bond interact with a single metal atom, refer to figure 6.10 (Chapter 6, section 6.3). However, the adsorption energy for the corresponding *enol* site stabilised by VASP on the Pd(111) surface differs by 7.4  $\text{kJ mol}^{-1}$ . From the adsorption energies relative to the gas-phase ketone, the *enol* isomer is thermodynamically preferred on both metals over the ketone and its adsorbed enolate. A summary of the adsorption data is included in the Conclusion (figure 7.11), however, on the Pd metal the *enol* is roughly 20  $\text{kJ mol}^{-1}$  stronger than the enolate (abstracted H atom occupying *fcc* hollow site) and the  $\eta^2(\text{C,O})$  *keto* isomer but only 10  $\text{kJ mol}^{-1}$  stronger than the alternative  $\eta^1(\text{O})$  mode. For the Pt case the corresponding values are on average 24  $\text{kJ mol}^{-1}$  for the *keto* adsorbed states and roughly 40  $\text{kJ mol}^{-1}$  for the stable enolate.

Note, that for surface adsorption calculations the correct treatment of the enolate is simple as the abstracted H atom adsorbs onto the metal surface. However, the problem lies in the gas-phase description. The gas-phase values of 258 and 256  $\text{kJ mol}^{-1}$  for the enolate modelled in the Pd and Pt simulation cells (discrepancies in the values occur for reasons mention above) were calculated by applying a uniform positive background charge to the anion in the unit cell. In this method an overall neutral repeat unit is modelled and thus, is a more stable solution than the alternative, which includes an H atom explicitly in the simulation cell. This is not surprising since the energy of abstraction of H in a reaction depends strongly on the species receiving the H atom.

## 7.5. Conclusions

The adsorption of simple ketone containing molecules to the (111) surface of Pd and Pt have been considered as representative structures for the adsorbed intermediates involved in the enantioselective hydrogenation reaction of  $\alpha$ -ketoesters over cinchona modified group 10 surfaces. Various orientations and possible isomeric forms of formaldehyde and acetone have been investigated with the use of the plane-wave periodic code VASP [42].

A repeat of the investigation of surface adsorption of ethene to Pt(111) originally conducted by Watson *et al.* [2] verified the procedure of modelling an adequate surface with the use of a fully relaxed 3-layer metal slab. The energetics of adsorption for ethene calculated with the use of the more recent version of VASP (release 4.4.5) were found to be in excellent agreement with the adsorption energies calculated by an earlier release of the code by Watson *et al.* [2]. The calculations showed that the di- $\sigma$  adsorption site was preferred over the two atop modes and that the weak interaction of the cross-bridge site was most unlikely to be observed under experimental conditions. The stabilisation of the di- $\sigma$  mode was found to agree with the experimental findings from EELS [21], UPS [19] and NEXAFS [10,20] studies and with the periodic calculations of Ge and King [25]. Only slight differences in the adsorption energies for the ethene modes were calculated in comparison to those modelled by Watson *et al.* [2]. The largest discrepancy in adsorption energies is 4% for the di- $\sigma$  adsorption. In our calculations the core of the atoms are modelled more accurately with the use of novel PAW-PPs [3,4]. However, if higher precision calculations are not required then standard Vanderbilt US-PPs [1,23] (as applied in the reference work [2]) can still be used.

For the interaction of formaldehyde, two adsorption geometries are stabilised on both the metal surfaces. The coordination of the molecule in the parallel,  $\eta^2(\text{C,O})$  mode is calculated to be roughly 42 and 52 kJ mol<sup>-1</sup> more strongly adsorbed than the alternative endon,  $\eta^1(\text{O})$  mode on Pd and Pt. Experimentally, the adsorption energies for the di- $\sigma$  formaldehyde on both Pd and Pt(111) have been reported by TPD to be iso-energetic at 51 and 52 kJ mol<sup>-1</sup> [27,28]. Our calculations contradict this as a clear energy difference of 16 kJ mol<sup>-1</sup> in preference for the Pt surface is modelled. The assignment for the TPD data could in fact relate to the adsorption of the formyl species, rather than molecular

formaldehyde modelled in our calculations, as this is the species known to decompose to CO and H<sub>2</sub> or initiate formaldehyde polymerisation on Pd and Pt(111) [27]. However, the preferential stabilisation of the di- $\sigma$  mode over the endon geometry in our calculations is also supported by extended Hückel calculations of Delbecq and Sautet [10,11].

The low adsorption energies calculated for the endon adsorbed formaldehyde imply that the transformation from the endon to the di- $\sigma$  mode and the direct adsorption to the di- $\sigma$  mode may be activated processes. Barrier calculations show that the direct adsorption of the di- $\sigma$  mode is an activated process on Pt(111) with a small activation energy of roughly 6 kJ mol<sup>-1</sup> required. For the Pd(111) surface the activation energy is much smaller at 2 kJ mol<sup>-1</sup> and is considered to be negligible. It can be assumed that adsorption directly into the di- $\sigma$  mode is most likely hindered by the narrow adsorption channel created by the very specific orientation of the molecule required for strong interaction, as implied for ethene adsorption [2]. The calculations also find the transformation from the endon to the di- $\sigma$  formaldehyde on both metal surfaces to be an activated process requiring the same activation energy as required for the direct adsorption into the di- $\sigma$  modes. Although the activation energies illustrate the origin of the stability of the endon mode at low temperature, the magnitudes imply the likelihood of rapid conversion between the adsorbed states, in support of the experimental observation whereby the species are known to decompose or polymerise rapidly [27].

The gas-phase calculations of acetone show the ketone to be considerably more stable than the *enol* or the enolate. This implies that any adsorption process will begin with the ketone interacting with the surface. The geometry in which the *keto* acetone stabilises on adsorption to the Pd and Pt surfaces is analogous to that found for formaldehyde, but the energetic ordering is reversed. Adsorption in the endon,  $\eta^1(\text{O})$  configuration is found to be roughly 10 and 9 kJ mol<sup>-1</sup> more strongly adsorbed than the alternative di- $\sigma$ ,  $\eta^2(\text{C},\text{O})$  mode on Pd and Pt(111). This energy difference is caused by the steric interaction between the methyl groups of the acetone and the surface and so is likely to be common to any substituted ketone adsorbed parallel to the surface. Barrier calculations show that the inter-conversion from the endon mode to the di- $\sigma$  configuration is an activated process requiring activation energy of approximately 10 kJ mol<sup>-1</sup> on Pt. This illustrates the origin of the stability of the endon adsorbed mode

below 220 K [13-15]. No barrier was observed on Pd for the *keto* acetone, supporting the rapid conversion from the  $\eta^1(\text{O})$  to the  $\eta^2(\text{C},\text{O})$  adsorbed state above 200 K [16].

The *enol* isomer of acetone was found to adsorb in a parallel  $\eta^2(\text{C},\text{C})$  coordination geometry on both Pd(111) and Pt(111). The interaction was calculated to be much stronger on the latter surface with the adsorption energy calculated to be roughly 75 kJ mol<sup>-1</sup>. In both cases the adsorption energy in the *enol* form is found to be sufficient to compensate for the gas-phase energy difference between the *keto* and *enol* isomers. This suggests that thermodynamically the *enol* form is the preferred adsorbed state on both metals, although it may not be kinetically accessible, as for ketones the  $\eta^1(\text{O})$  mode is dominant.

The enolate species were found to stabilise on both the surfaces in a  $\eta^1(\text{C})$  coordination geometry with the abstracted H atom occupying a surface *fcc* hollow site. The adsorption to the Pt surface at 34.2 kJ mol<sup>-1</sup> was stronger by approximately 26 kJ mol<sup>-1</sup> than that calculated for the Pd(111) surface. The energy barrier found for the diffusion of the abstracted H atom of the enolate across the Pt surface to give the di- $\sigma$ ,  $\eta^2(\text{C},\text{O})$  *keto* acetone species was 51 kJ mol<sup>-1</sup>, implying that the ketone is prevented from reforming once the enolate has formed. Since the enolate is more stable than the ketone it is reasonable to assume that the backward barrier is much higher than the forward barrier. A summary of the energetic ordering of the acetone adsorbed species over both metals is provided in figure 7.11.

Experimental TPD data reports the secondary, di- $\sigma$  adsorbed species of *keto* acetone to be more strongly bound than the endon geometry on both Pd [35] and Pt(111) [15], which is not supported by our own calculations. Our results find that the adsorption energy for the stable enolate on Pd(111) at 41.3 kJ mol<sup>-1</sup> to be in good agreement with the TPD value of 48 kJ mol<sup>-1</sup> for the second adsorbed state of acetone. We propose that this second species observed in the surface science experiments for acetone is a  $\eta^1(\text{C})$  enolate and that the assignment for the di- $\sigma$  mode is unlikely. This is also confirmed by an additional study conducted at Cardiff in which the calculated vibrational frequencies of the enolate were compared with the experimental vibrational spectra [36]. It is quite reasonable to assume that deprotonation of acetone to form the enolate ion on clean Pd and Pt surfaces can occur at low temperatures of surface science experiments as similar species have been reported on the (111) surface of Ni [17].

With respect to the model proposed to predict the selectivity in enantioselective hydrogenation, the parallel adsorption of the ketone group of the pyruvate ester is inferred. However, from our calculations we believe this to be incorrect as it is more than likely that the modifier interacts with the ketone adsorbed in an end-on geometry causing the plane of the molecule to tilt towards the surface, thereby allowing hydrogenation to take place.

To conclude, the results presented here illustrates the active role of the *enol* as an adsorbed species on Pd and Pt surfaces during the hydrogenation of ketones, for which *keto-enol* tautomerism is possible. The molecular models reinforce the findings made by Wells *et al.* [43] in which deuteration of the methyl group of MtPy was observed, indicating the hydrogenation to occur through either the *enol* or enolate species on Pd. The lower *ee* observed for pyruvate hydrogenation on Pd compared to the Pt surface can be rationalised in terms of competitive hydrogenation between the adsorbed *keto* and *enol/enolate* species.

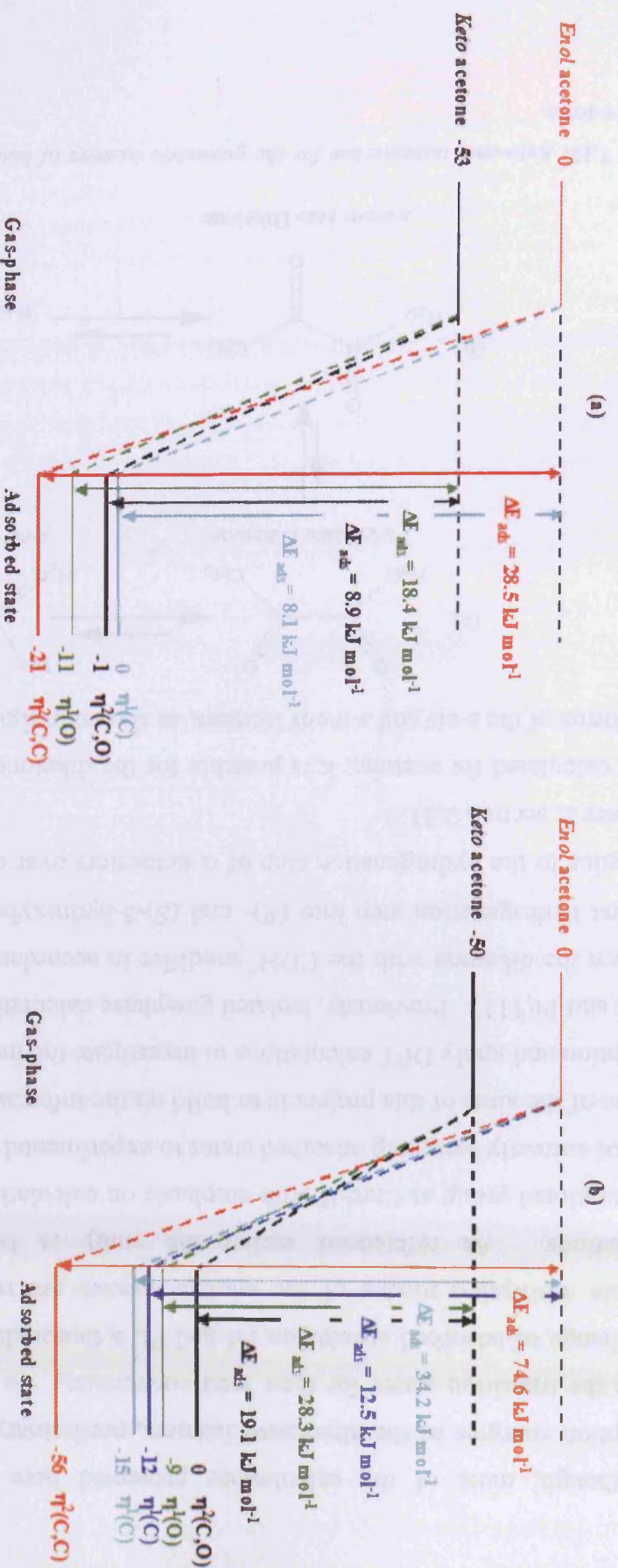


**Figure 7.11:** Energy profiles summarizing the VASP data for the surface adsorbed acetone intermediates on (a) Pd and (b) Pt(111). Profiles not drawn to scale. Adsorption energies measured relative to the keto isomer of acetone. Periodic DFT calculations performed using parameters as specified in Chapter 4, sections 4.3.2 and 4.3.3. Note that the unfavourable adsorption of the enolate with the H atom occupying a surface hcp hollow site is not included for the Pd surface. For the Pt surface the energies of the alternative adsorbed enolates are colour coded, dark blue represents the adsorption of the abstracted H atom in an hcp hollow site whereas light blue represents the adsorption in the fcc hollow site. Adsorption modes are defined for the following acetone isomers:  $\eta^1(O)$  and  $\eta^1(C,O)$ , keto acetone,  $\eta^1(C,C)$ , enol acetone and  $\eta^1(C)$  enolate acetone.

## 7.6. Future Work

Although, most of the calculations presented here are based on the relative adsorption energies of the alternative isomers, preliminary calculations have begun to locate the transition states for their inter-conversion. To fully understand the kinetic interchange of adsorbed species on Pd and Pt, a thorough investigation into all of the possible adsorption modes of the enolate species are required followed by barrier calculations. As referenced earlier the study is being continued within the computational group at Cardiff with emphasis on calculating vibrational frequencies in view of correctly assigning adsorbed states to experimental spectra [36].

One of the aims of this project is to build on the information gained so far for ketone adsorption and apply DFT calculations to investigate the interaction of butane-2,3-dione on Pd and Pt(111). Previously, isolated gas-phase calculations modelled the interaction between the diketone with the  $\text{CDH}^+$  modifier in accordance with the dimer model, as the first hydrogenation step into (*R*)- and (*S*)-3-hydroxybutan-2-one is assumed to be analogous to the hydrogenation step of  $\alpha$ -ketoesters over cinchona modified Pt and Pd (Chapter 2, section 2.3).

As calculated for acetone, it is possible for the diketone to adsorb through the *keto-enol* forms of the *s-cis* and *s-trans* isomers, as shown in figure 7.12.

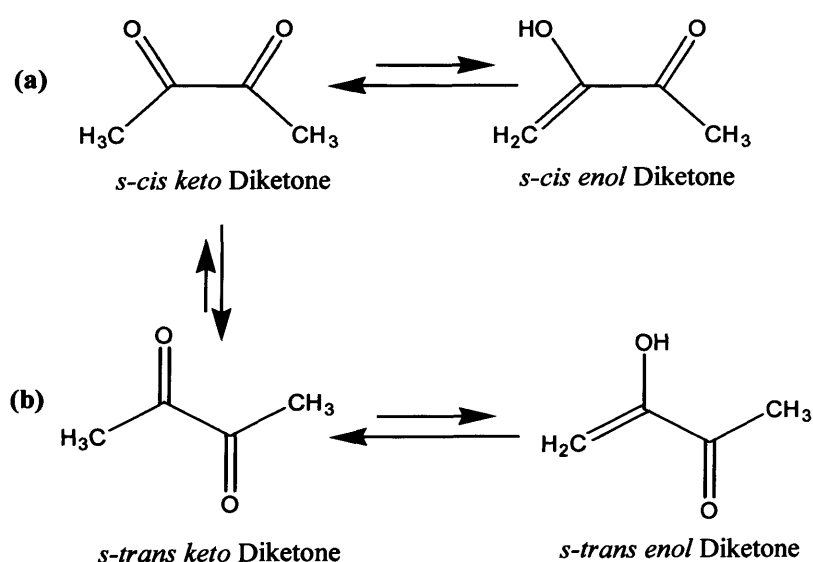


**Figure 7.12:** Keto-enol tautomerism for the geometric isomers of butane-2,3-dione (diketone): (a) *s-cis* and (b) *s-trans*.



The *s-trans* isomer is found to be 3 kJ mol<sup>-1</sup> lower in energy than the *s-cis* form, with the corresponding gas-phase *keto-enol* differences to be 33 and 17 kJ mol<sup>-1</sup>, stabilising the *keto* form. These energies were based on a slightly smaller Pd simulation box, than that used to model the reference gas-phase states for the Pt adsorption calculations (refer to section 7.4), for which the *s-cis/s-trans* difference is larger at 24 kJ mol<sup>-1</sup>, and the *keto-enol* differences are 7 and 25 kJ mol<sup>-1</sup>, respectively.

Initial DFT calculations have considered the adsorption of the *s-cis* diketone to the (111) surface of Pt. The adsorption energy is calculated *via* the expression stated earlier *i.e.* equation 6.2 (Chapter 6, section 6.1), and is appropriately referenced against the gas-phase state of the *keto s-cis* isomer of butane-2,3-dione. Two adsorption states were stabilised, the first in an endon,  $\eta^2(\text{O},\text{O})$  configuration, illustrated in figure 7.13(a) and the second, with the molecule parallel to the surface in which one C atom and both O atoms was found to bind to three different surface atoms in a geometry labelled  $\mu_3(\text{C},\text{O},\text{O})$ , figure 7.13(b). The adsorption energies are provided in table 7.7.

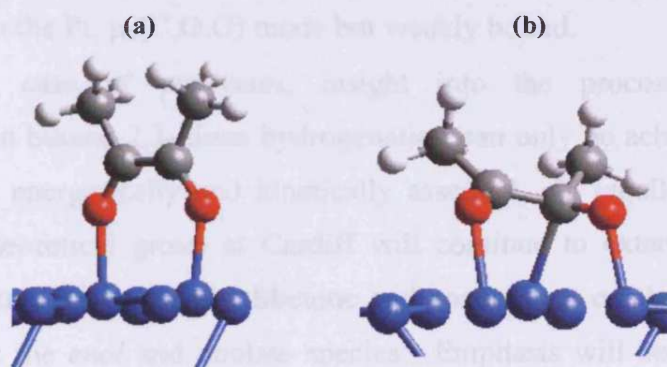


**Figure 7.13:** VASP adsorption geometry of the *s-cis* isomer of butane-2,3-dione on Pt(111): (a)  $\eta^2(\text{O},\text{O})$  and (b)  $\mu_3(\text{C},\text{O},\text{O})$  coordinations. Most of the metal (M) atoms have been removed for clarity. Geometry optimisation performed using periodic DFT parameters as specified in Chapter 4, section 4.3.2 and 4.3.3, *i.e.* those used for keto group adsorbed species. Note that the geometry of the endon adsorption on the Pd(111) surface is similar to the  $\eta^2(\text{O},\text{O})$  structure relaxed on the Pt surface and so for this reason is not provided here. Molecular atoms are colour coded: Pt blue, H white, C grey and O red.

(111) Surface	Surface Adsorption States Adsorption Energy (kJ mol <sup>-1</sup> )	
	$\eta^2(\text{O},\text{O})$	$\mu_3(\text{C},\text{O},\text{O})$
Pd	33.6	-
Pt	35.7	80.7

**Table 7.7:** VASP adsorption energies for the interaction of *s-cis* butane-2,3-dione on Pd and Pt(111), calculated relative to the clean surface and gas-phase keto isomer using the appropriately substituted form of equation 6.2 (Chapter 6, section 6.1). Periodic DFT computations performed using the same parameters used to relax keto group adsorbed states, i.e. those specified in Chapter 4, sections 4.3.2 and 4.3.3.

The calculated adsorption energies illustrate the significant stabilisation of the parallel adsorbed species over the endon structure and is comparable to the energy of the di- $\sigma$  bound *enol* acetone specie over Pd(111) relative to the gas-phase *enol* (refer to table 7.5). The results presented in this research have illustrated the reactive nature of the Pt metal and so the adsorption of the diketone, parallel to the Pd surface is predicted to be analogous to the Pt,  $\mu_3(\text{C},\text{O},\text{O})$  mode but weakly bound.

As with the case of pyruvates, insight into the processes which govern stereoselectivity in butane-2,3-dione hydrogenation can only be achieved if all reaction intermediates are energetically and kinetically assessed. In parallel with the acetone modelling, the theoretical group at Cardiff will continue to extend the surface DFT calculations presented here for the diketone and concentrate on the *s-trans* adsorption modes as well as the *enol* and enolate species. Emphasis will be placed on locating transition states for their inter-conversion so that kinetic interchange of species can be discussed.

In this research clean (111) surfaces have been employed for the sake of simplifying the DFT computations. In reality catalytic surfaces are very rarely flat and as emphasised in the literature (Chapter 2, section 2.6.1) adsorption of ketone groups on defect sites such as a step edge is favoured over the flat terrace. It would be of great interest to be able to further extend this project so that adsorption is investigated on more accurately modelled catalytic surfaces, thus improving comparability with experimental work.

## 7.7. References

- [1] D. Vanderbilt, *Phys. Rev. B*, **41**, 7892, (1990).
- [2] G. W. Watson, R. P. K. Wells, D. J. Willock and G. J. Hutchings, *J. Phys. Chem. B*, **104**, 6439, (2000).
- [3] G. Kresse and D. Joubert, *Phys. Rev. B*, **59**, 1758, (1999).
- [4] P. E. Blöchl, *Phys. Rev. B*, **50**, 17953, (1994).
- [5] VASP 4.4.5, G. Kresse and J. Furthmüller, Vienna, Austria, (2003). G. Kresse and J. Furthmüller, *Comput. Mater. Sci.*, **6**, 15, (1996). G. Kresse and J. Furthmüller, *J. Phys. Rev. B*, **54**, 11169, (1996).
- [6] Accelrys licensed software, <http://www.accelrys.com/cerius2>
- [7] G. A. Somorjai, in “*Surface Chemistry and Catalysis*”, John Wiley & Sons, New York, (1994).
- [8] J. L. Davis and M. A. Barteau, *Surf. Sci.*, **235**, 235, (1990).
- [9] I. Villegas, M. J. Weaver, *J. Chem. Phys.*, **103**, 2295, (1995).
- [10] F. Delbecq and P. Sautet, *Langmuir*, **9**, 197, (1993).
- [11] F. Delbecq and P. Sautet, *Surf. Sci.*, **295**, 353, (1993).
- [12] G. Mills, H. Jonsson and G. Schenter, *Surf. Sci.*, **324**, 305, (1995).
- [13] N. R. Avery, W. H. Weinberg, A. B. Anton and B. H. Toby, *Phys. Rev. Lett.*, **51**, 682, (1983).
- [14] N. R. Avery, *Langmuir*, **1**, 162, (1985).
- [15] N. R. Avery, *Surf. Sci.*, **125**, 771, (1983).
- [16] J. L. Davis and M. A. Barteau, *Surf. Sci.*, **208**, 383, (1989).
- [17] W. -S. Sim, T. -C. Li, P. -X. Yang and B. -S. Yeo, *J. Am. Chem. Soc.*, **124**, 4970, (2002).
- [18] A. Stuck, C. E. Wartnaby, Y. Y. Yeo and D. A. King, *Phys. Rev. Lett.*, **74**, 578, (1995).
- [19] B. E. Spiewak, R. D. Cortright and J. A. Dumesic, *J. Catal.*, **176**, 405, (1998).
- [20] J. Shen, J. M. Hill, M. Watwe, B. E. Spiewak and J. A. Dumesic, *J. Phys. Chem. B*, **103**, 3923, (1999).
- [21] H. Steininger, H. Ibach and S. Lehwald, *Surf. Sci.*, **117**, 685, (1982).
- [22] R. Doll, C. A. Gerken, M. A. van Hove and G. A. Somorjai, *Surf. Sci.*, **374**, 151, (1997).
- [23] G. Kresse and J. Hafner, *J. Phys.: Condens Matter*, **6**, 8245, (1994).

- [24] O. K. Andersen, *Phys. Rev. B*, **12**, 3060, (1975).
- [25] Q. Ge and D. A. King, *J. Chem. Phys.*, **110**, 4699, (1999).
- [26] R. M. Watwe, B. E. Spiewak, R. D. Cortright and J. A. Dumesic, *J. Catal.*, **180**, 184, (1998).
- [27] J. L. Davis and M. A. Barteau, *J. Am. Chem. Soc.*, **111**, 1782, (1989).
- [28] N. M. Abbas and R. J. Madix, *J. Appl. Surf. Sci.*, **7**, 241, (1981).
- [29] M. A. Henderson, G. E. Mitchell and J. M. White, *Surf. Sci.*, **188**, 206, (1987).
- [30] G. W. Watson, R. P. K. Wells, D. J. Willock and G. J. Hutchings, *Surf. Sci.*, **459**, 93, (2000).
- [31] S. K. Desai, M. Neurock and K. Kourtakis, *J. Phys. Chem. B*, **106**, 2559, (2002).
- [32] M. A. Barteau, *Catal. Lett.*, **8**, 175, (1991).
- [33] M. Green, J. A. K. Howard, A. Laguna, L. E. Smart, J. L. Spencer and F. G. A. Stone, *J. Chem. Soc., Dalton Trans.*, **278**, (1977).
- [34] G. Erker, *Acc. Chem. Res.*, **17**, 103, (1984).
- [35] M. A. Vannice, W. Erley and H. Ibach, *Surf. Sci.*, **254**, 1, (1991).
- [36] *Forthcoming*, E. L. Jeffery, R. K. Mann, G. J. Hutchings, S. H. Taylor and D. J. Willock, *Catal. Today*, (2005).
- [37] [www.chemie.uni-hamburg.de/studium/praktika/pc\\_v/TDSengl.pdf](http://www.chemie.uni-hamburg.de/studium/praktika/pc_v/TDSengl.pdf)
- [38] R. Alcalá, J. Greeley, M. Mavrikakis and J. A. Dumesic, *J. Chem. Phys.*, **116**, 8973, (2002).
- [39] F. Tureček, L. Brabee and J. Korvola, *J. Am. Chem. Soc.*, **110**, 7984, (1988).
- [40] J. L. Holmes and F. P. Lossing, *J. Am. Chem. Soc.*, **104**, 2648, (1982).
- [41] F. Tureček and C. J. Cramer, *J. Am. Chem. Soc.*, **117**, 12243, (1995).
- [42] G. W. Watson, R. P. K. Wells, D. J. Willock and G. J. Hutchings, *J. Chem. Soc., Chem. Commun.*, 705, (2000).
- [43] T. J. Hall, P. Johnston, W. A. H. Vermeer, S. R. Watson and P. B. Wells, *Stud. Surf. Sci. Catal.*, **101**, 221, (1996).

## ***Chapter 8***

### ***Conclusions***

## 8.0. Conclusions

The aim of this thesis was to use computational techniques to investigate the role of reaction intermediates in enantioselective heterogeneous catalytic reactions. The model reaction used was that of the hydrogenation of  $\alpha$ -ketoesters over cinchona modified Pt, as the mechanism to account for the high *ee* and *ra* of the reaction has received much attention and has been shown to be a valuable guide for the rational design of new reactants and modifiers [1]. Although it must be emphasised that modelling of the complete system has still not been successfully resolved because it is out of reach of the capability of quantum mechanic calculations. To understand the molecular interactions relevant to the catalytic process and catalyst design two different aspects of the system were modelled in this work. In Chapter 5 the objective of our calculations was to try and correctly predict the sense of enantio-discrimination of the reaction as observed experimentally by modelling the surface dimer proposed in the mechanistic model [2], whereas the effect of chemisorption on stability and structure of small ketone molecules was the focus of Chapters 6 and 7. The underlying aim of the modelling work was to discuss the implications for models of hydrogenation selectivity.

In this work and in agreement with most authors the enantioselective hydrogenation is taken to proceed through a two-step, two-cycle mechanism (refer to Chapter 2, section 2.2.11 for details) and that the enantio-differentiating transition state complex involves the adsorbed chiral modifier and the reactant molecule in a 1:1 stoichiometry [3-7]. By performing a series of *ab initio* HF calculations the conformation of CD was found to be important. Four different conformations of CD were stabilised: two each of the Open and Closed forms, in agreement with several experimental and theoretical reviews [8-10]. The most abundant conformer is the Open(3) form as it is calculated to consume 91% of a mixture whereas only 6% will be the Closed(1) CD. The other conformers, Closed(2) and Open(4) occupy only trace amounts. This implies that CD will adopt the Open(3) conformation, where the quinuclidine N points away from the quinoline moiety in the diastereomeric complex. The different conformations of CD are provided in figure 5.3(b) (Chapter 5, section 5.2.1). The start point geometries for the *ab initio* calculations were CD structures optimised with semi-empirical calculations employing the PM3 Hamiltonian. Initially it was thought that the lower theory level calculations could accurately model the conformations, but the stabilities of the CD

structures in comparison to literature models [8] showed that accuracy was lost at the expense of the rapid optimisation time. Good energies for the ground state configurations are essential to this work as the mechanistic model assumes enantioselectivity to be thermodynamically controlled, *i.e.* by the relative stabilities of the enantio-differentiating diastereomeric complexes.

As with CD the conformation of the reactant was also found to be essential to the structure and stability of the pro (*R*) and pro (*S*) diastereomeric complexes. For CD to appropriately interact with the reactant *via* a hydrogen bond as proposed in the model the quinuclidine N atom of the modifier must be protonated. In acidic media the relative proportions of the CD conformations are altered as the Closed structures were found to stabilise relative to the Open(3) CD. The concentration of the Closed(1) form was found to increase to 22% of the mixture, implying a definite presence on the catalytic surface. Only a marginal increase of 3% was observed for the Closed(2) CD and the stability of the Open(4) was not affected.

All four conformations of  $\text{CDH}^+$  were found to interact with the reactants in either its *s-cis* or *s-trans* form to give the corresponding complexes. However, only those complexes found to be the most abundant as well as fulfilling the geometric requirements of the mechanistic model [2] are the important dimers. For  $\text{CDH}^+$  adopting the Open(3) form and the EtPy the *s-cis* conformation, the complex yielding (*R*)-ethyl lactate upon hydrogenation is calculated to be more stable than the pro (*S*) complex by  $1.7 \text{ kJ mol}^{-1}$ , corresponding to 33% *ee*. These complexes are illustrated in figure 5.4 (Chapter 5, section 5.2.3). The calculated *ee* is considerably lower than the experimental value of 95% [11]. However, upon changing the conformation of EtPy to the *s-trans*, the energy difference between the two enantio-differentiating complexes increases to  $2 \text{ kJ mol}^{-1}$ , increasing the *ee* to 37%. This is despite the fact that the complexes (regardless of the conformation of the modifier) with the *s-cis* EtPy are considerably more stable than the corresponding *s-trans* complexes. The pro (*R*) complex for the hydrogenation of butan-2,3-dione is found to be analogous to the case of EtPy and the pro (*S*) is taken to be the Open(4) CD hydrogen bonded to the *s-cis* isomer. The energy difference between these complexes, given in figure 5.5(a) and 5.5(c) (Chapter 5, section 5.2.5), provides an *ee* of 98% and is larger than the experimental value of 50% [12]. The repulsion between the reactant and the anchoring group are found to play an important role for enantio-differentiation. The effect is more important for EtPy than the diketone as the substituents on the two carbonyl groups are

different. For either reactant the *s-cis* conformation is found to form a bifurcated hydrogen bond to the quinuclidine H of the protonated CD involving the O atoms of both carbonyl groups. The hydrogen bond distance to the *keto* group of EtPy is very slightly shorter for the pro (*R*) complex, implying that hydrogen addition to this complex in the case of *s-cis* EtPy could be favoured.

For these types of models the magnitude of the *ees* are secondary to being able to correctly predict the sense of selectivity for the reaction. With reference to Appendix A, a small error in the energy of the complex will lead to a large error in the calculated *ee* as the *ee* is exponentially related to the calculated energies. Two ways of improving the calculations within the reach of quantum mechanics is by introducing the effect of a solvent *via* a self-consistent reaction field model and by fixing the coordinates of the anchoring moieties of the CD and the reactant to simulate the geometric constraints imposed by the Pt surface. In an analogous study involving MtPy and the Open(3) CDH<sup>+</sup> such modifications to *ab initio* calculations were found to improve the reaction *ee* [2].

For the DFT study of the adsorption of ketone molecules on Pd and Pt(111) two common plane-wave codes: CASTEP and VASP were used. Calculations for the adsorption of ethene to the (111) surface of Pt was used as a test to identify which program would be most suitable for modelling the chemisorption of formaldehyde and acetone. Calculations with the CASTEP program found ethene to adsorb on the surface in four different geometries, the most stable of which were the di- $\sigma$  (in agreement with experimental EELS [13], UPS [14] and NEXAFS [15,16] data) and the two atop modes: atop-bridge and atop-hollow, for which similar adsorption energies were calculated. The least stable site was the cross-bridge, which realistically would probably not be observed under experimental conditions. The structures for these adsorption sites are illustrated in figure 6.3 (Chapter 6, section 6.1).

In comparison to the analogous study performed with the VASP code by Watson *et al.* [17], the trend in adsorption modelled by CASTEP was in full agreement although the calculated adsorption energies were overestimated by between 10-20%. Although the same computational procedure was used in both studies, the CASTEP calculations differed by the type of Vanderbilt US-PPs employed. In Watson's VASP work GGA derived US-PPs were combined with gradient corrected DFT calculations [17] whereas in the CASTEP calculations LDA US-PPs were used instead. The LDA functionality is



found to be responsible for the overestimation in adsorption, as it is known to increase cohesion energies and bond lengths and energies [18]. The GGA corrections in the DFT calculations do not rectify the problem in the CASTEP models. Since user selection for PPs is restricted in the 4.2 release of the CASTEP code (used in our calculations), it is anticipated that this problem of over binding will be consistent for surface adsorption calculations. However, it must be noted that this could possibly be rectified in the more recent versions of the code and it is recommended that atom US-PPs files are viewed in particular the information regarding the tests performed to validate the PPs. This preliminary work emphasised the use of VASP to obtained better energies than CASTEP as Watson *et al.* [17] found the adsorption energies for ethene over Pt(111) to be in agreement with the available thermodynamic data.

On modelling formaldehyde and acetone to the (111) surface of Pd and Pt a rough idea of the adsorption characteristics was obtained with CASTEP, whereas with VASP a more accurate description of the adsorption geometry and stability was gained as accurate PAW-PPs were employed in the calculations. At low temperature conditions surface science experiments [19-22] have rationalised two adsorption geometries for aldehydes and ketones: the endon,  $\eta^1(\text{O})$  and the di- $\sigma$ ,  $\eta^2(\text{C},\text{O})$  mode. For formaldehyde both of these coordinations were modelled on both the metal surfaces by both programs. In each case the di- $\sigma$  was stabilised over the endon and the adsorption was preferred on the Pt surface. The respective CASTEP adsorption energy for the di- $\sigma$  on Pd and Pt(111) was calculated to be 60.3 and 77.6 kJ mol<sup>-1</sup>, whereas with VASP the energies were reduced to roughly 54 and 70 kJ mol<sup>-1</sup>. This energy difference implies there is barrier to adsorption from the endon to the di- $\sigma$  adsorbed state. Barrier calculations showed the direct adsorption of the di- $\sigma$  mode to be an activated process on Pt(111) requiring a small activation energy of roughly 6 kJ mol<sup>-1</sup>. The barrier for adsorption on the Pd surface was calculated to be much smaller at 2 kJ mol<sup>-1</sup>. The activation energies confirm the stability of the endon mode at low temperature and the rapid conversion between the adsorbed states determined under experimental conditions [19,23,24].

Our adsorption energies for formaldehyde are found to contradict the values derived in a number of studies. Experimental TPD reports the adsorption on both the metals to be the same, between 51-52 kJ mol<sup>-1</sup> [19,23], whilst the theoretical calculations of Desai *et al.* [25] and Delbecq and Sautet [26,27] stabilise the di- $\sigma$  mode on the Pd surface. A

poor comparison against these modelling studies against our own periodic calculations can be accounted for by the use of different levels of theory and different surface unit cell size. The TPD assignment is also found to correspond to the formyl adsorbed species and not molecular formaldehyde as modelled in our calculations, as this is the most likely species involved in the reaction of formaldehyde on the Pd and Pt(111) surface [19,23].

With acetone two different isomers can be present on the surface of metals: the *keto* or the *enol* as tautomerism readily occurs under acid or base conditions [28]. In the gas-phase both CASTEP and VASP was found to stabilise the *keto* form, which is significant as it implies that any adsorption process for catalysis involving any activated ketone will begin with this isomer interacting with the surface first. Only the  $\eta^1(\text{O})$  adsorption mode for the *keto* isomer was stabilised on the surfaces with CASTEP as illustrated in figure 6.9 (Chapter 6, section 6.3) and the di- $\sigma$  did not form even if the starting structure in the calculation was biased towards it. The VASP program however optimised both the adsorption modes as seen in figure 7.4 (Chapter 7, section 7.3) and in agreement with the CASTEP modelling the adsorption to the Pt surface was predominant. The CASTEP adsorption energy for the endon mode on Pt was calculated to be roughly  $43 \text{ kJ mol}^{-1}$  and was found to be in agreement with the energy derived from TDS [29,30] and the cluster calculations of Delbecq *et al.* [27]. In our CASTEP models the extended electronic states of the surfaces are poorly represented due to the use of a low number *k*-points in the calculations and that is why comparison is good with the cluster method. For the VASP structures the energetic ordering of the *keto* adsorptions were found to be reversed to that modelled for formaldehyde as the  $\eta^1(\text{O})$  is stabilised over the  $\eta^2(\text{C},\text{O})$  mode. It is likely that the steric interaction of the methyl groups with the (111) surface is responsible for destabilising the  $\eta^2(\text{C},\text{O})$  structure for acetone and therefore will be common to any substituted ketone adsorbed parallel to the surface. Both the  $\eta^1(\text{O})$  and the  $\eta^2(\text{C},\text{O})$  adsorption energies on Pt are calculated by VASP to be roughly  $10 \text{ kJ mol}^{-1}$  more strongly adsorbed than the Pd surface. The activation energy required for the inter-conversion of the *keto* isomer from the endon to the di- $\sigma$  mode on Pt was found to be  $10 \text{ kJ mol}^{-1}$  and in agreement with the experimental finding of the stabilisation of the endon mode below 220 K [29,31,32]. No barrier was calculated for the Pd(111) supporting the rapid conversion observed for this surface between the two adsorbed states above 200 K [20].

For both the periodic codes the *enol* isomer of acetone was found to adsorb onto both the metal surfaces but the energetics and the coordination geometries differed. With CASTEP, the interaction on the Pt surface *via* a  $\eta^1(\text{C})$  alkyl alcohol geometry was favoured with an adsorption energy of  $66.5 \text{ kJ mol}^{-1}$  over the  $\eta^2(\text{C,C})$  mode for the Pd. These geometries are illustrated in figure 6.10 (Chapter 6, section 6.3). However, with VASP the *enol* was found to stabilise in a  $\eta^2(\text{C,C})$  geometry only. In this case the bonding was much stronger as reflected in the calculated adsorption energies ( $28.5$  and  $74.6 \text{ kJ mol}^{-1}$  for Pd and Pt, respectively) than that found for the corresponding CASTEP adsorption (figure 6.10(a) (Chapter 6, section 6.3)) as the molecule was coordinated to two separate surface sites (figure 7.7 (Chapter 7, section 7.3) as opposed to a central atom site observed for the CASTEP geometry. The calculations show the adsorption energy in the *enol* form to be sufficient to compensate for the gas-phase energy difference between the *keto* and *enol* isomers, suggesting that thermodynamically the *enol* form will be favoured on surfaces of metal catalysts.

With the likelihood of the *enol* being present as an intermediate, a weaker enolate was found to adsorb in a  $\eta^1(\text{C})$  geometry on both the surfaces with a strong preference for the Pt site (figure 7.8 (Chapter 7, section 7.3). This implies that acetone can readily deprotonate on the clean Pd and Pt surfaces even at the low temperatures of typical surface science experiments to give the enolate. This may not be unreasonable since similar species have recently been observed on the (111) surface of Ni [33]. Barrier calculations show that an activation energy of  $51 \text{ kJ mol}^{-1}$  would be required to reform the ketone once the enolate is formed on the Pt surface. It can be assumed that this backward barrier is much higher than the forward barrier as the enolate is stabilised over the ketone.

Experimentally, TPD data reports a secondary, di- $\sigma$  adsorbed species of *keto* acetone to be more strongly bound than the endon geometry on both Pd [29] and Pt(111) [30], which is not supported by our own calculations. The TPD adsorption energies of  $48$  and  $49 \text{ kJ mol}^{-1}$  are found to correspond to the adsorption energies of the adsorbed enolate species, in which the proton occupies a *hcp* hollow site. In doing so, it appears that the second adsorbed species observed in the surface science experiments for acetone on Pd and Pt(111) is not the di- $\sigma$  bound *keto* or *enol* acetone but the corresponding enolate and therefore the assignment made by Avery is incorrect.

Further studies confirm this by showing the calculated vibrational frequencies of the enolate to be in agreement with the experimental spectra [34].

In reference to the dimer model used to predict selectivity in enantioselective hydrogenation, the pyruvate ester is thought to adsorb *via* the ketone groups parallel to the surface [2]. However, our calculations indicate otherwise, as it is more than likely that the role of the modifier is to interact with an endon adsorbed ketone group. This interaction is expected to tilt the plane of the molecule towards the surface, thereby allowing hydrogenation to take place.

From our calculations we can conclude that the dominant species for the ketones is the endon geometry and that, although the *enol* is thermodynamically preferred it may not be kinetically accessible. However, both the *enol* and enolate species will be present on the Pd and Pt surface during the hydrogenation of ketones. In the case of MtPy hydrogenation on Pt the kinetic studies of Wells *et al.* [35] (discussed in Chapters 2 and 5, sections 2.2.3 and 5.5) suggest that these species are spectators or lead to side products. However, over Pd deuteration of the methyl group is observed and so there must be hydrogenation through the *enol* or enolate species. Competitive hydrogenation of the ketone and *enol/enolate* may explain the lower *ee* observed for Pd.

One of the major conclusions to be drawn from this work is the fact that CASTEP is a good program to qualitatively examine the nature of chemisorption of surface intermediates key to catalysis. More quantitative data can be achieved with the use of the alternative plane-wave program VASP. Older versions of CASTEP are found to restrict the level of accuracy employed to describe atom centres whereas with VASP a comprehensive library of PPs is available. Unlike VASP, which is interfaced with the NEB algorithm, no facility is available with CASTEP to study transition states. However, for inexperienced users CASTEP is recommended as it has graphical interface allowing automatic generation of input files, with VASP the files have to be manually created. For such reasons it is therefore highly recommended that the continued use of VASP should be perused in future works.

At present the mechanistic work in the literature regarding the surface adsorbed dimer concentrates on the interaction between the most stable conformation of the modifier and the *s-cis* and *s-trans* conformation of the pyruvate. There is no mention of the *enol*, despite the fact that reference to the modifier-*enol* complex has been proposed for sometime [35,36]. It would be interesting to model the corresponding *s-cis* and *s-trans* EtPy *enol* CD complexes as illustrated in figure 5.8(a) (Chapter 5, section 5.5),

and to analyse the stability and the energetics of them over the pro (*R*) and pro (*S*) complexes to help clarify the role of the *enol*. This could also be extended to the butan-2,3-dione system *via* the complex shown in figure 5.8(b) (Chapter 5, section 5.5).

For the surface calculations a thorough investigation of all of the possible adsorption modes of the acetone enolate species is required, as so far only preliminary calculations have been performed. To build on the conclusions drawn from the modelling work of the CDH<sup>+</sup>-diketone diastereomeric complexes (Chapter 5, section 5.2.4), the interaction of the butan-2,3-dione with the (111) surface of Pd and Pt can be investigated. Initial calculations are presented in Chapter 7, section 7.6 and at present adsorption data for the *s-trans keto* isomer as well as the *enol* and enolate species is missing. Where necessary barrier calculations to locate transition states should also be conducted to examine the kinetic interchange of adsorbed species on the surfaces.

It would also be of prime interest to investigate the adsorption of ketones to surfaces that accurately represent catalytic planes such as those consisting of steps and defects. In the literature the adsorption of ketones to these sites is favoured over a flat terrace [27]. In this work clean surfaces for Pd and Pt were used so to simplify the DFT calculations.

## 8.1. References

- [1] A. Baiker, *J. Mol. Catal. A: Chemical*, **163**, 205, (2000).
- [2] T. Bürgi and A. Baiker, *J. Catal.*, **194**, 445, (2000).
- [3] T. J. Wehrli, Ph. D Thesis ETH-Zürich, No. 8833, (1989).
- [4] M. Garland, H. -U. Blaser, *J. Am. Chem. Soc.*, **112**, 7048, (1990).
- [5] J. Wang, C. LeBlond, C. F. Orella, Y. Sun, J. S. Bradley, D. G. Blackmond, *Stud. Surf. Sci.*, **108**, 183, (1997).
- [6] D. Blackmond, *CATTECH* **3**, 17, (1998).
- [7] H. -U. Blaser, H. P. Jalett, M. Garland, M. Studer, H. Thies, A. Wirth-Tijani, *J. Catal.*, **173**, 282, (1998).
- [8] T. Bürgi and A. Baiker, *J. Am. Chem. Soc.*, **120**, 12920, (1998).
- [9] J. L. Margitfalvi and E. Tfirst, *J. Mol. Catal. A.*, **139**, 81, (1999).
- [10] J. L. Margitfalvi, P. Marti, A. Baiker, L. Bötzt and O. Sticher, *Catal. Lett.*, **6**, 281, (1990).
- [11] H. -U. Blaser, H. P. Jalett and J. Wiehl, *J. Mol. Catal.*, **68**, 215, (1991).
- [12] J. A. Slipszenko, S. P. Griffiths, P. Johnston, K. E. Simons, W. A. H. Vermeer and P. B. Wells, *J. Catal.*, **179**, 267, (1998).
- [13] H. Steininger, H. Ibach and S. Lehwald, *Surf. Sci.*, **117**, 685, (1982).
- [14] T. E. Felter and W. H. Weinberg, *Surf. Sci.*, **103**, 265, (1981).
- [15] J. Stohr, F. Sette and A. L. Johnson, *Phys. Rev. Lett.*, **53**, 1684, (1984).
- [16] J. A. Horsley, J. Stohr and R. J. Koestner, *J. Chem. Phys.*, **83**, 3146, (1985).
- [17] G. W. Watson, R. P. K. Wells, D. J. Willock and G. J. Hutchings, *J. Phys. Chem. B*, **104**, 6439, (2000).
- [18] R. O. Jones and O. Gunnarsson, *Rev. Mod. Phys.*, **61**, 689, (1989).
- [19] J. L. Davis and M. A. Barteau, *J. Am. Chem. Soc.*, **111**, 1782, (1989).
- [20] J. L. Davis and M. A. Barteau, *Surf. Sci.*, **208**, 383, (1989).
- [21] J. L. Davis and M. A. Barteau, *Surf. Sci.*, **235**, 235, (1990).
- [22] M. A. Barteau, *Catal. Lett.*, **8**, 175, (1991).
- [23] N. M. Abbas and R. J. Madix, *J. Appl. Surf. Sci.*, **7**, 241, (1981).
- [24] M. A. Henderson, G. E. Mitchell and J. M. White, *Surf. Sci.*, **188**, 206, (1987).
- [25] S. K. Desai, M. Neurock and K. Kourtakis, *J. Phys. Chem. B*, **106**, 2559, (2002).
- [26] F. Delbecq and P. Sautet, *Langmuir*, **9**, 197, (1993).
- [27] F. Delbecq and P. Sautet, *Surf. Sci.*, **295**, 353, (1993).

- [28] Z. Rappoport, in “*The Chemistry of Enols*”, Wiley, Chichester, West Sussex, (1990).
- [29] N. R. Avery, *Surf. Sci.*, **125**, 771, (1983).
- [30] M. A. Vannice, W. Erley and H. Ibach, *Surf. Sci.*, **254**, 1, (1991).
- [31] N. R. Avery, W. H. Weinberg, A. B. Anton and B. H. Toby, *Phys. Rev. Lett.*, **51**, 682, (1983).
- [32] N. R. Avery, *Langmuir*, **1**, 162, (1985).
- [33] W. -S. Sim, T. -C. Li, P. -X. Yang and B. -S. Yeo, *J. Am. Chem. Soc.*, **124**, 4970, (2002).
- [34] *Forthcoming*, E. L. Jeffery, R. K. Mann, G. J. Hutchings, S. H. Taylor and D. J. Willock, *Catal. Today*, (2005).
- [35] G. W. Watson, R. P. K. Wells, D. J. Willock and G. J. Hutchings, *J. Chem. Soc., Chem. Commun.*, 705, (2000).
- [36] A. Solladié-Cavallo, C. Marsol, F. Hoernel and F. Garin, *Tetrahedron Lett.*, **42**, 4741, (2001).

.

## ***Appendix A***

### ***Derivation of Relative Concentrations of Cinchonidine and Cinchonidine-Reactant Complexes***



## A.1. Kinetic Model

We have calculated the relative energies of the various conformations of the CD and pyruvate esters. Under thermodynamic equilibrium these energies allow us to estimate the relative concentrations for each species. For example if we have a concentration  $C_m$  of modifier and use the normal chemical notation of [O3] *etc* for concentrations we have:

$$[C1] + [C2] + [O3] + [O4] = C_m \quad (\text{Equation A.1})$$

The Gaussian calculations find that the Open(3) conformation is the most stable and so we have quoted the energies with reference to this conformer. The other concentrations can be estimated from their energy differences to conformer O3 *via*:

$$\frac{[X]}{[O3]} = \exp\left(-\frac{E_x}{RT}\right) \quad (\text{Equation A.2})$$

where  $[X]$  represents a general conformers concentration,  $E_x$  is the activation energy for the conformers,  $R$  is the gas constant at  $8.32 \text{ J K}^{-1} \text{ mol}^{-1}$  and  $T$  is the temperature in K.

For [O3] itself we can then re-arrange equation A.1 to give:

$$[O3] = \frac{C_m}{1 + \sum_{x \neq O3} \exp\left(-\frac{E_x}{RT}\right)} \quad (\text{Equation A.3})$$

The denominator here is the partition function for the system of conformers defined as:

$$Z = \sum_x \exp\left(-\frac{E_x}{RT}\right) \quad (\text{Equation A.4})$$

Then any conformation concentration can be estimated using:

$$[X] = \frac{C_m}{Z} \exp\left(-\frac{E_x}{RT}\right) \quad (\text{Equation A.5})$$

A similar procedure can be used for the pyruvate esters so that the calculated energies

can be used to estimate the equilibrium concentration of both the modifier and reactant. Then we can work out the relative concentrations of the intermediate dimers based on reaction schemes between the modifier and adsorbate *i.e.*



$$K = \frac{[X \cdots \text{EtPy}]}{[X][\text{EtPy}]} \quad (\text{Equation A.7})$$

K is related to the complexation energies for each dimer since:

$$\Delta G = -RT \ln(K) \quad (\text{Equation A.8})$$

So

$$K = \exp\left(-\frac{\Delta G}{RT}\right) \quad (\text{Equation A.9})$$

and

$$[X \cdots \text{EtPy}] = [X][\text{EtPy}] \exp\left(-\frac{\Delta G}{RT}\right) \quad (\text{Equation A.10})$$

To use this formula we make the assumption that the interaction energy is the determining factor in the free energy differences between alternative complexes.

## ***Appendix B***

***Vanderbilt Ultrasoft-Pseudopotentials  
Employed in CASTEP Calculations***

The following LDA derived Vanderbilt US-PPs were employed in the CASTEP surface adsorbate calculations for comparison tests with VASP in this thesis. The PPs are obtained from the Cerius<sup>2</sup> 4.6 resource library and are distributed by Accelrys, refer to <http://www.accelrys.com/cerius2/castep.html> for details. PPs for Pd and O were obtained from the same source. Note that only the information regarding the parameters used for the generation of the PPs and the tests performed to verify them are supplied here. For the actual output of the calculations refer to the relevant PP files.

The US-PPs are generated using the method as specified in article: D. Vanderbilt, *Phys. Rev. B*, **41**, 7892, (1990).

**B.1. Pt US-PP**

START COMMENT

180 COARSE  
220 MEDIUM  
250 FINE

Ultrasoft potential generated using the setting  
suggested by Prof. Lee group (mhl\_01).

```
=====
| pseudopotential report: version 7.2.1 date 4-22-1998 |
=====
| Pt                      ceperley-alder exchange-corr |
| z = 78.      zv = 10.    exfact = .00000             |
|                                     etot = -52.44998      |
| index      orbital      occupation      energy       |
| 1          520          9.00          -.47            |
| 2          600          1.00          -.44            |
| keyps = 3      ifpcor = 0                      |
| rinner =      1.00      for L= 1                |
| rinner =      1.00      for L= 2                |
| rinner =      1.00      for L= 3                |
| rinner =      1.00      for L= 4                |
| rinner =      1.00      for L= 5                |
| new generation scheme:                          |
| nbeta = 3      kkbeta = 683      rcloc = 2.3000      |
| ibeta  1      epsilon rcut                          |
| 1      0      -.44  2.40                          |
| 2      2      -.47  2.40                          |
| 3      2      .00  2.40                          |
| lloc   = 1  eloc   = .000                          |
| ifqopt = 3  nqf    = 8  qtryc = 9.000              |
| all electron calculation used koelling-harmon equation |
| *****logarithmic mesh*****                    |
=====
```

## Convergence test

Pt2 dimer, orthorombic cell, a=6.05, b=5.95, c=6.00 Angstrom, LDA  
Fractional coordinates:  
(0.67749 0.75362 0.70509) and (0.47954 0.42286 0.46157)

```
=====
| Ecut      Etot      dE      Force on atom 1      |
| (eV)      (eV)      (eV/atom)      (eV/A)      |
=====
180 (COARSE) -1429.586  1.301  -1.37210  -1.79124  -1.66906
220 (MEDIUM) -1432.071  0.059  -1.47510  -1.91270  -1.66469
250 (FINE)   -1432.158  0.015  -1.42610  -1.89596  -1.69043
280 (PRECISE) -1432.180  0.004  -1.42941  -1.92295  -1.66215
320          -1432.183  0.003  -1.42366  -1.91638  -1.66030
400          -1432.184  0.002  -1.43051  -1.91724  -1.68449
450          -1432.186  0.001  -1.42893  -1.91642  -1.68151
800          -1432.188        -1.42924  -1.91723  -1.68369
=====
```

## Validation test

-----  
 #1 Pt metal, exp. lattice constant a=3.9239, CASTEP gives  
 (GGA, PRECISE cutoff) 3.971 (+1.2%).

#2 PtS (SG 131), exp. lattice constants a=3.48, c=6.11,  
 CASTEP gives (GGA, FINE cutoff) 3.515 (+1.0%) and 6.120 (+0.2%).

END COMMENT

## B.2. C US-PP

START COMMENT

200 COARSE  
 240 MEDIUM  
 280 FINE

Ultrasoft potential generated using the setting suggested by  
 Prof. Lee's group (crhsing).

```
=====
| pseudopotential report: version 7.2.1 date 4-22-1998 |
=====
| C                      ceperley-alder exchange-corr |
| z = 6.      zv = 4.      exfact = .00000           |
|                      etot = -10.68750             |
| index      orbital      occupation      energy      |
| 1          200          2.00          -1.00         |
| 2          210          2.00          -.40          |
| keyps = 3      ifpcor = 0                    |
| rinner =      1.25      for L= 1              |
| rinner =      1.25      for L= 2              |
| rinner =      1.25      for L= 3              |
| new generation scheme:                        |
| nbeta = 4      kkbeta = 491      rcloc = 1.4000   |
| ibeta  1      epsilon rcut                    |
| 1       0      -1.00  1.40                     |
| 2       0       .50  1.40                     |
| 3       1      -.40  1.40                     |
| 4       1       .50  1.40                     |
| lloc   = 2      eloc   = .000                  |
| ifqopt = 3      nqf    = 8      qtryc = 10.000   |
| all electron calculation used koelling-harmon equation |
| *****logarithmic mesh*****                  |
=====
```

### Convergence test

-----  
 C2 dimer, orthorhombic cell, a=6.05, b=5.95, c=6.00 Angstrom  
 Fractional coordinates:  
 (0.64976 0.66268 0.65618) and (0.50726 0.51379 0.51048)

```
=====
| Ecut      Etot      dE      Force on atom 1      |
| (eV)      (eV)      (eV/atom)      (eV/A)      |
|-----|-----|-----|-----|
| 200 (COARSE) -297.888 0.672 -3.32704 -3.41086 -3.46849 |
| 240 (MEDIUM) -298.877 0.178 -3.59403 -3.69566 -3.66421 |
|-----|-----|-----|-----|
```

280 (FINE)	-299.126	0.053	-3.72837	-3.82055	-3.78202
310 (PRECISE)	-299.194	0.019	-3.76030	-3.86332	-3.81163
320	-299.206	0.012	-3.77009	-3.86986	-3.82002
400	-299.222	0.004	-3.78072	-3.88005	-3.82796
450	-299.223	0.004	-3.78155	-3.88078	-3.82871
800	-299.231		-3.78596	-3.88734	-3.83780

=====

## Validation test

-----

#1 Diamond, exp. lattice constant a=3.556, CASTEP with GGA  
(PRECISE cutoff) gives 3.539 (-0.5%)

#2 WC, exp. lattice constants a=2.906, c=2.837, CASTEP with GGA  
(PRECISE cutoff) gives 2.949 (+1.5%) and 2.873 (+1.3%)

#3 Graphite, exp. lattice constants a=2.46, c=6.8, CASTEP with GGA  
(PRECISE cutoff) gives 2.439 (-0.9%) and 7.109 (+4.5%)

#4 CO molecule, exp. bond length 1.1238, CASTEP with GGA  
(PRECISE cutoff) gives 1.1440 (+1.7%)

#5 UC2 (SG 87), exp. a=3.517, c=5.987, CASTEP (GGA, PRECISE)  
gives 3.524 (+0.2%) and 5.946 (-0.7%)

END COMMENT

**B.3. H US-PP**

START COMMENT

140 COARSE  
180 MEDIUM  
230 FINE

```
=====
| pseudopotential report: version 7.3.2 date 5- 5-1999 |
|-----|
| H                                ceperley-alder exchange-corr |
| z = 1.      zv = 1.      exfact = 0.00000                    |
|                                           etot = -0.89175      |
| index      orbital      occupation      energy              |
| 1          100          1.00          -0.47                |
| keyps = 3      ifpcor = 0                                |
| rinner = 0.60      for L= 1                                |
| new generation scheme:                                |
| nbeta = 2      kkbeta = 353      rcloc = 0.8000            |
| ibeta  1      epsilon      rcut                                |
| 1          0          -0.47      0.80                      |
| 2          0          0.50      0.80                      |
| lloc = 1      eloc = 0.000                                |
| ifqopt = 3      nqf = 6      qtryc = 9.000                |
| all electron calculation used koelling-harmon equation    |
| *****logarithmic mesh*****                             |
|-----|
=====
```

## Convergence test

-----

H2 dimer, orthorombic cell, a=6.05, b=5.95, c=6.00 Angstrom

Fractional coordinates:

(0.612294 0.622585 0.617397) and (0.544730 0.553885 0.549270)

=====					
Ecutoff (eV)	Etot (eV)	dE (eV/atom)	Force on atom 1 (eV/A)		
-----					
140	-30.183	0.342	1.87436	1.83226	1.85254
180	-30.603	0.132	1.39777	1.37852	1.38307
220	-30.750	0.058	1.36066	1.35873	1.37392
240	-30.800	0.034	1.36988	1.37669	1.37374
250	-30.810	0.029	1.38434	1.38151	1.38312
280	-30.845	0.011	1.40685	1.40778	1.40663
300	-30.850	0.008	1.41075	1.41136	1.41158
340	-30.859	0.004	1.43175	1.43275	1.43090
600	-30.867		1.43939	1.43735	1.43892
=====					

#### Validation test

-----  
 #1 H2 dimer, exp. bond length 0.7414, CASTEP (GGA, PRECISE)  
 gives 0.7517 (+1.4%)

END COMMENT



## ***Appendix C***

### ***Projector Augmented-Wave Pseudopotentials Employed in VASP Calculations***

In this work the VASP surface calculations were conducted using novel GGA generated PAW-PPs. The PP's were obtained from the file server:

[http://cms.mpi.univie.ac.at/~vasp/pot\\_GGA/potcar.date.tar](http://cms.mpi.univie.ac.at/~vasp/pot_GGA/potcar.date.tar)

Further information can be obtained by referring to section 11.2 in the VASP manual, which can be retrieved from: <http://cms.mpi.univie.ac.at/VASP/>.

Listed over leaf are the relevant details about the parameters used to generate the atom PP's for Pt, C and H, the actual output of the calculations are not specified but can be found appended after the information provided here in the corresponding files. The additional PP's for Pd and O used in this work were also obtained from the same source.

The PAW-PP's are generated using the method specified in the following articles: G. Kresse and D. Joubert, *Phys. Rev. B*, **59**, 1758, (1999) and P. E. Blöchl, *Phys. Rev. B*, **50**, 17953, (1994).

**C.1. Pt PAW-PP**

START COMMENT

10.000000000000000000

parameters from PSCTR are:

VRHFIN =Pt: s1d9

LEXCH = 91

EATOM = 730.0441 eV, 53.6567 Ry

TITEL = PAW Pt

LULTRA = F use ultrasoft PP ?

IUNSCR = 1 unscreen: 0-lin 1-nonlin 2-no

RPACOR = 2.330 partial core radius

POMASS = 195.080; ZVAL = 10.000 mass and valenz

RCORE = 2.500 outmost cutoff radius

RWIGS = 2.750; RWIGS = 1.455 wigner-seitz radius (au A)

ENMAX = 230.277; ENMIN = 172.708 eV

RCLOC = 1.896 cutoff for local pot

LCOR = T correct aug charges

LPAW = T paw PP

EAUG = 358.966

DEXC = -.016

RMAX = 3.038 core radius for proj-oper

RAUG = 1.300 factor for augmentation sphere

RDEP = 2.590 core radius for depl-charge

QCUT = -4.114; QGAM = 8.228 optimization parameters

END COMMENT

**C.2. C PAW-PP**

START COMMENT

4.000000000000000000

parameters from PSCTR are:

VRHFIN =C: s2p2

LEXCH = 91

EATOM = 147.4688 eV, 10.8386 Ry

TITEL = PAW C

LULTRA = F use ultrasoft PP ?

IUNSCR = 0 unscreen: 0-lin 1-nonlin 2-no

RPACOR = .000 partial core radius

POMASS = 12.011; ZVAL = 4.000 mass and valenz

RCORE = 1.500 outmost cutoff radius

RWIGS = 1.630; RWIGS = .863 wigner-seitz radius (au A)

ENMAX = 400.000; ENMIN = 300.000 eV

ICORE = 2 local potential

LCOR = T correct aug charges

LPAW = T paw PP

EAUG = 644.873

DEXC = .000

RMAX = 2.266 core radius for proj-oper

RAUG = 1.300 factor for augmentation sphere

RDEP = 1.501 radius for radial grids

RDEPT = 1.300 core radius for aug-charge

```

QCUT   =   -5.516; QGAM   =   11.033   optimization parameters
END COMMENT

```

### C.3. H PAW-PP

```

START COMMENT

```

```

1.00000000000000000000
parameters from PSCTR are:
  VRHFIN =H: ultrasoft test
  LEXCH  = 91
  EATOM  =   12.5313 eV,      .9210 Ry

  TITEL  = PAW H
  LULTRA =          F      use ultrasoft PP ?
  IUNSCR =          0      unscreen: 0-lin 1-nonlin 2-no
  RPACOR =         .000    partial core radius
  POMASS =   1.000; ZVAL  =   1.000    mass and valenz
  RCORE  =   1.100    outmost cutoff radius
  RWIGS  =   .700; RWIGS =   .370    wigner-seitz radius (au A)
  ENMAX  = 250.000; ENMIN = 200.000 eV
  RCLOC  =   .701    cutoff for local pot
  LCOR   =          T      correct aug charges
  LPAW   =          T      paw PP
  EAUG   = 400.000
  RMAX   =   2.174    core radius for proj-oper
  RAUG   =   1.200    factor for augmentation sphere
  RDEP   =   1.112    core radius for depl-charge
  QCUT   =  -5.749; QGAM  =   11.498    optimization parameters

```

```

END COMMENT

```

